Dissertation

Formation and Electronic Properties of In_2S_3/ $Cu(In,Ga)Se_2$ Junctions and Related Thin Film Solar Cells

Paul Pistor
2009

Im Fachbereich Physik der Freien Universität Berlin eingereichte
Dissertation

Eingereicht am 29. Mai 2009.
Verteidigt am 03. Juli 2009.

1. Gutachter: Frau Prof. M.C. Lux-Steiner
2. Gutachter: Herr Prof. W. Brewer

Contents

Chapter 1

Introduction

The Photovoltaic industry is approaching an important turning point, changing from a young new-comer industry into a more mature industrial branch. From being an industry with a highly subsidised market it is gradually turning into a more economically self-sustaining one. Decreasing production costs, growing market demand and the aid of political promotion have led to an explosive growth of the photovoltaic market during the last decade. With average growth rates of over 40 %/a since 2002, solar cell production is currently one of the fastest growing industries [1]. In 2007, the annual solar cell production increased by 68% (reaching 4 GWp [1]) with respect to the preceeding year [2].

As by 2007, more than 60 countries have had a policy to promote renewable energies in forms of feed-in tariffs, capital subsidies, grants or other promotional programs [3]. Feed-in tariffs had been enacted by 46 countries/states in 2007, with more than half of them coming into effect after 2002 [3].

The key issue for the photovoltaic industry at this point is a drastic decrease of the production costs in order to liberate itself from political incentive programs and enter the mainstream market. The aim is grid parity, the point where photovoltaic (PV) electricity can directly compete with conventional electricity prices. Under the assumption of a cost reduction in the order of 10% per year, the Solar Energy Report 2008 of the Sarasin Bank [2] expects average high growth rates of 25-30% per year for the upcoming decade. Cost reduction in terms of production costs per Wp can be achieved with upscaling effects, technological improvements (less material consumption, improved efficiencies, faster cycle times) or new technologies.

Chalcopyrite solar cells based on thin film deposition techniques are one of these new technologies with high cost reduction potential and an increasing number of companies now entering the market. In the standard configuration, the chalcopyrite solar cell requires a buffer layer between the p-type absorber and the n^+-type transparent front contact for an optimal pn-junction formation. Although the role of the buffer layer is still controversially discussed, the trend of the discussion within the scientific community is to attribute the beneficial effects of the buffer layer to improved interface properties and band alignment at the buffer/absorber junction as compared to a junction formed directly between absorber

---

[1] Wp: Watt peak- Measure of the rated maximum output power for a solar cell/module which is measured under standard testing conditions

and front contact. In practice, today nearly all industrial concepts use CdS deposited by chemical bath deposition as a buffer layer. An alternative to this buffer layer would be desirable and is the focus of substantial research activity due to several reasons including: potential future legislative and marketing concerns by incorporating the heavy metal Cd into solar cells, the absorption losses caused by the CdS layer and the incompatibility of the wet-chemical process step of the chemical bath deposition with the otherwise fully vacuum-based process steps of the standard solar cell fabrication. One of the candidates for a substitution of CdS is In_2S_3, and promising results have been achieved in the past using In_2S_3 as a buffer layer in Cu(In,Ga)Se_2 thin film solar cells (14.8 %: Cu(In,Ga)Se_2 devices with an evaporated In_2S_3 buffer, Strohm et al. [4]). The motivation of this work is to backup the promising empirical work with a systematic analysis and characterisation of Cu(In,Ga)Se_2 solar cells with an In_2S_3 buffer layer deposited by thermal evaporation.

The aims of this work can be summarised as follows:

1. Prepare highly efficient, state of the art Cu(In,Ga)Se_2 solar cells with an evaporated In_2S_3 buffer layer.
2. Identify factors limiting the performance of such a device through a systematic characterisation of the electronic properties of these solar cells.
3. Study the junction formation and interdiffusion phenomena between the In_2S_3 buffer layer and the Cu(In,Ga)Se_2 absorber with surface and bulk sensitive analysis methods.

In the following, a brief description of the structure of this dissertation and the content of the individual chapters is given.

In the beginning, in **Chapter 2** an introduction into the state of the art of chalcopyrite solar cells is presented. This includes the standard preparation techniques and material properties of the layers constituting the standard Cu(In,Ga)Se_2 solar cells with CdS buffer used as references in this work, the role of the buffer and work done on alternative buffer layers in the past.

This is followed in **Chapter 3** by the theoretical background necessary for the interpretation of the relevant solar cell parameters and the fundamental equations involved.

In **Chapter 4**, a description of the general material properties of In_2S_3 is given, including the phase diagram and crystal structure of In_2S_3 as reported in the literature. The details of the crystal structure are important for the identification of crystalline phases in In_2S_3 powders used as source materials in the thin film deposition process as well as for the interpretation of the diffusion phenomena observed in In_2S_3 thin films. From In_2S_3 reference powders synthesised during the course of this work, suitable references for X-ray diffraction (XRD) measurements are obtained. Based on the literature data, the crystal structure of the In_2S_3 reference powders are analysed in detail by a Rietveld refinement of the X-ray diffraction data. The full set of refined parameters can be found in Annex B. The structure and elemental composition of three commercial In_2S_3 powders is compared before testing their applicability as source materials in a thin film deposition process. In_2S_3 thin films are prepared by thermal evaporation of the three commercial In_2S_3 powders and examined for their structural, chemical and optical properties.

Chapter 5 discusses the performance and electronic properties of Cu(In,Ga)Se_2 solar cells prepared with In_2S_3 buffer layers in comparison with CdS references. In the beginning, the preparation and optimisation of In_2S_3 buffer layers are presented. In particular, the influence of the application of the different commercial In_2S_3 source materials on the device performance and the effect of post deposition annealing is investigated. This is followed by a physical interpretation of the individual solar cell parameters before and after various annealing steps including the spectrally resolved examination of the collection of photo-generated charge carriers (quantum efficiency) to evaluate changes in the short circuit current, a thorough analysis of the diode characteristics of the current-voltage response in the dark and an investigation of the dominant recombination mechanism by means of an illumination- and temperature-dependent current-voltage analysis ($jV(T)$).

Chapter 6 establishes interdiffusion as a prerequisite for the formation of a junction with low recombination. In particular, the diffusion of Cu from the Cu(In,Ga)Se_2 absorber layer into the In_2S_3 buffer layer during the annealing is examined in detail. Here, changes in the integral and surface concentration as well as the distribution of Cu in In_2S_3 thin films after annealing are investigated by the combination of high kinetic energy X-ray photoelectron spectroscopy (HIKE), standard X-ray photoelectron spectroscopy (XPS) and energy dispersive X-ray spectroscopy (EDX) coupled with a transmission electron microscope. Based on the results a semi-empirical model describing the diffusion of Cu in In_2S_3 is proposed.

A short description of structural, chemical and optical material analysis techniques that have been applied during the course of this work is given in Annex A.

The results of the individual chapters are combined in **Chapter 7**, together with a presentation of the obtained record cell efficiencies and an outlook including potential future improvement routes.

The work is completed with a summary of the presented results.

Chapter 2

Chalcopyrite Solar Cells

Thin film technologies in the PV segment are relatively new technologies with a high cost-reduction potential. This is the reason for the growing market share of thin-film technologies (10% market share in 2007) as compared to conventional mono-crystalline and poly-crystalline silicon based solar cells. A market share for thin film technologies of 25-30% is a realistic aim for 2010 [1]. A good review paper on the current status of different solar cell technologies can be found in [5].

There are three material systems applied as absorbers in the thin-film PV segment, which have all entered the market and are intensively investigated: (a) thin film Si, (b) CdTe and (c) chalcopyrites ($Cu(In,Ga)(S,Se)_2$ and related materials). Reference [6] gives an overview over the status of thin film solar cells in research, production and market.

Of the three available thin film technologies, solar cells based on $Cu(In,Ga)Se_2$ (CIGSe) have achieved the highest efficiencies up to date (laboratory scale: a-Si: 12.1%, CdTe: 16.7%, CIGSe: 20.0% [7]). In this work, solar cells based on $Cu(In,Ga)Se_2$ with an alternative buffer layer made by thermal evaporation of In_2S_3 are studied. Standard $Cu(In,Ga)Se_2$ solar cells with a CdS buffer layers will be used throughout this work as references. In the beginning of this chapter the cell design and preparation of $Cu(In,Ga)Se_2$ solar cells in the standard configuration with a CdS buffer layer will therefore be briefly introduced. Then, the role of the buffer layer in the cell structure will be outlined. Finally, a literature review over research on alternative buffer layers in the past will be presented and the industrial demands on a buffer layer deposition process will be addressed.

2.1 Advantages

Good reviews on chalcopyrite solar cells can be found in references [8], [9] and [10]. The absorber material of $Cu(In,Ga)Se_2$ solar cells is an interesting semiconductor as it allows efficient band gap tailoring: The system of relevant Cu chalcopyrites belongs to a group of the I-III-VI_2 material family (here I: Cu; III: In,Ga; VI: S,Se) with band gaps ranging from 1.04 eV ($CuInSe_2$) to 2.4 eV ($CuGaS_2$) [9]. The band gap can be deliberately matched by substituting In/Ga or S/Se to optimum performance under solar irradiation for single junction or tandem cell applications. Highest single junction efficiencies of up to 20.0 % (laboratory scale: 0.42 cm^2, [11], [7]) have been obtained for cells based on $Cu(In,Ga)Se_2$.

In general, thin film solar cells exhibit some inherent advantages over conventional, wafer-based silicon technologies [2]. For $Cu(In,Ga)Se_2$ solar cells, these can be summarised as follows:

(+) High absorption (absorption lengths in the range of micrometers), drastically reducing the necessary absorber thickness to few micrometers (as compared to several hundred micrometers in the case of crystalline silicon). This comes along with a decreased source material consumption.

(+) The usage of well established, cost-effective thin film deposition techniques such as sputtering, evaporation, etc. on a large scale bears the potential of very low production costs. (2008: Module direct production costs between 1.5-1.8 Euro/Wp, with an estimated potential of cost reduction down to 0.9 Euro/Wp by 2012 [2]).

(+) The potential to include the series-connection and contacting of various cells into a module in the production process by means of monolithical integration allows cost-reduction and high flexibility with respect to the electrical output and module geometry.

The general disadvantages as compared to conventional wafer-based solar cells can be summarised as:

(-) Lower module efficiencies, requiring a larger area for a constant power output

(-) Thin film photovoltaics are relatively new technologies that are still learning and can not count on the vast experience and technology that has been established for the crystalline Si semiconductor industry.

(-) The availability / toxicity of certain elements/compounds in use (e.g. Cd, In, Ga, Se)

2.2 Reference $Cu(In,Ga)Se_2$ Solar Cells with CdS Buffer

Solar Cell Structure and Preparation

A schematic sketch of the cross-section of a typical $Cu(In,Ga)Se_2$ thin film solar cell is depicted in Fig.2.1. The standard configuration of solar cells used in this work is based on a layer assembly constituted by the following elements:

- Glass substrate.
- Mo metal back contact.
- Absorber layer: $Cu(In,Ga)Se_2$.
- Buffer layer: CdS
- Transparent front contact: ZnO
- Metal front contact grid: Ni/Al

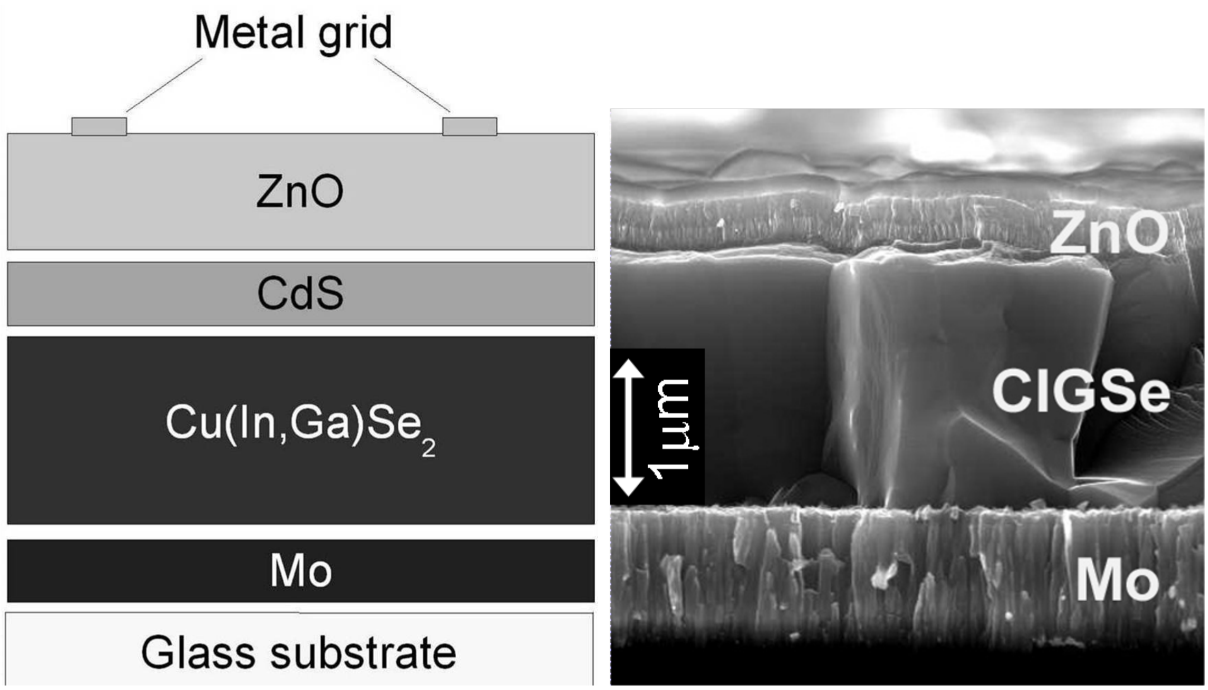

Figure 2.1: Left: Sketch of the cross-section of the standard Cu(In,Ga)Se$_2$ solar cells used as references in this work (thicknesses not to scale). Right: Scanning electron micrograph (SEM) of the cross-sectional view of a Cu(In,Ga)Se$_2$ solar cell. The CdS layer is not resolved due to the small layer thickness (approximately 30-40 nm).

Table 2.1: Material, layer thickness, deposition method and other selected properties of the thin film layers constituting a typical reference Cu(In,Ga)Se$_2$ solar cell with CdS buffer.

	Back contact	Absorber	Buffer	Front contact
Material	Mo	Cu(In,Ga)Se$_2$	CdS	i-ZnO/n-ZnO
Approx. Thickness	1 μm	1.5-2.0 μm	30-40 nm	0.5 μm
Typical Band gap (eV)		1.15	2.4	3.3
Conductivity type	Metal	p-type	n-type	n$^+$ type
Deposition method	Sputtering	Multi-source evaporation	Chemical bath	Sputtering

Selected properties of the different layers in the Cu(In,Ga)Se_2-based solar cell as well as the applied deposition methods are summarised in Table 2.1.

If not stated otherwise, reference solar cells in this work have been prepared in the standard cell configuration including CdS on absorbers prepared in the laboratory of the Helmholtz-Zentrum Berlin (HZB) by the standard absorber process. The process details can be found in Ref. [12]. The Cu(In,Ga)Se_2 absorbers in the standard process are deposited by multi-source evaporation and have a thickness of $d = 1.5\,\mu$m-2 μm. The deposition takes place in a three stage process consisting of the evaporation of (In,Ga,Se) in the first stage, (Cu,Se) in the second stage and again (In,Ga,Se) in the third stage. The final absorber layers have a ratio of Cu/(In+Ga) of $\approx$ 0.8-0.9 and an Ga/(In+Ga) ratio of $\approx$ 0.27-0.32. The band gap E_g varies between $\approx$ 1.11 eV-1.18 eV.

The CdS buffer layer in the standard configuration is deposited in a chemical bath process (CdS: E_g=2.4 eV, thickness d=30-40 nm). The ZnO front contact layer deposition is accomplished in two steps; at first an intrinsic ZnO layer (i-ZnO, 100-150 nm) is sputtered onto the buffer, then in a second step a highly conductive n-type Al-doped ZnO (n-ZnO, 200-300 nm) is deposited by RF-sputtering (ZnO: E_g=3.3 eV). The solar cells are completed with an evaporated Ni/Al contact grid. The total area of these laboratory scale solar cells is approximately 0.5 cm^2. Solar cells used in this work based on this configuration will in the following be referred to as CdS references. For solar cells with an In_2S_3 buffer layer, the CdS deposition step is substituted by the deposition of In_2S_3.

Design of Chalcopyrite Solar Cells

The design of highly efficient chalcopyrite solar cell devices obeys different criteria to conventional Si-based photovoltaic devíces.

Chalcopyrite solar cells are heterojunction devices, i.e. the pn-junction is formed between a p-type conducting material (the absorber) and another, n-type conducting material (the buffer/window). This brings the advantage of reduced surface recombination as the absorption can be shifted into the absorber and away from the device surface by the choice of suitable, transparent window/buffer materials. However, lattice mismatches lead to defect states at the heterojunction and therefore to inherently high surface recombination velocities at this metallurgical interface. As the recombination current has a direct, negative impact on the open circuit voltage of the device, this is a threat for high-efficiency devices.

However, Klenk [13] has shown that a favourable band structure can minimise the impact of high defect concentrations at the interface on open circuit voltage to a few mV. In order to lower the interface recombination for a given interface recombination velocity S, it is necessary to bring the conduction band of the p-type absorber as close as possible to the Fermi-energy E_F at the interface. This leads to a type inversion and the photogenerated electrons in the p-type absorber (minority charge carriers) reach the interface as majority charge carriers. The recombination is then effectively minimised because of the low concentration of recombination partners (holes) for the electrons. The type inversion is one of the key-points regarding the design of high efficiency heterojunction solar cells and may be achieved through asymmetric doping and/or donor-like states at the interface (Fermi-level pinning).

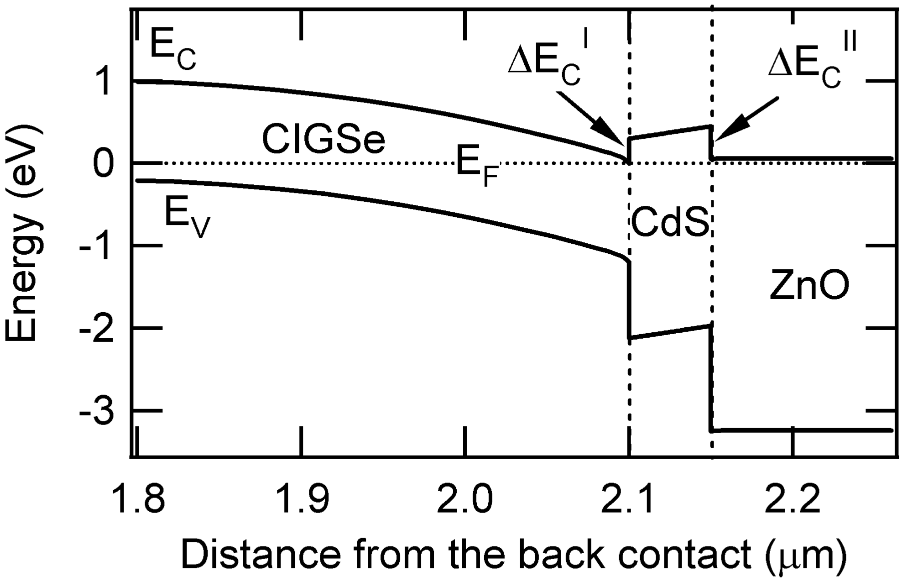

Figure 2.2: Calculated, simplified equilibrium band diagram of a typical Cu(In,Ga)Se$_2$ solar cell obeying the design criteria outlined in the text (following [13]). E_C: conduction band edge, E_V: valence band edge, E_F: Fermi level and ΔE_C^I, ΔE_C^{II}: conduction band offsets at the Cu(In,Ga)Se$_2$/CdS and CdS/ZnO interface, respectively.

Another important aspect for the device design is the band alignment at the junction, i.e. the offset ΔE_C between the conduction band edge of the absorber E_C^A and that of the buffer/window E_C^B ($\Delta E_C^I = E_C^B - E_C^A$). It could be shown, that a moderate spike ($\Delta E_C^I > 0$) does not harm the current collection of the device [14]. On the other hand, a cliff ($\Delta E_C < 0$) reduces the type inversion, opens a way to a recombination path with a reduced barrier and is therefore not desirable.

Fig 2.2 shows the band-diagram of a typical Cu(In,Ga)Se$_2$ solar cell in accordance with the criteria outlined above (following [13]). With these design criteria in mind, the role of the buffer layer will be examined in the following.

2.3 Role of the Buffer Layer

The application of a buffer layer is in the first instance of empirical nature: Chalcopyrite solar cells perform much better with a buffer layer (usually CdS), than without it. Experimental evidence leads to the conclusion that a simple ZnO/Cu(In,Ga)Se$_2$ structure does not naturally comply with the above mentioned design criteria for high efficiency devices. To do so, a buffer layer is required which meets the demands of the following design criteria:

- Transparency: The buffer layer has to be transparent to the main part of the solar spectrum. Each absorbed photon is assumed to create an electron-hole pair, and photons absorbed in the buffer layer are lost, as charge carriers generated inside the buffer layer contribute only in small parts to the photocurrent.

- Band alignment: Favourable conduction band alignment is needed at the buffer/ absorber interface, i.e. a moderate spike (0.0-0.3 eV).
- Type inversion: For low interface recombination a type inversion in the absorber at the interface is essential, i.e. a conduction band edge close to the Fermi level. This may be achieved through donor-like surface states or heavy doping of the buffer.

CdS performs well as a buffer layer in chalcopyrite solar cells and is a reliable, established technology. In fact most highest efficiency devices and nearly all current commercial production schemes are based on chemical bath deposited CdS as a buffer layer. CdS has a bandgap of approximately 2.4 eV and the buffer layer is consequently transparent to approximately 95% of the incoming sunlight [9]. Experimental values for the conduction band offset ΔE_C^I between Cu(In,Ga)Se_2 and CdS vary between 0.75 and -0.05 eV with typical values around 0.45 eV and theoretical predictions of 0.3 eV (see [9] and references therein). A typical conduction band offset at the buffer/window interface $\Delta E_C^I I$ is -0.4 eV [15]. Cd is believed to produce an n-type doping at the Cu(In,Ga)Se_2 surface in favour of the type inversion. Additional beneficial properties attributed to the CdS deposition are a cleaning of the absorber surface in the chemical bath (e.g. removal of surface oxides) and a better lattice match with Cu(In,Ga)Se_2 than ZnO [16].

Although CdS has proven to be a suitable buffer layer, research as well as industry have been eagerly looking for a substitute in the past decade. Reasons can be found in the environmental impact/ toxicity of Cd and legislation concerning this issue, a better in-line compatibility by the substitution of the wet-chemical CdS process step in the otherwise fully high-vacuum device production cycle and finally the attempt to overcome the absorption losses in the CdS layer by a less absorbent material.

2.4 Alternative Buffer Layers - State of the Art

Good reviews on the state of the art of alternative buffer layers can be found in references [17], [16] and more recently [18]. There are a variety of materials under investigation, the most relevant being ZnS, ZnMgO, ZnSe, In_2S_3 and related materials. Deposition methods include chemical bath deposition (CBD), atomic layer chemical vapour deposition (ALCVD), metal-organic chemical vapour deposition (MOCVD), sputtering, ion-layer gas reaction (ILGAR) and evaporation (or physical vapour deposition, PVD). Highest efficiencies for Cd-free devices have been achieved with CBD-ZnS buffers: 18.6% [19].

It has to be stated that direct comparison of reported efficiencies for devices is misleading due to the fact that the buffer layers have been applied to different absorbers. Promising results (with efficiencies well above 11%) have been achieved for buffers based on Zn-Compounds: CBD-ZnSe [20], ALD-Zn(O,S) [21], sputtered $Zn_xMg(1-x)O$ [22], ILGAR-ZnS [23], co-evaporated $ZnIn_xSe_y$ [24] [25], to name a few. Another promising Cd-free buffer material is In_2S_3 and its derivates. Buffer layers based on In compounds

Table 2.2: Literature review of record efficiencies for Cu(In,Ga)Se_2 solar cells with In_2S_3-based buffer layers and best results obtained in this work.

Method	Institute	Efficiency (%)	$T_{substrate}$ (°C)	Annealing (°C)	Reference
ALCVD	ENSCP	16.4	220	-	[26]
CBD	ZSW	$15.7^{a,ls}$	70	200	[28]
ILGAR	HZB	14.7^{*}	220	-	[27]
PVD	IPE	14.8	120	200	[4]
Sputtering	ZSW	13.3	220	200	[17]
PVD (This work)	HZB	15.2^{*}	<50	200	[31]

* independently confirmed, ^{a} active area, ^{ls} light soaked, ENSCP: Ecole Nationale Superieure de Chimie de Paris, ZSW: Zentrum für Sonnenenergie- und Wasserstoff-Forschung, HZB: Helmholtz-Zentrum Berlin, IPE: Institut für physikalische Elektronik, Uni Stuttgart

have been succesfully deposited by a vast variety of different deposition techniques with attractive results, e.g. ALCVD [26], ILGAR [27], CBD [28], MOCVD [29] and PVD [4].

On the one hand, the fact that highly efficient devices could be prepared by such different methods is an indication for the robustness of the buffer layer performance with respect to alterations in the deposition conditions. On the other hand, as will be seen in Chapter 4.2, there is no consensus on the variation of the optic and structural properties of In_2S_3 thin films deposited by different methods and laboratories. These two aspects motivated the detailed analysis of PVD In_2S_3 layers in this work with a focus on their application as buffer layers in Cu(In,Ga)Se_2 solar cells.

A detailed review paper about the progress of buffer layers based on In_2S_3 is given by Barreau [30]. In Table 2.2 the highest reported efficiencies obtained with In-based buffer layers in other laboratories are summarized. The highest efficiency obtained during the course of this work is also stated. Columns reporting on the substrate temperature and/or applied annealing treatments are added to the table. This column shows that all devices needed a temperature step of 190 °C-250 °C for optimum performance, either during the deposition or in a post-deposition annealing. The effect of annealing at 200 °C in the case of the buffer layers deposited in this work is examined in detail in Chapter 5 and 6.

Although research on alternative buffer layers has been manifold and quite successful in many cases, alternative buffer layers could not displace chemical bath deposited CdS in industrial applications so far (with few exceptions, e.g. CBD-ZnS at Showa Solar, [18]). This is due to the strong performance, the robustness of the deposition process with respect to the performance of the cells, and the long experience and confidence gained already in the field with CdS buffered devices.

2.5 Industrial Demands

At this point it might be helpful to review shortly the requirements that an industrially relevant alternative buffer layer should fulfil in order to be accepted. For the industrial feasibility optimal device performance is a natural precondition, but is not by far the only issue. Ultimately, the production costs in Euro/Wp are the strongest driving forces for industry at this moment as outlined above. These costs also depend on the reproducibility of the process, in-line compatibility, material availability and consumption, et cetera. Some of the most import issues for the successful industrial implementation of an alternative buffer layer process will be shortly summarised:

- High efficiency: At least comparable to devices with CdS buffer layer.
- Industrial feasibility of the deposition method: In terms of cycle times, ability for upscaling to large areas, process reproducibility and stability.
- In-line compatibility: Preferentially a vacuum deposition method.
- Transparency: Preferentially less absorption than in the CdS, e.g. higher band gap and/or lower absorption coefficient.
- Stability: Long-term stability of the device under working conditions.

In this work the In_2S_3 evaporated from compound powders by thermal evaporation (sometimes called physical vapour depositon, PVD) will be examined in detail and In_2S_3 layers in combination with ZnO and $Cu(In,Ga)Se_2$ will be analysed in view of their photovoltaic properties. Although not of primary scientific interest in the case of this work, it is beneficial to bear the industrial implication in mind in order to properly evaluate the context and the potential impact of In_2S_3 as a Cd-free buffer alternative.

Chapter 3

Basics of the Physical Interpretation of Solar Cells

Chalcopyrite thin film solar cells are semiconductor devices that convert solar light into electricity. In this chapter, some basic principles of photovoltaic devices based on pn-junctions will be reviewed, with a focus on those aspects needed for the physical interpretation of chalcopyrite thin film solar cells in the course of this work. This review will be kept as short as possible and the reader is referred to the vast number of existing textbooks, e.g. [32], [33], [34], [35] for more details and a more complete derivation.

3.1 Depletion Approximation

Incident light with sufficient photon energy creates electron-hole pairs in a semiconductor. A separation of these photo-generated charge carriers is necessary for the building of a photovoltage. In thin film solar cells, a pn-junction in the devices is responsible for the separation of electron-hole pairs. The pn-junction is obtained by an opposite effective doping of different regions of the semiconductor (homojunction) or by joining a p-type and a n-type semiconductor (heterojunction).

In a semiconductor in thermodynamic equilibrium, the electron concentration n and the hole concentration p are given by [33]:

$$n = N_C e^{-(E_C - E_F)/kT}, \tag{3.1}$$

$$p = N_V e^{-(E_F - E_V)/kT}. \tag{3.2}$$

Here, N_C denotes the effective density of states in the conduction band, N_V the effective density of states in the valence band, k is the Boltzmann constant, T the temperature, E_F the Fermi level and E_C, E_V the conduction band and valence band edge, respectively.

The product of the two equation yields

$$np = n_i^2 = N_C N_V e^{-(E_g)/kT} \tag{3.3}$$

with $E_g = E_C - E_V$ being the bandgap of the material and n_i the intrinsic carrier concentration of the material.

If two regions of opposite carrier type are brought into contact, an exchange of charge carriers takes place. The concentration gradient is the driving force for the diffusion of electrons to into the p-type region and the diffusion of holes into the n-type region, leaving behind a net charge of opposite sign on either side of the junction from the uncompensated donors and acceptors. An electric field builds up caused by these net charges on either side of junction until in thermodynamic equilibrium the effect of the concentration gradient exactly cancels the effect of the electrostatic potential and the net particle flow is zero. In other words, under thermodynamic equilibrium conditions the position of the Fermi level is the same through all the device.

In the depletion approximation introduced by Schottky [36], an abrupt and well defined, negatively charged region with width x_p builds up on the p-type side of the junction which is completely depleted of mobile charge carriers. As no holes remain in this region, the charge density ρ in this region is determined by the acceptor concentration N_A. The same holds for the n-type side of the junction, where a region with width x_n is positively charged and totally depleted of mobile charge carriers. The rest of the bulk is considered neutral. The total depletion width (also called space charge region width) w is given by $w = x_n + x_p$. The device is therefore divided into two regions on either side of the junction: The completely depleted space charge region (SCR) and the quasi neutral rest of the bulk, called QNR (quasi neutral region). With conservation of charge it follows:

$$x_n N_D = x_p N_A. \tag{3.4}$$

The Maxwell equations relate the electric field $F(x)$ to the the charge distribution according to:

$$\frac{dF(x)}{dx} = \frac{\rho}{\epsilon_m \epsilon_0}, \tag{3.5}$$

where ϵ_m is the dielectric constant of the considered material, and ϵ_0 the permittivity of free space. With the electrostatic potential $V(x)$ and $F(x) = -\frac{dV(x)}{dx}$ this leads to the Poisson equation,

$$\frac{d^2V(x)}{dx^2} = -\frac{\rho}{\epsilon_m \epsilon_0}, \tag{3.6}$$

With the junction at $x = 0$, q being the elementary electric charge and the indices n, p referring to the corresponding quantities in the n-type and p-type region, the following expressions for the charge density, electric field and electristatic potential are established for the depletion approximation (see also Fig. 3.1):

$$\rho_p(x) = -qN_A \qquad for \qquad -x_p < x < 0 \tag{3.7}$$

$$\rho_n(x) = qN_D \qquad for \qquad 0 < x < x_n \tag{3.8}$$

$$F_p(x) = -qN_A(x + x_p)/\epsilon_p \epsilon_0 \qquad for \ -x_p < x < 0 \tag{3.9}$$

$$F_n(x) = \ qN_D(x - x_n)/\epsilon_n \epsilon_0 \qquad for \ \ 0 < x < x_n \tag{3.10}$$

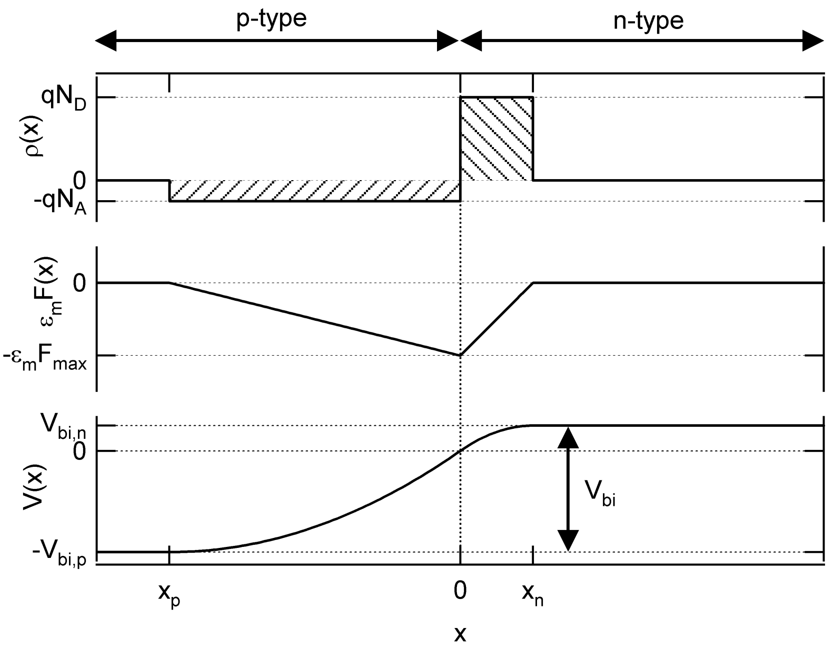

Figure 3.1: Illustration of the charge distribution ρ, electric field F and electrostatic potential V in a pn-junction according to the depletion approximation by Schottky.

$$V_p(x) = -qN_A(\frac{1}{2}x^2 + x_p x)/\epsilon_p\epsilon_0 \qquad for \; -x_p < x < 0 \tag{3.11}$$

$$V_n(x) = \; qN_D(\frac{1}{2}x^2 - x_n x)/\epsilon_n\epsilon_0 \qquad for \; 0 < x < x_n \tag{3.12}$$

Here, the integration constants have been chosen to fulfil $F(x_p) = F(x_n) = 0$ and $V_{n,p}(0) = 0$.

These relations are graphically illustrated in Fig. 3.1. The total potential drop across the pn-junction is called the build-in voltage V_{bi}, which is the sum of the potential drop in the p-type and n-type side of the junction $V_{bi,p}$ and $V_{bi,n}$ given by [35]:

$$V_{bi,p} = V(0) - V(-x_p) = \frac{qN_A x_p^2}{2\epsilon_0\epsilon_p}$$

$$V_{bi,n} = V(x_n) - V(0) = \frac{qN_D x_n^2}{2\epsilon_0\epsilon_n}$$

$$V_{bi} = V_{bi,p} + V_{bi,n} = V(x_n) - V(-x_p) = \frac{q}{2\epsilon_0}\left(\frac{N_D x_n^2}{\epsilon_n} + \frac{N_A x_{p^2}}{\epsilon_p}\right) \tag{3.13}$$

For chalcopyrite solar cells with an asymmetrically doped pn-junction and $N_D >> N_A$, nearly all the potential drop is taking place in the p-type side of the junction and to a good approximation $V_{bi} = V_p$ which leads to an approximation of the space charge region width:

$$w \approx x_p \approx \sqrt{\frac{2\epsilon_p\epsilon_0}{qN_A}V_{bi}}. \tag{3.14}$$

To a good approximation, an externally applied forward bias V_{ex} merely reduces the junction potential so that the potential across the junction is just $V = V_{bi} - V_{ex}$ and the change in charge takes place at the depletion layer edges x_n and x_p [33]. Still for the case $N_D >> N_A$, the dependency of the space charge region width on an applied external bias voltage can therefore be approximated by:

$$w \approx \sqrt{\frac{2\epsilon_p\epsilon_0}{qN_A}(V_{bi} - V_{ex})}. \tag{3.15}$$

3.2 Current-Voltage Characteristics

As a consequence of the pn-junction, the current-voltage response of a solar cell in the dark shows a rectifying behaviour and can in the simplest approach be described by a diode with the saturation current density $j_{0,1}$ and diode quality factor A_1:

$$j(V) = j_{0,1}\left(e^{\frac{qV}{A_1 kT}} - 1\right). \tag{3.16}$$

Here, k is the Boltzmann constant, T the temperature, V is the applied bias voltage, $j(V)$ the current density and q the elementary electric charge. Resistive losses have to be added to this simplest, ideal model for a better description of the real device. These resistances are namely a series resistance R_s, corresponding to resistive losses e.g. at the contacts and a parallel resistance R_p accounting for all possible electronic paths of the electronic transport alternative to that of the diode branch, e.g. through pinholes or at the sample edges. This parallel resistance is also often called shunt resistance.

The photo-generated current density j_L of the device under illumination is introduced as an additional current source into the model. In a first approximation, j_L is considered a constant. However, in thin film solar cells this is generally not the case and in a more detailed analysis j_L is shown to depend on the applied bias voltage V ($j_L(V)$). In the dark, $j_L = 0$.

In this so called 1-diode-model [35], the current flowing through the device is therefore the sum of the diode current density j_{Diode}, the current density flowing through the shunt j_{Shunt} and the photo-generated current density j_L. Equation 3.17 describes the jV-behaviour of a solar cell according to the 1-diode-model:

With:

$$j_{Diode}(V) = j_{0,1}\left(\exp\left\{\frac{q\,(V - R_s j(V))}{A_1\,kT}\right\} - 1\right),$$

$$j_{Shunt}(V) = \frac{V - R_s j(V)}{R_p},$$

$$j(V) = j_{Diode}(V) + j_{Shunt}(V) - j_L,$$

we have

$$j(V) = j_{0,1}\left(\exp\left\{\frac{q\,(V - R_s j(V))}{A_1\,kT}\right\} - 1\right) + \frac{V - R_s j(V)}{R_p} - j_L. \tag{3.17}$$

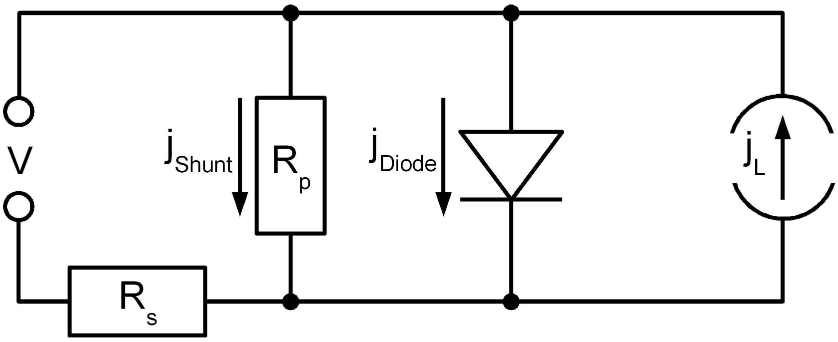

Figure 3.2: Equivalent circuit diagram of the solar cell in the 1-diode-model.

The equivalent circuit diagram of the solar cell in the 1-diode-model is shown in Fig. 3.2. In Fig. 3.3 calculated jV-curves according to the 1-diode-model are depicted illustrating the influence of the four parameters j_0, A, R_s, R_p describing the device in the dark.

The 1-diode-model describes very well the behaviour of many solar cells. However, due to its simplicity it does not account for the behaviour of solar cells in general, and additional components have to be added to the model *a posteriori* if the agreement between measurement and model are not satisfying.

The dark jV-data of a real Cu(In,Ga)Se_2 device with a CdS buffer is presented in Fig. 3.4 (left) together with a fit according to the 1-diode-model. The correlation between measured data and fit is only poor and the residual shows systematic deviations of up to 20 %. The 1-diode-model is therefore considered a too simple approach for an appropriate description of the real devices in this case and additionally to the main diode (A_1, $j_{0,1}$) a second diode has to be added to the model. This second diode is described by the saturation current density $j_{0,2}$ and quality factor A_2. The fit according to the resulting 2-diode-model correlates much better to the data and results in a residuum below 5%. This fit is shown in the right part of Fig. 3.4.

In the 2-diode-model, the second diode has to be added in parallel to the first diode in the equivalent circuit diagram in Fig. 3.2 and the corresponding equation gives:

$$\begin{aligned} j(V) =& j_{0,1}\left(\exp\left\{\frac{q\,(V-R_s j(V))}{A_1\,kT}\right\}-1\right)+\ldots \\ &\ldots + j_{0,2}\left(\exp\left\{\frac{q\,(V-R_s j(V))}{A_2\,kT}\right\}-1\right)+\frac{V-R_s j(V)}{R_p}-j_L. \end{aligned} \tag{3.18}$$

3.3 Solar Cell Performance

Under illumination, two points of the jV-curve are of special importance for the analysis, the short circuit current density j_{SC} and open circuit voltage V_{OC}. At zero bias voltage the only the current flowing through the device corresponds to the photo-generated current density $j_{SC} = j(0\,V)$ and under the assumption of a constant, voltage independent photo-generated current density: $j_L = j_{SC}$. In open circuit mode, no current is flowing through

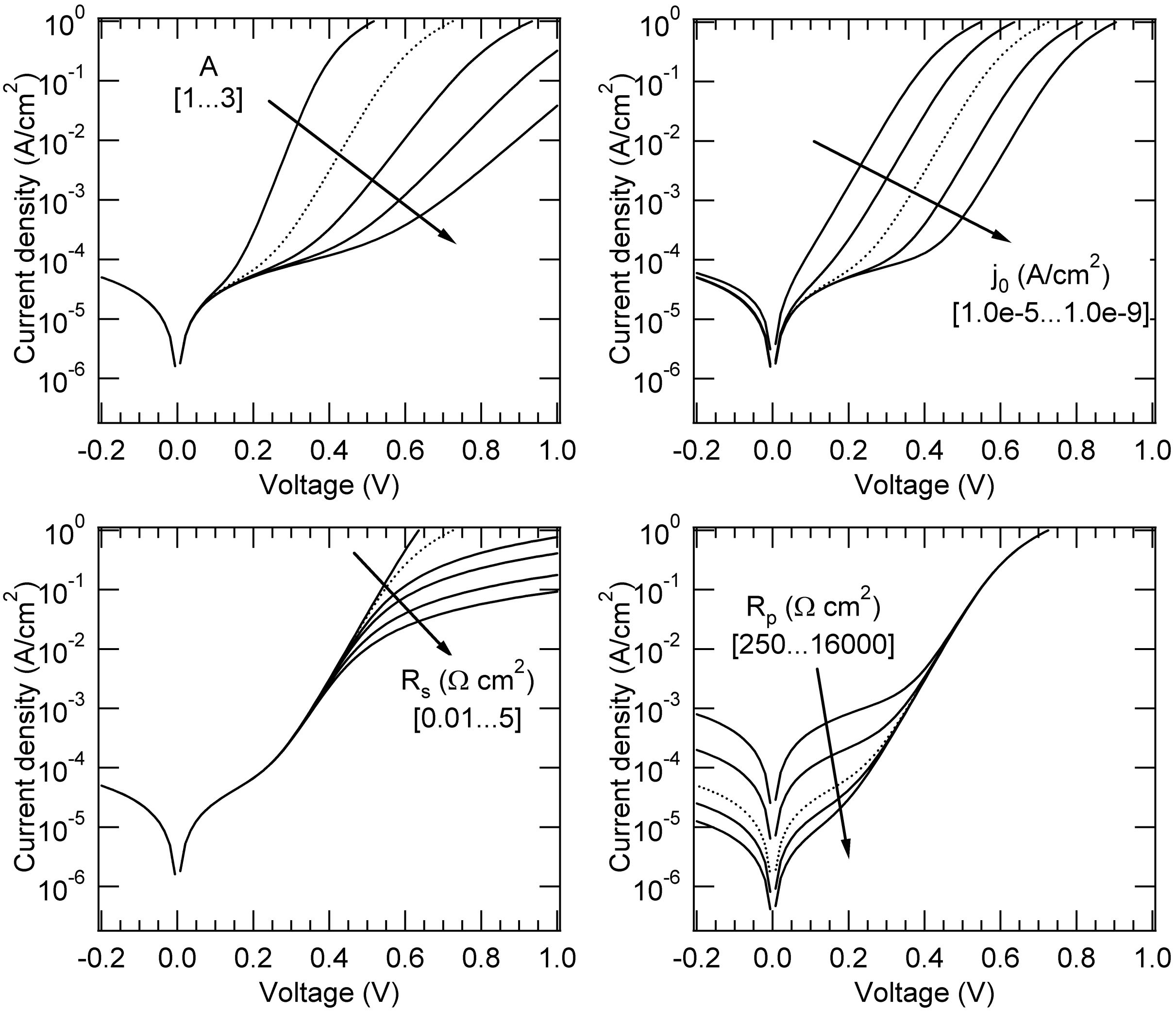

Figure 3.3: Calculated jV-curves corresponding to the 1-diode-model. The four graphs show a variation of the four parameters describing the jV-curve of a solar cell in the 1-diode-model (clockwise): A, j_0, R_p, R_s. The starting values (dotted line) were the same for the four graphs ($A = 1.5$, $j_0 = 1 \times 10^{-7}\text{A/cm}^2$, $R_p = 4000\,\Omega\text{cm}^2$, $R_s = 0.1\,\Omega\text{cm}^2$)

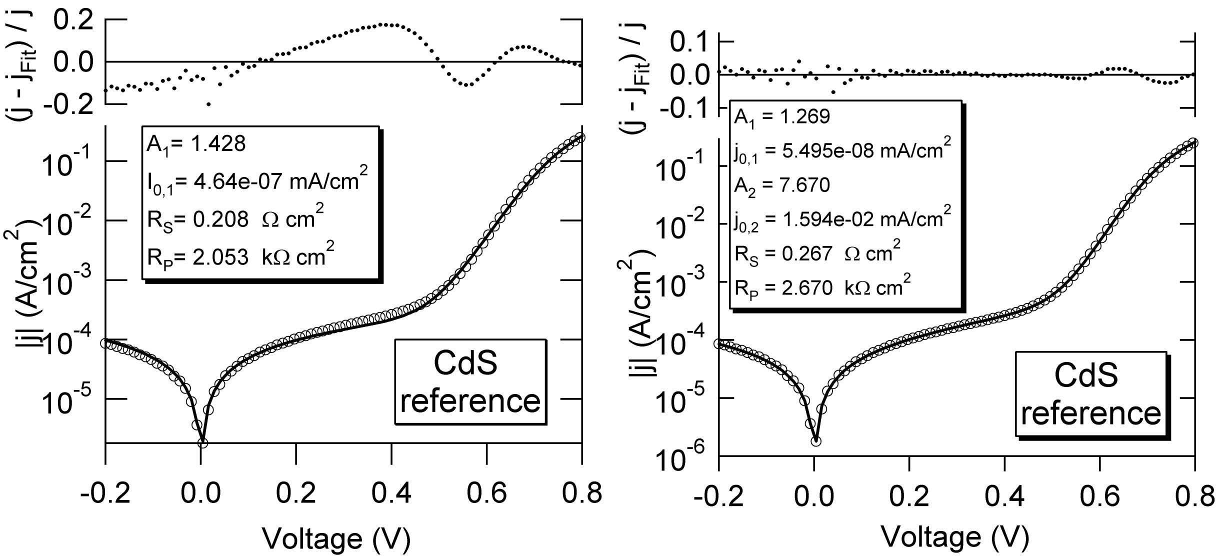

Figure 3.4: Left: Semi-logarithmic presentation of the measured dark jV-curves of a CdS reference (circles) and a fit according to the 1-diode model (line). The residuum $(j - j_{Fit}/j)$ is displayed in the graph above. Right: Same data with a fit according to the 2-diode model.

the device ($j(V_{OC}) = \ 0$) and there are no resistive losses by the series resistance. As a consequence, the following relation holds for the open circuit mode:

$$j_{SC} = j_0(e^{\frac{qV_{OC}}{AkT}} - 1) + \frac{V_{OC}}{R_p} \tag{3.19}$$

Solar cells are built to convert sunlight into electricity and consequently the most important parameter to classify solar cells is the power conversion efficiency η. The power conversion is defined as the ratio of electric power output at the maximum power point P_{MPP} to the incoming irradiative power P_{in}. P_{MPP} is often described as a product of the current under short circuit conditions I_{SC} (with $j_{SC} = I_{SC}/A$, A being the area of the device), the voltage under open circuit conditions V_{OC} and the fill factor FF:

$$\eta = \frac{P_{el}}{P_{in}} = \frac{I_{SC}\,V_{OC}\,FF}{P_{in}}. \tag{3.20}$$

In order to determine the maximum power output of the device it is necessary to measure the current flowing through the device as a function of the applied bias voltage, a measurement that in the following will be called an IV-curve or jV-curve, depending if it is referring to the current I (in mA) or the current density j (in mA/cm^2). The current I_{MPP} and voltage V_{MPP} correspond then to the point of the IV-curve where the power is at its maximum (Maximum Power Point, P_{MPP}). The fill factor is defined as

$$FF = \frac{I_{MPP}\,V_{MPP}}{I_{SC}\,V_{OC}}. \tag{3.21}$$

Graphically it can be understood as the ratio between two rectangles: (1) The rectangle between the point of maximum power of the IV-curve and the two axes (P_{MPP}). And

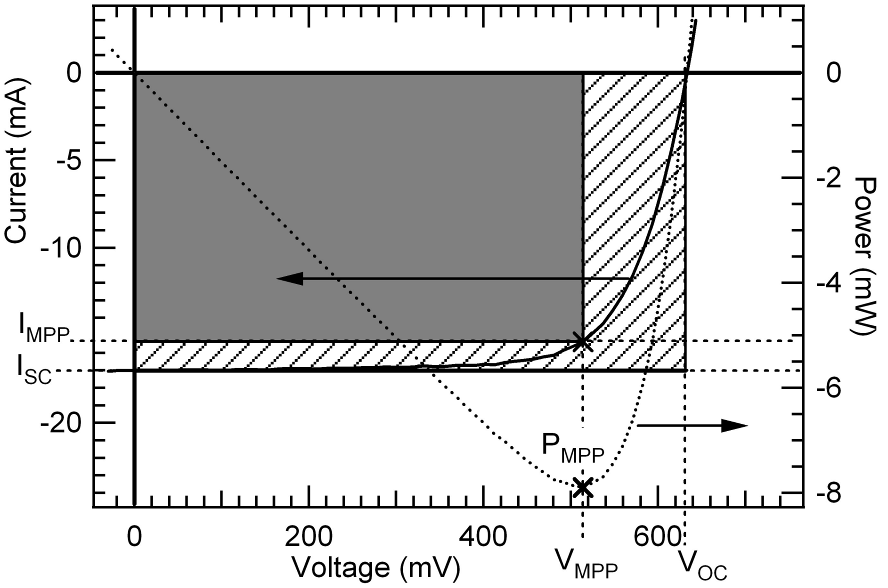

Figure 3.5: IV-curve and power output of a typical Cu(In,Ga)Se$_2$ solar cell. The relevant solar cell parameters I_{SC}, I_{MPP}, V_{OC}, V_{MPP} and P_{MPP} as introduced in the text are marked in the graph. The grey rectangle represents the power output at the maximum power point P_{MPP}, the patterned rectangle corresponds to the power $P_{MPP}/FF = I_{SC}\ V_{OC}$.

(2) the rectangle defined by V_{OC} , I_{SC} and the two axes, corresponding to the power $P = P_{MPP}/FF = V_{OC} \times I_{SC}$. These parameters are displayed in Fig.3.5.

As the response of solar cells is not constant for different parts of the solar spectrum, it is necessary to define a common spectrum for usage in standard testing conditions. There are different definitions for this standards, but the one used in this dissertation is the most common one referred to as global AM1.5 solar spectrum (IEC 60904-3: 2008, see [7] and references therein for more details). This spectrum simulates the terrestrial sunlight with an air mass of 1.5 [1] and has a total intensity of 1000 W/m^2. In practice, this spectrum is simulated with a carefully calibrated sun simulator which uses a combination of a Xe lamp and a Ha lamp to match the reference spectrum. In the standard testing conditions the efficiency is measured at a cell temperature of 25 °C.

3.4 Quantum Efficiency

The quantum efficiency (QE(λ)) denotes the ability of the device to collect the photogenerated charge carriers. It is defined as the ratio between number of collected photogenerated charge carriers to the number of irradiating photons. A quantum efficiency of 1 means therefore that for each photon one charge carrier is contributing to the photo-

---

[1] The airmass 1 (AM1) corresponds to the air mass that sun light irradiating perpendicular to the surface of the earth has to traverse in order to reach a surface at sea level. AM1.5 corresponds to 1.5 times this air mass, consequently the AM1.5 solar spectrum approximately corresponds to the sunlight reaching a surface at sea level under an zenith angle of 48.2°

generated current.

It has to be distinguished between the external and internal QE. While the former includes all photons arriving at the surface of the device, the latter only takes the photons into account, that enter into the device, i.e. neglecting reflected photons. In practice, the external QE (EQE) is measured, while the internal QE (IQE) can *a posteriori* be calculated if the reflectivity of the device is known. The corresponding formulas can be stated as:

$$EQE(\lambda) = \frac{j(\lambda)}{q\ \phi_0(\lambda)} = (1 - R_\lambda) IQE(\lambda). \tag{3.22}$$

Here the initial photon flux ϕ_0 is given in photons/(m^2 s), $j(\lambda)$ is the electric current density of the device as a function of the incident photon wavelength, R_λ is the reflectivity of the device and q is the elementary electric charge.

The quantum efficiency is typically measured under zero bias voltage, and in this case the quantum efficiency together with the solar spectrum can be used to calculate the short circuit current density j_{SC}

$$j_{SC} = \int q\ EQE(\lambda)\ \phi_0(\lambda)\ d\lambda \tag{3.23}$$

The quantum efficiency of an ideal device would be 1 for photons with an energy above the band gap of the absorber and 0 for photons with a lower energy, giving an ideal maximum short circuit current density $j_{SC}^{max}(E_g)$ of

$$j_{SC}^{max}(E_g) = \int_{E_g}^{\infty} q\ \phi_0\ E\ dE \tag{3.24}$$

In reality, the measured short circuit current density will always be lower due to several reasons. In the first place, there are reflection losses. Secondly, photons with sufficient energy (above the corresponding bandgap) are absorbed in the window/buffer layer and are lost entirely or in parts for the photo-generated current. Finally there are other losses due to a non-ideal current collection. For example, charge carriers generated deep within the absorber are unlikely to contribute to the photo-generated current if they are absorbed at a distance x with respect to the edge of the space charge region larger than their diffusion length L_D. The measurement of the quantum efficiency gives a means to characterise these losses as a function of the wavelength. As photon absorption is taking place deeper within the device for longer wavelengths, the quantum efficiency can offer information on where in the device losses occur mainly. Generally speaking, a decreasing quantum efficiency in the lower wavelength part (blue reponse, λ<650 nm, higher absorption coefficient) corresponds to loss regions more related to the front of the device, while losses in the longer wavelength part (red response, λ>650, lower absorption coefficient) are absorbed deeper in the device.

With the following model the variation of the quantum efficiency can be approximated in the longer wavelength part of the spectrum (λ <650 nm), where absorption takes mainly place in the absorber side of the junction. The following considerations will be derived for chalcopyrite solar cells with a n^+p-type heterojunction and are based on the work by

Gärtner [37], which was carried on by Klenk [38]. In this model the absorber is divided into two regions: the depletion region and the quasi-neutral region. The collected photocurrent density j_L is then given as the sum of the contributions from both regions:

$$j_L = j_w + j_{diff}. \tag{3.25}$$

Here, j_w denotes the contribution from the depletion region with the depletion width w and j_{diff} denotes the contribution from charge carriers diffusing to the depletion region from within the quasi-neutral region. The charge carrier collection in the depletion region is approximately one, as the electric field is assumed to be strong enough to sweep all photo-generated minority charge carriers across the junction. The Beer-Lambert law of absorption gives the fraction of light absorbed within the depletion region $(1 - \exp(-\alpha(\lambda)w))$, with $\alpha(\lambda)$ the absorption coefficient. Consequently,

$$j_w = q\ \phi_0(\lambda)\ \left(1 - e^{-\alpha(\lambda)\ w}\right) \tag{3.26}$$

The contribution of from the quasi neutral region is given by:

$$j_{diff} = q\ \phi_0(\lambda)\ e^{-\alpha(\lambda)w}\ \frac{1}{1 + \frac{1}{\alpha(\lambda)L}} \tag{3.27}$$

This equation means that photo-generated charge carriers from the quasi-neutral region are likely to contribute to the photocurrent if they are generated within the characteristic diffusion length L. Combining Eq. 3.25, 3.26 and 3.27 gives

$$\begin{aligned} j_L &= q\ \phi_0(\lambda)\ \left\{1 - e^{-\alpha(\lambda)\ w} + \frac{e^{-\alpha(\lambda)\ w}}{1 + \frac{1}{\alpha(\lambda)\ L}}\right\} && (3.28)\\ &= q\ \phi_0(\lambda)\ \left\{1 - \frac{e^{-\alpha(\lambda)w}}{1 + \alpha(\lambda)\ L}\right\} && (3.29)\\ & && (3.30)\end{aligned}$$

It is convenient to define the effective collection length L_{eff} as the sum of diffusion length L and space charge region width w:

$$L_{eff} = L + w. \tag{3.31}$$

Following Klenk [38] the quantum efficiency can then be approximated as:

$$EQE \approx K\ \left(1 - e^{-\alpha(\lambda)L_{eff}}\right). \tag{3.32}$$

Here, K is a constant which accounts for optical losses (reflection and absorption in the buffer/window layer) and electric losses (e.g. due to recombinative losses at the interface).

3.5 Recombination Mechanisms in Chalcopyrite Solar Cells

In the following section, different recombination mechanisms in chalcopyrite solar cells will be presented and their effects on the temperature dependence of the jV-response will be discussed.

The lifetime of charge carriers in a semiconductor device is limited by recombination processes and recombination therefore directly influences the electrical transport mechanisms of the device. The diode-character of a pn-junction device is related to the dominant recombination mechanism, which therefore governs the current-voltage response of the device under forward bias. For solar cells it is essential to minimise recombination in order to achieve high open circuit voltages and to increase the performance. The identification of relevant recombination mechanisms plays therefore a key role in the development of improved solar cell devices.

In a pn-junction device, the electric transport is controlled by hole transport in the p-type side and by electrons in the n-type side. If no external bias is applied, the generation of electron-hole pairs just counterbalances the recombination. This changes if an external voltage is applied. If a negative bias voltage (negative voltage at the p-type side) is applied, electrons are extracted from the p-type side of the junction and holes from the n-type side of the junction. Consequently, more electron-hole pairs have to be generated in the device than are recombining and the current flow through the device is limited by the generation of electron-hole pairs within the device.

If a forward bias voltages (positive voltage at the p-type side) is applied, electrons are injected into the n-type side and holes into the p-type side. In this case, for an effective current flow across the junction, electrons from the n-type side and holes from the p-type side have to recombine. The total current density j_R as a result of the recombination processes in the device can be obtained through an integration over the region, where the dominant recombination with recombination rate R takes place:

$$j_R = \int qRdx \tag{3.33}$$

If the recombination in the device is assumed to be dominated by recombination in the QNR of the absorber via a single defect level with an energetic position E_{def} within the bandgap of the absorber, the integration has to be extended over the whole quasi neutral region of the absorber, with the main part of the recombination taking place within the diffusion length of the charge carriers involved on either side of the junction. The recombination rate R_{SRH} is given by the classical Shockley-Read-Hall (SRH) description [39]:

$$R_{SRH} = \frac{np - n_i^2}{\tau_{n0}\,(n + n_1) + \tau_{p0}\,(p + p_0)} \tag{3.34}$$

$$n_1 = N_C e^{-(E_{def}-E_C)/kT}\ , \qquad p_1 = N_V e^{-(E_{def}-E_V)/kT}$$

Here, τ_{n0} is the minimum electron lifetime in the case of completely unoccupied defect states, τ_{p0} is the minimum hole lifetime in the case of completely occupied defect states, n_1

would be the electron density if the Fermi level lay at the energetic position of the defect and p_1 would be the hole density if the Fermi level lay at the energetic position of the defect.

In this case, the current-voltage characteristic of the device can be expressed as [35]:

$$j(V) = qn_i^2 \left\{ \frac{D_n}{N_A L_n} + \frac{D_p}{N_{DL_p}} \right\} \left(e^{qV/kT} - 1 \right). \tag{3.35}$$

Here, D_n, D_p are the diffusion constant for electron and holes, respectively and L_n, L_p the corresponding diffusion lengths. Eq. 3.35 in fact resembles the jV-dependence of an ideal diode with a diode quality factor $A = 1$ and a saturation current density of

$$j_0 = qn_i^2 \left(\frac{D_n}{N_A L_n} + \frac{D_p}{N_D L_p} \right).$$

In this assumption, recombination in the space charge region is neglected. This approximation is often justified in the case of crystalline silicon solar cells, where the electron diffusion lengths are large compared to the space charge region width (e.g.: L_n of up to $1000\,\mu$m for very pure silicon, $w \approx 0.35\,\mu$ [34]).

In thin film chalcopyrite solar cells, other recombination mechanisms have to be additionally considered, such as recombination in the SCR or at the interfaces. Different recombination mechanisms for chalcopyrite solar cells have been discussed in the past by several authors. In the following, the most relevant ones will be shortly presented, following the work by Hengel [40]. A schematic presentation of the recombination paths considered is depicted in Fig. 3.6. The general form of the voltage dependence of the diode current density is here given by:

$$j(V) = j_0 \exp\left\{ \frac{qV}{AkT} \right\} = j_{00} \exp\left\{ \frac{-E_x}{AkT} \right\} \exp\left\{ \frac{qV}{AkT} \right\}. \tag{3.36}$$

where A and and the energy E_x may be functions of the temperature.

(1) Recombination in the quasi neutral region

Following Eq. 3.35, a diode quality factor of 1 is expected for a dominant recombination in the quasi neutral region and the temperature dependence of j_0 and V_{OC} are given by:

$$j_0 = j_{00} e^{-E_g/kT}, \tag{3.37}$$

$$qV_{OC} = E_g - kT \ln \left(j_{00}/j_{SC} \right). \tag{3.38}$$

(2) Recombination in the space charge region

a) Thermally activated, single defect level

In order to calculate the recombination current density for a recombination via a single defect level with defect density N_{def} in the space charge region, the integral in Eq. 3.33 has to be extended over the space charge region from

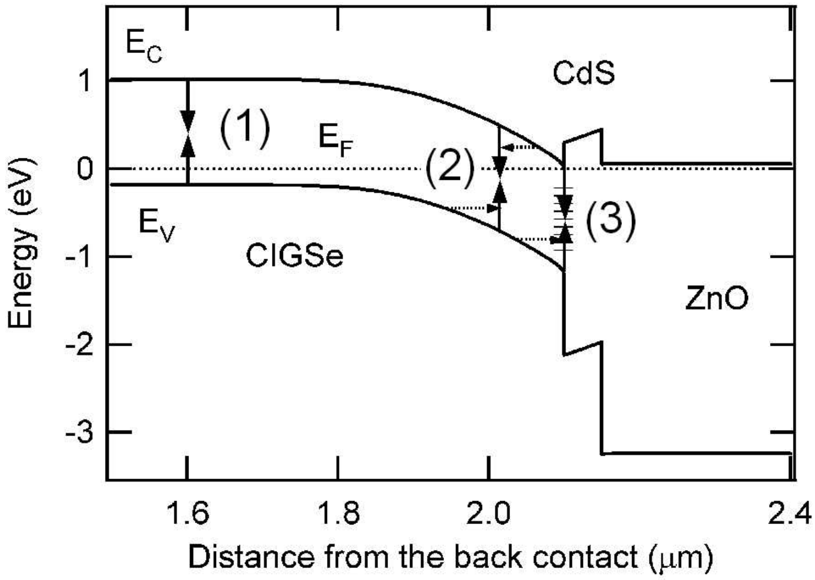

Figure 3.6: Schematic presentation of the expected recombination paths in chalcopyrite solar cells. (1) Recombination in the quasi neutral region. (2) Recombination in the space charge region. (3) Interface recombination. Possible tunneling enhanced recombination paths are indicated by dotted arrows (corresponding to the cases (2)c and (3)b discussed in the text).

$-x_p$ to x_n. The recombination rate is again given by the SRH-recombination stated in Eq. 3.34. In the space charge region the term $np = n_i^2 \exp(qV/kT)$ can to a good approximation be considered constant [33]. It follows, that the numerator in Eq. 3.34 is constant over the space charge region width. Without loss of generality, the electron and hole lifetimes will be considered equal. The recombination is at its maximum when the denominator is minimal, which is the case when the Fermi level is approximately midgap and $n = p$.

The recombination decreases exponentially on either side of the maximum with the characteristic length $\delta x = kT/qF_{max}$. In the expression for the recombination current density the integral can therefore be approximated by $R_{max} 2\delta x$ which gives an approximation for the current-voltage relation under forward bias:

$$j(V) \approx qR_{max} 2\delta x \approx \frac{qn_i}{\tau}\delta x \left(\exp\left\{\frac{qV}{2kT}\right\} - 1\right) \tag{3.39}$$

It follows from this approximation, that the recombination via a single defect level in the space charge region describes the behaviour of a diode with diode quality factor A=2 and saturation current density $j_0 = \frac{qn_i\delta x}{\tau}$. Further:

$$j_0 = j_{00}\left(\exp\left\{\frac{qV}{2kT}\right\} - 1\right) \tag{3.40}$$

$$qV_{OC} = E_g - 2kT\ln(j_{00}/j_{SC}) \tag{3.41}$$

b) Thermally activated, defect distribution

The model of recombination via a single defect level has been extended by Walter et al. [41] to the case of a continuous defect distribution. The defect density is assumed to decay exponentially from the band edges into the bandgap with the characteristic energy kT^*. For this defect distribution and $T^* > T$ a slightly temperature dependent diode quality factor with $1 \leq A \leq 2$ is found using the SRH-recombination:

$$A = 2\frac{T^*}{T + T^*} \tag{3.42}$$

$$j_0 = j_{00} \exp\{-E_g/AkT\} \tag{3.43}$$

$$qV_{OC} = E_g - AkT \ln(j_{00}/j_{SC}) \tag{3.44}$$

c) Tunneling enhanced recombination

Rau [42] extended the model used by Walter to the case of tunneling enhanced recombination. The tunneling enhanced recombination describes the case where free charge carriers tunnel from the bands into trap states where they recombine. Rau considered a parabolic band bending and a defect distribution as suggested by Walter in the previous paragraph, i.e. an exponentially decaying defect distribution with characteristic energy kT^*. Using a modified recombination rate in order to account for the tunneling processes, he finds the following relations through an integration over the defect distribution and space charge region width:

$$j_0 = j_{00} \exp\{-E_g/AkT\} \tag{3.45}$$

$$\frac{1}{A} = \frac{1}{2}\left(1 - \frac{E_{00}^2}{3(kT)^2} + \frac{T}{T^*}\right) \tag{3.46}$$

for $kT > E_{00}$, with E_{00} being the characteristic energy of the transition from tunneling assisted to thermally activated recombination.

(3) Interface recombination

For highly efficient Cu(In,Ga)Se$_2$ solar cells recombination at the interface has to be minimised and recombination in the space charge region dominates the recombination mechanism. For Cu(In,Ga)Se$_2$ solar cells prepared with Cu deficiency, Turcu et al. [43] report that recombination in the bulk of the absorber dominates over the interface recombination in contrast to samples prepared in excess of Cu. Klenk discusses in Ref. [13] how the position of the Fermi level ultimately determines the recombination losses at the interface. Considering the classical SRH-recombination,

Table 3.1: Expected recombination mechanisms in chalcopyrite solar cells. QNR: Quasi neutral region, SCR: space charge region, IF: interface. Adapted from [40].

Location	Recombination mechanism	Activation energy of j_0	V_{OC} (T=0 K)	Diode quality factor A
(1) QNR	Thermally activated	E_g	E_g	1
(2) SCR	a) Thermally activated, single defect at midgap	$E_g/2$	E_g	2
	b) Thermally activated, exp. defect distribution	E_g/A	E_g	$1 \leq A \leq 2$ $2T^*/(T+T^*)$
	c) Tunneling enhanced			$2\left(1-\frac{E_{00}^2}{3(kT)^2}+\frac{T}{T^*}\right)^{-1}$
(3) IF	a) Thermally activated	E_b	$E_b \leq E_g$	$1 \leq A \leq 2$
	b) Tunneling enhanced			$\frac{E_{00}}{\alpha kT}\coth(E_{00}/kT)$

the recombination is maximum if the Fermi level lies midgap where $n = p$. In the case of surface recombination, the carrier lifetime can be expressed in terms of a surface recombination velocity (S $\sim 1/\tau$). Klenk shows how interface recombination has to be minimised in order to minimise losses in the open circuit voltage. This can be achieved by bringing the Fermi level as close to the conduction or valence band as possible, which can be done through asymmetric doping or a high density of donor-like defects at the interface, that pin the Fermi level at a certain energetic position. A brief introduction into results taken from [40] considering interface recombination will be briefly introduced in the following.

a) Thermally activated

Following the work of Nadenau [44], the parameters governing the current-voltage response for a thermally activated interface recombination are given by:

$$j_0 = j_{00}\exp\left\{-E_b/AkT\right\} \tag{3.47}$$

$$qV_{OC} = E_b - AkT\ln\left(j_{00}/j_{SC}\right) \tag{3.48}$$

Here, E_b is the minimum distance between valence band edge and conduction band edge on either side of the junction, which may be smaller than the absorber bandgap for the case of a negative conduction band offset (cliff). The diode quality factor A depends on the position of the Fermi level at the interface and is approximately 1 for the case of an asymmetrically doped n$^+$p-junction with $N_D >> N_A$ (no charged interface states considered.)

b) Tunneling enhanced

Following an approach by Padovani and Stratton [45], Nadenau [44] has stated the relation for the saturation current density j_{00} and diode quality factor A in the case of a tunneling enhanced recombination at the interface as:

$$j_0 = j_{00} \exp\left\{-E_b/AkT\right\} \tag{3.49}$$

$$A = \frac{E_{00}}{\alpha_\nu kT} \coth\left(\frac{E_{00}}{kT}\right) \tag{3.50}$$

α_ν is here a correction factor related to the part of the band bending occuring in the absorber ($\alpha = V_{bi,p}/(V_{bi,p} + V_{bi,n})$ and E_{00} the characteristic energy for the transition from a purely thermally activated to an tunneling enhanced recombination.

This completes the review on expected recombination mechanisms in chalcopyrite solar cells. Several other models exist attempting to correlate theoretical derivations of the recombination current density to measured $jV-$data, see e.g. [33] or [46], so this list is by no means complete. Care has to be taken at the time of choosing a model and only the good agreement to experimental data can justify the choice of one model or the other in each case.

The analysis is further complicated as often several recombination mechanisms are competing with each other. In this case the current behaviour can be described as the sum of the individual diode current densities. However, the recombination is often dominated by one process or the other in different bias voltage intervals (e.g. if the diode quality factor differ sufficiently) which allows the extraction of several diode parameters from one curve as has been shown in Fig. 3.4.

Chapter 4

Indium Sulphide Powder and Thin Films

This chapter introduces the general powder and thin film properties of indium sulphide as well as aspects of the thin film deposition process. The chapter will start with a review on literature presenting the phase diagram of the In-S system and data on the crystal structure of In_2S_3.

Details of the crystal structure are important for the identification of crystalline phases in In_2S_3 powders used as source materials in the thin film deposition process and will also be important for the interpretation of the diffusion phenomena observed in In_2S_3 thin films. From In_2S_3 reference powders synthesised from the elements, suitable references for X-ray diffraction (XRD) measurements are obtained in a preliminary experiment. Based on literature data, the crystal structure of the In_2S_3 reference powders are analysed in detail by a Rietveld refinement of X-ray diffraction data.

In a thin film deposition by thermal evaporation special attention has to be paid to the selection of the source material, as the quality of the source material ultimately determines the quality of the deposited thin film.

Consequently, the structure and elemental composition of three commercial In_2S_3 powders are analysed before their applicability as source materials in a thin film deposition process is tested. General aspects of the sublimation behaviour of In_2S_3 and the thermal evaporation process are discussed and In_2S_3 thin films prepared from the three commercial In_2S_3 powders are examined for their structural, chemical and optical properties.

4.1 The Crystal Structure of In_2S_3

4.1.1 Phases in the In-S System

The In-S system has been extensively studied in the past, but considerable confusion exists regarding the existence of several phases and the nomenclature to describe them. For example, different names have been assigned to the same phase and different phases have been assigned with the same name. It seems therefore necessary to review the In-S phase diagram and explicitly state the phases that will be referred to in this thesis. The existence of a phase with composition In_3S_4 stable above 380°C is controversially discussed in the literature [47][48][49][50]. Although additional phases with different compositions have been proposed in the past (such as, e.g., In_4S_5 or In_5S_6), Duffin et al. [51] and Ansell et el. [47] proved that in thermodynamic equilibrium conditions at room temperature and atmospheric pressure only three phases exist:

- InS (orthorhombic)
- In_6S_7 (monoclinic)
- In_2S_3 (tetragonal/cubic)

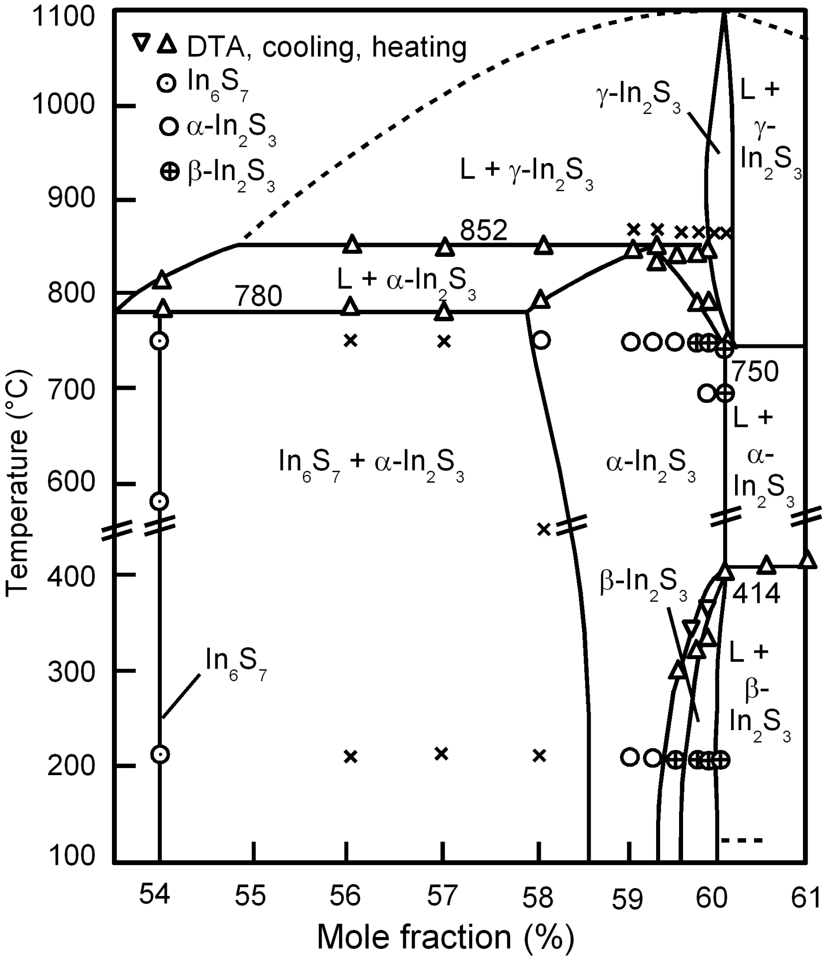

Figure 4.1: Excerpt of the phase diagram of the In-S system (adapted from [52]).

The phase diagram of the In-S system following Gödecke et al. [52] is shown in figure 4.1. Gödecke chose different denotations for the phases, and the denotations in this graph were adapted to the nomenclature used throughout this work. The focus of this work is indium sulphide with a composition of In_2S_3. Three structural modifications exist for this compound. The stable phase of stoichiometric In_2S_3 at room temperature exists up to a temperature of 420 °C and has a tetragonal crystal structure. Following the nomenclature that seems to be the most commonly found in the current literature, this modification is called β-In_2S_3 in this thesis. Above 420 °C it transforms into cubic α-In_2S_3 which is stable up to 750 °C. Between 750 °C and the melting point at 1090 °C is the stable range of the trigonal γ-In_2S_3. The crystal structures of these phases will be discussed in detail below. In general terms, all three modifications are based on an arrangement of the sulphur atoms in a cubic closed-packed sublattice. In the α- and β-modification, the tetrahedral and octahedral gaps of this structure are occupied by indium atoms in the same way as cations in the spinel structure (e.g. $MgAl_2O_4$), although not all cation sites are completely occupied. In the γ-modification the indium atoms are exclusively found on octahedral sites. The structural phase transition between α- and β-In_2S_3 is an order/disorder transition: For the α-modification the unoccupied cation sites (vacancies) of the spinel type structure are randomly distributed over the tetrahedral sites and the cubic symmetry is preserved. In β-In_2S_3 the vacancies are ordered along a 4_1 screw axis parallel to the c-axis, causing a distortion of the crystal structure which lowers the symmetry and results in a tetragonal crystal structure.

β-In_2S_3 is capable of incorporating an excess of indium in its lattice, assuming the composition $In_{2+x}S_3$. The β->α transition is still present if x is very small. However, the degree of order in the tetragonal spinel superstructure decreases continuously with increasing x. If the In surplus surpasses a critical value ($x = 0.01$, corresponding to 40.1 at.% In), the transition into the ordered β-modification becomes entirely blocked and the α-modification is now stable at room temperature ([53]). In contrast to the stoichiometric β-In_2S_3 crystals which are bright red, the latter are dark red to black, depending on the amount of excess indium. Gödecke et al. [52] estimates the critical amount of In for the formation of β-In_2S_3 as below 40.5 at.% In.

This means that the cubic α-modification exists at room temperature at the In-rich phase boundary of β-In_2S_3 and forms a solid solution with considerable composition range [49]. As can be seen in the phase diagram, at 750 °C the α-modification covers the regime from nearly 40 at.% In (corresponding to In_2S_3) up to approximately 42 at.% In ([52]), or even 45 at.% [50]. The composition range at room temperature is smaller but still stretches up to 41.5 at.% In [52] (44 at.% In in [50]). The composition ranges of these two phases are important as they offer the possibility to estimate the composition of a given sample if it is assumed to be composed of one known crystalline phase.

4.1.2 Crystal Structure of In_2S_3 in Literature

There are three known modifications of In_2S_3, but considerable confusion exists concerning the nomenclature and the details of the crystal structure, which may in part be due to the small composition range of the tetragonal β-In_2S_3 at room temperature. There is a large number of entries in the JCPDS (Joint Committee on Powder Diffraction Standards) database, but many entries are of a very low quality. It seems therefore necessary to review the literature concerning the crystal structure In_2S_3 in detail in a first step. In order to verify the data found in the literature and to provide suitable references for future XRD measurements, in a second step In_2S_3 will be synthesised from the elements, the crystal

Table 4.1: Structural parameters for the three In_2S_3 modifications extracted from literature.

phase	β	α	γ
Crystal system	tetragonal	cubic	trigonal
Space group	$I4_1/amd$ (No. 141)	$Fd\overline{3}m$ (No.227)	$P\overline{3}m1$ (No. 164)
Lattice parameter [55], [58], [53]	a_0=7.623 Å c_0=32.36 Å	a_0=10.72 Å	a_0=3.8 Å c_0=9.05 Å
Transition temperature	420 °C [57]	755 °C [59]	1090 °C [53]

structure characterised and the results compared to the literature data. In the following, a selection of literature data on the crystal structure of In_2S_3 will be presented.

The spacegroup of the tetragonal β-In_2S_3 was determined by King et al. as $I4_1\,amd$ (space group No. 141) with lattice parameters $a_0 = 7.61$ Å, $c_0 = 32.24$ Å using Weissenberg photographs [54]. The spacegroup was confirmed by Goodyear et al. [55] who stated the lattice parameters as $a_0 = 7.623$ Å. Steigman et al. [56] used the Weissenberg method to determine the atomic sites, assuming the lattice parameters of Goodyear. The crystal structure of β-In_2S_3 is best characterised with a defect spinel-type model. The sulphur atoms form a cubic closed-packed sublattice, in which the In atoms occupy the octahedral and tetrahedral interstitials the same way cations do in a regular spinel (as in $MgAl_2O_4$ or $CdIn_2S_4$, for example). While all of the octahedral sites of the regular spinel are occupied, 1/3 of the tetrahedral sites remain empty. As a consequence, the structure is sometimes described with a quasi-quaternary compound formula: $[In_{2/3}\square_{1/3}]^{Th}[In]_2^{Oh}\,S_4$, where $[\ ]^{Th}$ and $[\ ]^{Oh}$ denote tetrahedral and octahedral sites and $\square$ the vacancies. The vacancies are ordered along a 4_1 screw axis parallel to the c-axis for the case of the tetragonal β-In_2S_3. The ordering of the vacancies causes a small distortion of the cubic symmetry of the regular spinel resulting in a tetragonal structure.

At 420 °C an order/disorder transition takes place and the In_2S_3 transforms to the α modification (Landuyt et al. [57]). At this temperature the In-atoms on the tetrahedral sites reorder and the vacancies become now randomly distributed over all tetrahedral sites. The structure becomes cubic with $a_0(\beta) \approx a_0(\alpha)/\sqrt{2}$ and $c_0(\beta) \approx 3a_0(\alpha)$. The α-modification crystallises in the $Fd\overline{3}m$ spacegroup [58]. The trigonal γ-In_2S_3 exists above 755 °C (Binsma et al. [59]) and is best described as a layered structure (spacegroup $P\overline{3}m1$) [53]. In this modification the sulphur sublattice remains in a nearly densed-packed structure, while the In atoms are now exclusively found in octahedral sites forming a layered structure of subsequent S-In-S-In-S slabs [60]. The fundamental crystallographic properties of the three In_2S_3 modifications as found in the literature are summarised in Table 4.1.

Table 4.2: Sample list of synthesised In_2S_3 references. Listed are the sample name, the chemical formula and the elemental composition corresponding to the weighed amounts of sulphur and indium.

Sample	Formula	at.% In	at.% S
PP-SYN-111	$In_{2.13}S_3$	41.50±0.01	58.50±0.01
PP-SYN-112	$In_{2.00}S_3$	40.00±0.01	60.00±0.01
PP-SYN-113	$In_{1.87}S_3$	38.50±0.01	61.50±0.01

4.1.3 Analysis of the Crystal Structure of In_2S_3 Reference Samples

In order to obtain In_2S_3 reference samples for a pure, single phase and crystalline In_2S_3 powder, $In_{2+x}S_3$ ingots with compositions between $0.13 > x > -0.13$ have been synthesised following a high temperature route (up to 1100 °C). The following section reports on the experimental conditions for the synthesis of these $In_{2+x}S_3$ powders and the analysis techniques used to characterise them. In the next step, In_2S_3 powders from standard commercial laboratory suppliers are analysed and tested as source materials for thin film deposition, as will be described in the following sections.

Synthesis of In_2S_3 Reference Samples

Indium sulphide was synthesised by heating weighted amounts of the pure elements in evacuated quartz ampoules. Three samples have been prepared with varying In / S ratios. Source material were indium granulate (Chempur, CH119997, 99.999 % purity) and sulphur (Alfa Aesar, E31R052, 99.999 % purity). If the indium sulphide compound formula is stated as $In_{2+x}S_3$, the weighted amounts of In and S of the three samples correspond to $x = 0.13$; 0.0 ; -0.13. The sample denotations and characteristics are summarised in Table 4.2. The weighed amounts of indium and sulphur were placed in a graphite boat, placed in a quartz glass ampoule, evacuated (10^{-3} mbar) and sealed. The ampoules were then placed in a two zone oven. In a first step, the zone containing the graphite boat was heated to 300 °C for one day, to 1100 °C for three days and then maintained at 800 °C for eight days. The other side of the ampoules was kept at 400 °C in order minimise the risk of breaking the ampoules due to the increasing sulphur pressure. In a second step both zones of the ampoules were heated to 1100 °C (above the melting point of indium sulphide) for 24 h. At this point the oven cooled uncontrolled down to room temperature due to a power failure. In order to assure that the phase transitions could completely take place the samples were heated again to and maintained at 800 °C for 2 days, 600 °C for 2 days and 400 °C for 4 days. (as stated before, the last phase transition is supposed to be at 410 °C-430 °C). Inside the ampoules, $In_{2+x}S_3$ was formed as dark grey/black polycrystalline substance in the boat and some small crystals at the ampoule walls. The $In_{2+x}S_3$ was withdrawn from the boats and stored in an argon glovebox while not in use. Just before usage, the $In_{2+x}S_3$ was taken out of the glovebox and ground manually in a mortar. The colour of the ground powder changed from black to dark brown to red for $x = 0.13$; 0.0; -0.13, respectively.

Structural Characterisation of Synthesised In_2S_3 Reference Samples

Experimental

In order to confirm the crystal structure and to obtain X-ray diffraction (XRD) reference data, for one of the powders the XRD pattern was recorded in the temperature range from 31 °C to 1049 °C using synchrotron radiation. The sample with the highest sulphur amount (PWD-SYN-113: $x = -0.13$) was chosen for this purpose as according to the phase diagram no phase with sulphur concentration higher than in In_2S_3 exists and the excess sulphur minimises the risk of a sulphur deficiency due to losses during the preparation of the ingots. Powder of sample PP-SYN-113 was ground in a mortar and sealed in an evacuated quartz ampoule ($p < 10^{-4}$ mbar). The XRD measurements were performed at the European Synchrotron Radiation Facility (ESRF), Grenoble, at the beamline ID15B with a wavelength of 0.14276 Å. More details on the used experimental setup can be found in reference [61]. XRD patterns were recorded every 5 K while the sample was heated with a constant heating rate of 300 K/h from 31 °C to 1049 °C. The three modifications of In_2S_3 (see section 4.1.1) could be identified in the resulting XRD patterns in three different temperature regimes. Rietveld refinement were performed using the program FullProf [62], [63].

Results

A map of the X-ray diffractograms of powder PP-SYN-113 recorded at various temperatures is shown in Fig. 4.2. At room temperature the pattern reflects the defect-spinel structure of In_2S_3 and shows the superstructure peaks corresponding to the tetragonal β-In_2S_3. Above 441 °C, the characteristic peaks of the tetragonal superstructure disappears and the sample turns into the cubic α-In_2S_3 which is detected up to a temperature of 806 °C. While the first phase transition is very fast and is completed between two subsequent measurements within a temperature interval of 5 °C, the second transition takes place during the measurements in the temperature range between 776 °C and 811 °C. Above 811 °C only the trigonal γ-$In_2S_3$is observed.

Separate XRD patterns of the tetragonal, cubic and trigonal phase are presented in Fig. 4.3. On the basis of these XRD patterns a full Rietveld refinement was carried out with the help of the program FULLPROF [62]. In these graphs, the measured and calculated XRD pattern as well as the position of the calculated Bragg peaks and the residuals are diplayed. An good agreement of the structural refinement with the experimental data is found with R-Bragg factors between 1.38 and 2.84. A summary of the results of the Rietveld refinement is given in Table 4.3. In Annex B the full set of refinement parameters, calculated atom sites and some graphical representations of the crystal structure of the three refined In_2S_3 modifications can be found.

The results of the Rietveld refinements carried out in this work confirm the basic crystallographic properties extracted from literature with only small variations in the lattice parameters and coordinates as well as occupation factors of atomic sites. Fig. 4.4 shows a structural model of the unit cell for the tetragonal β-In_2S_3 measured at room temperature.

The temperatures for β-α and α-γ-transition of the analysed powder were found to be slightly higher than in literature: 440 °C (±10°C) and 770 °C (±10°C). This might be

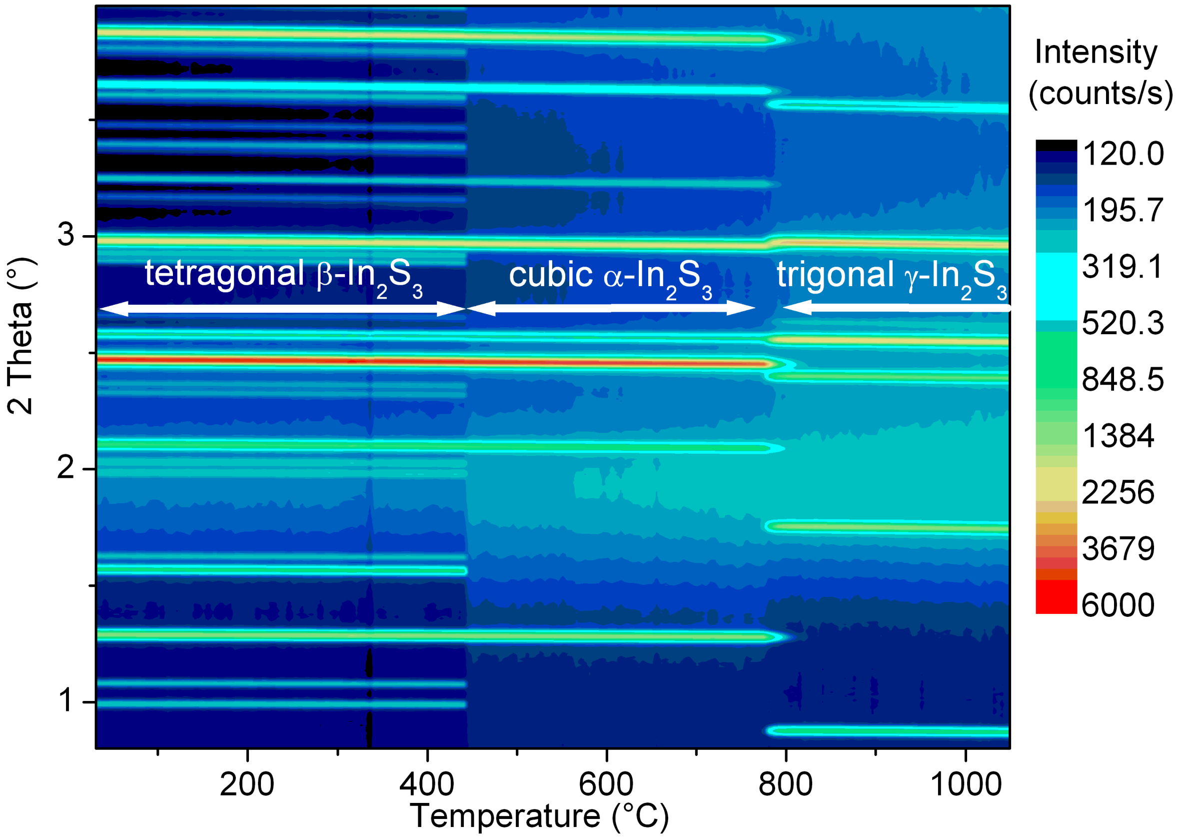

Figure 4.2: Map of temperature-dependent X-ray diffractograms (XRD) for powder PP-SYN-113. Each diffractogram measured at a specific temperature corresponds to one column in the graph with the y-direction displaying the 2Θ diffraction angle. The position of the column in x-direction corresponds to the temperature at which the diffractogram was recorded, while the colour indicates the XRD intensity (dark blue = low intensity, red = high intensity). Three structural modifications of In_2S_3 in different temperature regimes can be distinguished. Wavelength of the incident X-ray photons: 0.14276 Å (synchrotron radiation).

related to deviations in the heating rate, or the slightly higher sulphur content of the sample than in stoichiometric In_2S_3.

In addition, the three synthesised $In_{2+x}S_3$ reference powders (PP-SYN-111, PP-SYN-112, PP-SYN-113) were analysed at room temperature in a high-resolution laboratory X-ray diffractometer (a PanAlytical X´pert PRO MPD with a two-dimensional PIXcel detector) using Cu Kα-radiation (Fig. 4.5). The two samples with higher sulphur content (PP-SYN-112: 60 at.% S, PP-SYN-113: 61.5 at.%S) crystallised in the tetragonal modification of In_2S_3. For sample PP-SYN-113 this had already been observed in the synchrotron-based XRD measurements. The tetragonal β -modification shows additional Bragg-peaks due to the tetragonal superstructure that are absent in the cubic α -modification of In_2S_3. In Fig. 4.5, four of the most intense of these additional peaks have been marked and indexed ((1 1 2),(1 0 5),(0 0 8) and (1 0 7)) as examples. These additional peaks can be used to distinguish the tetragonal from the cubic modification.

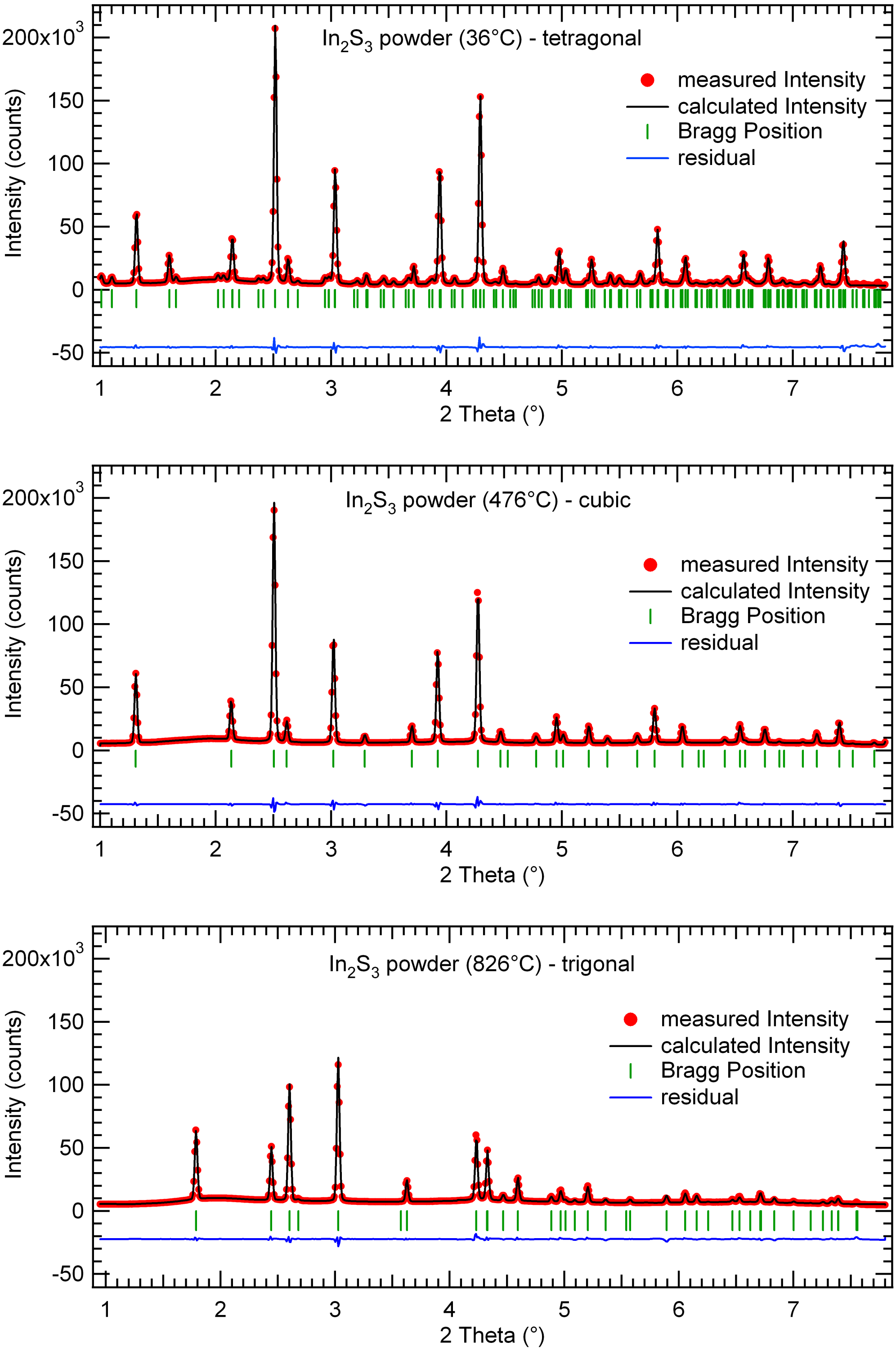

Figure 4.3: XRD patterns and Rietveld refinements for powder PP-SYN-113 showing the three structural In_2S_3 modifications. The displayed residuals have been vertically shifted for a better comparison. Top: Tetragonal β-In_2S_3 (at 36 °C). Middle: Cubic α-In_2S_3 (at 476 °C). Bottom: Trigonal γ-In_2S_3 (at 826 °C).

Table 4.3: Results of the Rietveld refinements of the XRD measurements performed on powder from sample PP-SYN-113 at 36 °C (tetragonal), 476 °C (cubic) and 826 °C (trigonal)

Phase	β	α	γ
measured at	36 °C	476 °C	826 °C
structure	tetragonal	cubic	trigonal
space group	$I4_1/amd$	$Fd\bar{3}m$	$P\bar{3}m1$
lattice	$a_0 = 7.623 \pm 0.001$	$a_0 = 10.831 \pm 0.001$	$a_0 = 3.866 \pm 0.001$
parameters (Å)	$c_0 = 32.358 \pm 0.004$		$c_0 = 9.157 \pm 0.001$
R_B (%)	1.34	1.64	2.84
R_{wp} (%)	3.12	2.77	2.96

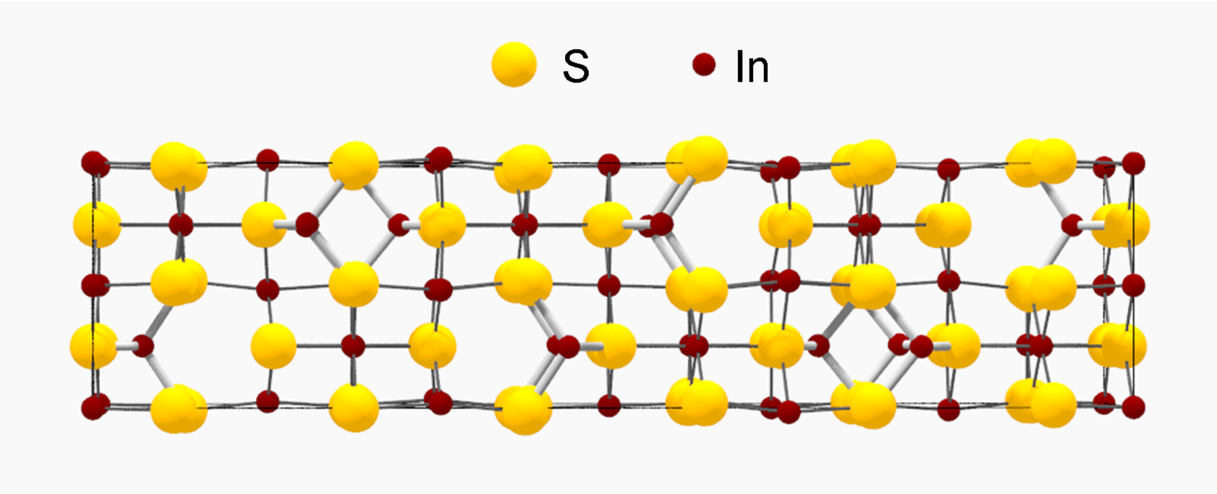

Figure 4.4: Structural model of a unit cell for the tetragonal β-modification of In_2S_3 measured at room temperature.

These peaks are absent in the XRD pattern of the sulphur poor sample PP-SYN-111 (58.5 at.% S). This sample showed a XRD pattern corresponding to the cubic In_2S_3 as it was found and refined for the sample PP-SYN-113 measured at 476°C. The sulphur poor sample crystallises therefore in the cubic α-modification at room temperatures rather than in the tetragonal β -modification. This is in agreement with the phase diagram of Gödecke [52], who claimed a small composition range for the β -In_2S_3 at room temperature and the crystallisation of In_2S_3 in the α -modification for sulphur poor samples (see Section 4.1.1). The phase diagram presented by Gödecke et al. is therefore substantially correct and for $x \geq 0.13$ $In_{2+x}S_3$ can be found in the cubic modification at room temperature.

This offers the opportunity to use the characteristic XRD pattern of a single phase material as an indicator for its stoichiometry. If it crystallises in the tetragonal β -modification of In_2S_3, it can be assumed to have a sulphur concentration of $> 58.5\,\%$. This result will be used to investigate if crystalline, stoichiometric In_2S_3 suffers preferential evaporation of sulphur during the thin film deposition process. A sample of the synthesised reference powder PP-SYN-113 (61.5 at.% S) was stressed by a thermal treatment simulating multiple thin film deposition processes (12h at 720 °C in vacuum at a pressure $p < 5 \times 10^{-5}$ mbar).

The XRD pattern of the stressed powder is added to the graph in Fig. 4.5. The XRD pattern exhibits clearly the characteristic peaks of the tetragonal β -modification, indicating a composition near stoichiometry even after the thermal treatment. For crystalline samples, no strong preferential evaporation of sulphur is therefore expected.

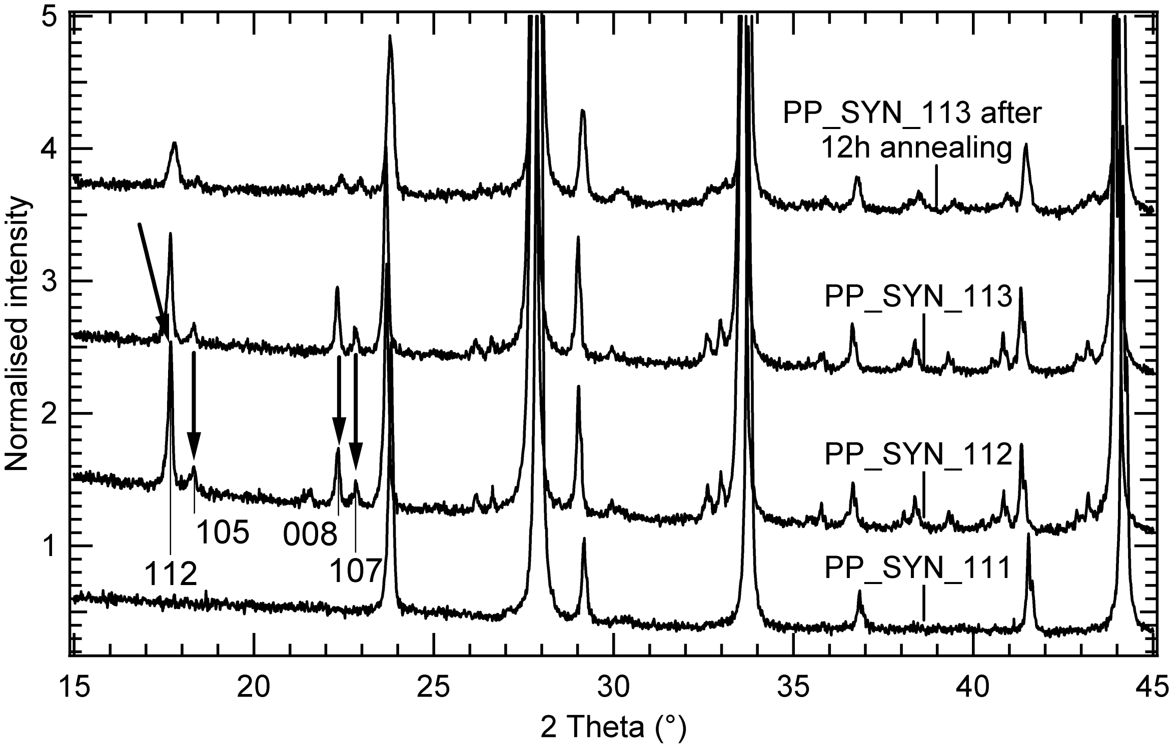

Figure 4.5: XRD patterns of the three synthesised $In_{2+x}S_3$ reference powders (XRD excitation: Cu Kα). The indium rich powder corresponding to $x = 0.13$ (PP-SYN-111) crystallises in the cubic α-modification, while the other powders (PP-SYN-112: $x = 0$; PP-SYN-113: $x = -0.13$) show the additional characteristic peaks corresponding to the tetragonal superstructure of β-In_2S_3. The XRD pattern of a sample of PP-SYN-113 that had been stressed in a thermal treatment (12h at 720 °C, $p < 5 \times 10^{-5}$mbar) is added to the graph. The XRD patterns have been shifted vertically for a better comparison.

4.2 Indium Sulphide Thin Films

Thin film deposition of In_2S_3 was demonstrated by substantially all kinds of (wet and dry) standard thin film deposition techniques in the past: electrodeposition [64], chemical bath deposition (CBD) [28], sputtering [17], atomic layer deposition ALD [65], metal-organic chemical vapour deposition (MOCVD) [66], sulphurisation of metal precursors [67], spray ion-layer gas exchange reaction (ILGAR) [27] co-evaporation of the elements [68], compound evaporation (PVD) [4], to name a few.

All techniques result in $In_{2+x}S_3$ thin films with S/In ratios in the order of 1.5. However, as a result of the varying deposition conditions, the film properties differ considerably in terms of stoichiometry, crystallinity and incorporation of additional elements. Many wet-chemical deposition methods incorporate oxygen or chlorine (depending on the precursor solution used) in variable amounts into the films. This makes a comparison of thin film properties such as the optical band gap a difficult task. Most publications agree on the n-type conductivity of the films (see e.g. [69]).

A considerable amount of publications on In_2S_3 thin films deposited by thermal evaporation (also named physical vapour deposition, PVD) has been released in the last years, for example Spiering et al. [70], Timouni et al. [71], Kumar et al. [72], Jacob et al. [73]. Efficiencies of up to 14.8 % for solar cells with evaporated In_2S_3 buffer layers have been reported by Strohm et al. [4]. This shows the extraordinary interest in this material due to its potential as a substitute for the CdS buffer layer.

However, published work is mainly of empirical nature and lacks a systematic investigation of the crystalline phases involved and the influence of the source material used and deposition conditions. It is the task of this work to review the crystal structure of In_2S_3 in detail and relate the properties of the source materials used to the performance of the $Cu(In,Ga)Se_2$ solar cells with an In_2S_3 buffer.

In the following, the structural properties and elemental composition of three commercial In_2S_3 powders will be studied. After some considerations concerning the sublimation behaviour of In_2S_3, the three commercial In_2S_3 powders will be used as source materials for thin film deposition. The optical, structural and chemical properties of the resulting thin films will be analysed. The solar cell performance of devices with In_2S_3 buffer layers prepared from the different commercial In_2S_3 powders will be compared in the next chapter.

4.2.1 Source Materials for In_2S_3 Thin Film Deposition

Commercial Indium Sulphide Powders as Source Materials

In this section, the composition and structure of In_2S_3 powders from three different commercial laboratory suppliers will be analysed and tested in view of an application as source materials in a thermal evaporation (PVD) process. The first visual inspection showed differences in colour and in the size of the powder grains. Table 4.4 shows the sample names, nominal purity and some general aspects of the three In_2S_3 powders named PWD A, PWD B and PWD C. The three commercial powders are analysed for their crystal structure and chemical composition.

Structural Characterisation

The crystalline phases were determined for all three powders with a standard laboratory X-ray diffractometer and Cu K-α excitation.

The XRD analysis revealed fundamental differences in the crystallinity of the three samples. The resulting XRD patterns are presented in Fig. 4.6. Only powder PWD B shows pronounced XRD peaks corresponding to the tetragonal β-In_2S_3 while the diffraction peaks from powder PWD A and PWD C have a much lower intensity and are extremely broadened (PWD C: FWHM approximately 1°). This indicates that only powder B is

Table 4.4: In_2S_3 powders from commercial laboratory suppliers. Note that purity in all cases is specified on metal basis (m.b.).

Sample	Supplier	purity (m.b.)	Colour	Comment
pwd A	Testbourne [74]	99.999%	red (ochre)	crumbs
pwd B	Alfa Aesar [75]	99.995%	dark/ brick red	small crystallites
pwd C	Strem Chem. [76]	99.999%	red (light brown)	crumbs

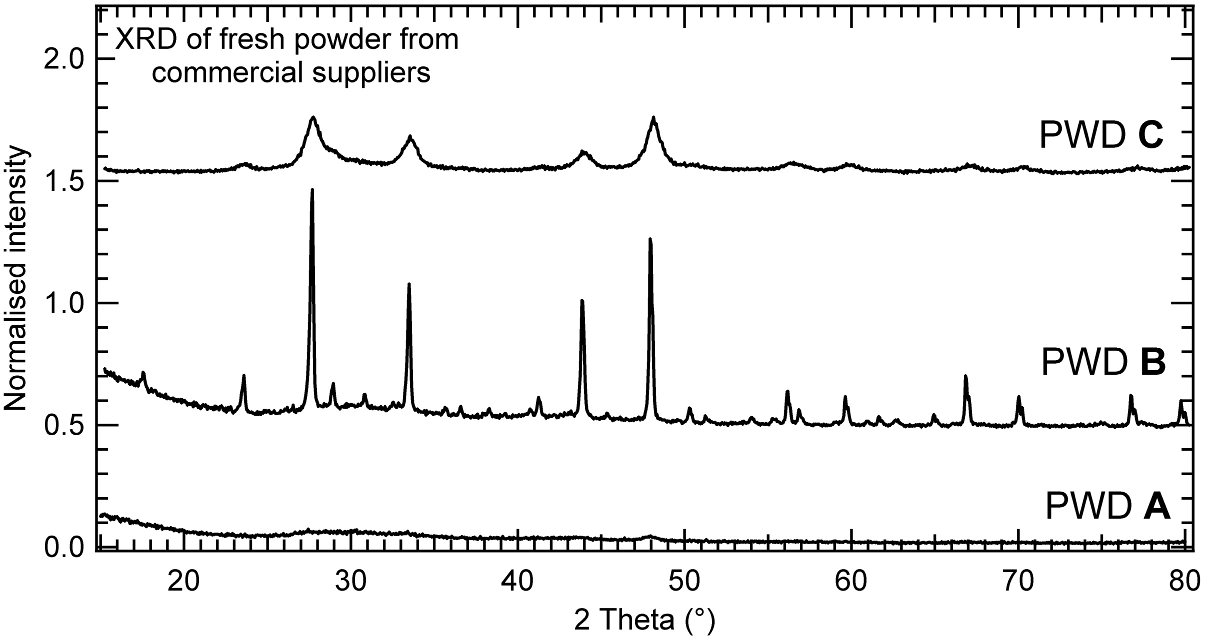

Figure 4.6: XRD patterns of the three commercial In_2S_3 powders. Only powder B shows sharp XRD reflections while all other powders show very broad/no peaks.

crystalline with grain sizes large enough (several hundreds of nanometers) for a meaningful XRD analysis, while the other powders either have much smaller grain sizes or are even amorphous. As no homogeneous grain size distribution can be expected for these powders, an estimation of the grain size based on the XRD peak width has not been carried out.

Chemical Characterisation

For composition analysis, approximately 0.3 g of each powder was ground and filled into a pressing tool. The tool was evacuated and tablets with a diameter of 10 mm were pressed by applying a maximum load of 3.5 t for 3 times during 10 minutes. While powder A and C where easily pressed into solid tablets, powder B did not stick well and showed the tendency to crumble and break into pieces. However a sufficiently large part of the tablet was introduced together with the other tablets into a standard laboratory X-ray

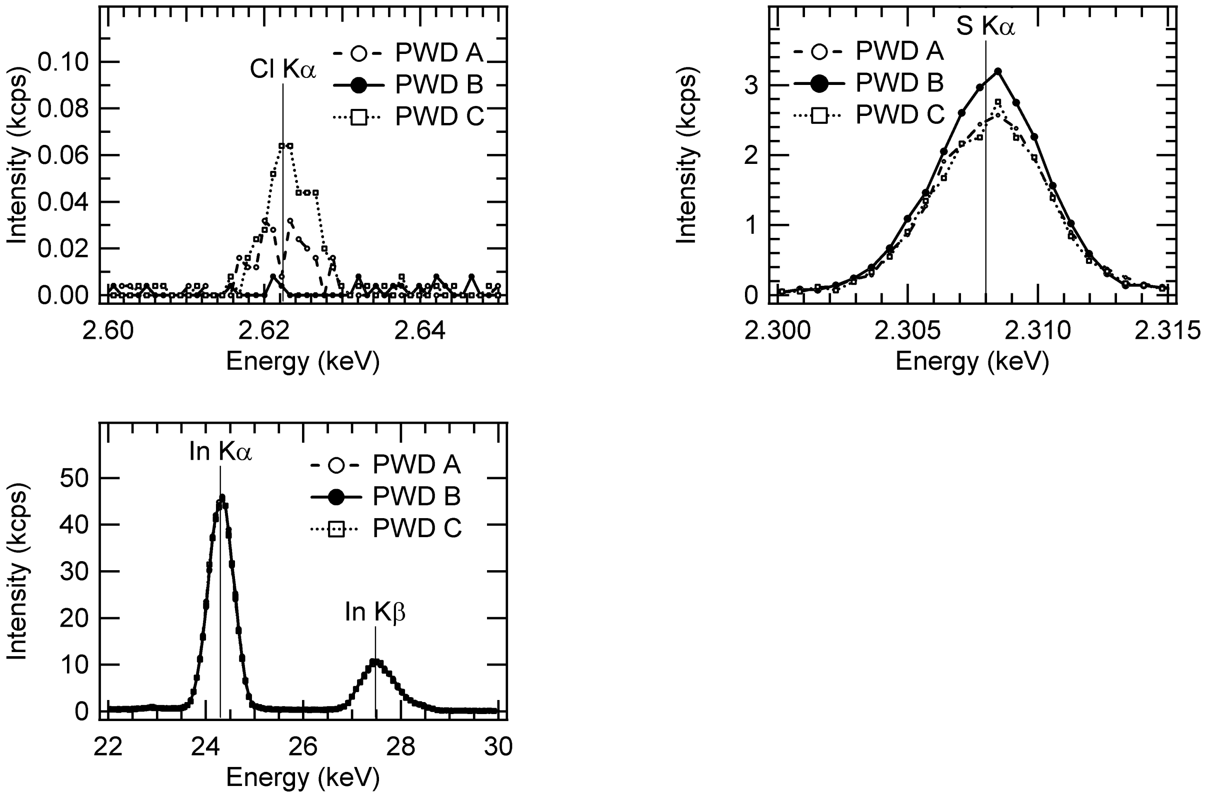

Figure 4.7: XRF spectra of the Cl Kα (top left), S Kα (top right) and In Kα (bottom left) emission lines of the three commercial In_2S_3 powders.

fluorescence (XRF) analyser (a Philips MAGIX Pro PW2440 with a Rh-anode as X-ray source.) and the tablets were scanned for their In and S XRF emission and for foreign elements. Unfortunately, light elements like oxygen are not detected with this setup.

The XRF composition analysis revealed that powders A and C contained a significant contamination of chlorine. The highest amount of chlorine was detected for powder C. Fig. 4.7 shows the measured XRF spectra. The recorded indium peak intensity was the same for all four tablets, while the S content showed a decrease with increasing Cl content in the sample. A precise quantification of the individual elements in the tablets via the XRF emission depends on an exact calibration of the system with accurate references. At this point therefore only a qualitative comparison of the relative fluorescence intensities of the four powders will be carried out. Powder A and even more powder C show a lower S Kα emission as compared to powder B. All three powders show approximately the same In Kα emission intensity. If the crystalline powder B (crystallised in the β-configuration) is considered as stoichiometric reference, the sulphur deficiency of sample C accounts to approximately 2 at.% .

For an detailed external analysis of the chemical composition, fresh powder A, B, C and a residual of powder B (after being used for up to 970 min. in the thermal evaporation process) were sent to the Microanalytical Laboratory Pascher (MLP) [77]. Here, inductively coupled plasma atomic absorption spectroscopy (In, S), vacuum thermal extraction

(O) and ion-chromatography (Cl) were used for the compositional analysis. The results confirmed the pronounced contamination by Cl in PWD A ($\approx 0.5\,\text{at.\%}$) and PWD C ($\approx 1.0\,\text{at.\%}$). Furthermore these two powders showed a much higher O/OH content than PWD B. The details of the results of the chemical analysis at the MLP can be found in Annex C. These results indicate a different synthesis process for the three commercial In_2S_3 powders; while PWD A and PWD C have most likely been (incompletely) synthesised by a low temperature (wet-chemical) synthesis route on the basis of $InCl_3$ precursors, PWD B is assumed to have been synthesised through a high temperature route. This is important as the crystal structure of the constituting phases of the source material determine its sublimation behaviour as will be shown in the following.

4.2.2 Sublimation Behaviour of In_2S_3

The sublimation of In_2S_3 determines the thin film deposition process and literature on the sublimation behaviour of In_2S_3 will be examined in short, before the deposition of In_2S_3 thin films will be treated in detail.

A significant sublimation of solid In_2S_3 for thin film deposition starts in vacuum (10^{-5} mbar) at temperatures above 690 °C. It has been shown by Miller et al. [78] that the principal constituents of the gas phase are S_2(g) and In_2S(g) (in contrast to In_2S_3(g) as was assumed in earlier works). The principal reaction takes place according to the equation:

$$\mathrm{In_{2x}S_{3x}}(s) \Longleftrightarrow \mathrm{x\,In_2S}(g) \ + \ \mathrm{S_{2x}}(g). \tag{4.1}$$

Miller et al. measured the time-dependent variation of the vapour phase composition using a mass-spectrometer for a range of compositions between InS and In_2S_3 and assumed a congruent sublimation for In_2S_3 [78][50]. More precisely, the composition for congruent sublimation (where a constant S_2:In_2S ratio in the vapour phase was found) was determined to be slightly In-rich (S :In$= 1.45 \pm 0.03$) and to vary for less than 0.1 atomic percent in the temperature range from 600 °C to 825 °C. This places the point of congruent sublimation in the homogeneity range of the α-In_2S_3. However, at temperatures above 850 °C the S_2:In_2S ratio of the vapour phase changed. When a sample of composition (S :In$= 1.45 \pm 0.03$) was heated up to 880 °C-950 °C the ratio increased initially to 2 before dropping to 0.5. Miller et al. presumed that the composition for congruent sublimation at steady-state conditions reached a phase boundary of the In_2S_3 solid solution at approximately 850 °C. According to the phase diagram presented in 4.1.1 at this temperature the cubic α-In_2S_3 phase reaches the solidus line.

These aspects are fundamental for the evaporation of In_2S_3 in a thin film deposition process. First, in order to keep a constant In:S ratio in the source material and vapour phase, the crucible temperature must not exceed 850 °C. Second, as there exist several In_xS_y phases close to the In_2S_3 composition with different homogeneity ranges (each with a different sublimation behaviour), it is of major importance for a controlled sublimation to know the crystalline constituents in addition to the total stoichiometry. It is not sufficient to have a S:In ratio of 1.5 in the source material for the deposition of In_2S_3 thin films, as this ratio might be achieved through a mixture of different phases with totally different evaporation behaviour. It is rather necessary to have a single phase material with known composition in order to assure a constant sublimation behaviour in the long term, i.e. for multiple depositions.

For the synthesised reference material it is shown that at least the majority of the starting source material remains in the β-In_2S_3 modification after 12h of deposition time (Section 4.1.3). This is a clear indication that no strong preferential sulphur evaporation takes places, at least at the used crucible temperatures of 720 °C, in agreement with the work of Miller regarding the congruent sublimation stated at the beginning.

4.2.3 Deposition of In_2S_3 Thin Films

Experimental Setup

After having identified some differences between the commercial In_2S_3 powders, their evaporation behaviour will be analysed and the chemical, structural and optical properties of thin films deposited by them.

In_2S_3 thin films are prepared by thermal evaporation (also called physical vapour deposition, PVD) of the compound In_2S_3. The vacuum chamber is equipped with effusion cells from Createc Fischer & Co GmbH. (model SFC-40-25-SH-MO) and is operated at a base pressure of $< 5.0 \times 10^{-5}$ mbar. Crucible temperature for In_2S_3 evaporation was set to 720 °C with a ramp time of 30 min. resulting in an typical deposition rate of 1-2 nm/min. The substrate was not actively heated and stayed below 50 °C. The distance between crucible and sample is approximately 40 cm. The layer thickness is monitored with an oscillating crystal microbalance, which was calibrated by cross-checking the deposited layer thicknesses with a DEKTAK profilometer. The layer thickness variation was found to be less than 10% over the sample size of 5 cm x 5 cm.

In a preliminary study, In_2S_3 thin films were prepared from the synthesised powder PP-SYN-113. A detectable evaporation of powder PP-SYN-113 started at approximately 690 °C and at a crucible temperature of 720 °C the deposition rate was constant at approximately (1.0±0.2) nm/min. over a time period of 12 h. Thin films with a thickness of (260±20) nm were deposited on quartz glass and Na-containing soda-lime glass in order to check the influence of sodium on thin film properties.

The deposited films on both substrates were homogeneous and ochre-orange in colour and had comparable sheet resistivities of approximately $(200\pm20)\mathrm{M}\Omega_{\square}$, measured with a four-point-probe.

In addition, thin films were prepared from all three commercial In_2S_3 powders. The coverage and roughness of the films were checked by scanning electron microscopy (SEM). All films were found to smoothly cover the substrate in the SEM micrographs and no individual grains inside the films could be identified for an estimation of the grain size. The evaporation behaviour during the first deposition run differed for two of the source materials (PWD A and PWD C), see Fig. 4.8. For these powders a significant evaporation started already at temperatures as low as 450 °C. This preliminary evaporation was only detected during the beginning of the first deposition run and decreased fast after a few minutes. This suggests the evaporation of a more volatile contamination from the In_2S_3 powders at the beginning of the heating process, e.g. the Cl contamination that had been detected in both of them. This behaviour will be investigated in more detail below. Fig. 4.8

illustrates the evaporation behaviour of the three commercial powders during the first deposition run and plots the deposition rate and crucible temperature as a function of the deposition time.

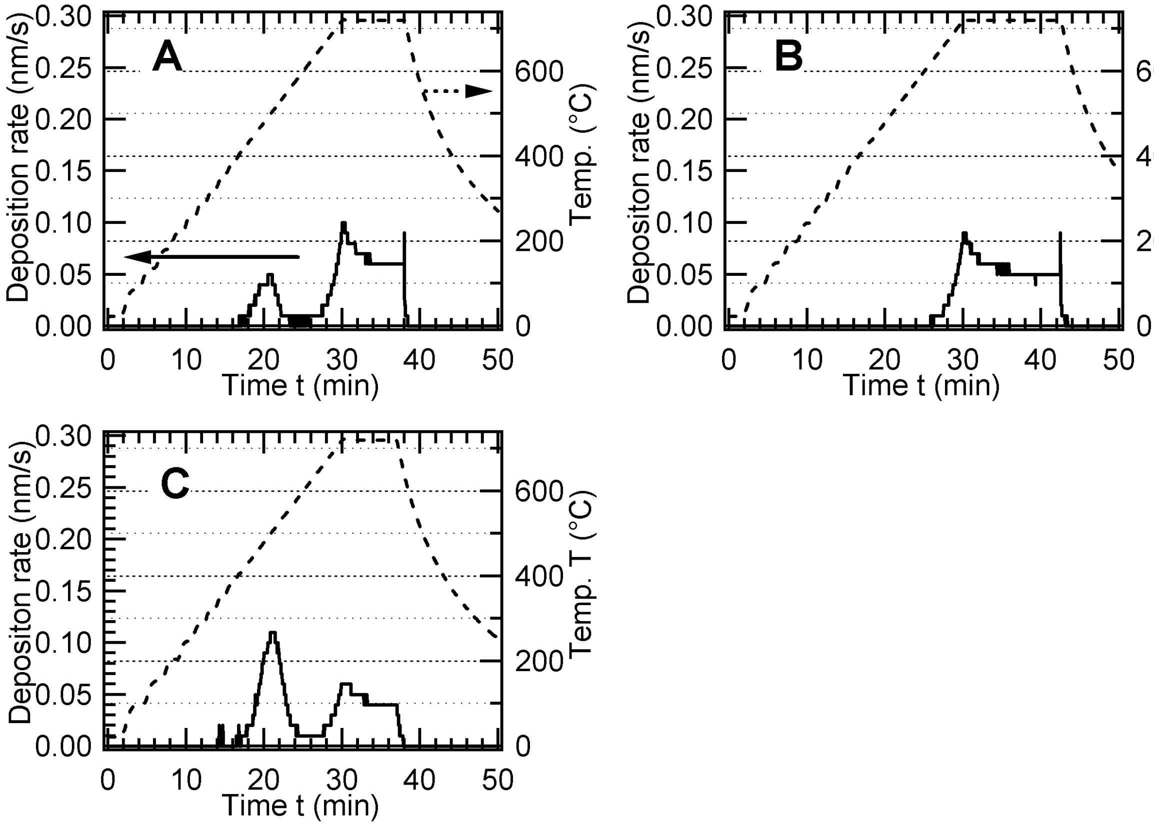

Figure 4.8: Evaporation behaviour of the three commercial In_2S_3 powders PWD A, PWD B, PWD C. In the upper part of each graph the crucible temperature is plotted vs. the time (dashed line). Below, the corresponding deposition rate is depicted (continuous line).

Thin films from the three commercial In_2S_3 powders were prepared on soda-lime glass for optical, chemical and structural analysis. In a first step as-received source material was used to deposit a 50 nm thick In_2S_3 layer at a crucible temperature of 720 °Cwith the aim to exclude the effect of the foreign species evaporating during the first deposition runs. The actual films for optical, chemical and structural analysis were deposited in the subsequent, second deposition run with a thickness of 200-300 nm and a deposition time of 120 minutes. These films are labeled TF-A, TF-B and TF-C according to commercial In_2S_3 powder PWD A, PWD B, PWD C, respectively, that were used for their preparation. At the end of this chapter, Table 4.5 summarises the properties of these thin film samples stating the sample name, source material, thickness as well as the results of the optical and chemical analysis.

4.2.4 Characterisation of In_2S_3 Thin Films

Structural Characterisation

Fig. 4.9 shows the XRD pattern of the 260 nm thick film prepared from the synthesised powder PP-SYN-113 on quartz glass measured under grazing incidence conditions. The broad peaks appear at the position of the main peaks of the cubic/tetragonal In_2S_3 structure. The structure is indexed as cubic α-In_2S_3, although an unambiguous distinction is difficult as the peaks clearly identifying the tetragonal superstructure have low intensity and might not be resolved.

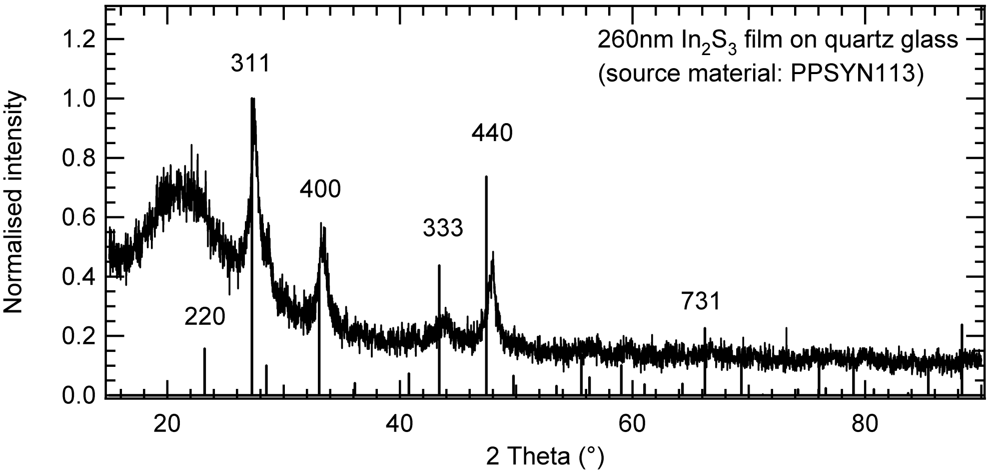

Figure 4.9: X-ray diffraction pattern of a 260±20 nm thick film grown by evaporation of powder PP-SYN-113 on a quartz glass substrate.

In_2S_3 thin films deposited from all three commercial powders generally showed only weak or even no reflections in XRD measurements when measured in the as grown state. The crystallinity (i.e. intensity and width of the XRD peaks) varied from sample to sample. The crystallinity ranged between the two extreme cases of thin films in the as-grown state showing: case a) broad peaks or case b) no XRD peaks at all. No correlation between the used source material and the observed crystallinity was found, i.e. the variation found in XRD peak width and intensity of the thin films from one powder varied stronger than the comparison of three thin films prepared by the three different commercial source materials. However, an annealing of the samples in air at 200 °C generally increased the crystallinity of the samples as will be shown below.

As examples for case a), thin films in the as-grown state with relatively strong X-ray diffraction as compared to other samples, the XRD pattern of the films TF-A, TF-B and TF-C are shown in Fig. 4.10.

Figure 4.11 shows , the XRD pattern of a thin In_2S_3 film ((270±20) nm, deposited from powder PWD B) in the as-grown state with no detectable XRD peaks as an example for case b). The XRD pattern of a part of the same sample after being annealed for 3 min. at 200 °C on a hot plate in air is added in 4.11 to the XRD pattern of the film in the as grown state. In the annealed state the XRD pattern of α-In_2S_3 can clearly be identified.

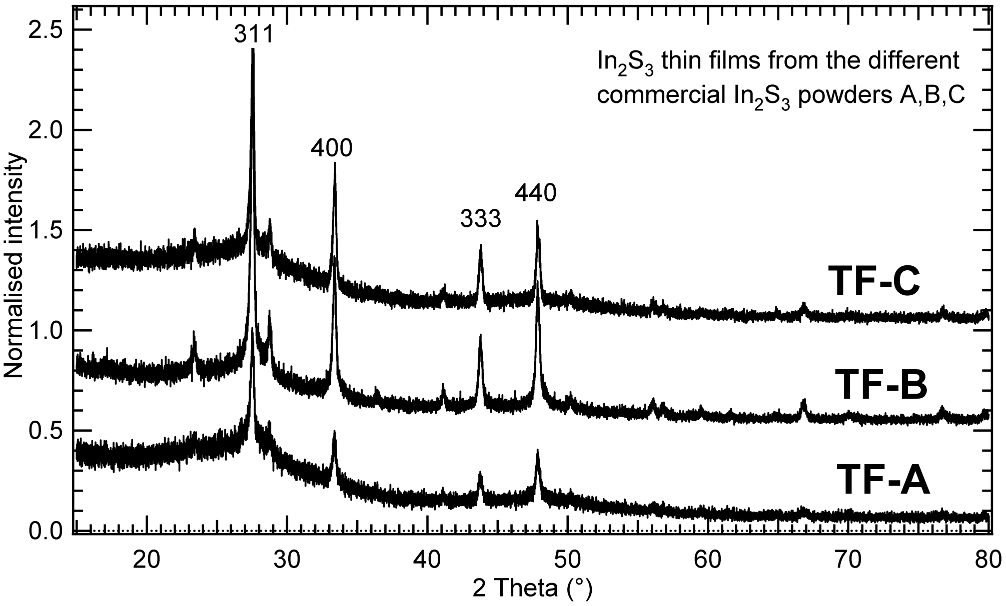

Figure 4.10: XRD patterns of In_2S_3 films TF-A, TF-B and TF-C (as grown) prepared with powders PWD A, PWD B, and PWD C on soda-lime glass substrates (thickness 220-270 nm). In these cases, some broad peaks corresponding to α -In_2S_3 are detected.

In order to examine the recrystallisation process in detail, the unannealed substrate with the In_2S_3 thin film from was broken into 6 pieces. Each piece was then heated in air on a hot plate for 3 min. at a different temperature (100 °C, 150 °C, 165 °C, 180 °C, 200 °C and 250 °C). The main diffraction peaks of In_2S_3 were recorded and compared.

The development of two characteristic XRD peaks of the cubic α-modification ((311) and (222)) upon annealing for 3 min. at different temperatures is depicted in the right part of Fig. 4.11. A clear increase in the XRD intensity for annealing temperatures above 180 °C is detected. After an annealing of 3 min. thin films deposited by all three commercial powders generally showed broad XRD peaks corresponding to cubic α-In_2S_3.

In literature on In_2S_3 thin films grown by thermal evaporation or other deposition techniques, thin films are generally stated to be poorly crystalline (or even amorphous) for deposition temperatures below 150°C, with an improving crystallinity for higher substrate temperatures or after a post-deposition annealing step [72], [69]. If XRD data is presented, it is mostly interpreted as patterns of tetragonal β-In_2S_3. However, the quality of the XRD data is generally poor due to the low crystallinity, small grain sizes and/or small thickness of the films. The interpretation as tetragonal β-In_2S_3 is therefore critical and ambiguous, as the diffraction pattern of the cubic α- and tetragonal β-modification are identical apart from a few small diffraction lines in the tetragonal structure that are induced by the ordered defect superstructure as had been shown before. Considering the presented XRD pattern and the small composition range of β-In_2S_3, many films presented in literature as β-In_2S_3 are most likely in fact α-In_2S_3.

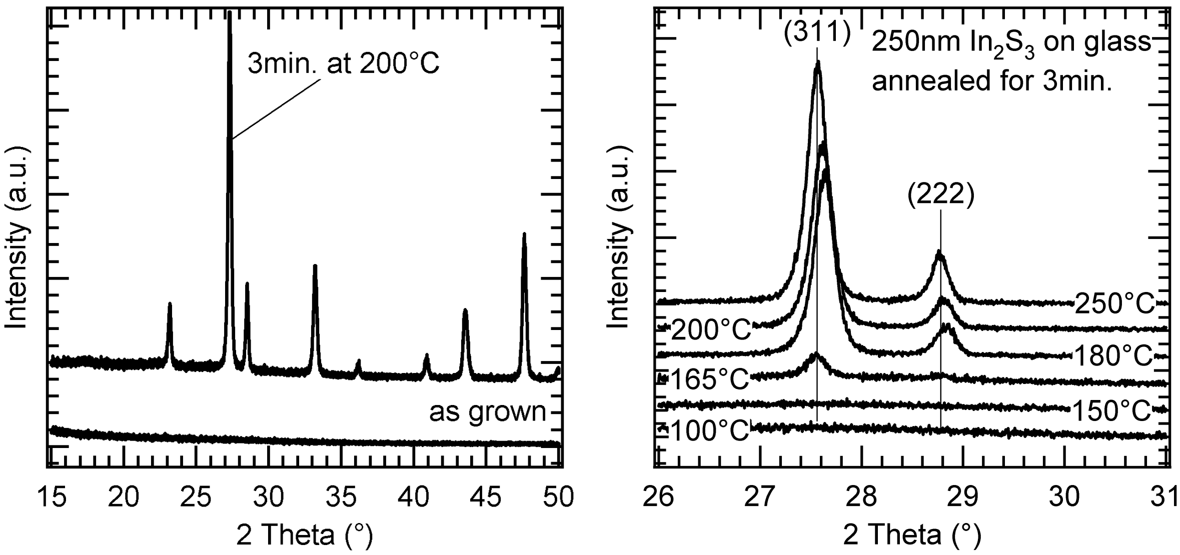

Figure 4.11: Left: XRD patterns of a (270±20) nm thick In_2S_3 film prepared with powder B on a glass substrate. In the as grown state no XRD reflections were detected, after 3 min. annealing at 200 °C the pattern of the cubic α-In_2S_3 can be identified. Right: Increasing intensity of the main XRD peaks of cubic α -In_2S_3 after submitting the samples to a heat treatment for 3 min on a hot plate in air at different temperatures.

Elemental composition

The elemental composition of the thin films TF-A, TF-B, TF-C deposited from the three commercial powders were analysed with an Philips MagiX Pro PW2440 X-ray fluorescence analyser (XRF). More details on the experimental setup can be found in Annex A.2.3. For the evaluation of the XRF data the XRF analyser was calibrated with data from an In_2S_3 thin film with known composition (determined by Elastic Recoil Detection Analysis (ERDA)).

No significant deviation from stoichiometry was detected for any of the three films. The results of the chemical analysis by XRF is summarised in Table 4.5. The estimated error of 1 at.% is due to the total error of the corresponding reference thin film used for the calibration of the XRF system which is higher than the relative error of the individual measurements.

In addition, three thin films (T1: (330±30) nm, T2: (380±30) nm), T3: (150±15) nm) were deposited on soda-lime glass with powder B that had already been used for 130 min. (T1), 350 min.(T2) and 670 min.(T3), in order to check the source material stability. The composition of these samples was checked with XRF. No significant deviation of the stoichiometry was found (T1: after 130 min., (40.5±1.0) at% In), (T2: after 350 min., (40.6±1.0) at% In), (T3: after 670 min., 41.0±1.0) at% In).

First deposition from powder PWD C

To investigate the deposition of a foreign phase at the beginning of the first heating process from powder PWC C, two samples have been processed:

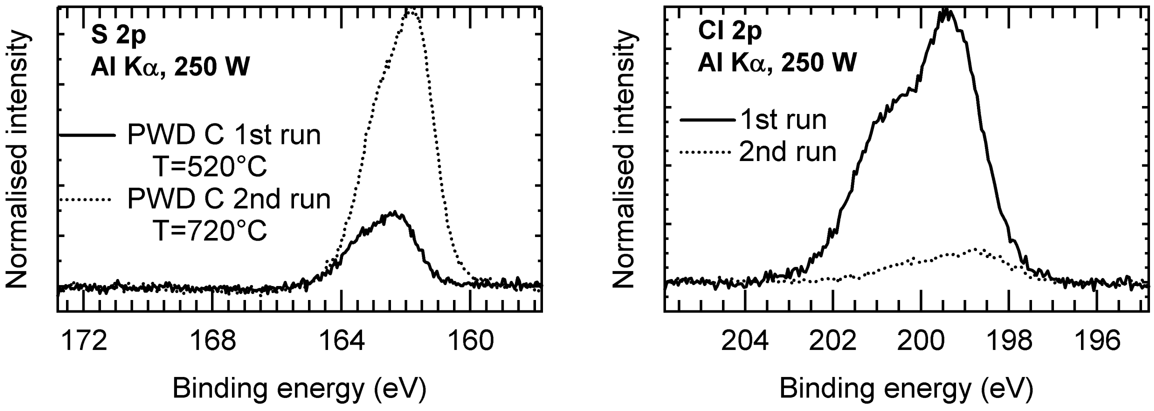

Figure 4.12: Left: XPS spectra of the S 2p emission of two thin films deposited from as-received powder PWD C. The first film was deposited in the first deposition run I, at a crucible temperature of 520 °C. The second film was deposited in a second, subsequent deposition run II, with a crucible temperature of 720 °C. Right: XPS Cl 2p peaks of the same films. Instead of sulphur, chlorine is found for the sample from the first deposition run I.

I) In the first deposition run, the crucible was filled with fresh powder C and heated to a temperature of 520 °C. At this temperature, no significant amount of In_2S_3 should be deposited. However, a thin film with a mass corresponding to (24 ± 5) nm In_2S_3 was deposited when the crucible was kept at this temperature for 20 minutes.

II) Another thin film was deposited during the subsequent, second deposition run with the crucible at 720 °C (20 min., film thickness (53 ± 5) nm).

The composition of both thin film was analysed by X-ray photo-electron spectroscopy (XPS) (see Fig. 4.12). The XPS results of the thin films deposited first at 520 °C and then at 720 °C indicates the deposition of indium chloride at the beginning of the evaporation of fresh source material from powder C. Indium is found on both films (not shown). The first film (I: 520 °C) shows mainly XPS contributions from Cl rather than from S. For the second films (II: 720 °C) the opposite is the case, here the S peak intensity exceeds the Cl contribution. The presented XPS spectra have been normalised to the background and a linear background has been subtracted.

With these and the results from the XRF analysis, the Cl content of powder PWD C can be roughly approximated considering the following:

1) Based on the XRF results and the chemical analysis it is reasonable to assume that part of the powder consists of $InCl_3$, most probably a residue of a synthesis route via a sulphurisation of $InCl_3$.

2) From the relation between deposited layer thickness and evaporated source material it can be estimated that 1 g of powder is enough to deposit approximately 1200 nm of In_2S_3 (with a density of $4.9\,g/cm^3$) onto the substrate.

3) If it is assumed that in the beginning of the evaporation the $InCl_3$ is completely evaporated and an amount of $InCl_3$ (density $3.46\,g/cm^3$) corresponding to a mass of

24 nm In_2S_3 is deposited instead, the total mass ratio of of $InCl_3$ / In_2S_3 is in the order of a few percent.

Optical Characterisation

The transmission and reflection properties of thin films prepared from powder PWD PP-SYN-113 in the preliminary experiment were measured with a Cary 500 Scan UV-Vis-NR Spectrophotometer (for details, see Annex A.3). The absorption coefficient and optical bandgap were calculated following Sect. A.3. The left part of Fig. 4.13 shows the transmission/reflection measurements of the thin film deposited from PWD PP-SYN-113 on quartz glass. An analysis of the optical bandgap following Section A.3 agrees best for an coefficient $m = 2$ as given for an indirect bandgap (Eq. A.12). In the right part of Fig. 4.13 the value of $(\alpha h\nu)^{0.5}$ is therefore plotted versus the photon energy. From the intersection of a linear fit with the abscissa an optical bandgap of (2.01±0.03) eV is obtained. The same procedure applied to the sample prepared during the same deposition but on soda-lime glass instead of quartz glass showed no change in the optical behaviour and the evaluation yielded a bandgap of (2.00±0.03) eV.

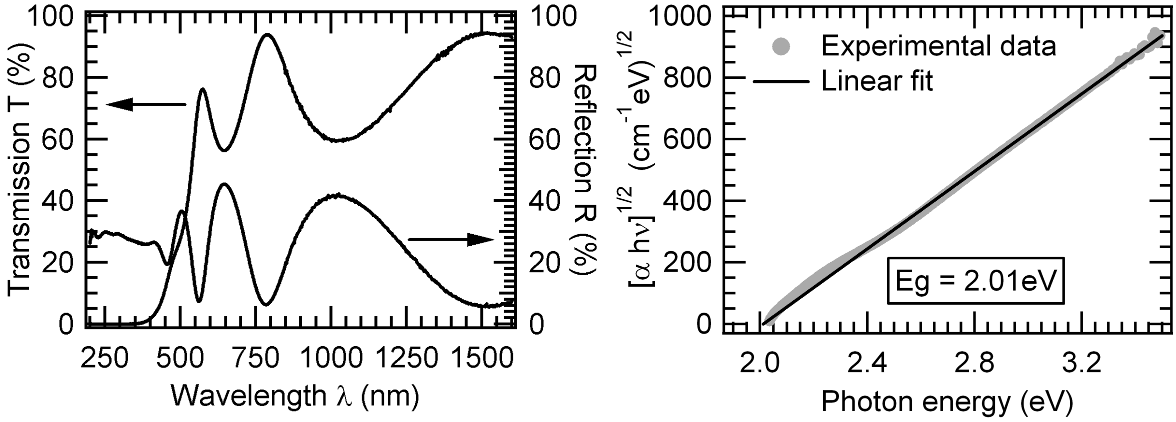

Figure 4.13: Left: Transmission and reflection spectra of a In_2S_3 thin film prepared with synthesised In_2S_3 powder (PP-SYN-113) on a quartz substrate. Right: Representation of $(\alpha h\nu)^{0.5}$ and a linear fit showing the indirect character of the fundamental absorption edge. The linear fit intersects $y = 0$ at (2.01±0.03) eV.

The optical properties of the In_2S_3 films from the three commercial source materials are evaluated equivalent to the case of the samples presented above. The optical bandgap is in all three cases close to 2.0 eV and is described best with an indirect transition. For example, the thin film deposited from powder PWD B showed an optical bandgap of (1.99±0.03) eV (indirect transition). This value did not change even after annealing the sample for 5 min. at 200°C in air. The extracted bandgap values for all three thin films deposited from the commercial In_2S_3 powders can be found in Table 4.5. This table also includes the results of the XRF analysis of the thin films.

Table 4.5: Basic properties of In_2S_3 thin films prepared with the three commercial powders determined in this work.

	TF-A	TF-B	TF-C
Source material	PWD A	PWD B	PWD C
Film thickness	(220±20) nm	(270±30) nm	(220±20) nm
Optical bandgap	(1.94±0.03) eV	(1.99±0.03) eV	(1.95±0.03) eV
At.% S (XRF) (± 1 at.%)	40.7	40.7	40.8
At.% In (XRF) (± 1 at.%)	59.3	59.3	59.2

Comparison with Literature

A fundamental optical absorption edge is found for In_2S_3 around 2 eV, and there seem to be direct and indirect transitions present, which makes a clear attribution to one or the other sometimes a difficult task. Kambas et al. [79] found a direct band gap of 2.0 eV for bulk β-In_2S_3 at room temperature and a linear decrease of the bandgap with temperature in the range from 90 K to 450 K. Rehwald et al. also stated a direct (but forbidden) bandgap at 2.03 eV. Other values found in literature are: 1.97 eV (Bube et al. from photoconductivity measurements [80]); 1.98 eV (indirect, single crystal from melt, Nakanishi et al. [81]); 1.89 eV (indirect) and 2.03 eV (direct) (Radautsan et al. [82], single crystals by chemical transport method using iodine as transport agent) and 2.240 eV (indirect) and 2.629 eV (direct) (Choe et al. [83], single crystals by chemical transport method using I_2 and $ZnCl_2$ as transport agents, the slightly higher band gap value is probably due to the preparation method).

For pure In_2S_x thin film samples, the optical band gap depends on the S / In ratio. Kim et al. found in increasing bandgap (with an indirect transition, the bandgap was stated to range from 2.15 eV to 2.43 eV) for thin films with x ranging from 1.5 to 3. Stoichiometric and crystalline In_2S_3 thin films in the pure tetragonal β-modification show band gaps similar to the bulk crystalline material, as should be expected. A bandgap value of 2.01 eV and in indirect fundamental absorption edge is for example reported by Barreau et al. [84] for highly crystalline and carefully chosen stoichiometric samples prepared by co-evaporation. The same author stated a strong dependence of the bandgap on the incorporation of impurities in the thin films such as sodium [85], oxygen [68] or copper [86]. In the case of sodium and oxygen a linearly increasing bandgap up to nearly 2.9 eV for an increasing impurity concentrations was found. When copper was incorporated into the films, the band gap decreased down to 1.55 eV. (at a atomic ratio Cu/In of 0.2). It is fair to say that the principal reason for the huge differences in optical band gap values ranging between 2 eV-3 eV reported for In_2S_3 thin films in literature ([30] and references therein) can be found in the different properties of the thin films induced by the different experimental conditions and deposition methods involved.

Despite the huge differences in reported optical properties, many of the thin films investigated led to high efficiency photovoltaic devices when combined with $Cu(In,Ga)Se_2$ absorbers, which is an indication for the broad process window offered by the In_2S_3 type buffer layers.

4.3 Summary

In this chapter fundamental material properties of In_2S_3 and its application as a source material in a compound thermal evaporation process for the deposition of thin films have been studied.

High quality, crystalline $In_{2+x}S_3$ reference material has been successfully synthesised and its crystal structure was examined in detail for different compositions. For a selected sample the crystal structure has been determined over the temperature range from 40 °C to 1040 °C. Three different modifications could be identified in three different temperature regimes showing tetragonal, cubic and trigonal symmetry. Diehl et al. [53] reported data for the trigonal In_2S_3 that he had stabilised at room temperature through the incorporation of As and Sb, but up to the authors knowledge no detailed structure data for the pure, trigonal, high-temperature phase had been presented so far. The presented analysis offers detailed reference data extending and clarifying the existing literature on In_2S_3 and helps to quickly evaluate other XRD measurements.

Commercially provided In_2S_3 was examined in order to establish some selection criteria for a suitable source material in a thermal evaporation process. The evaluated powders were found to differ significantly in terms of their purity, stoichiometry and crystallinity as well as their evaporation behaviour. One important criteria for a high quality source material apart from purity and stoichiometry is identified to be its crystallinity, i.e. it needs to be a stoichiometric, pure and crystalline single phase material. Single phase source material was found to be stable during multiple depositions and resulted in stoichiometric, homogeneous thin films with an indirect optical bandgap of 2.0 eV.

For commercial powders it is important to realise that the stated purity in general only refers to the metal basis. Other impurities such as the identified chlorine are not included. The main difference in the examined commercial powders apart from the pronounced Cl contamination was the crystallinity, in terms of the width and intensity of the recorded XRD reflections. Only one powder showed a crystallinity comparable to the synthesised reference sample. This is assumed to be the result of different synthesis routes used to synthesise the individual In_2S_3 powders, i.e. the low crystallinity being a result of a low temperature (wet-chemical) synthesis. From the different evaporation behaviour of these powders it is clear that a defined initial state of the source material is very important for a controlled evaporation process. It is not sufficient to have a pure and stoichiometric material to start with, as this might be obtained through a mixture of different In-S phases or even a mixture of the elements in the worst case. For a controlled evaporation it is rather essential to start with a defined, crystalline single phase material. This is proven not to be guaranteed for commercially provided In_2S_3.

The stoichiometry, purity and crystallinity has to be checked prior to the application of compound In_2S_3 in a thin film deposition process as a consequence. The best advice is to only use material for which the synthesis process is known and controlled or to apply a purification/recrystallisation treatment (e.g. by resublimation) to the In_2S_3 before using it in a thermal evaporation thin film deposition process. If not stated otherwise for the rest of this work, the crystalline powder PWD B was used as a source material for the In_2S_3 thin film deposition.

Chapter 5

Solar Cells with In_2S_3 buffer

In this chapter the photovoltaic performance and electronic properties of Cu(In,Ga)Se_2 thin film solar cells with an evaporated In_2S_3 buffer layer are analysed in detail and compared to reference Cu(In,Ga)Se_2 solar cells with a CdS buffer. The preparation conditions for optimum photovoltaic performance are presented in the first section, starting with a short review on the general experimental part of the solar cell preparation, which is followed by the experimental requirements for the buffer layer deposition in order to obtain optimum performance. This includes an examination of the influence of the quality and stability of the source materials used for the In_2S_3 deposition and the beneficial effect of post deposition annealing.

It is found that an annealing treatment is essential for optimum device performance in the case of devices with an In_2S_3 buffer. Optimised devices and the effect of the annealing treatment will be analysed in detail in the corresponding sections of this chapter: First, the spectral dependence of the collection of photo-generated charge carriers will be investigated with an analysis of the quantum efficiencies. In addition, a comparison of the jV-data measured in darkness with the 2-diode-model and the detailed analysis of the temperature- and illumination-dependent $jV-$ characteristics of the devices in Section 5.2.3 help to identify changes in the dominant recombination mechanism and the resulting impact on the open circuit voltage.

The best cell efficiencies obtained for devices with an evaporated In_2S_3 buffer layer obtained during the course of this work are presented at the end of this work in Chapter 7.

5.1 Preparation and Performance Optimisation

5.1.1 Deposition of Indium Sulphide Buffer Layers

The preparation of CdS buffer layers by a chemical bath deposition in the reference Cu(In,Ga)Se_2 solar cells has been replaced by a thermal evaporation process for devices with an In_2S_3 buffer. For optimum cell performance the following standard deposition parameters have been established and used throughout this work:

- Buffer layer thickness. The established layer thickness is a trade-off between low absorption losses in the buffer layer for small layer thicknesses and good reproducibility, i.e. reducing the probability of pinholes with increasing buffer layer thickness. In a preliminary study the efficiency was found to vary by less than 15 % in the thickness range 15 -50 nm, which is in the order of the sample to sample variation. X-ray photoeletron spectra suggest a closed In_2S_3 layer for thicknesses around 20 nm. In favour of a good reproducibility the standard buffer layer thickness was set to 50 nm.

- Evaporation source temperature. The evaporation source temperature is a trade-off between fast deposition cycles and the risk of source material degradation. The standard crucible temperature was set to 720 °Cwhich ensures a reasonable deposition rate (1-5 nm/min.) while minimising the risk of source material degradation.[1]
- Substrate temperature. The substrate temperature has not been systematically varied in this work as one fundamental question was the effect of the subsequent annealing treatment on samples growing at room temperature. It can be expected that the annealing treatment can be shortened by higher substrate temperatures. Few experiments conducted with In_2S_3 buffer layers deposited on substrates at temperatures up to 200 °C did not show a priori a beneficial effect of higher substrate temperatures on the cell efficiency. In the standard deposition conditions the substrate is therefore not actively heated and stayed below 50 °C.
- Base pressure. During the In_2S_3 buffer layer deposition the base pressure was $<5.0\times10^{-5}$ mbar.
- Selection of source material. As the source material quality in terms of stoichiometry, purity and crystallinity determines the thin film quality, it is fundamental to choose a suitable source material for high efficiency devices. The influence of the source material will be adressed in a separate section of this chapter, see Section 5.1.3.
- Absorber surface condition. Absorbers that were not directly introduced into the In_2S_3 deposition chamber were stored under an inert gas atmosphere. The In_2S_3 buffer layers were deposited ex-situ, i.e. in a vacuum chamber that was separated from the absorber deposition chamber. This means that absorber samples had to be air-exposed during sample handling and transfer from the absorber deposition chamber to the In_2S_3 deposition chamber. A disadvantage of the ex-situ thermal evaporation process in comparison with wet-chemical deposition methods is that e.g. oxides resulting from the air exposure are not removed prior to the buffer layer deposition. However, samples prepared on absorbers that had been stored under inert gas for several months were not found to show significantly lower performances than their fresh counterparts.

The first optical transition for the In_2S_3 was found to be indirect with a band gap of the (2.0±0.1) eV (see Chap.4.2). Solar cells with alternative buffer layers often need “light

---

[1] In_2S_3 is found by Miller et al. to evaporate congruently up to a temperature of approximately 850 °C [50]. See also the discussions on source material stability in Chapter 4 and later on in this chapter in Section 5.1.3.

soaking" to achieve optimum performance. This means that devices exhibit metastabilities which cause an increase of the efficiency as a function of the illumination time, see e.g. [87], [88]. Solar cells with evaporated In_2S_3 buffer layers prepared in this work did not need light soaking, i.e. their performance was found to be stable and did not vary as a function of the illumination time.

For an optimum performance, samples were found to need a post deposition annealing. The post annealing was performed with the completed device on a hot plate in air in several steps for generally 5 -45 min. at a temperature of 200 °C. Generally, solar cells will be annealed in subsequent steps of 5 min., 10 min. and 20 min. The annealing status of the devices will then be stated as the accumulated annealing time, i.e. the integral time that the device had been subjected to the annealing temperature of 200 °C. The annealing status of a device under the above conditions will be referred to as X min. ann. in this and the following chapters, (e.g. read "15 min. ann." as "the completed device has been annealed for an accumulated, integral annealing time of 15 min. in air on a hot plate at 200 °C"). The effect of varying the annealing conditions will be separately treated in Section 5.1.4.

5.1.2 Performance and Reproducibility

Before comparing the effect of different source materials, the source material stability or details of the annealing treatment the performance of a solar cell with an In_2S_3 buffer layer will be presented as an example and the efficiency variation for different cells on the same sample will be discussed. The efficiency of devices with an In_2S_3 buffer layer was found to increase upon annealing on a hot plate in air at 200 °C. It is therefore important in the following sections to distinguish between samples in the as grown state and annealed samples. An example for the development of the cell efficiency after various subsequent annealing steps is shown in Fig.5.1.

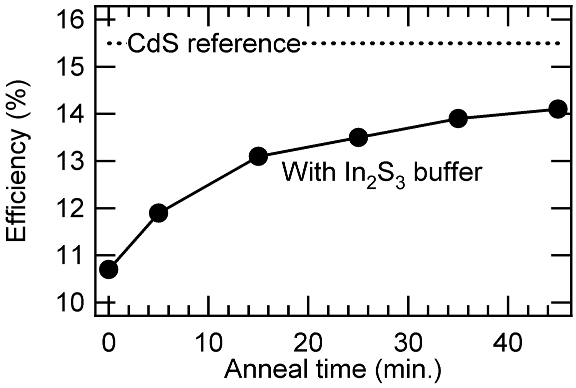

Figure 5.1: Development of the efficiency of a $ZnO/In_2S_3/Cu(In,Ga)Se_2/Mo$ solar cell after subsequent annealing treatments at 200 °C. The average efficiency of the CdS reference device is added as a dotted line.

The presented sample has been prepared on a standard HZB absorber as outlined in Section 2.2, with the In_2S_3 deposited from pure, crystalline powder B (Alfa Aesar,

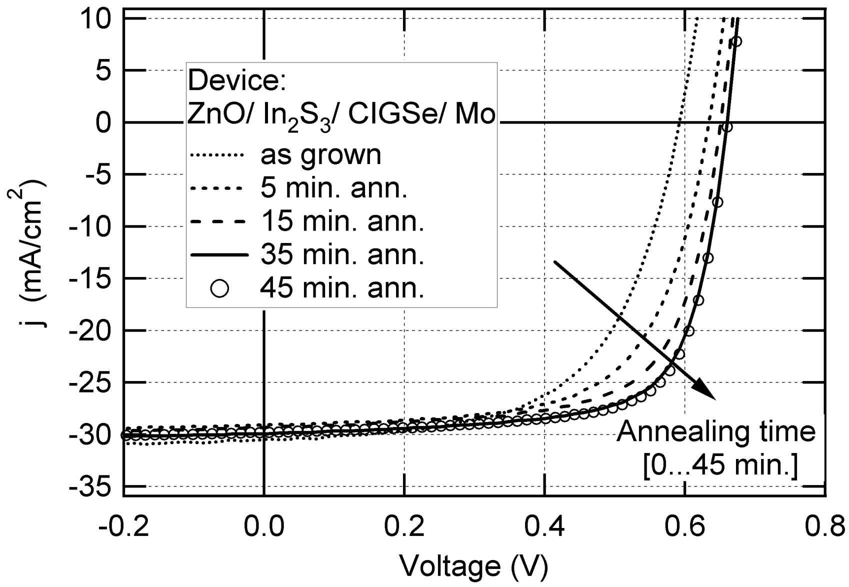

Figure 5.2: jV-curve of a Cu(In,Ga)Se$_2$ solar cell with a In$_2$S$_3$ buffer layer under illumination (AM1.5). The different curves show the same cell after subsequent annealing steps.

see Chapter 4 for details on the powder characterisation.) The finished ZnO/ In$_2$S$_3$/ Cu(In,Ga)Se$_2$/ Mo sample had a size of 2.5 cm×5 cm and consisted of 16 individual solar cells each with an approximate area of 0.5 cm^2.

The *jV*-curve of the cell under AM1.5 illumination is shown in Fig. 5.2, the measured cell parameters are listed in Table 5.1. The cell parameters of the best CBD CdS solar cell prepared from the same batch with an efficiency of 16.3 % is added to the table for comparison. In the as grown state, a relatively low efficiency of 10.1 % is found mainly due to a low fill factor and open circuit voltage (59.4 % and 592 mV, respectively). Upon annealing at 200 °C for 5-45 min., the fill factor increases up to 71.7 %. The open circuit voltage is improved, too, with a final value of 661 mV after 45 min. Compared to these changes, the short circuit current density is only slightly decreased (variation ranging from 30.5-29.1 mA/cm^2). As outlined above, the effect of the annealing on cell parameters and the electric transport mechanisms of the device will be discussed in more detail in the upcoming sections.

The efficiency distribution of the ZnO/ In$_2$S$_3$/ Cu(In,Ga)Se$_2$/ Mo sample with 16 cells is shown in the left part of Fig. 5.3 in the as grown state. After annealing, the efficiency distribution is narrower than in the as grown state (right part of the same figure). The average efficiency and standard deviation for the In$_2$S$_3$ -buffered device give (10.7±0.9) % in the as grown state and (13.8±0.3) % after 45 min. of annealing. Average efficiency over 21 cells for the CBD CdS reference was 15.5 % with a standard deviation of 0.4 %, which is comparable to the In$_2$S$_3$ device after annealing.

Some cells after repeated measuring and annealing cycles got short-circuited, probably due to mechanical scratching. Short-circuited cells (shunt resistance $R_p < 100\Omega\mathrm{cm}^2$) were excluded from statistical considerations in this and the following cases. For the device under consideration, this was the case for two cells and consequently only 14 cells

Table 5.1: Development of the solar cell parameters of a Cu(In,Ga)Se_2 solar cell with an In_2S_3 buffer after various annealing times. The cell parameters of the best CBD CdS solar cell prepared from the same batch is added as a reference.

Annealing time (min.)	η (%) ±0.2 %	j_{SC} (mA/cm^2) ±0.5 (mA/cm^2)	FF (%) ±0.2 %	V_{OC} (mV) ±2mV
0	10.7	30.5	59.4	592
5	11.9	29.1	64.8	634
15	13.1	29.3	68.6	651
25	13.5	29.6	69.4	654
35	13.9	29.9	70.4	660
45	14.1	29.8	71.7	661
CBD CdS Ref.	16.3	32.8	76.4	651

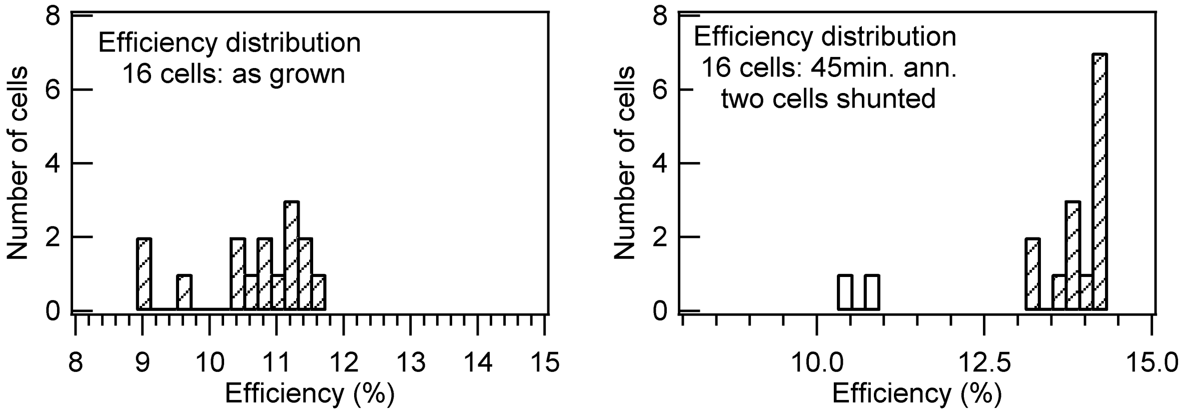

Figure 5.3: Performance variation of a sample with 16 solar cells before and after annealing at 200 °C. Displayed is the number of cells for each efficiency interval in the as grown state (left) and after 45 min. annealing (right). Two cells were shunted (no pattern).

contribute to the average efficiency and standard deviation of the sample annealed for 45 min. ann.

5.1.3 Cell Performance Vs. Source Material

In this section the relationship between device performance and the source material used for the buffer layer deposition will be investigated. In Chapter 4 In_2S_3 powders named PWD A (Testbourne), PWD B (Alfa Aesar) and PWD C (Strem Chemicals) from three commercial suppliers have been introduced and their chemical and structural properties were examined in detail. It was found that only powder B showed good crystallinity (i.e. it showed sharp XRD reflections) and purity in the as-received state, while the other two showed pronounced contamination by Cl and low crystallinity.

Experimental

To evaluate the effect of the different source materials on device performance, sets consisting of five samples were deposited from each powder. For these sets $Cu(In,Ga)Se_2$ absorbers from the Würth Solar pilot line [89] were used instead of the standard HZB $Cu(In,Ga)Se_2$ absorbers because the latter were only available in small quantities. The samples were cut out of large 60 cm×120 cm substrates resulting in many samples from the same batch, ensuring a better comparability. Following a suggestion from D. Hariskos et al. [90] these absorber samples have been heated prior to the buffer layer deposition in vacuum for 30 min. at 200 °C, as this had been found to be beneficial for this kind of absorber. The solar cells were completed with the standard i-ZnO/n-ZnO window layer and front contacts.

For each sample, the averaged efficiency and standard deviation have been obtained from the measurement of 6-8 cells under AM1.5 illumination. The samples were named after the source material used, i.e. A1-A5 stemming from powder PWD A, B1-B5 from PWD B and C1-C5 from PWD C. The averaged efficiencies and standard deviations of the three sample series are displayed in Fig. 5.4 together with their corresponding CdS references.

Samples Prepared from Powder PWD A

The first set of buffer layers was deposited from PWD A and the results are depicted in Fig. 5.4 (top) in the as grown state and after 5, 15 and 35 min. of device annealing. To avoid the deposition of volatile contaminations of the source material, the crucible shutter stayed closed for 15 min. after the crucible reached the set temperature (720 °C.) The average efficiencies of the samples annealed for 35 min. varied between 7.9 % and 8.9 % while the average intensity of the CBD CdS reference was (13.3±0.4) %. All cell parameters (FF, V_{OC}, j_{SC} contributed to the lower cell efficiency in this case. The cell parameters for the best cell from this and the other sample sets are presented in Tab. 5.2 together with the best reference cell.

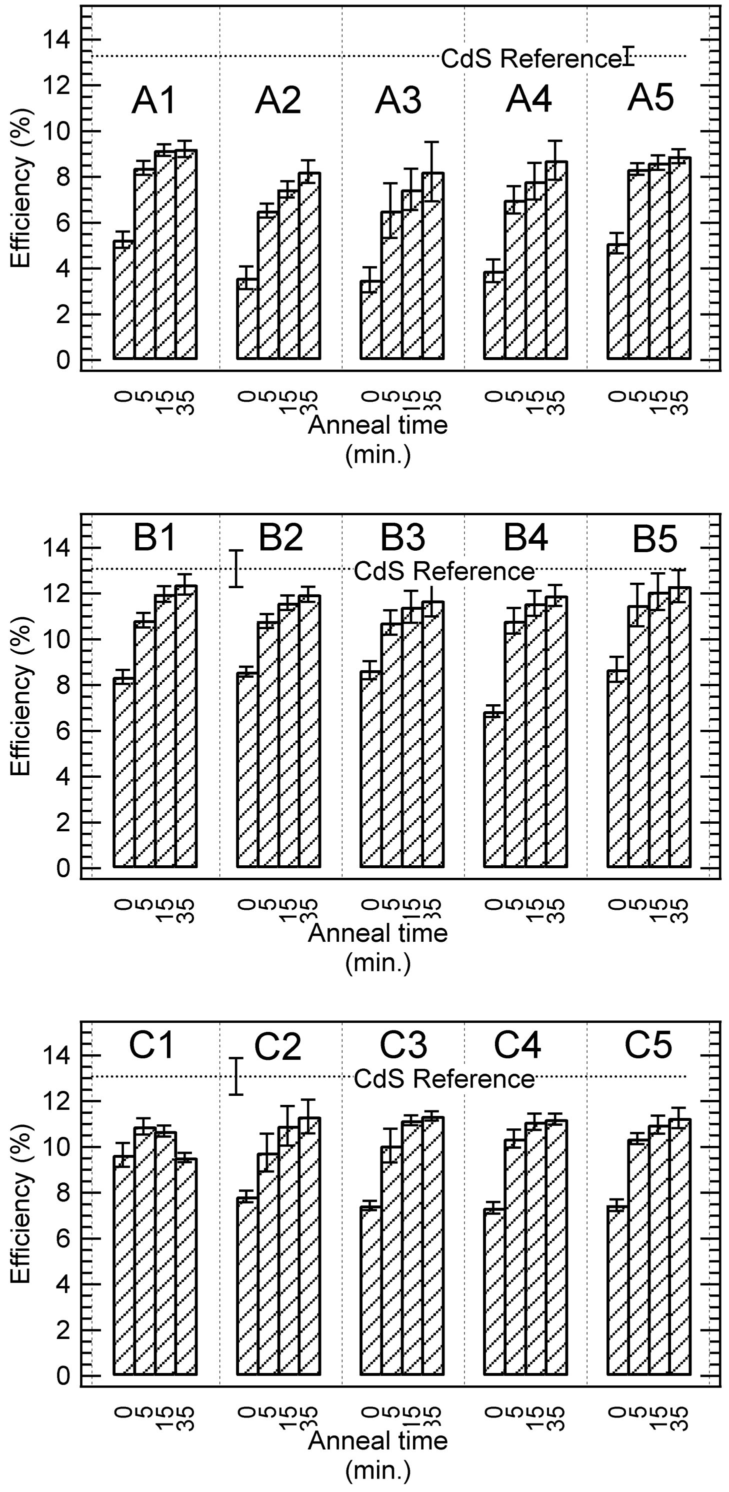

Figure 5.4: Efficiencies for the sample series with In_2S_3 buffer layers deposited from powder PWD A, PWD B and PWD C. Five samples have been prepared for each powder. Displayed are the average efficiencies and standard deviations at annealing times 0-35 min. for each sample.

Samples Prepared from Powder PWD B

The samples B1-B5 prepared from source material PWD B performed better than the other two sample sets. The average efficiencies are illustrated in Fig. 5.4 (centre). In the as grown state, the samples showed average efficiencies ranging from 8.3-8.7 %. The performance improved upon annealing to 11.7-12.3 % after 35 min. ann. The sample sets B1-B5 and C1-C5 have been prepared from the same batch and the corresponding CdS reference is therefore the same with an efficiency of (13.1±0.8) %. The best cell efficiency obtained for this sample set was 12.8 %.

Samples Prepared from Powder PWD C

The averaged efficiencies of the samples C1-C5 with buffer layers originating from powder PWD C are illustrated in Fig. 5.4 (bottom). Here, efficiencies in the annealed state are generally closer to the CBD CdS reference as compared to samples A1-A5, but lower than B1-B5. In this sample set, the crucible shutter was specifically left open during the heat up phase and therefore volatile contaminations of the source material contribute especially to the performance of the first sample. Samples C2-C5 showed a steadily increasing efficiency upon annealing with highest efficiencies after 35 min. ann. ranging from 11.2 %-11.4 % as was observed for the other samples A1-A5 and B1-B5.

Sample C1 is the first sample prepared from fresh powder PWD C and shows a different annealing behaviour than the rest of the samples C2-C5. The as grown efficiency (9.7±0.5) % is higher than in the case of samples C2-C5 (7.3-7.8 %). Optimum performance is achieved after 5 min. annealing ((10.9±0.4) %), for longer annealing times the efficiency decreases again (35 min.ann.: (9.5±0.3) %). This different behaviour for the first deposition run was consistently and reproducibly also found for other devices fabricated from powder PWD C in the first deposition run. It seems clear that the explanation of the different behaviour for cells prepared with fresh powder PWD C can be found in the complete $InCl_3$ evaporation during the first deposition run, as has been shown in Chapter 4. This influence of the Cl contamination will be discussed below. The cell parameters of the best cell from the sample C1 as well as the best cell from the set C2-C5 are presented in Tab. 5.2.

Comparison of the Different Source Materials

The device performance was shown to clearly depend on the source material used for the In_2S_3 evaporation. Best single cell as well as best average cell efficiencies could be obtained from the highly pure, crystalline source material PWD B. The best cells and their corresponding cell parameters for the sample sets A1-A5, B1-B5 and C1-C5 are listed in Table 5.2 for comparison. It is important to distinguish between best single cell results and averaged results, as both have different impacts on the data interpretation. While best single cell results present a proof of concept, average cell results can be more reliably interpreted in terms of the reproducibility of the result. A good reproducibility is of mayor importance in an industrial application.

The sample set prepared from the source material PWD A showed lowest efficiencies. This sample showed also a Cl contamination in the chemical analysis, although to a lower

Table 5.2: Cell parameters of the best cells from sample sets A1-A5, B1-B5, C1, C2-C5 and their corresponding CdS references.

Sample set	Ann. time (min.)	η (%) $\pm 0.2\,\%$	FF (%) $\pm 0.2\,\%$	j_{SC} (mA/cm^2) $\pm 0.5\,\text{mA/cm}^2$	V_{OC} (mV) $\pm$2mV
A1-A5	0	5.2	48	25.9	424
	5	8.8	56	28.1	558
	15	9.6	58	28.7	573
	35	9.7	58	28.2	595
CdS ref.	-	13.7	66	31.2	656
B1-B5	0	9.1	60	29.0	523
	5	12.1	65	28.9	647
	15	12.7	66	29.0	661
	35	12.8	66	29.2	663
CdS ref.	-	14.7	72	31.5	646
C1	0	10.2	64	29.0	545
	5	11.3	65	29.8	582
	15	11.0	63	29.8	583
	35	9.8	58	29.9	572
C2-C5	0	7.6	55	28.5	478
	5	10.6	60	30.0	587
	15	11.5	62	29.8	621
	35	12.1	63	30.2	632
CdS ref.	-	14.7	72	31.5	646

extent (appr. 0.5 at.%) than in the case of powder PWD C (appr. 1 at.%) The influence of the Cl evaporation at the beginning of the first evaporation cycle could not be observed in this series with powder PWD A as a result of the chosen experimental setting (closed source shutter). Due to the low cell efficiencies, this powder has not been extensively investigated further on. However, in a single experiment using powder PWD A in the first deposition cycle conducted with an open source shutter, a behaviour similar to the first deposition runs with powder PWD C was observed, i.e. an optimum in efficiency after 5 min. of annealing, with a best cell efficiency reaching 10.0 %.

The highly pure and crystalline powder PWD B performed reproducibly better as a source material for In_2S_3 buffer layer deposition and as a consequence of these results, for the rest of this work it was the chosen standard source material. The reproducibility for this sample set was quite good, averaged efficiencies of the five samples varied by less than 0.7 %, comparable to the standard deviation within each sample. It is clear that the reproducibility does not only depend on the buffer layer deposition, but also on the absorber, and the results can be expected to be less reproducible for varying absorber batches.

The samples prepared from PWD C showed slightly lower (total average C2-C5 11.3 %), but similar performance except for the first deposition run. The different behaviour with respect to the annealing for the first deposition run can be attributed to Cl contaminations in the source material which are shown to evaporate during the beginning of the first evaporation cycle (see Chapter 4).

The Cl contamination seems to have a beneficial effect in terms of the as grown efficiency and a reduced necesary annealing time. This is an interesting aspect especially in view of the usage of Cl-containing In-precursors in other deposition methods (e.g. ILGAR). The ILGAR In_2S_3 buffer layer deposition also results in high efficiency devices [27] and Cl has been found in amounts of up to 10 at.% in the buffer layers prepared by this method [91]. Although the effect of Cl in the buffer layer deserves a detailed analysis, the usage of Cl contaminated In_2S_3 powders can not be the way to do so and is of no practical interest. This work focusses therefore on the examination of the reproduceable, highest efficiency devices prepared from the pure, crystalline powder B.

Source Material Stability

In contrast to the sample sets A1-A5 and C1-C5, where the buffer layers were deposited during the first five subsequent buffer layer depositions, samples B1-B5 were not prepared in subsequent deposition runs. The aim was in this case to test the source material for degradation in a long-term usage as would be the case in an industrial application. In between the depositions of the buffer layers for B1-B5 several long-term deposition runs on glass substrates have been performed. This allows the interpretation of the sample series A1-A5 also in terms of the stability of the used source material. Fig. 5.5 shows the obtained efficiencies for the annealed samples A1-A5 (35min. ann.) as a function of the accumulated, integral deposition time, i.e. the time that the source material had been subjected to the evaporation temperature of 720 °C. No trend in terms of the device performance can be observed from these data, i.e. the efficiencies are scattered which supports the postulation that single-phase, pure In_2S_3 is evaporating congruently, i.e. without a

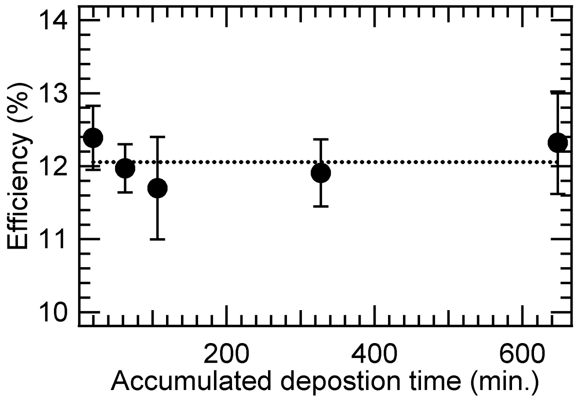

Figure 5.5: Efficiencies of the sample set B1-B5 as a function of the accumulated deposition time, i.e. the time that the source material had been subjected to the evaporation temperature of 720 °C. Displayed are the efficiencies after 35 min. of annealing. The average of the five data points is additionally displayed as a dotted line.

decomposition or preferential evaporation of the source material (see also the discussion in Section 4.2.2). Even after 650 min. accumulated deposition time no degradation in terms of cell performance was observed. At this point, most of the In_2S_3 source material had already been evaporated, e.g. more than 75% of the initial In_2S_3 had been evaporated.

5.1.4 Post Deposition Annealing

Only the annealing of the completed devices increases the performance of ZnO/ In_2S_3/ Cu(In,Ga)Se_2/ Mo devices to efficiencies comparable to reference devices with CdS buffer. It is interesting to review other deposition techniques using In_2S_3 as buffer, which all need a temperature step above 200 °C for optimal device performance. In this section the details of the annealing step and its impact on the individual solar cell parameters will be studied. At the beginning the general impact of the annealing on the cell parameters and some variations of the annealing conditions will be examined.

The efficiency of devices reproducibly improved the efficiency by a factor of 1.3-1.6 after 35 -45 min. of annealing at 200 °C. The first questions arising with respect to the annealing treatment are (a) How does the annealing effect the individual cell parameters? and (b) Is there a critical point for the annealing at which the performance is at an determined maximum, that is, does it decrease again for extended annealing times or does stay at its maximum? These two questions are answered in the first part of this section.

A device was prepared with the standard In_2S_3 deposition conditions (50 nm thickness, absorber from standard HZB absorber preparation, source material PWD B, annealing at 200 °C). jV-curves were recorded under AM1.5 illumination after various annealing times, including extended annealing times of up to 240 min. The development of the average cell efficiency (8 cells) is depicted in Fig. 5.6. The graph shows a sharp decrease of the efficiency up to annealing times of 35 min., where the efficiency reaches (14.1±0.3) %. For annealing times between 35-95 min. the efficiency stays within the range of (14.3±0.2) %. For still longer annealing times the efficiency slowly decreases again and reaches a value of

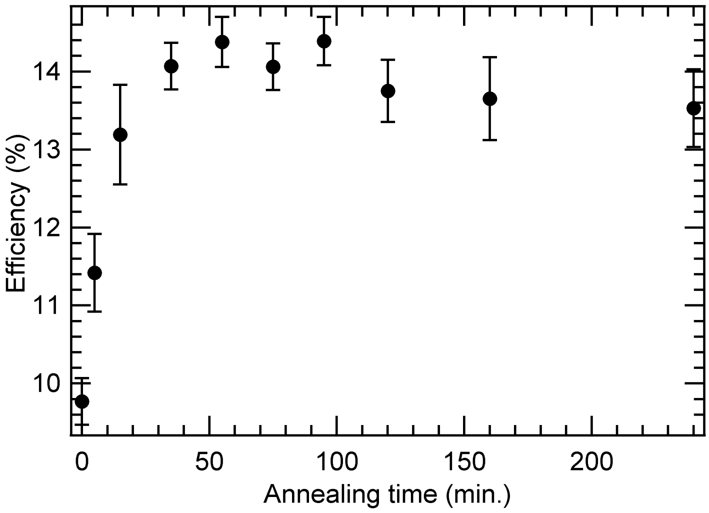

Figure 5.6: Development of the averaged efficiency of a standard ZnO/ In_2S_3/ Cu(In,Ga)Se_2/ Mo device for extended annealing times.

(13.7±0.5) % after 240 min. of annealing. This shows that there is a quite broad plateau in which the device is at optimum performance and there is a very slow degradation for excessive annealing.

The behaviour of the efficiency will become more clear when the individual cell parameters are examined. It has already be shown, that mainly the open circuit voltage and fill factor contribute to the efficiency gain. In Fig. 5.7 the effect of the annealing on the different cell parameters is depicted. In this presentation, the cell parameters have been normalised to their maximum value. There are two opposite trends observable: (1) Open circuit voltage and fill factor behave similar: After a sharp increase from approximately 80 % in the as grown state for the first 0-35 min. of annealing, for annealing times longer than 35 min. the value stays within a 2 % range around the maximum value (100 %, V_{OC}: 632 mV, FF: 72.2 %). The open circuit voltage and fill factor therefore do not show any degradation even for the extended annealing times of up to 240 min. (2) In contrast to this, the short circuit current density slowly decreased nearly linearly from the maximum value at 100 % to 92 % after 240 min. of annealing.

The two contrary trends together give the observed evolution of the efficiency with a rather broad plateau around 35-95 min. The two trends do not necessarily belong to the same effect and the annealing may easily trigger two independent effects within the device having opposite impact on the device performance. Possible explanations for this behaviour will be given at the end of this chapter after a more detailed examination of the two trends. The influence of the annealing on the short circuit current density and open circuit voltage will be separately investigated by an analysis of the quantum efficiency and temperature-dependent jV-characterisation in Section 5.2.1 and 5.2.3, respectively.

In the standard procedure, the annealing conditions is accomplished on a hot plate in air, which results in the presented optimisation of the device performance. The question arises, if the annealing atmosphere is influencing the device behaviour, e.g. through an oxidation by the oxygen contained in the air, as has been discussed for different air-

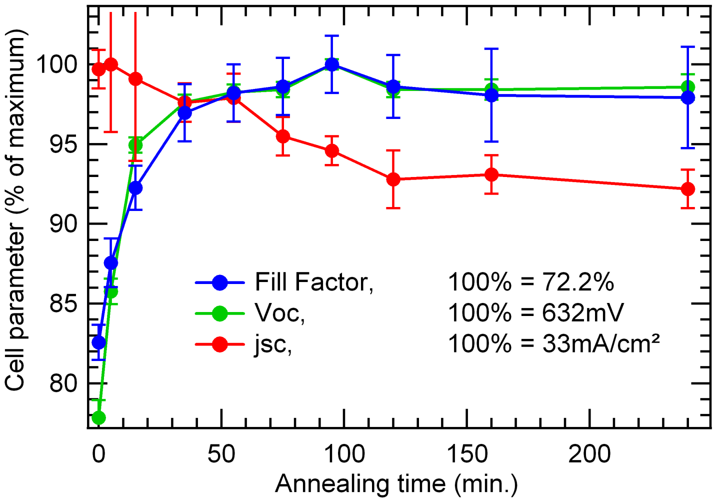

Figure 5.7: Development of the averaged cell parameters of a standard ZnO/ In_2S_3/ Cu(In,Ga)Se_2/ Mo device for extended annealing times. A linear interpolation between the data points has been added as a guide to the eye.

annealed devices in the past, see e.g. [92]. In order to check this, twin samples have been prepared under the same conditions and were annealed at the same temperature (200 °C), with one of the samples being annealed in an Ar-glovebox (O_2: $<$ 1ppm, H_2O: $<$12 ppm) and the other in air. The resulting average efficiencies of the two devices (annealed in air and annealed in the glovebox) are compared in Fig. 5.8.

No difference in the annealing behaviour can be found for the two devices, which rules out oxidation effects as an explanation for the annealing improvement. To this graph the averaged efficiencies of the corresponding CdS reference is added. The CdS reference has been subjected to the same annealing treatment as the In_2S_3 buffered devices. No improvement of the device performance upon annealing in air can be observed for the case of the CdS reference. The average efficiencies are slightly decreasing from (15.2±0.8)% in the as grown state to (14.8±1.0) % after 55 min. annealing, which is within the range of the observed data scattering. In contrast to the behaviour observed for devices with an In_2S_3 buffer, the short circuit current density was not found to decrease within the applied annealing times for the CdS reference (as grown: (34.1±0.4) mA/cm^2, 55 min. ann.: (34.4±0.3) mA/cm^2).

5.2 Physical Interpretation of Solar Cell Parameters

5.2.1 Collection of Photo-Generated Charge Carriers

The short circuit current density is a global parameter of the device, demonstrating its ability to collect photo-generated charge carriers if no external voltage is applied. The measurement of the quantum efficiency expands this information and enables an interpretation of how the photo-generated charge carrier collection is accomplished for the various wavelengths of the incident photons. An introduction into the physical interpretation of

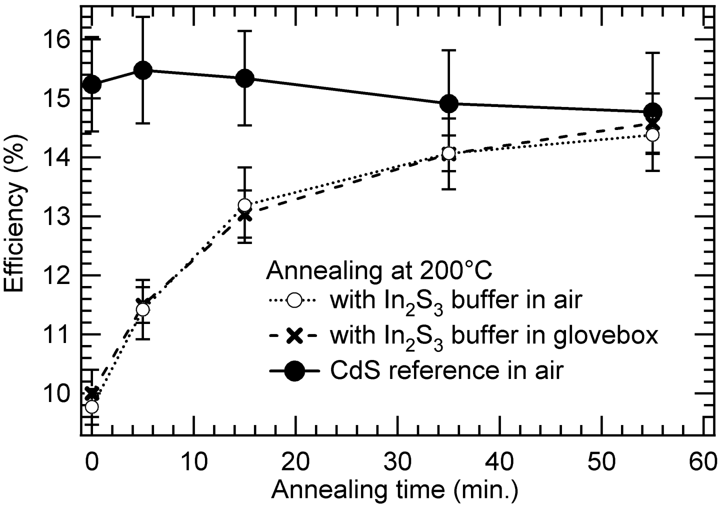

Figure 5.8: Averaged efficiencies of two standard ZnO/ In_2S_3/ Cu(In,Ga)Se_2/ Mo devices annealed at 200 °Cin air and in an Ar-glovebox, respectively. Additionally, the development of the averaged efficiency of a CdS reference device upon annealing is displayed.

the quantum efficiency is given in Section 3.4. In the ideal case, where all incident photons with an energy above the absorber bandgap (E$g(absorber) = 1.1 - 1.2\,\mathrm{eV}$) are absorbed inside the absorber layer and all photo-generated charge carriers are separated and collected, the quantum efficiency is a step function with value 1 above the absorber band gap and 0 below it. In fact, the onset of the quantum efficiency is often used to estimate the bandgap of the absorber. In an empiric approach, the photon energy E_0 corresponding to the point where the slope of the EQE is at its maximum ($dQE/d\lambda = max$) can be used as an indicator for the bandgap position.

For the heterojunction devices under consideration, not all incident photons reach the absorber layer. Photons with energies above the bandgap of the ZnO window layer ($E_g \approx 3.3\,\mathrm{eV}$) are absorbed inside the window layer and generally do not contribute to the photocurrent. In consequence, the QE of Cu(In,Ga)Se_2 solar cells decreases rapidly for energies above the ZnO bandgap. Absorption in the buffer layer introduces further losses at photon energies above the buffer band gap E_g(buffer).

In practice, the quantum efficiency is measured in a self-made setup at the Helmholtz-Zentrum Berlin. Illumination source is a lamp setup with an Ha and Xe lamp, analog to the type of lamps used in the sun simulator. The light is chopped (chopping frequency ν =60-70 Hz) and fed into a double-grating monochromator. Subsequently the monochromatic light is focussed to a small spot (spot size $< 1\,\mathrm{mm}^2$). The photon flux at the sample is measured with reference diodes at the same spot prior to the actual QE measurement. The sample is then contacted and the photocurrent recorded as a function of the incident photon wavelength.

In this section the quantum efficiency of devices with an In_2S_3 buffer layer will be compared to the CdS references and the evolution of the quantum efficiency upon annealing will be presented. The quantum efficiency of a ZnO/ CdS/ Cu(In,Ga)Se_2/Mo reference device is depicted in Fig. 5.9. Here, a clear bump in the EQE for photons with energies

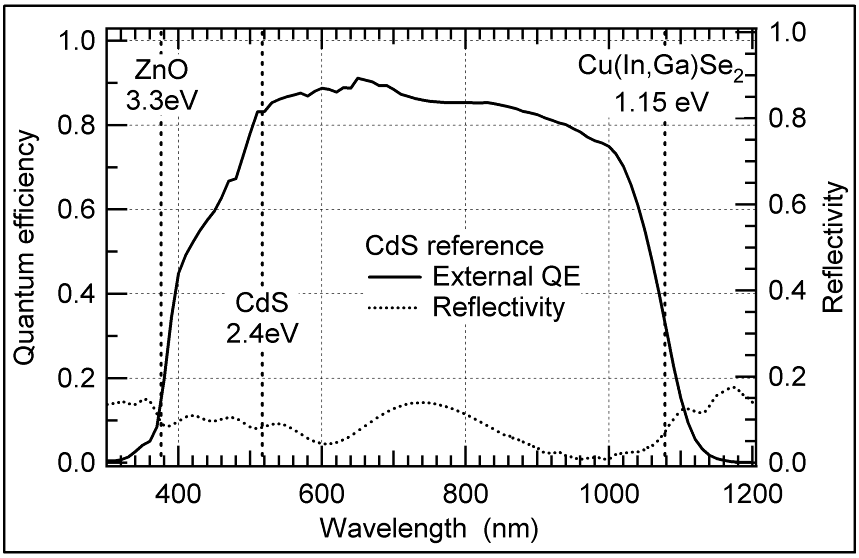

Figure 5.9: External quantum efficiency and reflectivity of a ZnO/ CdS/ Cu(In,Ga)Se$_2$/ Mo reference device with CdS buffer. The first optical transition of CdS at 2.4 eV is marked with a vertical dotted line as well as the bandgap E_g of the absorber at 1.15 eV and the ZnO-layer at 3.3 eV.

above E$_g$(CdS)=2.4 eV can be observed. The bandgap energies of the absorber and the ZnO layer that determine the onsets of the quantum efficiency are marked in the graph as dotted vertival lines. In addition to the EQE, the reflectivity of the device is depicted in the graph as a dotted line.

The absorption loss in the CdS layer is one reason for the search for an CdS substitute. In_2S_3 has a lower bandgap (2.0 eV), but is an indirect semiconductor with a lower absorption coefficient. In Fig. 5.10 the external quantum efficiency and reflectivity of a ZnO/ In_2S_3/ Cu(In,Ga)Se$_2$/ Mo device with a evaporated In_2S_3 buffer layer is depicted. As absorbers from the batch were used, the onset of the quantum efficiency is here approximately the same as for the CdS reference (E_{onset}(with CdS)= (1.15±0.2) eV, E_{onset}(with In_2S_3)= (1.16±0.2) eV).

The reflectivity of the In_2S_3 device shows pronounced interference fringes in the blue range with maxima at 460 nm and 615 nm. These reflectivity maxima are also observed as losses in the EQE. A reduction of these reflection losses through an optimisation of the buffer/window thicknesses or the application of a suitable anti-reflection coating could help to increase the short circuit current density of devices with an In_2S_3 buffer. However, the comparison of the external quantum efficiencies of the two devices with different buffer layers shows that the EQE of the device with CdS buffer is in general slightly higher than the device with In_2S_3 buffer layer indicating a better charge carrier collection (maximum with CdS: 0.91, maximum with In_2S_3: 0.87). The active area short circuit current densities for the two devices can be compared using Eq. 3.24 and give 32.9 mA/cm^2 for the CdS reference and 32.3 mA/cm^2 for the device with In_2S_3 buffer.

Fig. 5.11 (left) depicts the development of the EQE upon extended annealing in air of a ZnO/ In_2S_3/ Cu(In,Ga)Se$_2$/ Mo device. The solar cell parameters and efficiencies of this device have been presented in Fig. 5.6 and 5.7. A decrease in the quantum efficiency

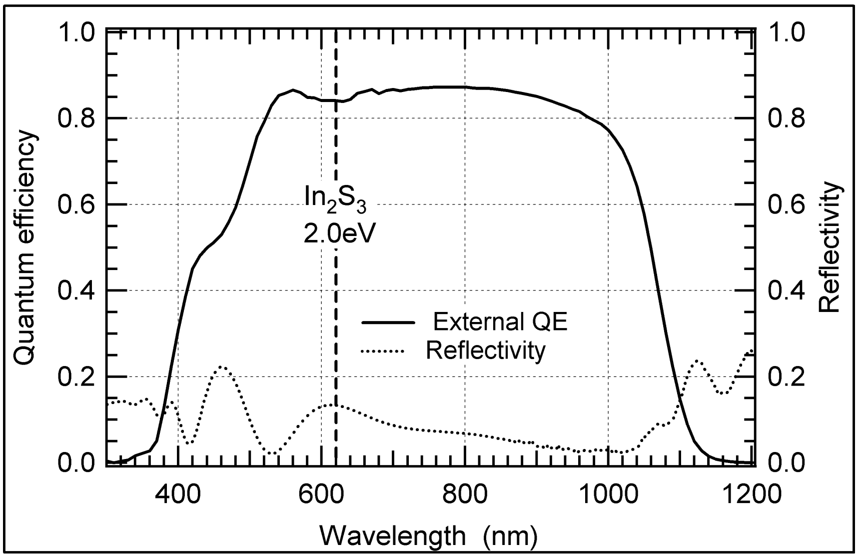

Figure 5.10: External quantum efficiency and reflectivity of a $Cu(In,Ga)Se_2$ device with In_2S_3 buffer. The first optical (indirect) transition of In_2S_3 at 2.0 eV is marked with a vertical dotted line.

is observed, in agreement with the presented decrease of the short circuit current density. The external quantum efficiency shows that losses are more pronounced in the longer wavelength part of the spectrum (≈700 nm-1200 nm). This part of the spectrum corresponds to photons absorbed deeper in the absorber and the observed losses in the quantum efficiency indicate therefore a decreased collection of photo-generated charge carrier from deep within the absorber, e.g. as a result of a decreasing effective collection length L_{eff}.

In the right part of Fig. 5.11 the EQE has been normalised and plotted as a function of the photon energy. In order to illustrate the dependence of the quantum efficiency on the effective collection length $L_{eff} = w + L$ (with w being the space charge region width and L the electron diffusion length in the absorber as introduced in Chapter 3), the quantum efficiency is calculated according to Eq. 3.32 for a set of normalised effective collection lengths L_eff (with norm. L_{eff}= 0.7, 1.0, 1.5) and plotted in Fig. 5.11 together with the measured EQE. The calculated plots resemble well the qualitative behaviour of the measured EQE. The effective collection length decreases if either the space charge region width or the diffusion length (or both) decrease. The space charge region width decreases for example for an increasing doping concentration, while a decrease in the diffusion length is equivalent to decreased electron lifetime. If the defect concentration in the bulk of the absorber is assumed to stay constant upon the annealing the decreasing collection length can be attributed to a decreasing space charge region width. These results motivate the further direct investigation of changes in the space charge width, e.g. through electron-beam induced current (EBIC) measurements or admittance spectroscopy in future experiments.

The decreasing quantum efficiency corresponds to a decreasing short circuit current density and the (active area) short circuit current density calculated from the EQE is tabulated in Table 3.24.

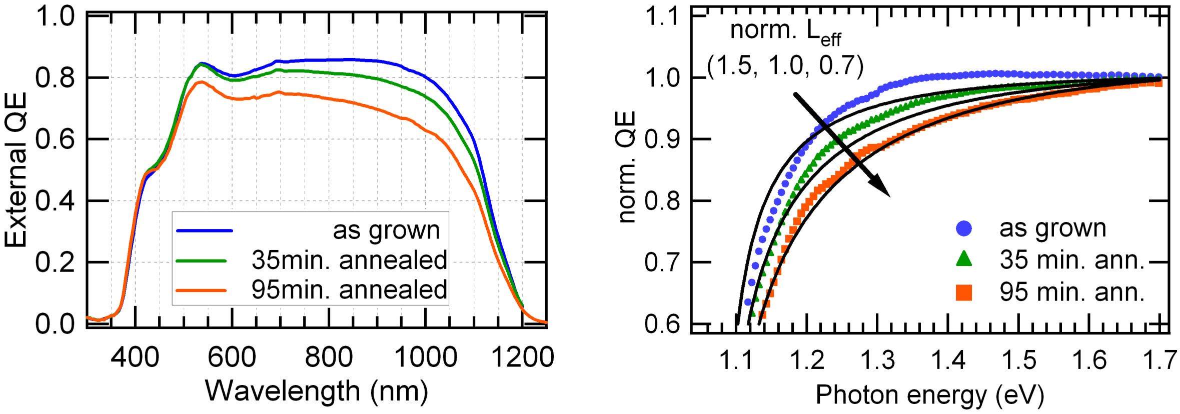

Figure 5.11: Left: Development of the external quantum efficiency after various annealing times for a device with In_2S_3 buffer. Right: Red response of the normalised quantum efficiency of the device with In_2S_3 buffer after various annealing steps as a function of the photon energy. A set of calculated quantum efficiencies with normalised effective collection length $L_{eff} = 0.7, 1.0\ , 1.5$ calculated according to Eq. 3.32 is added to the graph.

Table 5.3: Active area short circuit density calculated from the EQE presented in Fig. 5.11 by Eq. 3.24.

Annealing time (min.)	0	35	95
j_{SC} (mA/cm^2, active area)	33.8	32.5	29.3

5.2.2 Current-Voltage Characteristics in the Dark

In this section, the jV-curves of CdS- and In_2S_3-buffered devices recorded in darkness will be interpreted in terms of the 2-diode model. The description of the model and the corresponding equivalent circuit diagram can be found in Section 3.2 together with examples of the different parameters describing the jV-behaviour of solar cells in this models. In the 2-diode model, the dark jV-curve of a given device can be described according to Eq. 3.18 by six parameters: A_1, $j_{0,1}$ the diode quality factor and saturation current density of the first or main diode, A_2, $j_{0,2}$ the diode quality factor and saturation current density of the second diode, R_s the series resistance and R_p the parallel or shunt resistance. As here the current density will be considered, the resistances are given in $\Omega\,\mathrm{cm}^2$.

The measured jV-curves of the In_2S_3-buffered device are displayed in a semi-logarithmic presentation in Fig. 5.12 for various annealing times. The fits of the data according to the 2-diode-model are presented in Fig. 5.13, the results of the fitting parameters are tabulated in Table 5.4. The fitting results show, that mainly the first diode changes during the annealing, with A_1 decreasing from 2.35 (as grown) to 1.30 (45 min. ann.) and $j_{0,1}$ from 9.7×10^{-4} mA/cm^2 down to 5.7×10^{-8} mA/cm^2. After 45 min. of annealing the diode characteristics are comparable to the CdS reference (A_1=1.27, $j_{0,1}$=5.5×10^{-8} mA/cm^2.

The first diode with the lower diode quality factor (A_1) and saturation current density

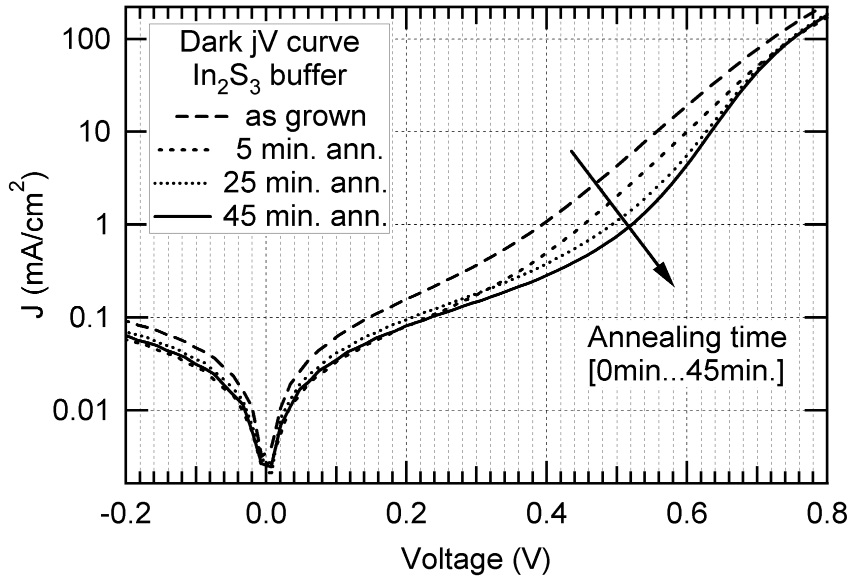

Figure 5.12: Semi-logarithmic presentation of the dark jV-curves of the ZnO/ In_2S_3/ Cu(In,Ga)Se_2/ Mo device discussed in the text after various annealing times.

j_1 is called the main diode as it dominates the current for higher voltages and in the range from approximately 0.5 V to 0.7 V. This is the relevant voltage under operating conditions for the solar cells as it typically includes the maximum power point and open circuit voltage. In Fig. 5.14 the different contributions from the two diodes and the shunt resistance ($j_{0,1}$, $j_{0,2}$ and j_{Rp}, respectively) to the total saturation current density j_{total} have been plotted according to the parameters obtained with the fit to the 2-diode-model for the sample in the as grown state and after 45 min. of annealing (the series resistance is here neglected.). The graph shows the dominance of the main (first) diode for voltages above approximately 0.5 V.

If the total saturation current density is approximated by just the main diode, the open circuit voltage for a given constant photo-generated current density j_L follows directly from the diode characteristics (Eq. 3.16):

$$qV_{OC} = -A_1 kT \ln\left(\frac{j_L}{j_{0,1}}\right) \tag{5.1}$$

This means, that a decreasing saturation current density $j_{0,1}$ is directly related with a gain in open circuit voltage (for a constant diode quality factor), e.g. for j_L= 35 mA/cm^2 and A_1=1.3 an increase of approximately 80 mV can be expected for every decade that the saturation current density decreases.

A diode quality factor >2 in the main diode as observed for the diode before the annealing is generally interpreted in terms of a tunneling (assisted) recombination process [42]. The decreasing quality factor indicates therefore a decreasing contribution of the tunneling process to the dominant recombination mechanism in the device. The examination of the recombination behaviour of the devices including the temperature dependency of the diode quality factor will be continued in the next section.

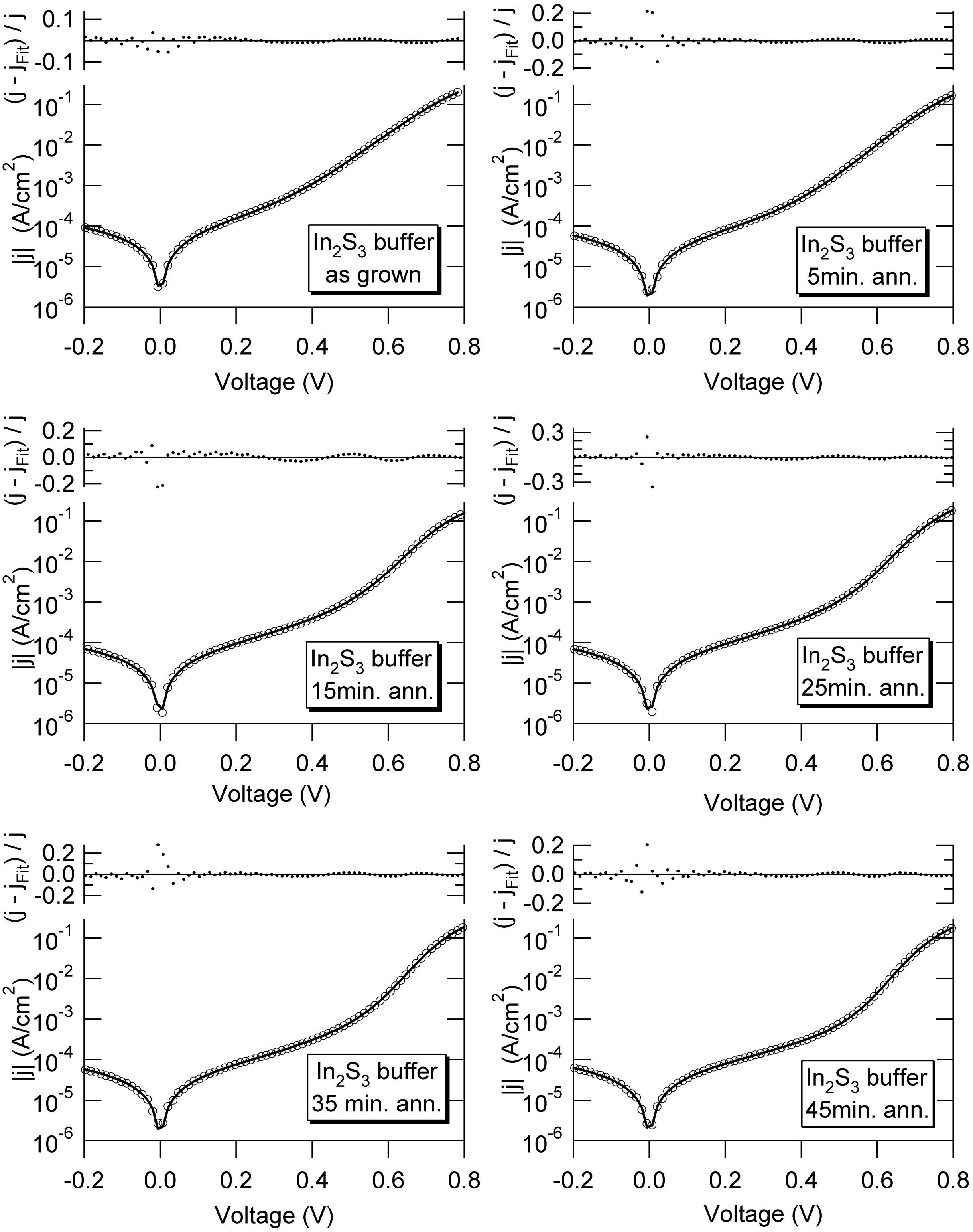

Figure 5.13: Measured dark jV-curves of a Cu(In,Ga)Se_2 solar cell with In_2S_3 buffer after various annealing times and fits to the data according to the 2-diode model. The corresponding fit and solar cell parameters are tabulated in Table 5.4 and Table 5.1, respectively.

Table 5.4: Fit parameters according to the 2-diode model of the fits to the dark jV-curve of the In_2S_3 buffered sample after various annealing times (corresponding to Fig. 5.13) and a CdS reference . Here, $j_{0,i}$ denotes the saturation current density, A_i the diode quality factor ($i = 1, 2$), R_s the serial and R_p the parallel (shunt) resistance.

Ann. time (min.)	A_1	$j_0, 1$ (mA/cm^2)	A_2	$j_{0,2}$ (mA/cm^2)	R_s ($\Omega\,$cm^2)	R_p (k$\Omega\,$cm^2)
0	2.35	9.7×10^{-4}	7.15	3.2×10^{-2}	0.21	3.0
5	1.93	4.8×10^{-5}	3.3	2.2×10^{-3}	0.31	3.6
15	1.46	4.9×10^{-7}	3.82	4.3×10^{-3}	0.39	3.0
25	1.37	1.6×10^{-7}	3.73	3.9×10^{-3}	0.34	3.0
35	1.33	7.6×10^{-8}	3.76	3.1×10^{-3}	0.30	3.6
45	1.30	5.7×10^{-8}	3.97	3.3×10^{-3}	0.37	3.3
CdS	1.27	5.5×10^{-8}	7.67	1.6×10^{-2}	0.27	2.7

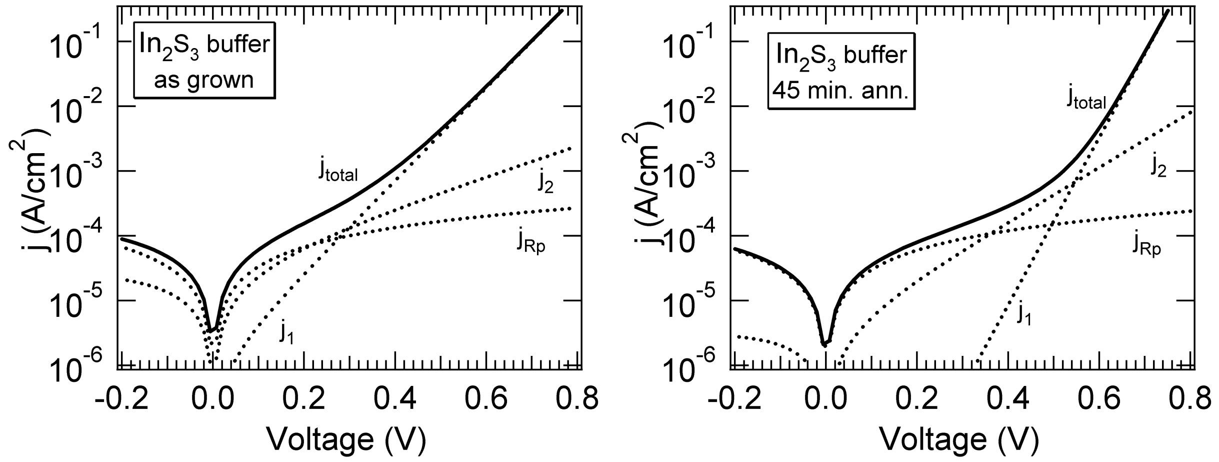

Figure 5.14: Calculated partial contributions to the total current density from the two diodes and the shunt resistance for the fit parameters obtained for the ZnO/ In_2S_3/ Cu(In,Ga)Se_2/ Mo sample corresponding to Table 5.4 in the as grown state and after 45 min. of annealing at 200 °C. The series resistance has been set to zero in this calculation.

5.2.3 Temperature and Illumination Dependent Current-Voltage Characterisation

The last section has shown, how an annealing treatment effects the diode parameters of Cu(In,Ga)Se_2 solar cells with a In_2S_3 buffer. In order to investigate the details of the changes in the recombination behaviour, in this section the analysis is extended to an temperature and illumination dependent analysis of the jV-response.

The analysis will start with a highly efficient In_2S_3 buffered solar cell (In_2S_3 deposited from powder PWD B, after annealing of 35 min. in air at 200 °C, η: 15.13 %, FF: 72.0 %, j_{SC}: 33.5 mA/cm^2, V_{OC}: 627 mV) which will be compared to the best CdS reference solar cell from the same absorber batch. The reference showed a similar performance with slightly higher short circuit current density (η: 16.02 %, FF: 72.9 %, j_{SC}35.0 mA/cm^2, V_{OC}: 628 mV).

Then changes in the dominant recombination upon annealing for Cu(In,Ga)Se_2 devices with In_2S_3 buffer will be investigated in detail by comparing the $jV(T)$ analysis of a sample in the as grown state and after successive annealing steps up to a total annealing time of 35 min.

High efficiency device with In_2S_3 buffer

Ultimately, the device behaviour under illumination is the relevant situation as it resembles the solar cell in operating conditions. Therefore, in this section the discussion will be aimed at the analysis of jV-curves under illumination (light jV-curves) with the focus of the device behaviour at illumination intensities around AM1.5 illumination (1000 W/m^2) and in the voltage range between 0.5 V and 0.8 V, which includes the typical values for the maximum power point and open circuit voltage.

Before coming to the case of illuminated samples, in the beginning the qualitative behaviour of jV-curves measured in the dark at various temperatures will be briefly presented and discussed. In Fig. 5.15 dark jV-curves of the In_2S_3-buffered sample recorded at various temperatures from 320 K down to 150 K (ΔT=10 K) are displayed. The semi-logarithmic presentation shows that for higher temperatures ($\approx$ 280-320 K), the main diode is dominating the jV-response in the linear section (indicated by the dotted square) extending over 1-2 decades from $\approx 5 \times 10^{-4}$A/cm^2 to 2×10^{-2}A/cm^2 at approximately 0.4 V to 0.6 V (the diode quality factor of the main diode is $\approx$1.5 at 300 K). For lower temperatures, the influence of secondary recombination mechanisms becomes more pronounced in this current density interval resulting in a deviation from the linear behaviour for the temperature range 220 K-150 K. The relatively high series resistances for this experimental set (due to contacting problems) result in a linear part of the curves that extends over less than two decades. This and the secondary recombination mechanism (or mechanisms) competing with the recombination associated with the main diode impede a clear identification of the diode characteristics of the main diode in the dark. A detailed diode characterisation including the diode quality factor and saturation current density will therefore be left to the (j_{SC}, V_{OC})-curves from illuminated samples presented below, where the influence of the series resistance can be neglected. In general, a shift of the jV-curves to higher voltages is observed for decreasing temperatures, which is explained by the temperature dependence of the saturation current density (see for example Eq. 3.40).

The equivalent set of dark jV-curves for the CdS-reference is shown in Fig.5.16. The qualitative behaviour of the dark jV-set is similar, e.g. a shift to higher voltages of the whole jV-curves at decreasing temperatures. However, the influence of a secondary recombination mechanism and the corresponding deviation from linear behaviour at lower temperatures could not be observed for the reference.

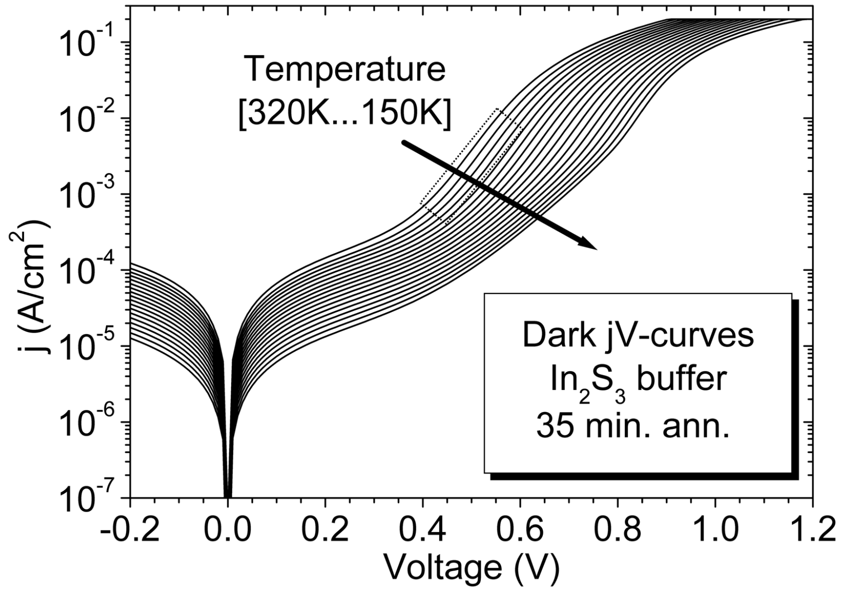

Figure 5.15: Measured jV-curves of a ZnO/ In$_2$S$_3$/ Cu(In,Ga)Se$_2$/ Mo device recorded in the dark. Displayed is a set of curves recorded at absolute temperatures ranging from 320 K to 150 K (ΔT=10 K).

In the ideal case, the jV-response of a solar cell under illumination follows directly from the dark jV-curve through the addition of the constant photocurrent density j_L as stated by Eq. 3.17. In practice, the superposition principle generally does not hold for chalcopyrite solar cells, e.g. a subtraction of the short circuit current density from a jV-curve recorded under illumination does not resemble the dark jV-curve. This is illustrated for an ZnO/ CdS / Cu(In,Ga)Se$_2$/ Mo reference device in Fig. 5.17. In this case an extreme example has been chosen to illustrate the principle.

The superposition principle is not valid for chalcopyrite solar cells for two reasons:

- An alteration of the diode character of the device itself upon illumination. There is an evident proof for the fact that the diode characteristics of certain devices may be changed under illumination which is the effect known as light soaking. Light soaking denotes the fact that the efficiency and diode quality factor of certain solar cells are improving significantly upon illumination in the time scale of 2-40 min [87] as a result of illumination-dependent metastabilities. Igalson et al. [93] have presented experimental data from admittance spectroscopy and calculations explaining these and other effects related to illumination induced changes with defect levels participating in a charge redistribution upon illumination. No light soaking was observed

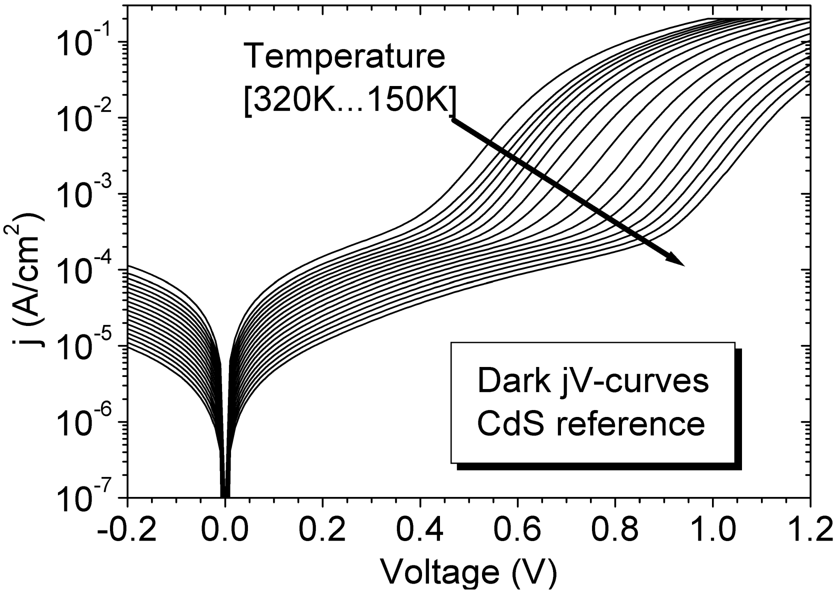

Figure 5.16: Measured jV-curves of the reference with CdS buffer corresponding to the sample presented in Fig. 5.15 recorded in the dark. Displayed is a set of curves recorded at absolute temperatures ranging from 320 K to 150 K (ΔT=10 K).

for the solar cells presented in this work in the time scale 1-40 min., but still very fast changes in the diode properties upon illumination are possible.

- The photo-generated current density j_L is voltage dependent ($j_L(V)$). As has been discussed in Sect. 3.4 and 5.2.1, an effective collection of photo-generated charge carriers can be expected within the effective diffusion length $L_{eff} = L_n + w$, where L_n is the diffusion length for electrons in Cu(In,Ga)Se$_2$ and w is the space charge region width. As w is a function of the applied bias voltage (see Eq. 3.15), the photo-generated current density j_L in turn becomes a function of the applied bias

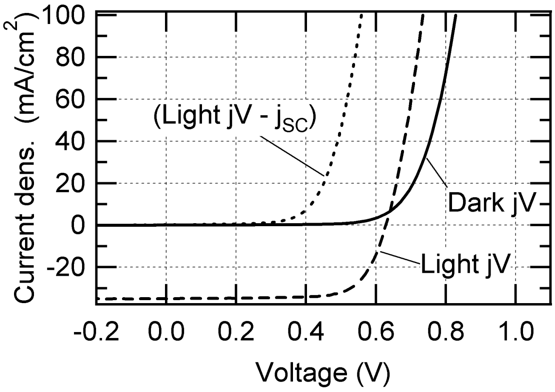

Figure 5.17: Measured dark jV-curve, jV-curve under AM1.5 illumination and jV(illuminated)-j_{SC} for a CdS reference device.

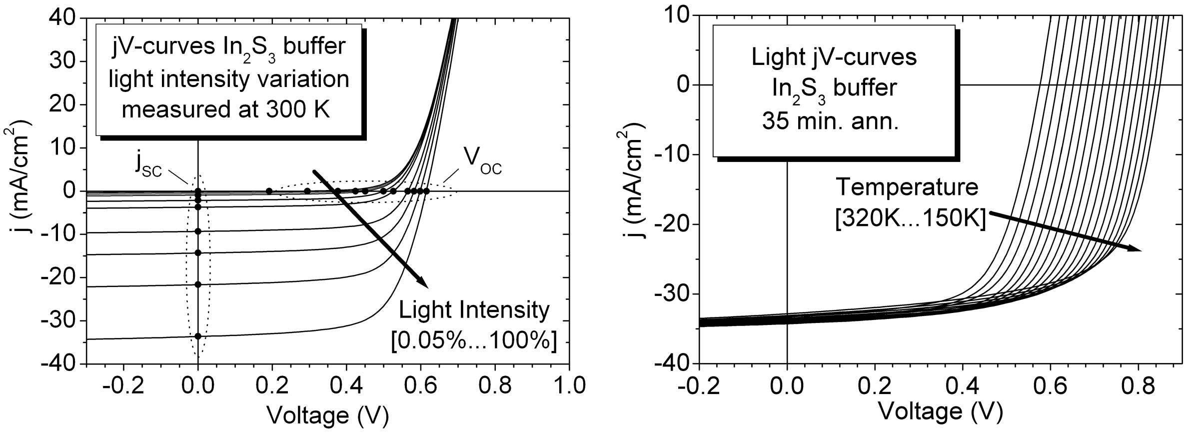

Figure 5.18: Left: Measured jV curves of a In_2S_3-buffered Cu(In,Ga)Se_2 solar cell (35 min. annealed) with various light intensities, recorded at 300 K. Right: Measured jV curves of the same solar cell at various temperatures, recorded at full illumination ($L_{100\%} \approx 1000\,W/m^2$).

voltage.

In order to circumvent these problems and still extract the relevant diode characteristics of a given sample under illumination, a procedure has been developed in the past that uses the short circuit current densities and open circuit voltages extracted from jV-curves under various illumination intensities instead of analysing jV-curves for one illumination intensity. A detailed description of the procedure including an error analysis can be found in Ref. [40].

The procedure consists of measuring the jV-curves of the sample at a given temperature for a set of illumination intensities. The spectral content of the illumination was maintained constant and the intensity was varied by a set of gray filters from 100 % down to 0.05 %. Light source was a halogen lamp and the full intensity L_{100} for full illumination (100 %) was calibrated to produce the same short circuit current density in the sample as measured under the solar simulator ($\approx 1000 W/m^2$). Such a set of jV-curves recorded at 300 K on the sample with In_2S_3 buffer is presented in the left part of Fig. 5.18. For each light intensity, the j_{SC} and V_{OC} values are extracted from the jV-curve as indicated in the figure.

For a given temperature, the measurements at different light intensities give a set of (j_{SC},V_{OC}) data pairs. The procedure is then repeated at various temperatures (150 K-320K, $\Delta K = 10$ K), resulting in a set of temperature dependent (j_{SC}, V_{OC})-curves. In the right part of Fig. 5.18, jV-curves at different temperatures are presented as an example for the full light intensity (100 %). The figures shows very illustratively the increasing open circuit voltage V_{OC} for decreasing temperatures.

The (j_{SC},V_{OC})-values corresponding to the measurements at different temperatures and illumination intensities are plotted in Fig. 5.19 for the ZnO/ In_2S_3/ Cu(In,Ga)Se_2/ Mo device (35 min. ann.). The discussion will start at the higher temperatures (320 K-280 K). Here, a linear behaviour of the (j_{SC},V_{OC})-values is found in this semi-logarithmic presentation, indicating that the main diode is dominating the jV-response for the last six datapoints at high j_{SC}-values (in the range $\approx 2\,mA/cm^2$ - $35\,mA/cm^2$, corresponding to light intensities of $\approx 5\,\%$-$100\,\%$).

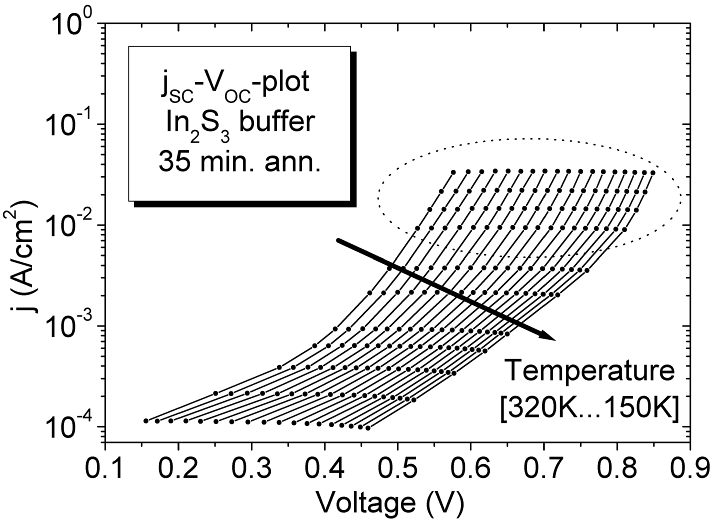

Figure 5.19: Plot of the (j_{SC},V_{OC})-values obtained from jV-curves at various temperatures and light intensities for a In_2S_3-buffered Cu(In,Ga)Se_2 solar cell (35 min. annealed). The datapoints recorded at a given temperature (T=[150...320] K, ΔT= 10 K) are connected by lines for a better distinction of the individual light intensity sets.

For lower j_{SC}-values (light intensities), a deviation from the linear behaviour is found, as was for the dark jV-curves presented in Fig. 5.15. A similar behaviour is found for the plots at lower temperatures, although the extension of the linear part of the (j_{SC},V_{OC})-curves decreases down to approximately the last four datapoints at 150 K ($\approx$ 9 mA/cm^2 - 35 mA/cm^2). This also resembles the qualitive behaviour of the dark jV-curves, where the influence of secondary recombination mechanisms was found to increase at lower temperatures. Consequently, for a consistent evaluation of the linear part of the (j_{SC},V_{OC})-curves only the four highest light intensities were further evaluated for all samples and temperatures sets, as indicated by the dotted ellipse in the graph. These datapoints provide the best description of the jV-behaviour of the main diode under illuminations close to the full solar irradiation.

The same measurement procedure has been performed for the CdS reference and the corresponding set of (j_{SC},V_{OC})-values is plotted in Fig. 5.20. The qualitative behaviour of the (j_{SC},V_{OC})-curves is very similar. As in the case for the dark jV-curves, the linear behaviour extends down to lower current densities (2×10^{-2}A/cm^2) than for the In_2S_3-buffered device, even down 150 K.

Fits to the linear part of the (j_{SC},V_{OC})-curves at higher current densities yield the diode quality factor A and saturation current j_0 for each temperature. The temperature dependence of A is plotted in Fig. 5.21 (left) for the In_2S_3-buffered Cu(In,Ga)Se_2 device. A nearly constant diode quality factor of 1.5-1.6 is found for temperatures down to 220 K. Following the description of the different possible recombination paths in Section 3.5, a weakly temperature dependent diode quality below 2 means that the main recombination mechanism at these temperatures is thermally activated. This behaviour is typical for a Cu(In,Ga)Se_2 device with high efficiency where the dominant recombination mechanism is located in the space charge region [43]. At lower temperatures, the diode quality factor

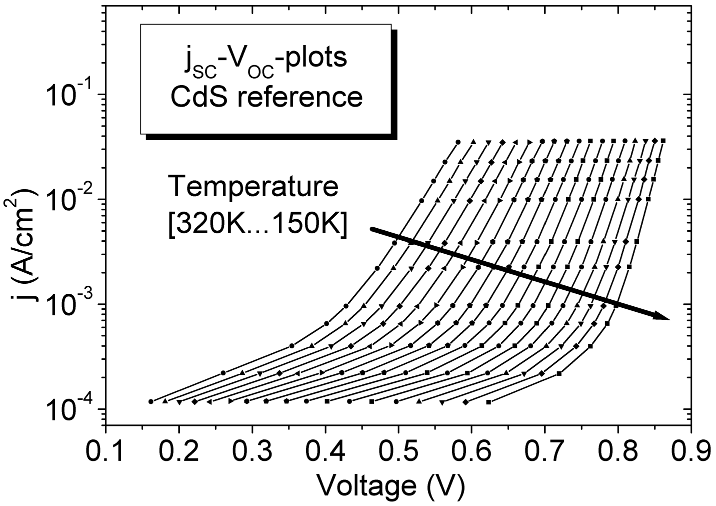

Figure 5.20: Plot of the (j_{SC},V_{OC})-values obtained from jV-curves at various temperatures and light intensities for a reference Cu(In,Ga)Se$_2$ solar cell with CdS buffer. The datapoints recorded at a given temperature (T=[150...320] K, ΔT= 10 K) are connected by lines for a better distinction of the individual light intensity sets.

slowly increases up to a value of 2.2 at 150 K which suggests a very slowly increasing contribution from a tunneling process to the recombination mechanism.

For a tunneling enhanced recombination process for an exponentially decaying defect distribution in the space charge region, Rau [42] suggested an analytical expression for the diode quality factor given by (Eq. 3.46):

$$\frac{1}{A} = \frac{1}{2}\left(1 - \frac{E_{00}^2}{3(kT)^2} + \frac{T}{T^*}\right).$$

Here E_{00} is the characteristic energy of the tunneling process and T^* the characteristic temperature of the exponential function describing the defect distribution. For more details,

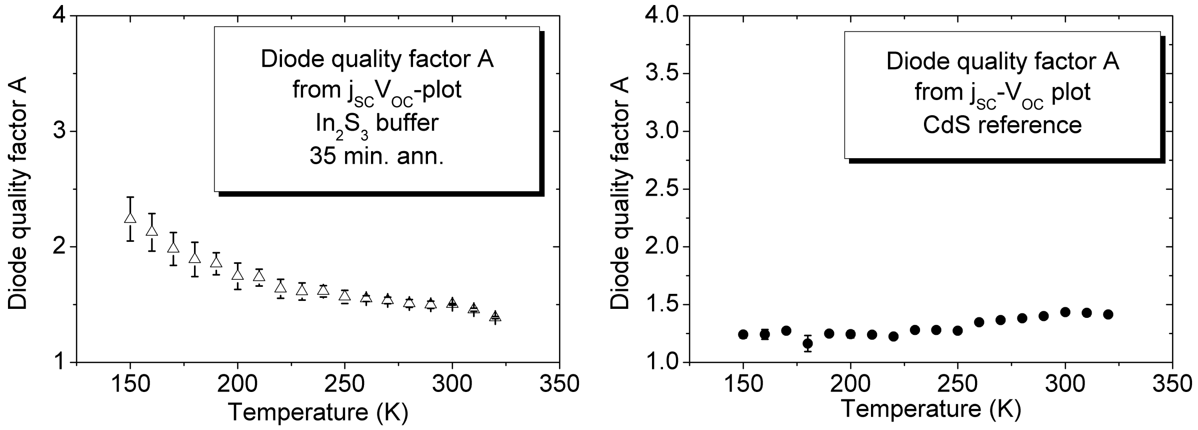

Figure 5.21: Diode quality factors extracted from (j_{SC},V_{OC})-plots at different temperatures. Left: In$_2$S$_3$-buffered Cu(In,Ga)Se$_2$ solar cell (35 min. ann.) Right: CdS reference.

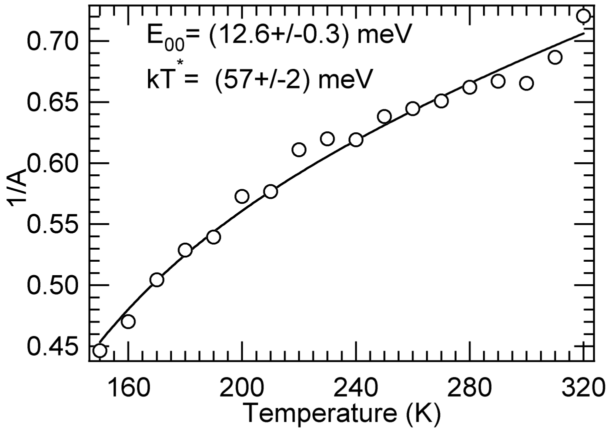

Figure 5.22: Plot of the inverse diode quality factor as a function of the absolute temperature. The fit according to the expression for a tunneling enhanced recombination in the space charge region given by Rau [42] is additionally displayed.

see Chapter 3.5.

The results of this fit is presented in Fig. 5.22, with the fit parameters $E_{00} = (12.6 \pm 0.03)$ meV, and $kT^* = (57 \pm 2)$ meV.

The right part of Fig. 5.21 allows a comparison with the CdS reference. For the CdS reference, a similar diode quality factor of $\approx$1.2 -1.4 is found, which is not increasing at lower temperatures. This indicates a similar dominant recombination mechanism at elevated temperatures (>220 K) for both devices, which can be attributed to a thermally activated recombination process located in the space charge region of the absorber. At lower temperatures, recombination is increased for the case of the In_2S_3-buffered device. This increase is explained by a weakly tunneling enhanced recombination process.

For a thermally activated recombination process located in the SCR dominating the device an extrapolation of measured V_{OC} values to 0 K should yield the absorber band gap (see Eq. 3.44). From Eq. 3.43 it follows further that for this recombination mechanism a plot of $A \ln j_0$ against the inverse temperature should present a slope given by $-E_g/k$. The presentations of the V_{OC}-values against temperature can be found in Fig. 5.23 and 5.24 for the In_2S_3-buffered device and the CdS reference, respectively. The extrapolation of V_{OC} leads indeed to an energy qV of (1.12±0.01) eV and (1.15±0.01) eV for the In_2S_3-buffered device and the CdS reference, respectively. In these presentation, only the light intensities corresponding to the linear part of the (j_{SC}, V_{OC})-plots and therefore the range where the main diode dominates have been included.

A linear regression of the expression $A \ln j_0$ vs. $1/T$ results in similar energies E_0 in both cases: 1.16 eV for the In_2S_3-buffered sample and 1.09 eV for the CdS reference, which is in good agreement with the bandgap of the absorber (E_g=(1.11±0.2) eV. The data and corresponding fits are displayed in Fig. 5.25

The results obtained in this section can be summarised as follows. The analysis of the jV-response under illumination showed that the dominant recombination mechanism of the device with In_2S_3 buffer exhibits similar properties to the CdS reference with diode quality factors extracted from the plot of (j_{SC}, V_{OC})-values that are nearly independent of

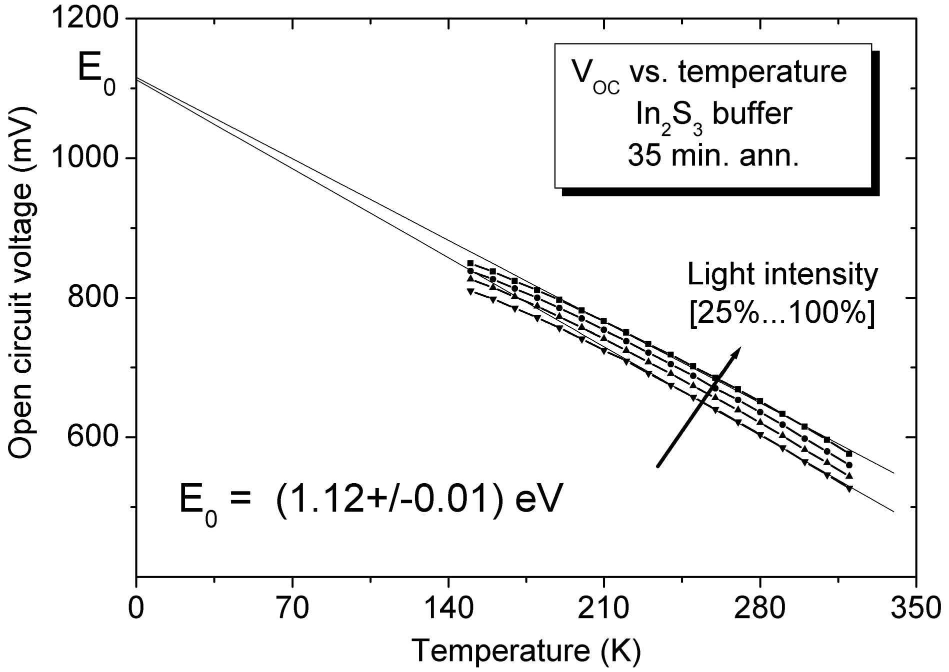

Figure 5.23: Plot of the measured V_{OC} values of a Cu(In,Ga)Se$_2$ device with In$_2$S$_3$ buffer (35 min. ann.) as a function of the absolute temperature for various light intensities. The linear extrapolation of the data to 0 K gives 1.12 V and is represented in the graph as a line.

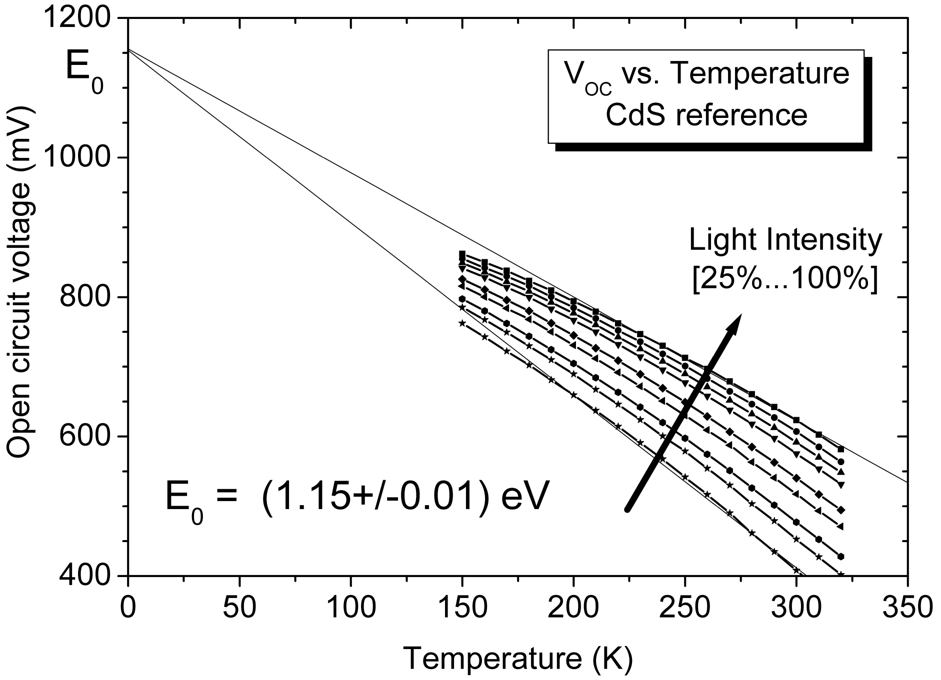

Figure 5.24: Plot of the measured V_{OC} values of a CdS reference as a function of the absolute temperature for various light intensities. The linear extrapolation of the data to 0 K gives 1.15 V and is represented in the graph as a line.

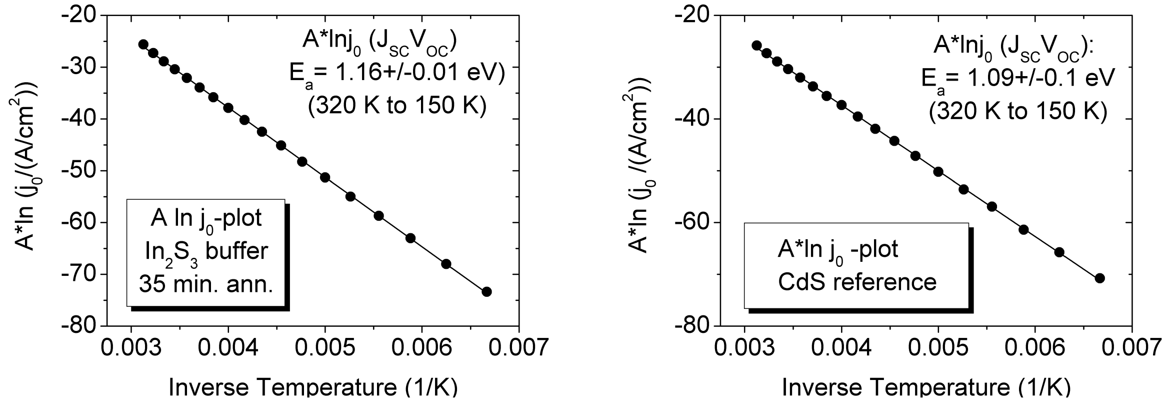

Figure 5.25: Plot of $A \ln j_0$ vs. the inverse temperature and a linear regression of the data from which the activation of the saturation current density is determined. Left: Cu(In,Ga)Se$_2$ solar cell with In$_2$S$_3$ buffer (35 min. annealed). Right: CdS reference.

the temperature in the range of 1.5 to 1.6 (In$_2$S$_3$ buffer) and 1.2 to 1.5 (CdS buffer). Similar diode quality factors have also been reported for Cu(In,Ga)(S,Se)$_2$ solar cells with In$_2$S$_3$ buffer layers prepared by the ion-layer gas reaction technique (ILGAR, Allsop et al. [27]). An exception is found for temperatures below 220 K, where a small contribution from a most likely tunneling enhanced recombination mechanism to the dominant recombination resulting in increasing diode quality factors of up to 2.2 was found. The extrapolation of the V_{OC} to 0 K leads in both cases to values close the bandgap of the absorber of (1.11±0.02) eV. A fit of $A \ln j_0$ versus the inverse temperature also yields an energy E_0 in the range of 1.12-1.16 eV for both devices.

A comparison with the different possible recombination mechanism and their influence on the diode quality factor and saturation current density shows that this behaviour is best explained with a thermally activated recombination in the space charge region, in agreement with the dominant recombination mechanism typically attributed to highly efficient standard Cu(In,Ga)Se$_2$ solar cells. This proves that high quality junctions between In$_2$S$_3$ and Cu(In,Ga)Se$_2$ are in fact obtained for annealed devices and that device performance of the In$_2$S$_3$ buffered devices are not necessarily stronger limited by interface recombination than their CdS counterpart. This is an important finding for the future prospect of In$_2$S$_3$ buffered devices. As a consequence, devices with high open circuit voltages can be expected from In$_2$S$_3$-buffered devices. In fact devices with even higher open circuit voltages than the corresponding CdS references have been obtained during this work (see for example Tab. 5.1). In the next section, the effect of the annealing treatment will be discussed.

Development upon annealing

In the following, an equivalent analysis will be performed on an In$_2$S$_3$-buffered Cu(In,Ga)Se$_2$ solar cell in the as-grown state, from the same deposition run as the one presented in the previous section (deposition from powder B, as grown state: η: 9.75 %, FF: 60.7 %, j_{SC}: 33.3 mA/cm^2, V_{OC}: 487 mV). The analysis is then repeated on the same cell after several

Table 5.5: Efficiencies and cell parameters before and after several annealing steps for the ZnO/ In_2S_3/ Cu(In,Ga)Se_2/ Mo device for which the jV-analysis at various temperatures and light intensities is carried out and displayed in Fig. 5.26-5.28.

Integral annealing time (min.)	η (%) ±0.2 %	FF (%) ±0.2 %	j_{SC} (mA/cm^2) ±0.5 mA/cm^2	V_{OC} (mV) ±2mV
0	9.75	60.7	33.3	487
5	11.05	62.7	32.8	537
15	12.48	65.0	32.7	587
35	14.12	69.8	32.6	621
CdS ref.	16.02	72.9	35.0	628

annealing steps at 200 °C in air up to a total annealing time of 35 min. The cell parameters after the individual annealing steps are presented in Table 5.5 together with the corresponding CdS reference.

Fig. 5.26 summarises the jV-curves of the solar cell in the dark at various temperatures (320 K to 150 K, ΔT: 10 K). In this figure, the graphs corresponding to the individual annealing steps are displayed next to each other for a direct comparison (0 min, 5 min, 15 min, 35 min.). The measurement of the solar cell after 35 min. annealing showed an decreased parallel resistance which means that there was a small shunt present, most likely as a result of the subsequent contacting steps. For the higher temperatures, a decreasing saturation current density and diode quality factor upon annealing is observed, similar to the case of the dark jV-analysis in Section 3.2.

For the lower temperatures (220 K to 150 K), a strong deviation from the diode-like behaviour is found, indicating the presence of at least one additional recombination mechanism. The shape of the jV-curves at the lower temperatures changes upon the annealing as a result of the changing contributions from different recombination mechanisms. This clearly shows that the dominant recombination mechanism is altered as a result of the annealing.

The analysis of the illuminated jV-curves follows the analysis presented in the previous section and the (j_{SC}, V_{OC})-plot of the solar cell after different annealing times is presented in Fig. 5.27. Very low V_{OC}-values are observed for the as grown sample (as grown, full illumination, 300 K: 476 mV), that increase slowly for decreasing temperatures (150 K: 641 mV). Upon annealing the V_{OC} values increase as well as the slope of $V_{OC}(T)$ (35 min. ann., full illumination, 300 K: 613 mV; 150 K: 849 mV). An evaluation of the four highest light intensities as in the previous section give the diode quality factors diplayed in Fig. 5.28.

The diode quality factor after 35 min. resembles the diode quality factor of the In_2S_3-buffered solar cells presented in the previous section, which is an indication for the good reproducibility of the annealing effect. The analysis of the as grown solar cell reveals a diode quality factor that increases strongly for decreasing temperatures from approximately 2 to values over 6. This is a clear indication of an strong contribution from a

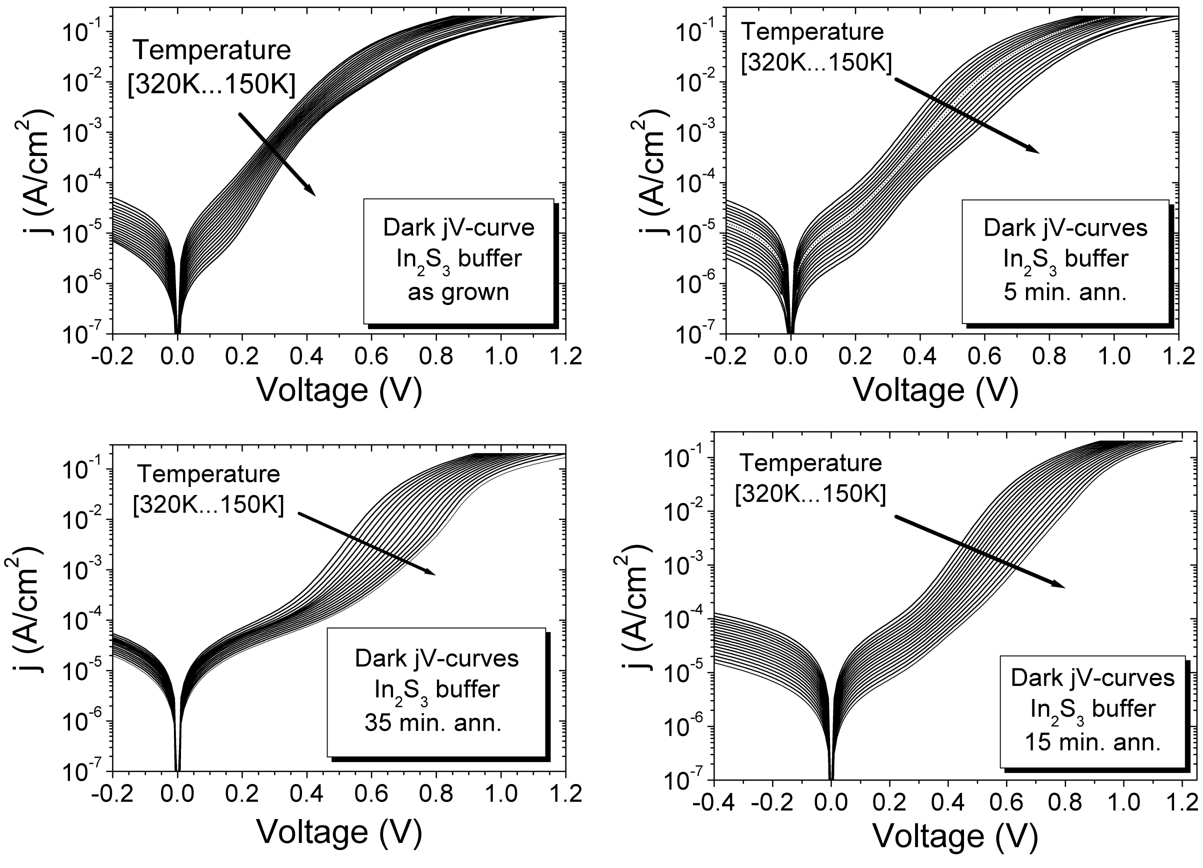

Figure 5.26: Measured dark jV-curves of a ZnO/ In_2S_3/ Cu(In,Ga)Se_2/ Mo solar cell after various annealing steps. Clockwise: As grown, 5 min. ann., 15 min. ann., 35 min. ann.

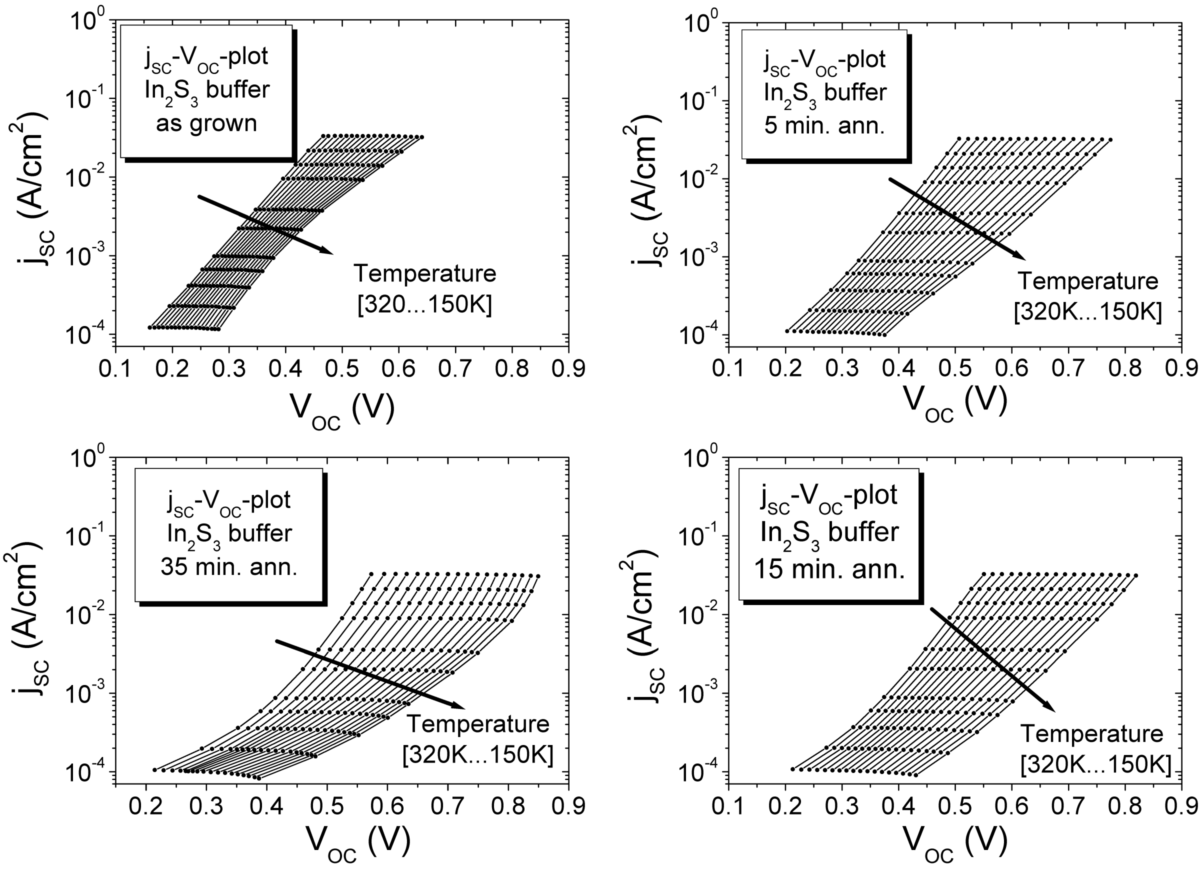

Figure 5.27: j_{SC}, V_{OC}-plots of a ZnO/ In_2S_3/ Cu(In,Ga)Se_2/ Mo solar cell after various annealing steps. Clockwise: As grown, 5 min. ann., 15 min. ann., 35 min. ann.

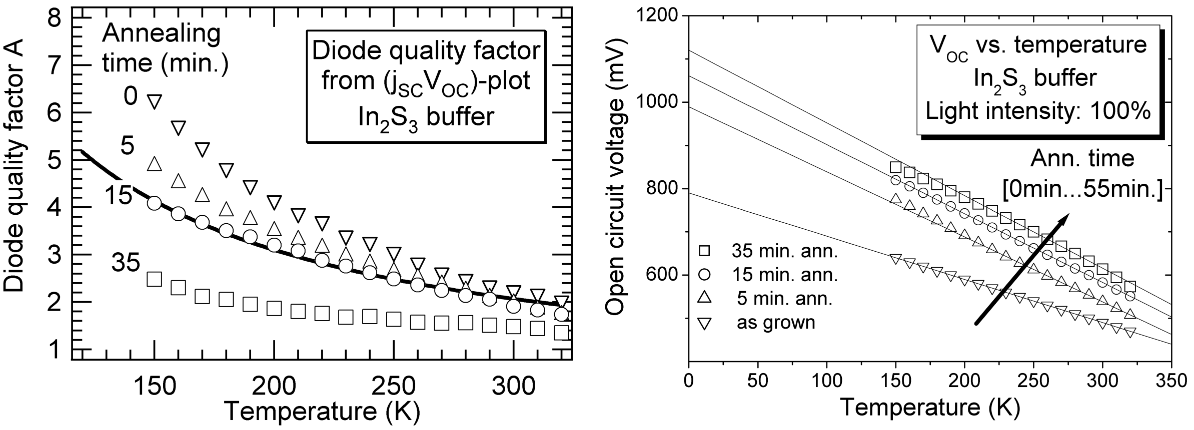

Figure 5.28: Left: Diode quality factors extracted from the (j_{SC},V_{OC})-plots of the In_2S_3-buffered solar cell after various annealing steps. A fit describing tunneling enhanced recombination at the interface as described in text is also displayed (continuous line). Right: Measured V_{OC}-values under full illumination (≈1000 W/m^2) of the same solar cell for various annealing times (0 min., 5 min., 15 min, 35 min.).

recombination process associated with tunneling. The absolute value and the slope of the diode quality decreases for increasing annealing times and reaches values of just below 2 for the solar cell after 35 min. in the temperature range from 320 K to 190 K.

The fit of the diode quality factors with the expression for tunneling enhanced recombination in the space charge region (Eq. 3.46) did not show any correlation to the data for the sample at annealing times 0-15 min. A fit to the expression for tunneling enhanced recombination at the interface (Eq. 3.50) did not correlate very well to the data neither in the as grown state, but at least described the qualitative temperature dependence of the diode quality factor in the right way. A fit to the data of the device after 15 min. annealing according to Eq. 3.50 is added to the measured data in Fig. 5.28 for comparison.

The plot of the V_{OC}-values under full illumination is depicted in the right part of Fig. 5.28. The extrapolation of V_{OC} to 0 K for the solar cell after 35 min. with the mainly thermally activated recombination yields the bandgap, just as in the case presented before. The V_{OC} values of the as grown sample with the high tunneling contribution do not extrapolate to E_g/q, as for a pure tunneling process for example the thermal activation energy is not well defined.

The conclusion of these results is that the dominant recombination mechanisms are indeed strongly and reproducibly altered during the annealing of the In_2S_3-buffered solar cells. The annealing allows to obtain devices with decreased recombination, which in turn leads to high open circuit voltages comparable or even outperforming the CdS references. Before the annealing an increased recombination behaviour is observed, with high diode quality factors indicating a strong contribution from tunneling effects. Due to several competing recombination mechanisms in the as grown solar cell, it is not possible to clearly identify the location and exact nature of the recombination before the annealing. The most likely case is a tunneling enhanced recombination at the interface. Upon annealing, this second recombination mechanism is gradually decreased until finally the contribution from a mainly thermally activated recombination from the space charge region is established, as found also in the CdS reference.

It is interesting to note that Turcu et al. [43],[94] found a strong dependence of the type of recombination mechanism on the Cu/(In,Ga) ratio of $Cu(In,Ga)Se_2$ solar cells with a CdS buffer. For samples with high Cu content tunneling enhanced recombination was found which was attributed to recombination at the buffer/absorber interface. Cu-poor samples showed a much lower tunneling contributions and the recombination was in this case assumed to be located in the bulk of the absorber. This suggests to relate the changing recombination mechanisms to changes in the elemental distribution at the interface. The effect of diffusion across the interface and its effect on the junction formation will be studied in the next chapter.

5.3 Summary

In this chapter the preparation and performance of $Cu(In,Ga)Se_2$ solar cells with an In_2S_3 buffer layer have been described and analysed in detail. An optimisation of the preparation conditions led to solar cell efficiencies that were comparable to references samples prepared with a standard CdS buffer. Two key factors were identified as important for optimum performance: (A) Usage of a single phase, pure source material. (B) A post deposition annealing of the completed solar cells for 35 min. to 55 min. at a temperature of 200 °C. The annealing was found to improve mainly the fill factor and open circuit voltage of devices with an In_2S_3 buffer, independent of the atmosphere in which the annealing was carried out (e.g. annealing in air or inert gas). The influence of the annealing on the solar cell performance and the individual solar cell parameters was further studied in detail by the analysis of the quantum efficiency and the current-voltage characteristics in the dark and an analysis of the temperature dependent current-voltage characteristic at various illumination intensities.

The short circuit current densities of devices with In_2S_3 buffer were found to be slightly lower than CdS references and to decrease upon annealing. Quantum efficiency analysis showed that losses at higher wavelengths were increasing during annealing. This means collection is decreased for charge carriers generated deep within the absorber.

The analysis of the current-voltage characteristics in the dark showed that the increasing open circuit voltage (from $\approx 590\,\text{mV}$ in the as grown state to 660 mV after 45 min. of annealing) is the result of a decrease in the saturation current density of three decades for the main diode (down to $\approx 6 \times 10^{-8}\text{mA/cm}^2$), which indicates substantially less recombination.

This is confirmed by the analysis of temperature dependent current-voltage characteristics under illumination. Here, high efficiency devices with In_2S_3 buffer after 35 min. of annealing were found to show diode quality factors in the range of 1.5 to 1.6 down to temperatures 220 K that were only weakly temperature dependent and similar to the CdS reference ($A \approx 1.3$ to 1.4). The result of the extrapolation of the temperature dependent open circuit voltage to 0 K ($qV_{OC}(0\,\text{K})$) resembled the bandgap energy of the absorber in both case. This shows, that it is possible to produce high efficiency $Cu(In,Ga)Se_2$ devices with In_2S_3 buffer layers, with a recombination similar to the CdS reference and associated with a weakly tunneling enhanced recombination in the space charge region. A fit of the diode quality factor to this model gave excellent correlation with measured data.

It was shown that the recombination decreases during the annealing and gradually changes from being dominated by a mechanism with high tunneling contribution (diode quality factors of up to 6) associated with the interface to a recombination located in the space charge region of the device. This shows the potential for In_2S_3 to produce high quality junctions as a result of the annealing treatment and in fact devices with In_2S_3 buffer layer showed better open circuit voltages than their CdS counterparts.

Due to the optimisation processes new record efficiencies for chalcopyrite solar cells with an evaporated In_2S_3 buffer layer have been achieved which are presented in Chapter 7.

Chapter 6

Diffusion of Cu from $Cu(In,Ga)Se_2$ into In_2S_3

The last chapter showed that performance of In_2S_3-buffered solar cells substantially increases after an annealing at 200 °C. The relevant interface in view of the dominant recombination is the absorber/buffer heterojunction and this chapter deals with diffusion processes at this interface induced by the annealing process.

In this work, the substrate is at room temperature during the In_2S_3 deposition. For In_2S_3 buffer layers deposited by other deposition methods that use higher substrate temperatures during the deposition process ($T_{substrate}$=140-300 °C) the presence of Cu in the buffer layer has been reported by several authors [95],[96],[97],[98]. This means that a substantial Cu diffusion has taken place already during the deposition process of these In_2S_3 buffer layers.

In this chapter, diffusion processes upon annealing at temperatures in the order of 200 °C will be systematically investigated on In_2S_3/ $Cu(In,Ga)Se_2$ bilayer structures with different analysis techniques.

At the beginning, a first direct proof of the Cu diffusion into the In_2S_3 at the concerned temperatures will be given. Here, the integral Cu signal from a thin In_2S_3 layer will be monitored during annealing with high kinetic energy (HIKE) X-ray photoelectron spectroscopy capable of probing the entire In_2S_3 layer thickness.

Then, with laboratory X-ray photoelectron spectroscopy (XPS) the surface composition of In_2S_3(50 nm)/$Cu(In,Ga)Se_2$ samples will be studied as a function of the annealing time.

Finally, the elemental distribution of In_2S_3/$Cu(In,Ga)Se_2$ stacks will be studied with energy-dispersive X-ray spectroscopy (EDX) in combination with a transmission electron microscope (TEM). Here TEM micrographs and EDX linescans will be recorded on cross sections of samples before and after the annealing. The chapter is completed with a discussion of the obtained results and the presentation of a semi-empirical model for the diffusion based on the results of this chapter.

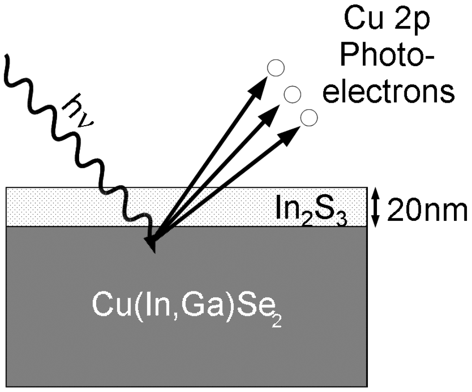

Figure 6.1: Schematic drawing of the layer assembly used in the HIKE experiments. (Not to scale.)

6.1 Monitoring the Integral Cu Concentration

The first step is to verify the formulated assumption of a Cu diffusion during the annealing process and to clarify which temperatures are needed to trigger the diffusion. For this purpose, advantage has been taken of a new tool that had recently been established at the Berlin Synchrotron facility (BESSY): HIKE. HIKE stands for High Kinetic Energy XPS and is a variation of XPS where the excitation source is a high-flux high-resolution synchrotron beamline with excitation energies up to 12 keV. By increasing the energy of the exciting X-rays, the kinetic energy of the emitted photoelectrons is increased. This means that the photoelectrons have a higher inelastic mean free path (IMFP), which increases approximately with $(E_{kin})^{0.5}$ for kinetic energies $E_{kin} > 30\,\mathrm{eV}$ [99] (see also Section A.2.2). Consequently, photoelectrons from deeper within the sample and even XPS signals through thin, closed overlayers can be detected. This makes HIKE a powerful tool for the analysis of interdiffusion phenomena. The idea of these experiments is to select an excitation energy high enough to enable a probing depth larger than a thin In_2S_3 layer (i.e. all atoms inside this layer contribute then to the corresponding XPS signals detected.) When measuring the Cu 2p, e.g., it is then possible to monitor any Cu atoms entering into the In_2S_3 layer by an increase in the Cu 2p peak intensity.

6.1.1 Sample Preparation and Experimental Setup

Sample preparation

In a preliminary experiment, samples were prepared by evaporating thin (in the thickness range between 10-40 nm) layers of In_2S_3 on top of a $Cu(In,Ga)Se_2$ absorber (a stack of $Cu(In,Ga)Se_2$/Mo/ glass substrate) prepared by the standard absorber process at the HZB. With standard laboratory XPS (excitation Al Kα, 250W) it was checked if the layers were closed. The absence of the Cu 2 p peak for layers with thickness $d > 15\,\mathrm{nm}$ was taken as a proof for a closed layer.

No Cu could be detected for these samples by conventional XPS in the as grown state. This is an important finding because it distinguishes the evaporation of compound In_2S_3

from several other deposition methods. For example, deposition methods like Ion Layer Gas Reaction (ILGAR), atomic layer chemical vapour deposition (ALCVD) or evaporation from the elements usually need higher substrate temperatures for a complete reaction of precursors/ reactants. Here, Cu is usually already found in the In_2S_3 layer without further annealing treatments as a result of the deposition process (Spiering et al. [100], Allsop et al. [95], Barreau et al. [98]). The low deposition temperature of the thermally evaporated samples presented in this work therefore enable for the first time an systematic investigation and detailed analysis of the Cu diffusion under controlled conditions and separated from the deposition process.

Relatively thin layers (20 nm) are needed to achieve a complete coverage (in terms of the absence of a Cu signal in XPS spectra with Al Kα excitation). This is true for the perpendicular view onto the sample, as is the case for the XPS setup. In fact surface microstructures, e.g. with a vertical local surfaces orientation, might be covered to a smaller extent. This is because the molecular beam of the thermal evaporation is oriented perpendicular to the sustrate as is viewing angle of the XPS setup.

The nominal In_2S_3 layer thickness for HIKE experiments was chosen to be 20 nm. To illustrate the sample configuration for the HIKE experiments, Fig. 6.1 shows a schematic drawing of the layer assembly.

Setup HIKE (High kinetic energy X-ray photoelectron spectroscopy)

High kinetic energy X-ray photoelectron spectroscopy (HIKE) experiments were performed at the high resolution high flux beam-line KMC-1 with dipole source and a double crystal monochromator at the BESSY II synchrotron (Berliner Elektronenspeicherring), Berlin, Germany. The beamline provides synchrotron light between 1.7 keV and 12 keV and a high photon flux (in the range of 10^{11} -10^{12} photons/s) [101]. The HIKE beamline and endstation are optimised to measure fast high energy photoelectron spectra with a sub-eV energy resolution. The HIKE endstation is equipped with a high resolution concentric hemispherical electron analyser (SCIENTA R4000) capable of measuring electrons from few eV up to 10 keV [102]. The analysis chamber has a standard operative pressure of 10^{-8} mbar and a heatable sample holder. For more details on the beamline KMC-1 and the HIKE setup the reader is referred to [101], [102] and [103].

Selection of Excitation Energy

Inelastic mean free paths (IMFP) (see Section A.2.2 for details) for the Cu $2p_{3/2}$ photoelectrons in In_2S_3 and the applied excitation energy range have been calculated with the QUASES program provided by Tanuma et al. following their TPP2M formula [104][105]. For an excitation energy of 2010 eV an IMFP of 2.2 nm is obtained, 4000 eV corresponds to an IMFP of 5.1 nm. The TPP2M formula was not originally designed and tested for kinetic energies above 2000 eV so the IMFP have to be handled with care and have probably a lower accuracy than the ±15 % stated by Tanuma et al. for $E_{kin} < 2000$ eV. If the IMFPs are used as an approximated attenuation length for the photoelectrons, the Cu $2p_{3/2}$ signal intensity is decreased to 0.01% (2%) of its original value by a 20 nm thick In_2S_3 layer in the case of $E_{exc.}$=2010 eV (4000 eV). However, apart from the signal intensity the actual detection limit depends also on the detection sensitivity and noise level and is difficult to determine ab initio. The detection limit will therefore be determined experimentally in the following.

In a preliminary set of measurements the ability of HIKE to detected photoelectrons through the closed In$_2$S$_3$ layer is tested. The aim is to experimentally determine the excitation energy at which the Cu 2 p photoelectrons from the absorber have sufficient kinetic energy to traverse the In$_2$S$_3$ overlayer and can be detected. For this purpose, overview spectra as well as In 3 d$_{5/2}$ and Cu 2 p$_{3/2}$ detail spectra have been recorded at excitation energies of 2010 eV, 3100 eV, 4000 eV, 5000 eV, 6000 eV and 8000 eV, respectively. Overview spectra have been normalised to the In 3 d$_{5/2}$ peak intensity.

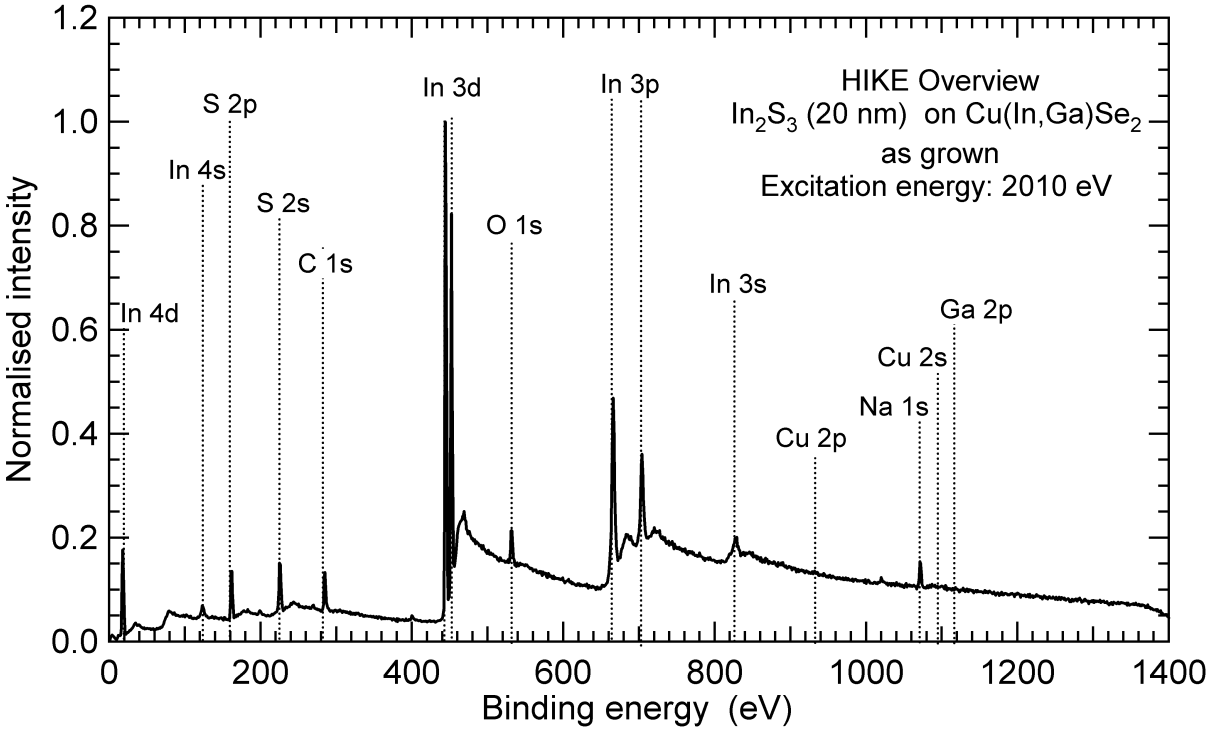

Figure 6.2: HIKE overview spectrum at an excitation energy of 2010 eV of the sample described in Fig. 6.1 (20 nm In$_2$S$_3$ on a Cu(In,Ga)Se$_2$ absorber). The spectrum has been normalised to the In 3d$_{5/2}$ peak intensity.

As an example, the overview spectrum of the as-grown sample at an excitation energy of 2010 eV is shown in Fig. 6.2. The main features of the overview spectra are the same for all excitation energies. They stem from the In$_2$S$_3$ overlayer and consist of In peaks (3s, 4s and 4d, 3p, 3d doublets) and S peaks (2s and 2p doublet). Furthermore, small contributions by surface contaminations of C and O are found, which are more pronounced for lower excitation energies (which are more surface sensitive).

In contrast to copper, sodium is found in the In$_2$S$_3$ sample in the as grown state even for low excitation energies. The Na is either incorporated into the In$_2$S$_3$ on In sites [106] or might be accumulated at the surface. A strong sodium signal is found even on thick (>200 nm) In$_2$S$_3$ samples on Cu(In,Ga)Se$_2$ absorbers in XPS (Al Kα excitation, not shown here, for thinner samples see for example Section 6.2), which suggests that sodium might float at the surface during the deposition process.

The aim of this preliminary study is to determine the minimum excitation energy for which the Cu 2 p peak is clearly detected. The Cu 2 p doublet is absent in the overview spectra recorded at low excitation energies. The Cu 2 p photoelectrons are emitted from the absorber and need sufficient kinetic energy in order to traverse the In_2S_3 layer. In Fig. 6.3, the detailed Cu $2p_{3/2}$ spectra recorded at different excitation energies are presented. Here the increase of the Cu $2p_{3/2}$ signal at higher excitation energies is clearly visible. For $E_{exc.}$= 4000 eV and higher, the peak intensity is clearly above the background noise level.

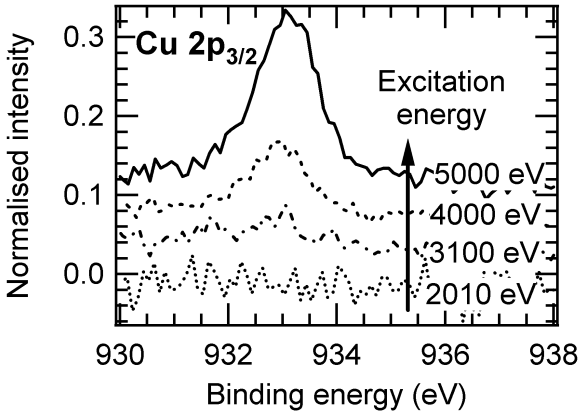

Figure 6.3: HIKE XPS Cu $2p_{3/2}$ spectra at different excitation energies. At high excitation energies the photoelectrons have sufficient kinetic energies and traverse the 20 nm thick In_2S_3 overlayer. Spectra have been normalised to and corrected for a linear background and have been shifted vertically.

For an excitation energy of above 4000 eV, the Cu 2 p photoelectrons are found to have sufficient kinetic energy to traverse the In_2S_3 layer and can be detected. Consequently, the whole In_2S_3 layer can be probed for Cu at this energy and the diffusion experiments were carried out at a excitation energy of 4000 eV.

6.1.2 Cu Diffusion Experiment

In order to monitor the diffusion in-situ during annealing, a sample with a 20 nm thick In_2S_3 layer on a Cu(In,Ga)Se_2 absorber substrate was mounted onto the HIKE sample holder. Cu $2p_{3/2}$ spectra were continuously measured every two minutes while the sample holder was heated from room temperature up to 320 °C with a heating rate of 2 °C/min. After the heating process and subsequent cooling, the sample was measured again with excitation energies of 2010 eV and 4000 eV (overview, Cu 2 $p_{3/2}$ and In $3d_{5/2}$ detail spectra.) In Fig. 6.4 the Cu 2 p spectra recorded during the heating of the sample at $E_{exc.}$=4000 eV are displayed.

In this presentation, the Cu spectra are plotted against the temperature at which they were measured. At the beginning of the heating process, the Cu $2p_{3/2}$ peak intensity

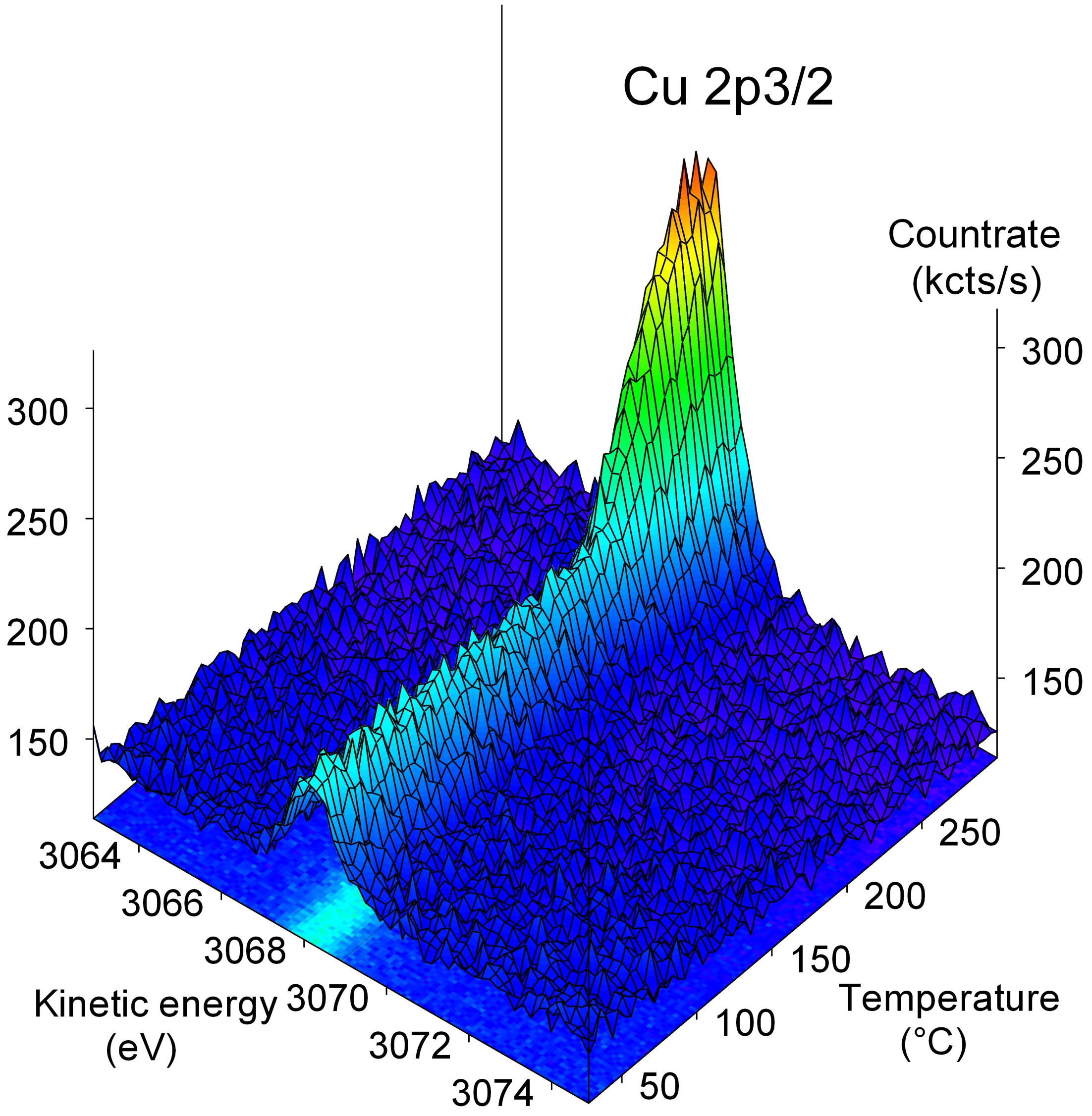

Figure 6.4: HIKE XPS spectra of the Cu $2p_{3/2}$ signal at different temperatures. The high kinetic energy of the emitted photoelectrons as a result of the high excitation energy (4000 eV) allows to detect a small Cu signal (binding energy approximately 932 eV, [107]) from the Cu(In,Ga)Se_2 through the 20 nm thick In_2S_3 top layer at low temperatures. The increase of the Cu signal at higher temperatures indicates a diffusion of Cu into the In_2S_3 top layer.

remained unchanged. A strong increase of the emission intensity takes place for temperatures just above 200 °C. This can be better seen if the integrated Cu $2p_{3/2}$ peak intensity is plotted as a function of the temperature (Fig. 6.5). The onset of the increase is located around (210±20) °C. The accuracy of the temperature has to be approximated in this case, as no accurate temperature calibration could be carried out and the stated temperature is the temperature of the thermocouple in the substrate holder. The surface temperature of the sample might be lower.

Finally, Fig. 6.6 shows overview spectra at 2010 eV and 4000 eV before and after the

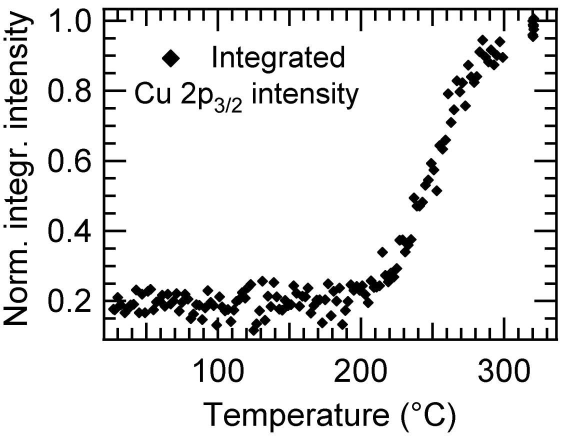

Figure 6.5: Normalised integrated Cu $2p_{3/2}$ peak intensity from the spectra shown in Fig. 6.4 plotted as a function of the temperature. A clear increase above T=(200±20) °C demonstrates the diffusion of Cu into the buffer layer.

heating process. Due to the diffusion of Cu into the buffer, in the overview spectra at 4000 eV, the Cu 2p emission is increased after the heating step. The peak intensities of the other peaks do not show pronounced changes apart from a small decrease of the surface contaminants C and O after annealing. The spectra recorded at an excitation of 2010 eV show no Cu before the heating (no Cu at the In_2S_3 surface) but do show a clear Cu signal after the annealing process. In order to be detected at the lower excitation energy of 2010 eV, the Cu atoms diffusing into the In_2S_3 must have reached the surface near region of the buffer layer during the annealing process.

It was possible to directly monitor the increasing Cu amount in the In_2S_3 layer at temperatures above 200 °C. This is a clear proof of a pronounced Cu diffusion at temperatures comparable to the annealing temperature used for the post deposition annealing of solar cell devices (see Chapter 5.1.4). Furthermore, the presented data suggest a saturation of the Cu at a certain level. The limited temperature range applied during the experiment leaves room for interpretation, but the slope of the integrated signal intensity decreases for the last datapoints (290 - 320 °C).

A precise quantification of the actual amount of copper diffused into the In_2S_3 layer from these experiments is complicated by the following:

- Due to the increased sampling depth the measured signal is the integral signal of the entire In_2S_3 layer. The integral is far from being easily formulated, as the copper profile as well as the XPS excitation/absorption profile in the layer are functions of the depth x.

- The quantities necessary for a quantification of the XPS signal intensity, such as the photo-ionisation cross section, IMFP or angular distribution function are well defined and tabulated for standard XPS. However, for the high excitation energies involved, accurate data is scarce.

- Finally the diffusion is a function of time and temperature. The fact that the heating

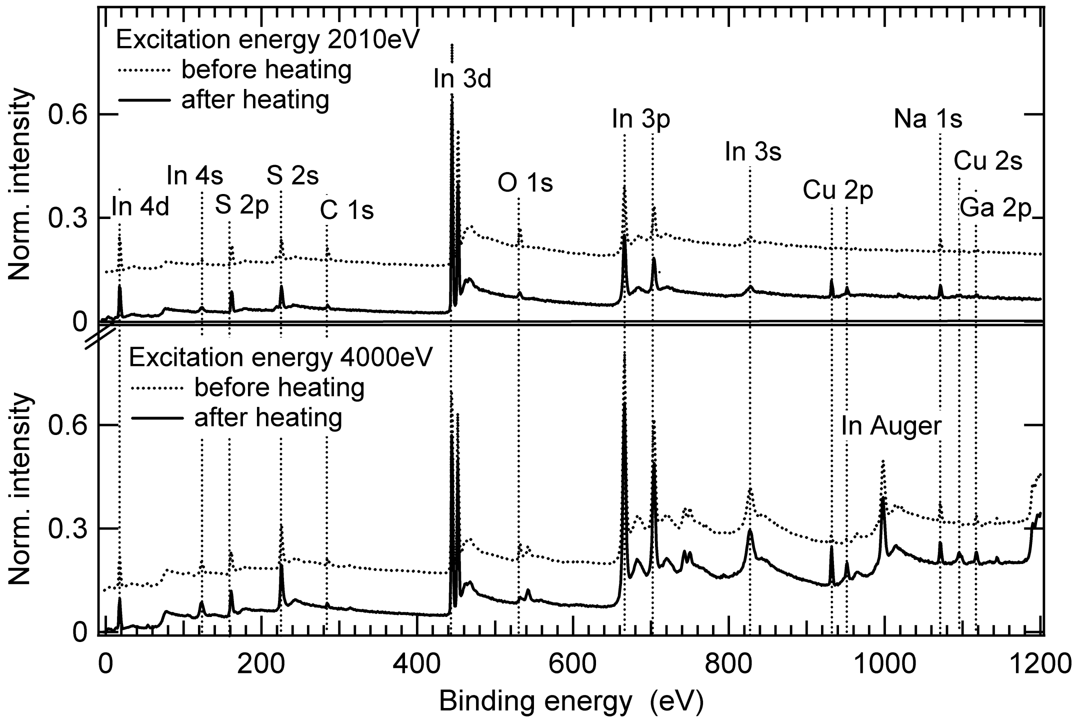

Figure 6.6: HIKE XPS overview spectra before and after the heating, for excitation energies of 2010 eV and 4000 eV. Spectra have been normalised and shifted vertically for better comparison.

was not performed at a fixed temperature and duration, but with a heating ramp due to the experimental possibilities of the setup, makes it impossible to state a simple diffusion relation for the experiment.

Therefore, the experiment has to be regarded as a proof of concept. The Cu diffusion was clearly demonstrated, a quantification has to postponed and will be the aim of the following sections. In this section, the new HIKE setup has been proven to be a powerful tool for the chemical analysis of stacked layer systems, as it effectively allows to vary the probing depth and look through thin covering overlayers.

6.2 Cu Amount at the In$_2$S$_3$ Surface After Annealing

In this section the amount of Cu at the In$_2$S$_3$ surface will be examined and quantified with the help of XPS measurements for different annealing times.

As has been already pointed out in Section 6.1, the information depth in XPS with a laboratory Al/Mg X-ray source is limited to a few monolayers. As the last experiments have shown, the Cu traverses easily the whole In$_2$S$_3$ layer during the annealing treatment at 200 °C. It is therefore possible to measure with XPS the amount of Cu that has traversed the buffer layer and has reached the surface opposite to the interface. The aim of this section is the quantification of the Cu concentration at the buffer surface after the annealing treatment. For this purpose, two sets of experiments were conducted: (1)

Table 6.1: Index of samples prepared for the quantitative XPS analysis annealed ex-situ at 200 °C for various annealing times t_{anneal}.

Material	(50±5) nm In_2S_3 on $Cu(In,Ga)Se_2$							
	1A	1E	1B	1C	1D	1F	1G	1H
t_{anneal} (min.)	0	2.5	5	10	20	40	80	160

XPS measurements on a sample series with different annealing times. (2) In-situ XPS measurements of the increasing Cu concentration during annealing.

6.2.1 Sample Preparation

In the first set (1), a sample with a (50±5) nm thick In_2S_3 layer on top of a standard $Cu(In,Ga)Se_2$ absorber was prepared. The sample was then cut into 8 pieces, each having a size of 2.5 cm× 2.5 cm. Each of these pieces was heated on a hot plate at 200 °C in an inert gas atmosphere for a different annealing time, ranging from 0-160 min. These samples were subsequently measured with XPS. This has the advantage of controlled annealing conditions equivalent to the post deposition annealing applied to solar cell devices and provides an idea of the scatter between different samples.

The samples were stored in an Ar-glovebox prior to the XPS measurements. Total air exposure time of the samples after In_2S_3 deposition was approximately 2h due to the transfer and cutting. The samples were heated on a hot plate at 200 °C for 0-160 min. In order to keep oxidation to a minimum, the whole heating process was carried out inside an Ar-glovebox (H_2O: < 0.329 ppm, O_2: < 1 ppm). The sample index with the annealing times for sample 1A-1H can be found in Table 6.1.

After annealing, the samples were introduced into the CISSY-UHV chamber for XPS analysis. Details on the fundamentals of XPS and the specific setup that was used can be found in Section A.2.2 and [108], respectively. For reference purposes a blank absorber and a In_2S_3 on Mo sample were added to the XPS measurements.

In the second set (2), one sample was prepared identical to the samples of the first set (50 nm In_2S_3 on $Cu(In,Ga)Se_2$). This sample was introduced into the XPS analytical XPS chamber without external heating. It was rather heated inside the XPS chamber on the sample holder, until a Cu diffusion could be detected. It was hold at a constant temperature while measuring XPS Cu $2p_{3/2}$ spectra every ten minutes. This set has the advantage of minimising the data scattering between different samples as all the data stems from the same sample. The disadvantage is a less controlled annealing temperature, as no accurate temperature calibration could be carried inside the ultra-high vacuum analytical chamber of the XPS measurement setup. In the following, the two sets of experiments and their results will be presented.

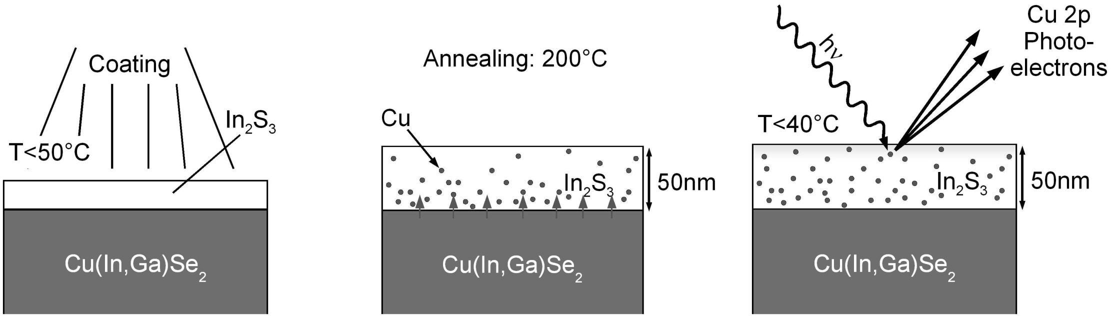

Figure 6.7: Schematic drawing of the experimental procedure for the Cu quantification by XPS on different samples annealed ex-situ. Left: Absorber substrates are coated with a 50 nm thick In_2S_3 film at room temperature. Middle: The Cu diffusion is triggered by an annealing on a hot plate at 200 °C for 2.5-160 min. Right: The Cu amount at the sample surface is quantified by XPS.

6.2.2 Set (1): Sample Series with Ex-Situ Annealing

Fig. 6.7 shows the principle of the first set of experiments conducted to quantify the Cu amount at the In_2S_3 surface.

For each sample 1A-1H a set of XPS spectra was recorded: overview and detail spectra of the In 3d, S 2p, Cu 2p, Ga 2p, Se 3d, O 1s, Na 1s and C 1s peaks. Excitation source was an Al Kα (energy: 1486.6 eV) X-ray tube operating at a power of 250 W. For energy calibration, prior and after each set the Au 4f peak of a sputter-cleaned gold foil was recorded. A linear background was subtracted from the detail spectra. For the quantification of the peak intensity spectra the peak area has been determined by fitting the spectra with a Voigt function in the program PeakFit.

Fig. 6.8 shows the overview spectra of the $Cu(In,Ga)Se_2$ reference, the In_2S_3 reference and sample 1A (as grown) and 1F (40 min. annealed).

The detail spectra of the 0 1s, C 1s, S 2p, Na 1s, Ga $2p_{3/2}$ and Se $3d_{5/2}$ peaks for sample 1A (no annealing) and sample 1F (40min. annealing) are shown in Fig. 6.9. The O 1s and C 1s peaks, which are a result of surface contaminations of the samples, are reduced due to the annealing. The Na 1s peak remains unchanged. The S 2p peaks are slightly increased after the annealing, which can be attributed to a stronger attenuation of the signal by surface contaminants for the sample without annealing. No Ga is detected before and after annealing. There is a slight increase in the Se $3d_{5/2}$ peak intensity during the annealing, indicating a small Se diffusion into the In_2S_3. However the peak intensity is in the order of the noise level. A quantitative analysis allows in this case only to estimate the Se content to be in the order of or less than (1±1) at.%.

The In $3\,d_{5/2}$ detail spectra are presented in Fig. 6.10. The sample that had not been annealed shows a slightly lower intensity than the other samples (intensity difference is <7 %). This is attributed to the evaporation of surface contaminants as in the case of the S peak. After the first few minutes of annealing, the In peak intensity is not altered significantly for the rest of the measurements. The Cu $2\,p_{3/2}$ spectra do show a significant change in intensity and are plotted in Fig. 6.11.

The increasing peak intensity demonstrates how the Cu concentration at the sample

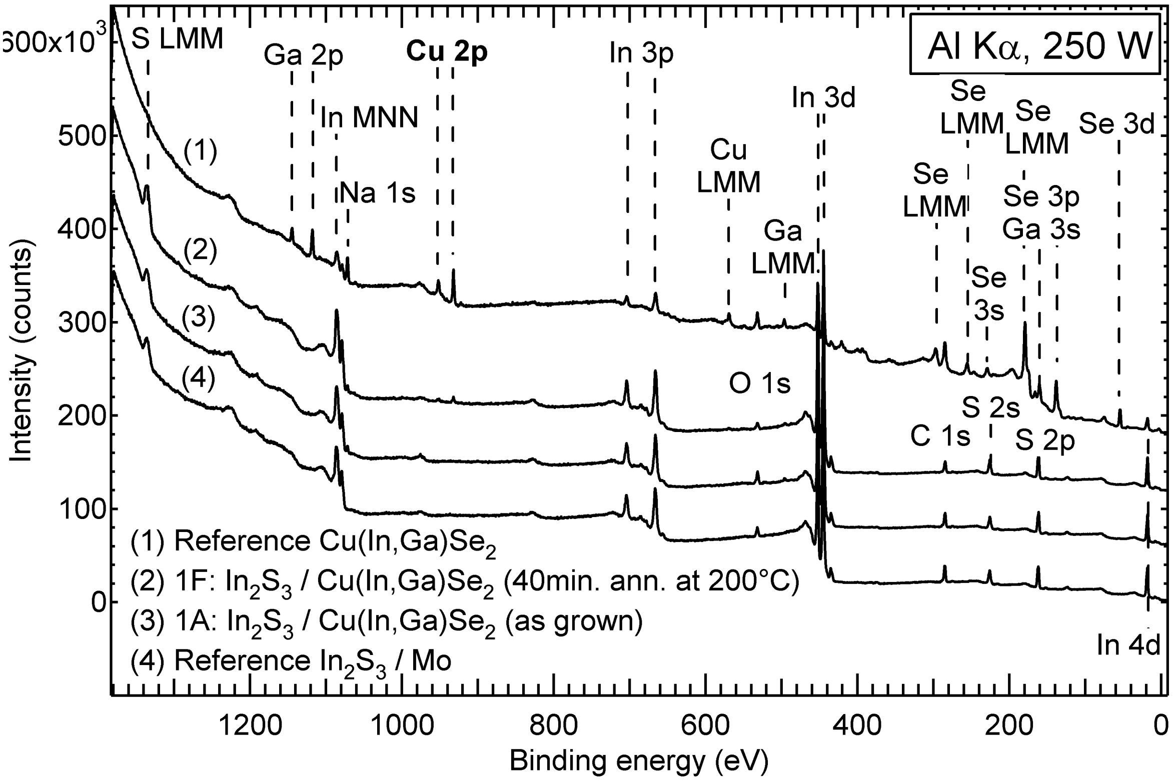

Figure 6.8: XPS overview spectra of the reference samples and sample 1A and 1F. Spectra have been shifted vertically for a better comparison.

surface increases for samples that had been annealed for longer times. This is even better illustrated, if the ratio of the integrated peak intensity of the Cu 2p and In 3d peak is plotted against the annealing time (Fig. 6.10). This ratio is directly proportional to the Cu concentration at the In$_2$S$_3$ surface if the In concentration is considered constant. The Cu concentration is clearly increasing for the samples that had been annealed for longer times. The slope of the intensity ratio corresponding to the Cu concentration at the surface decreases for longer annealing times, indicating a saturation of the Cu concentration after prolonged annealing times. However, the saturation level had not been reached in this experiment yet. Apart from the datapoint at 80 min. annealing time, the datapoint follow a smooth curve with low scattering, indicating a good reproducibility of the annealing process. In the following, the quantification of the Cu concentration at the In$_2$S$_3$ surface will be evaluated for the in-situ annaling of an equivalent sample.

6.2.3 Set (2): Sample with In-Situ Annealing

In this experiment, the annealing is not carried out ex-situ with different samples, but in-situ while measuring the XPS intensity on the same sample. This way, sample to sample scattering can be eliminated, as the Cu concentration at the surface can be determined for one and the same sample during the annealing. However, the temperature calibration in

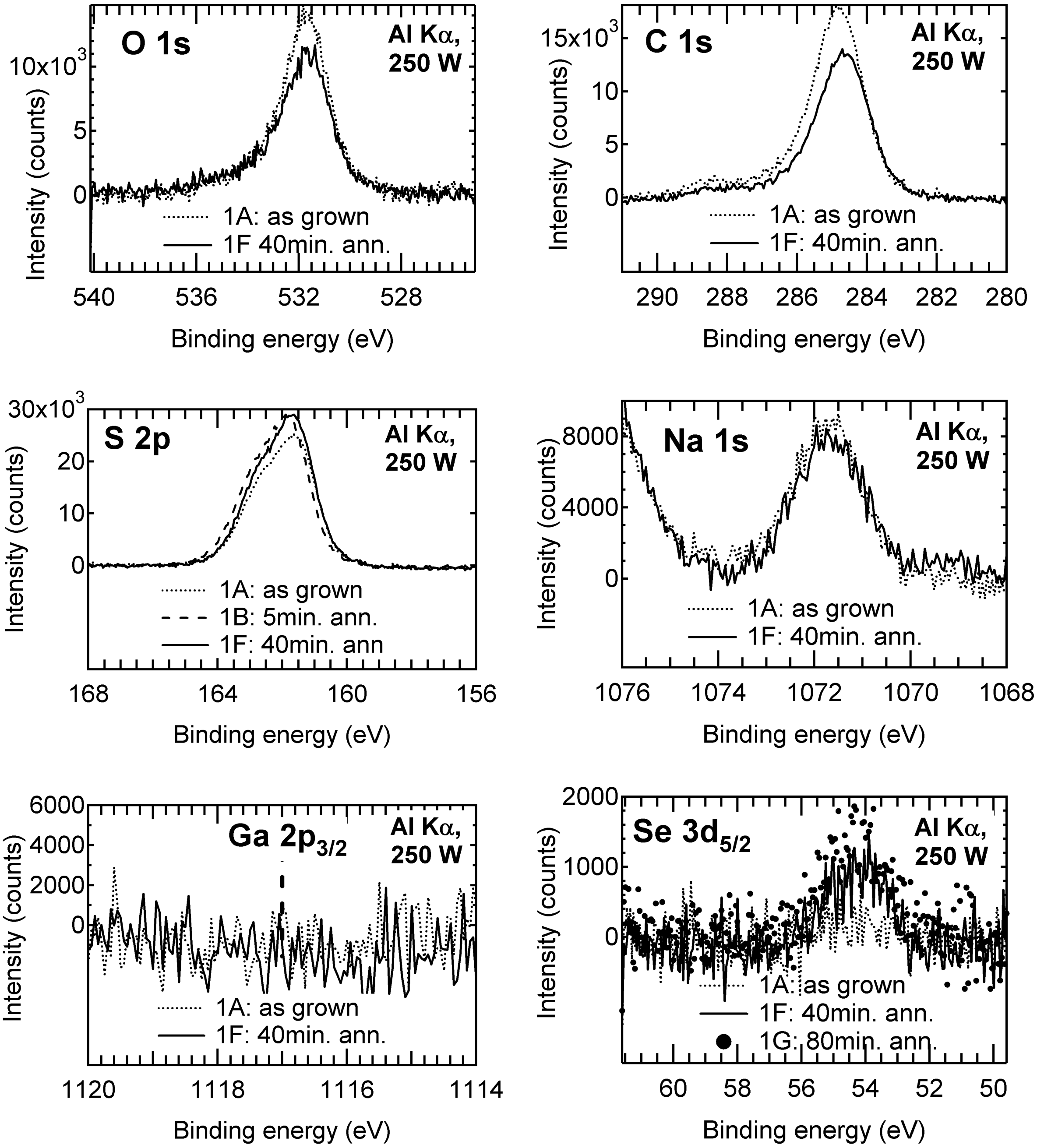

Figure 6.9: XPS detail spectra of sample 1A (as grown) and sample 1F (40min. annealed at 200 °C). A linear background has been subtracted from the spectra. Spectra recorded for sample 1B and 1G have appended to the graphs showing the S 2p and Se 3 d$_{5/2}$ XPS spectra, respectively.

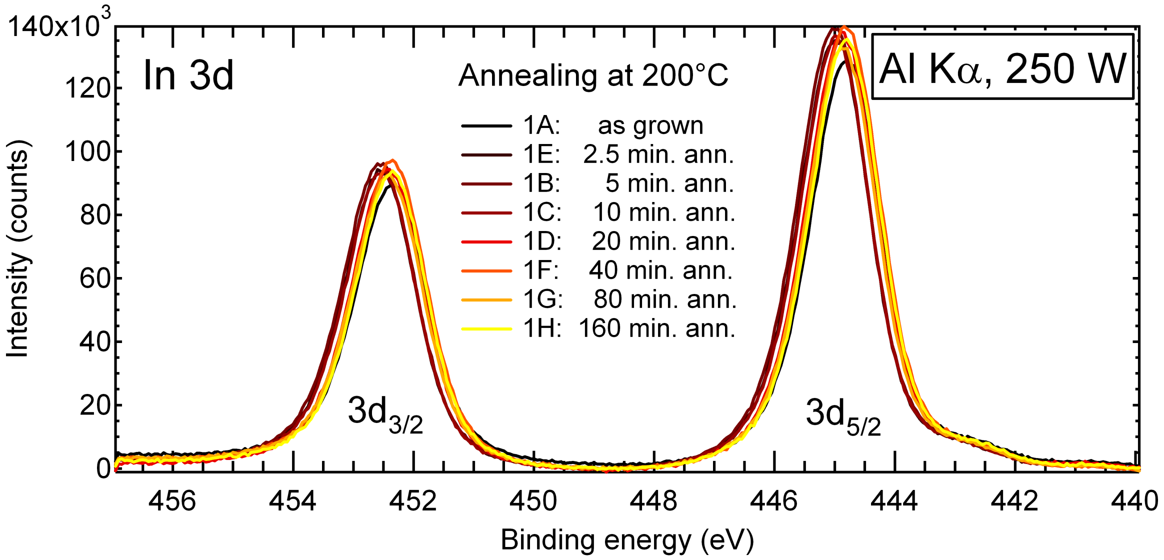

Figure 6.10: XPS In 3d spectra of the as grown and annealed In_2S_3/Cu(In,Ga)Se_2 samples. The In 3 d peak intensity is not significantly altered during the annealing. The slight increase (<7%) after the annealing can be attributed to the evaporation of C, O containing surface contaminants.

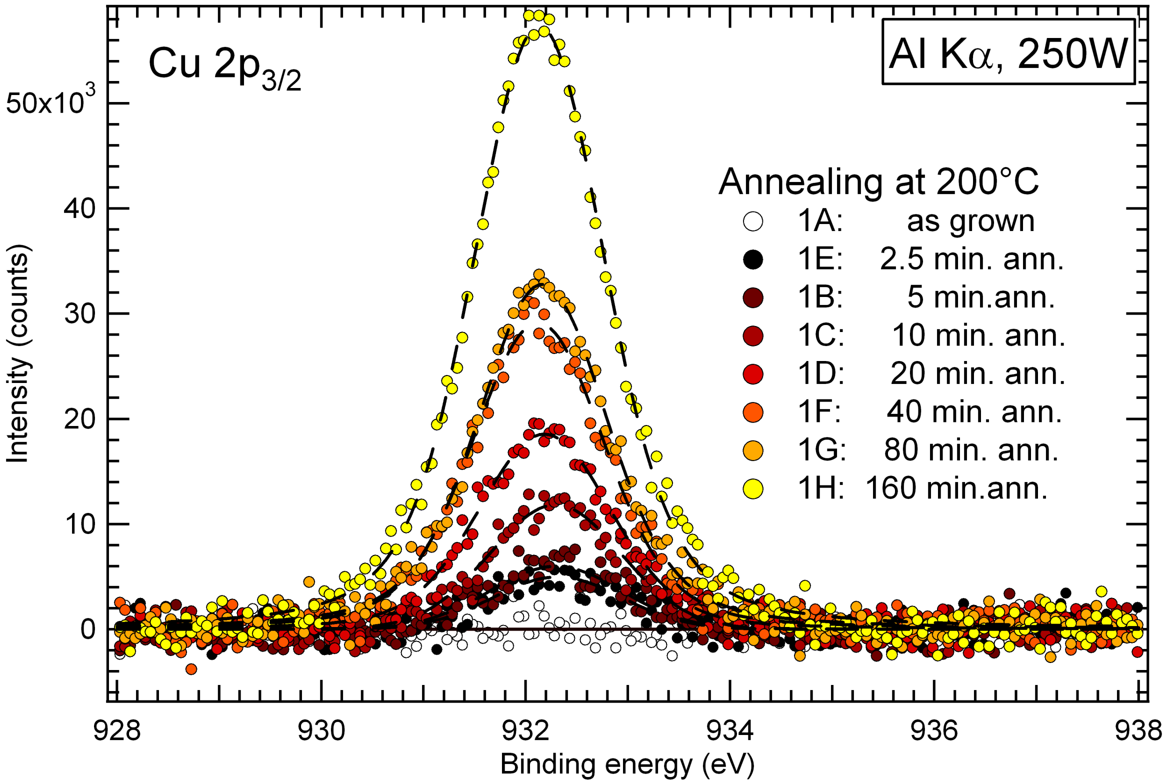

Figure 6.11: XPS Cu $2p_{3/2}$ spectra of the same samples as presented in Fig. 6.10. The Cu $2p_{3/2}$ peak intensity increases for longer annealing times as a result of the Cu diffusion into In_2S_3 buffer layer.

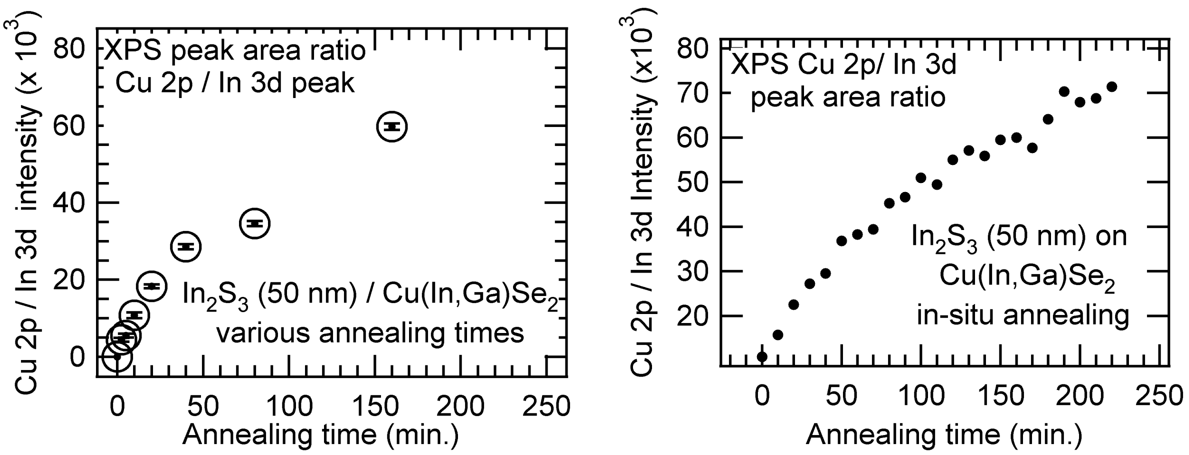

Figure 6.12: Ratio of Cu 2p$_{3/2}$/ In 3d$_{5/2}$ peak intensity at the In$_2$S$_3$ surface as a function of the annealing time for various samples consisting of In$_2$S$_3$ (50 nm) / Cu(In,Ga)Se$_2$. Left: Sample series for set (1), different samples annealed ex-situ for various annealing times. Right: Sample set (2), a sample measured during in-situ annealing in the XPS analytic chamber.

this in-situ heating setup is not well calibrated. The temperature is in this case only given for a thermocouple at the substrate holder and the actual temperature of the sample surface might be considerably less. The experiment was therefore conducted in the following way: The sample for this experiment was prepared identically to the samples in the last section ((50)nm thick In$_2$S$_3$ layer deposited onto a standard absorber). Sample size was 2.5 cm×2.5 cm. The sample was introduced into the CISSY UHV chamber and an overview and the In 3d$_{5/2}$ and Cu 2p$_{3/2}$ peaks were recorded.

The sample was then heated on the sample holder until the Cu 2p$_{3/2}$ peak increased above noise level. A thermocouple located at the sample holder showed a temperature of 250 °C at this point. The temperature was now kept constant for the rest of the experiment. Cu 2p$_{3/2}$ spectra were recorded every 10 min. up to a total annealing time of 220 min. In 3d$_{5/2}$ spectra measured at the start, end and during the annealing showed no systematic or significant change in peak intensity (differences between different measurements were $< 0.5\%$). As a result of the uncertainty in the annealing temperature, this experiment will not be directly comparable to the experiments conducted at annealing temperatures of 200 °C, though the general trend should be the same.

Fig. 6.12 (right) shows the ratio of the Cu 2p/In 3d peak intensities for this sample as a function of the annealing time. The comparison with the sample set (1), conducted with various samples that were ex-situ annealed for different annealing times, shows an excellent agreement between the two sample sets. This is another proof for the good reproducibility of the annealing.

For both sample sets, the solubility limit of Cu in In$_2$S$_3$ had not been reached yet, for example in the case of the sample set (2) the increase in the intensity ratio was still $\approx 5\,\%$ during between 200 min. and 220 min. of annealing time. However, the slope of the intensity ratio has considerably decreased indicating the existence of a saturation level also in this case.

The peak intensity ratios can be further evaluated in terms of a absolute Cu concen-

Table 6.2: Binding energy, photo-ionisation cross-section σ, inelastic mean free path $IMFP$ and normalised spectrometer transmission function TF used for the the evaluation of XPS data directly from Eq. A.6.

Line	Binding energy(eV) [111],[107]	σ (Mbarns) [112]	$IMFP$ (nm) [104]	TF [113]
In $3d_{5/2}$	445.6	0.3098	2.20	0.91
Cu $2p_{3/2}$	931.9	0.3438	1.38	1.02

tration at the In_2S_3 surface, if the In and S concentration at the surface are considered constant. Following the analysis outlined in Annex A.2.2, the concentration ratio of Cu to In at the surface is given by (Eq. A.8):

$$\frac{c_{Cu}}{c_{In}} = \frac{I_{Cu}/S_{Cu}}{I_{In}/S_{In}},$$

where c_i are the elemental concentrations, I_i are the measured intensities of the considered XPS emission lines, S_i are the corresponding sensitivity factors and the index ($I=$ Cu, In) refers to the Cu and In, respectively. There are two ways two obtain the involved sensitivity factors; either in an experimental approach involving the measurement of suitable references or in a theoretical/ semi-empirical approach involving the calculation of the sensitivity factors directly from the photoionisation cross section, inelastic mean free path and transmission function of the electron analyser (see Annex A.2.2 for details).

In the given experiment, the Cu 2 p and In 3d peak intensity of the bare absorber that was measured at the beginning could be used as references, if the composition of this sample was known. However, for the reference samples only the bulk concentration is known (concentration ratio of Cu / (In+Ga) = 0.79). A severe Cu depletion at the surface near region of Cu-poor $Cu(In,Ga)Se_2$ samples has been postulated in the past by various authors (see e.g. Schmid et al. [109], Liao et al. [110]). The measured Cu concentration that is probed at the surface in the XPS measurement of the bare absorber is therefore not exactly known and most likely lower than the actual bulk concentration. For this reason, in the evaluation of the data, the sensitivity factors will be derived from tabulated data for the photo-ionisation cross sections of the involved energy levels, the inelastic mean free paths, and the analyser transmission function. The values used for this evaluation are tabulated in Table 6.2, a more detailed description of the analysis of XPS measurements can be found in Appendix A.2.2.

With these data the absolute Cu concentration at the In_2S_3 surface can be estimated, if a constant S/In ratio of 1.5 is assumed. For the highest Cu concentration measured after 220 min. in the in-situ annealing measurement (Fig. 6.12, right part) the Cu concentration at the In_2S_3 surface amounts to (4±2) at.%. As was stated above, at this point the saturation limit was not yet reached.

6.3 Cu Distribution in the In$_2$S$_3$ Layer

The aim of this section is the resolution of the Cu distribution profile inside the In$_2$S$_3$ layer after the annealing. As has been shown in the previous sections, Cu diffuses rapidly into the In$_2$S$_3$ at moderate temperatures around 200 °C. In this section, the Cu diffusion from the Cu(In,Ga)Se$_2$ substrate into a 250 nm thick In$_2$S$_3$ layer will be examined by energy dispersive X-ray spectroscopy (EDX) in combination with a transmission electron microscope (TEM). The Cu distribution profile may offer more details on the diffusion process, e.g. information about the involved diffusion constant.

When considering the diffusion of Cu in In$_2$S$_3$, several questions arise:

- Is there a solubility limit for Cu in In$_2$S$_3$?
- How does the thickness of the In$_2$S$_3$ layer compare to the involved diffusion length, does the Cu diffuse through the whole layer or is there a pronounced gradient of the Cu concentration through the layer?

If the Cu concentration is limited by the diffusion of Cu inside the In$_2$S$_3$, the diffusion length is small compared to the layer thickness and the Cu(In,Ga)Se$_2$ layer is taken as an infinite Cu source supplying a constant Cu concentration c_0 at the interface, one would expect an concentration profile $c(x)$ inside the In$_2$S$_3$ layer corresponding to (Jost, [114]):

$$c(x) = c_0 \left\{ 1 - \operatorname{erf}\left(\frac{x}{L}\right) \right\} . \tag{6.1}$$

Here x is the distance from the interface, L is the diffusion length and erf is the error function. Fig. 6.13 shows the idealised concentration profile for three different diffusion lengths for the discussed boundary conditions.

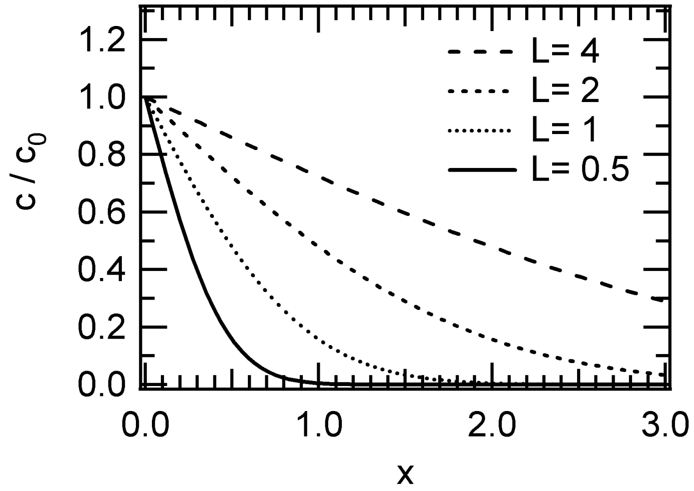

Figure 6.13: Idealised diffusion profile for a semi-infinite layer and an infinite source supplying a concentration c_0 at the surface at x=0.

The aim of this section is the investigation of the distribution of Cu atoms inside the In_2S_3 layer after annealing, i.e. the gradient of the Cu concentration through the layer. With the aim to increase the ratio between layer thickness d / diffusion length L, the nominal layer thickness is increased to 250 nm.

6.3.1 Sample Preparation

A (250±30) nm thick layer of In_2S_3 was deposited onto a standard absorber substrate ($Cu(In,Ga)Se_2$/Mo/glass) and the sample broken into two pieces. One piece was prepared directly (I: as grown) and the other subjected to an annealing step for 35 min. at 200 °C in air on a hot plate (II: annealed). The TEM preparation was the same for both samples. The TEM preparation consisted of cutting the sample in two pieces with dimensions approximately 2 mm×3 mm, which were glued face to face with epoxy glue. Subsequently the specimen were cut into slices perpendicular to the interface plane with approximately 0.5 mm thickness. The slices were first mechanically thinned with polishing discs (grit size 0.1 μm) to a thickness of approximately 10 μm and then ion-milled with Ar^+-ions under an incident angle of 6°. Final sample thickness for the TEM samples was approximately 50-100 nm.

6.3.2 Cu Distribution in In_2S_3 Resolved by EDX Linescans

For each sample, several cross-sectional TEM micrographs were recorded at different positions in TEM bright field mode (See section A.1.2 for more details) with an acceleration voltage of 200 kV. In STEM mode, EDX line scans were recorded perpendicular to the In_2S_3/ $Cu(In,Ga)Se_2$ interface. Fig. 6.14 shows the TEM micrographs of sample (I: as grown) and (II: annealed), respectively. The micrographs show the homogeneous coverage of the absorber by In_2S_3 and do not reveal any structural changes during the annealing. The positions of the EDX line scans are marked with arrows in the corresponding micrographs and plotted in Fig. 6.15 (I: as grown) and Fig. 6.16 (II: annealed). In these graphs the net counts of the EDX line scans are displayed.

The EDX line scan of sample (I:as grown) starts at the left hand side at the In_2S_3 surface. Inside the In_2S_3 layer only In and S peaks are present. After a scanning distance of approximately 300 nm the scan reaches the interface, the S signal disappears and Cu, Ga, In, Se signals appear at the $Cu(In,Ga)Se_2$ side of the layer stack. No Cu is found in the In_2S_3 side of the as grown layer stack, as was confirmed already in the last section. In the annealed sample however, a distinct Cu signal is detected throughout the whole In_2S_3 layer. The EDX Cu net counts are constant in this part, i.e. there is no Cu gradient found over the whole In_2S_3 layer thickness. No apparent further interdiffusion effects were found, e.g. no In, Ga, Se or S diffused across the interface in a detectable amount. No Cu depletion in the $Cu(In,Ga)Se_2$ interface near region was detected neither.

The EDX measurements confirm the results of the last section and provide a second proof of the pronounced diffusion of Cu into In_2S_3 at a temperature of 200 °C. No gradient was found in the Cu distribution inside the In_2S_3 layer. If the diffusion is assumed to be limited by the diffusion inside the In_2S_3 and not by the flux of Cu atoms through the interface, the constant Cu distribution indicates a solubility limit of Cu in the In_2S_3 layer.

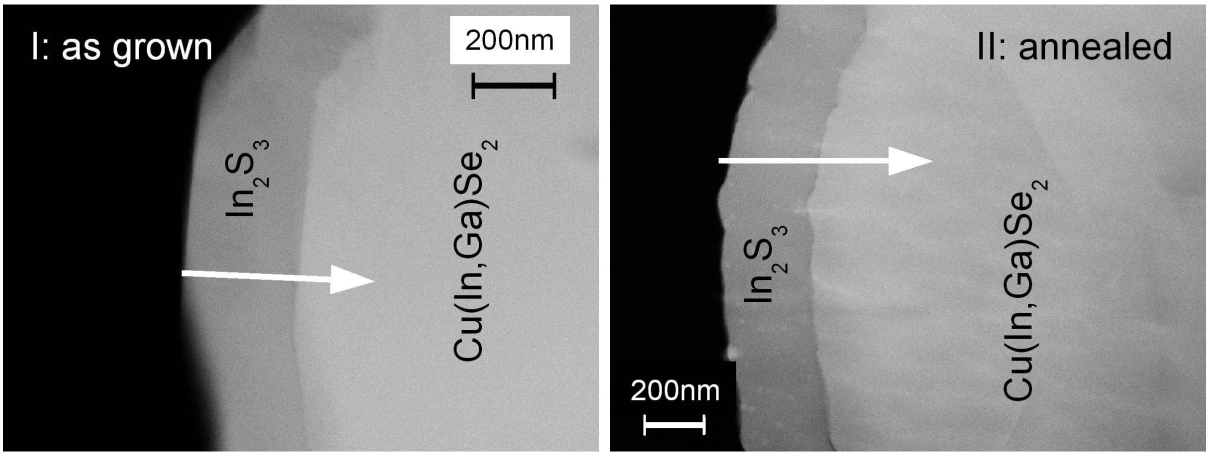

Figure 6.14: TEM micrographs of the In$_2$S$_3$/Cu(In,Ga)Se$_2$ layer stack. Left: without annealing (I: as grown). Right: after 35 min. annealing at 200 °C (II: annealed). The arrows mark the position of the corresponding EDX line scans.

The constant Cu amount can then be taken as an upper limit for the solubility of Cu in In$_2$S$_3$. The Cu/In concentration ratio c_{Cu}/c_{In} can be calculated from the EDX intensities $I_{Cu,In}$ under the thin film approximation (see for details on the EDX method and restrictions of the quantification Section A.2.1.):

$$\frac{c_{Cu}}{c_{In}} = k\frac{I_{Cu}}{I_{In}} \tag{6.2}$$

An experimental reference for the k-factor is found in the EDX linescans itself, as the ratio c_{Cu}/c_{In} is determined by XRF for each absorber batch in a standard routine and is therefore known for the Cu(In,Ga)Se$_2$ side of the sample: c_{Cu}/c_{In}= (1.25±0.13). Combined with the averaged measured Cu and In intensity ratios on the Cu(In,Ga)Se$_2$ side this gives an k-factor of k=(1.4±0.2). It is now possible to plot the Cu/In concentration ratio for the two samples, which is done in Fig. 6.17. In this graph, a thin dotted line is added which marks the average Cu/In concentration ratio of (0.24±0.03) inside the In$_2$S$_3$ layer.

The saturation level of Cu in In$_2$S$_3$ is therefore reached at an approximated Cu/In ratio of (0.24±0.03). With an constant S/In ratio of 1.5 this corresponds to ≈ (9±2) at.% Cu in total in the In$_2$S$_3$ layer after the annealing. Grazing incidence X-ray diffraction patterns recorded for the two presented samples did only show Bragg peaks that could be assigned to the Cu(In,Ga)Se$_2$ and In$_2$S$_3$ phases. However, the detection of possibly formed new Cu-containing phases is hindered by the superposition with Cu(In,Ga)Se$_2$ and In$_2$S$_3$ XRD reflections and low count rates due to the small film thickness involved and the small incidence angles necessary.

The presented experiments enable an approximation of the saturation level of Cu in the In$_2$S$_3$ ((9±2) at.%) and the derivation of an upper bound for the diffusion length $L > 250$ nm (for t=35 min. and T=200 °C). As no Cu gradient was found for this sample, the information on the diffusion process is limited. Still, combining these data with the data on the Cu concentration at the In$_2$S$_3$ surface derived in the previous section, a model

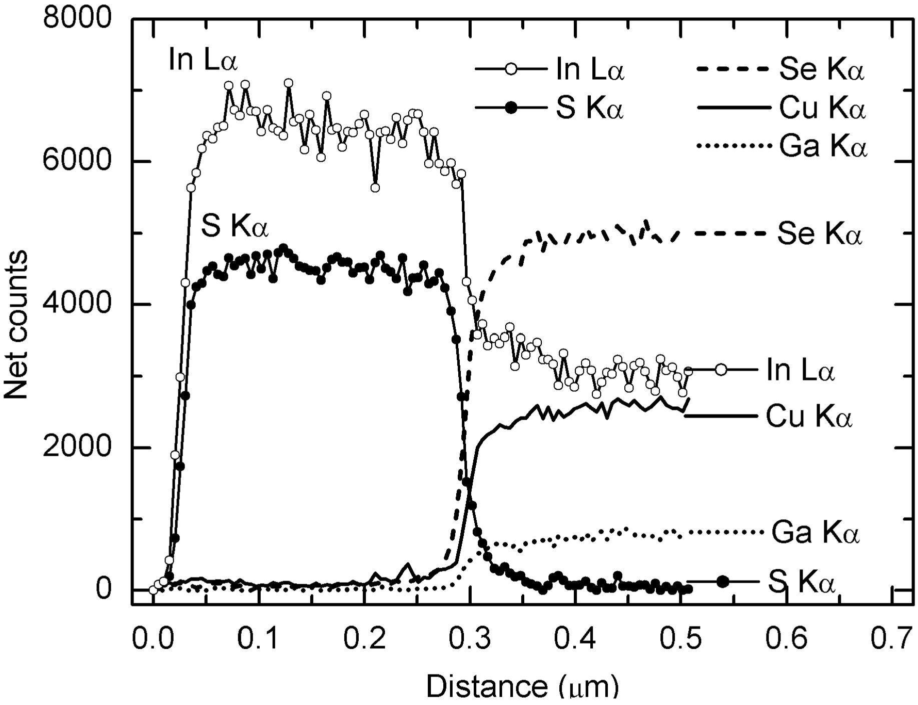

Figure 6.15: EDX line scan showing the elemental distribution profile of the In_2S_3/Cu(In,Ga)Se_2 sample I: as grown, corresponding to the micrograph presented in Fig. 6.14 (left).

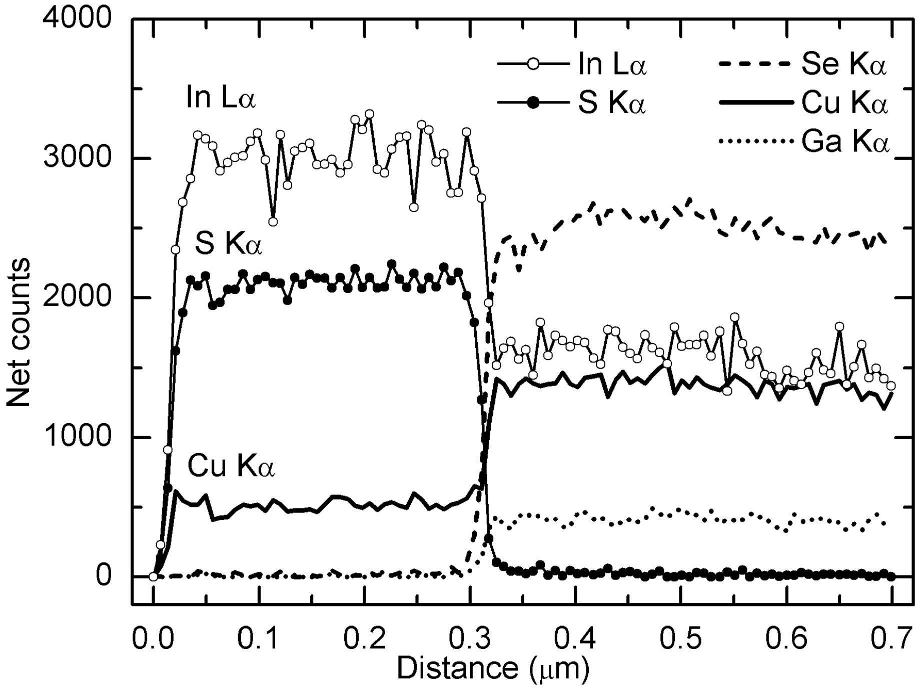

Figure 6.16: EDX line scan showing the elemental distribution profile of the In_2S_3/Cu(In,Ga)Se_2 sample II: annealed, corresponding to the micrograph presented in Fig. 6.14 (right).

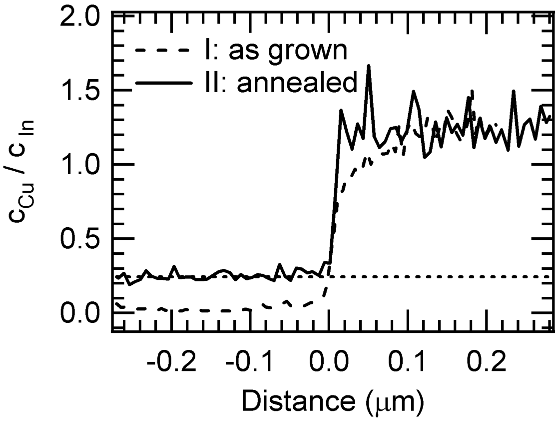

Figure 6.17: Cu/In ratio as calculated from the EDX scans plotted versus the distance from the interface. The saturation level inside the In_2S_3 side of the annealed sample corresponds to Cu/In=(0.24±0.03).

describing the Cu diffusion in the In_2S_3 layer will be proposed in Section 6.5.

6.4 Discussion of the Results

The experiments conducted on four different sample sets with three different methods evidenced a pronounced Cu diffusion in the range of 4-9 at.% from $Cu(In,Ga)Se_2$ into the In_2S_3 layer at temperatures of approximately 200 °C. In the following the main results of the previous sections will be shortly summarised and discussed. On the basis of the experimental results a diffusion model for the Cu diffusion into In_2S_3 layers will be proposed.

In all experiments, layered stacks of thermally evaporated In_2S_3 on top of standard $Cu(In,Ga)Se_2$ absorbers have been used. In the preparation conditions used for the thermal evaporation of In_2S_3 in this work, the sample was not actively heated and stayed below 50 °C in all experiments. No Cu was found in the In_2S_3 layer in the as grown sample. It is therefore assumed that Cu diffusion at room temperature is not significant compared to the diffusion during annealing.

1. In the HIKE experiments, the integral Cu 2p signal from a thin In_2S_3 (20 nm) could be probed. A sharp increase of the Cu signal for temperatures above approximately 200 °C was found.

2. For the two sets of XPS measurements, the Cu concentration at the In_2S_3 surface was found to increase as a function of the annealing time. After 220 min. annealing at an approximate temperature of 200 °C the Cu diffusion had not come to an end and a Cu concentration of approximately (4±2) at.% was detected.

3. The aim of the EDX/TEM measurements was the determination of the local distribution of Cu in the In_2S_3 layer. After an annealing time of 35 min. at 200 °C, a constant Cu concentration of (9±2) at.% was found through the whole In_2S_3 layer with thickness d=250 nm.

All experiments show a clear diffusion of Cu into In_2S_3 and indicate the existence of a limit for the diffusion, i.e. a solubility limit for the Cu diffusion. This can be understood if the crystal structure of In_2S_3 is considered. As presented in detail in Section 4.1, the crystal structure of In_2S_3 is best described as a defect-type spinel. In this presentation, In_2S_3 can be described by the quasi-quaternary compound formula $[In_{2/3}\square_{1/3}]^{Th}[In]_2^{Oh}\,S_4$, where $[\;]^{Th}$ and $[\;]^{Oh}$ denote tetrahedral and octahedral sites in the spinel structure and $\square$ the vacancies.

Cu can occupy the vacancies or In sites in this structure and Py et al. [115] have shown the existence of a solid-solution range for compositions in the range between In_2S_3 and $CuIn_5S_8$. $CuIn_5S_8$ has a spinel-type structure very similar to In_2S_3, in which the vacancies and some In sites are filled with Cu atoms. The structure of $CuIn_5S_8$ can be described in the quasi-quaternary description as $[In_{1/2}\,Cu_{1/2}]^{Th}[In]_2^{Oh}\,S_4$. The spacegroup of $CuIn_5S_8$ is $F\bar{4}3m$ with lattice constant a_0=10.686Å, (Gastaldi et al. [116]).

The composition of $CuIn_5S_8$ corresponds to a Cu concentration of approximately 7.1 at.%. Considering the solid-solution range and the defect-type crystal structures of In_2S_3 and $CuIn_5S_8$, an incorporation of Cu into the In_2S_3 layer up to a Cu concentration of 7.1 at.% can thereofore be explained without a reordering of the sulphur sublattice. As can be seen by comparing the quasi-quaternary compound formulas for In_2S_3 and $CuIn_5S_8$, there are less In atoms present in tetrahedral sites in the $CuIn_5S_8$ than in In_2S_3 ((1/2) as compared to (2/3)). Apart from the diffusion of Cu into the In_2S_3, a diffusion of In into the Cu(In,Ga)Se_2 is therefore required for the complete transformation of In_2S_3 into $CuIn_5S_8$. This is difficult to resolve experimentally due to the small relative change in the total In concentration.

The difference in the experiments concerning the Cu diffusion in this chapter lie in the different diffusion kinetics. For one sample with a 250 nm thick In_2S_3 layer the diffusion was completed already after 35 min. of annealing at 200 °C. For the samples with a 50 nm thick In_2S_3 layer presented in Section 6.2, diffusion had not reached saturation even after 160-220 min. at comparable temperatures. The following considerations will suggest explanations for this fact.

The ex-situ annealed XPS samples and the TEM/EDX sample were heated at nominally the same temperature but in different ovens. Differences in the temperature calibration of the used ovens might have led to faster/slower diffusion processes, although it is unlikely that the temperature difference accounted for more than 10 °C.

The differences were observed on separate samples prepared on similar absorbers. The absorbers were all prepared with the standard three-stage absorber deposition process described in Section 2.2. However, samples vary slightly from batch to batch in their total and surface composition. For these samples, the absorber substrates used for the XPS measurements were relatively Cu-poor (composition ratio of Cu/(In+Ga)= 0.79), while the absorber used in the EDX/TEM measurements had a composition ratio of Cu/(In+Ga)= 0.85. A lower Cu concentration in the absorber and especially a potentially lower surface composition of the absorber most likely decreases the Cu diffusion into the In_2S_3. A future investigation of this could be conducted with similar diffusion experiments on a series of In_2S_3 Cu(In,Ga)Se_2 samples prepared with absorbers ranging from Cu-poor to Cu-rich Cu(In,Ga)Se_2 in order to examine the effect of the Cu concentration on the Cu diffusion in detail.

Sodium was found on the surface of the In_2S_3 layer for several samples. It has been shown, that Na can occupy the vacancies in the In_2S_3 structure in competition to the Cu (Lafond et al, [117]), hindering the Cu diffusion into the In_2S_3. A different amount of Na at the absorber surface might therefore also lead to a changing diffusion behaviour.

Finally the crystal structure and microstructure of the In_2S_3 film might influence the Cu diffusion. In this sense, very small grain sizes or even an amorphous-like In_2S_3 thin film might have different diffusion properties than an In_2S_3 thin film with large crystal grains. It has been shown in Section 4.2.4, that In_2S_3 films may exhibit different crystallinity, i.e. in terms of the width and intensity of the X-ray diffraction peaks. This crystallinity was also shown to change during the annealing and might have an effect on the varying diffusion kinetics.

The Cu diffusion could be shown for all presented samples. The kinetics of the diffusion were found to vary for different samples and for an exact determination of the involved diffusion parameters more experimental data would be needed.

6.5 Model for the Cu Diffusion

Based on the results and considerations presented above, a model is proposed explaining the diffusion behaviour of the Cu from the Cu(In,Ga)Se_2 into the In_2S_3. In the following, the change in the In and S concentration will be considered small compared to the difference in the Cu concentration and S to In concentration ratio will be assumed to be 1.5 in the In_2S_3 layer.

The presented model will be based on the following assumptions:

1. The concentration is considered constant in y- and z-direction and only the concentration profile in x-direction (parallel to the sample surface normal) is considered. The origin is set to be at the In_2S_3 surface and the In_2S_3/ Cu(In,Ga)Se_2 interface at $x = d$.

2. The diffusion constant is assumed to be constant in x and to not depend on the concentration.

3. There exists an solubility limit for the diffusion of Cu into In_2S_3. For temperatures up to 200 °C the solubility limit c_0 is assumed to be approximately 7.1 at.%, following the considerations concerning the solid-solution range between In_2S_3 and $CuIn_5S_8$. This corresponds to a Cu/In ratio of aproximately 0.2.

4. The Cu(In,Ga)Se_2 can be considered as an infinite source of Cu. The surface to the Cu(In,Ga)Se_2 is therefore fixed at the solubility limit c_0: $\Rightarrow c(d,t) = c_0$.

5. The surface at $x = 0$ implies that no Cu atoms will diffuse through this boundary, the flux j_{Cu} being zero at this point: $\Rightarrow j_{Cu}(0,t) = \frac{\partial}{\partial x} c(l,t) = 0$.

6. There is no Cu in the buffer prior to the annealing: $\Rightarrow c(x,0) = 0$ for x< d.

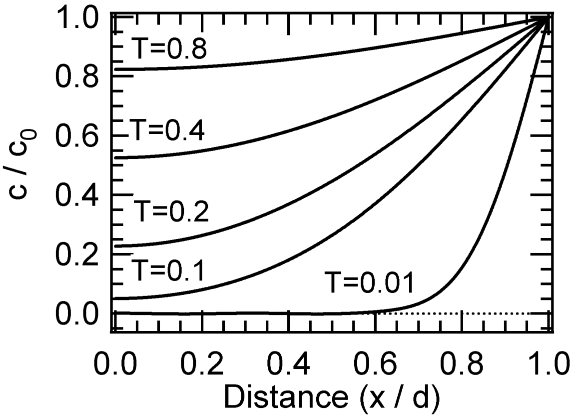

Figure 6.18: Concentration profile c/c_0 for a finite thin layer with boundaries at $x = 0$ and $x = d$ and a constant surface concentration c_0 at ($x = d$). The model and boundary conditions for this case are formulated in the text.

The diffusion in solids is described by the diffusion equation [114]:

$$\frac{\partial}{\partial t} c_A(x,t) = D \frac{\partial^2}{\partial x^2} c_A(x,t). \tag{6.3}$$

Here, c_A is the concentration of the diffusing species A and D is the diffusion coefficient.

The theory of diffusion and solutions of this differential equation can be found in various textbooks. For the following derivation references [114], [118] and [119] have been used. Considering the boundary conditions as stated above in the assumptions, the differential diffusion equation for the Cu diffusion into the In_2S_3 can be solved and gives the concentration as a function of time and space (adapted from [119]):

$$c(x,t)/c_0 = 1 - \frac{4}{\pi} \sum_{n=0}^{\infty} \frac{(-1)^n}{2n+1} \exp\left\{-D(2n+1)^2\pi^2 t/4d^2\right\} \cos\frac{(2n+1)\pi x}{2d} \tag{6.4}$$

A numerical solution of this infinite series is plotted in Fig. 6.18. Here, the dimensionless parameters $T = Dt/d^2$ and $X = x/d$ have been introduced. The function describing the increase of the Cu concentration at the surface $x = 0$ for increasing time is then given by:

$$c(0,t) = 1 - \frac{4}{\pi} \sum_{n=0}^{\infty} \frac{(-1)^n}{2n+1} \exp\left\{-D(2n+1)^2\pi^2 t/4d^2\right\} \tag{6.5}$$

This function is plotted in Fig. 6.19 for the generalised parameter T.

With this model the surface concentrations obtained from the XPS experiments can now be correlated with the model and the diffusion constant and solubility limit estimated by a fit of the data to Eq. 6.5. For $T > 0.1$ ($c/c_0 > 0.05$) the infinite series converges rapidly and it is sufficient to consider only the first two terms of the series (error $< 1\%$).

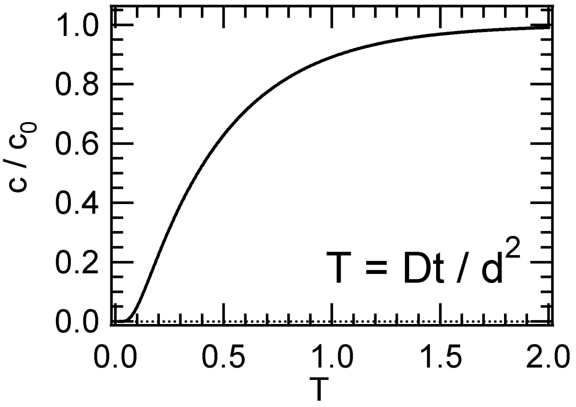

Figure 6.19: Evolution of the concentration c/c_0 at the surface ($x = 0$) with increasing $T = (Dt/d^2)$ for the case of constant surface concentration at $x = d$ and the sample boundary at $x = 0$ as described in the text.

The surface concentration ratio of Cu/In atoms as calculated from the XPS in-situ heating measurement is plotted in Fig. 6.20. A fit according to the function presented in Eq. 6.5 is added to the graph. The fits corresponds to a saturation limit for the Cu/In concentration ratio of $c_0 =$ $(0.11{\pm}0.03)$ and a diffusion constant in the order of $1{\times}10^{-15}$cm^2/s. For a constant In/S concentration this gives a total saturated copper concentration of approximately (4±2) at.%. A similar diffusion constant in the order of $1{\times}10^{-15}$cm^2/s to $1{\times}10^{-16}$cm^2/s was estimated by Abou-Ras from the evaluation of elemental distribution profiles for In$_2$S$_3$ layers on Cu(In,Ga)Se$_2$, where the In$_2$S$_3$ layers had been grown by atomic layer deposition at elevated substrate temperatures ranging from 170 °C to 240 °C [120].

For the EDX measurement, the saturation limit is given by the constant concentration after the annealing, which was estimated to (9±2) at.% . The diffusion constant can not be calculated from this experiment, but may be estimated considering that the diffusion length L_{Cu}=$2\sqrt{Dt}$ was large compared to the In$_2$S$_3$ layer thickness, and consecuently L_{Cu}=$2\sqrt{Dt}$ $250\,nm$ and consecuently $D > 7{\times}10^{-14}$cm^2/s in this case.

Although the observed diffusion kinetics were found to be different, the estimated values for the solubility limit in the range 4 at.% to 9 at.% support the formulated thesis of an solubility limit of approximately 7 at.% Cu in the In$_2$S$_3$. Possible explanations concerning the observed differences in the time-scale of the diffusion have been discussed in the previous section.

It has to be noted, that the diffusion model implies a diffusion constant which is independent of the concentration. This assumption might be too simple especially in the vicinity of the solubility limit, where diffusion is expected to slow down. However, the good correlation between data and fit justifies the simple model, at least for the presented measured concentrations, which are estimated to be lower than 80 % of the saturation limit.

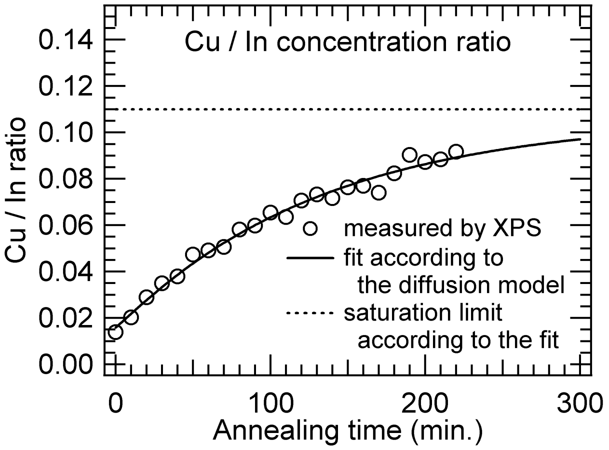

Figure 6.20: Surface concentration ratio c_{Cu}/c_{In} as calculated from the XPS measurements as a function of time during the in-situ annealing and a fit (continuous line) to the experimental data. The fit function is described in the text. The fit result gives a saturation limit of (0.11±0.03), which is displayed in the graph as a dotted line.

6.6 Summary

Sets of In_2S_3/ $Cu(In,Ga)Se_2$-bilayer structures have been analysed with respect to their elemental composition using different analysis techniques. For samples in the as-grown state, no Cu was found in the In_2S_3 layer. This fact enabled the detailed study of the diffusion phenomena observed during the annealing of the samples at temperatures in the order of 200 °C.

In the first part, the integral Cu signal was measured by probing the whole layer depth of a 20 nm thick In_2S_3 layer on top of $Cu(In,Ga)Se_2$ with High KInetic Energy X-ray photoelectron spectroscopy (HIKE). A sharp increase of the Cu $2p_{3/2}$ signal at temperatures just above 200 °C could be observed in a heating experiment with a temperature ramp up to 320 °C.

In the next step, the Cu concentration at the In_2S_3 surface was monitored with laboratory X-ray photoelectron spectroscopy (XPS) on samples with a 50 nm thick In_2S_3 layer on top of $Cu(In,Ga)Se_2$ substrates for samples annealed in-situ and ex-situ at approximately 200 °C. Upon annealing, an increasing Cu concentration of up to (4±2) at.% was observed at the In_2S_3 surface.

Finally the elemental distribution of the cross section of a In_2S_3(250 nm)/$Cu(In,Ga)Se_2$ stack was recorded before and after annealing for 35 min. at 200 °C with energy-dispersive X-ray spectroscopy (EDX) in combination with a transmission electron microscope. The EDX line scans revealed a constant Cu concentration of approximately (9±2) at.% throughout the entire In_2S_3 layer after annealing. No Cu was found in the In_2S_3 in the as-grown state.

The experimental results were discussed in the view of the crystal structure of In_2S_3 and the solid-solution to $CuIn_5S_8$. Different parameters were considered that might influence the Cu diffusion. On the basis of the obtained results a model was proposed, that describes the Cu diffusion from the $Cu(In,Ga)Se_2$ into the In_2S_3 layer.

Chapter 7

Record Cell Results, Discussion and Outlook

In this chapter, the results of the individual previous chapters will be combined and discussed. At the beginning, the best cell efficiencies obtained as a result of the optimisation processes outlined previously and the transfer to other Cu(In,Ga)Se_2 absorber types are presented. Then, the results from of the electronic solar cell characterisation and the diffusion experiments are reviewed and combined to provide a coherent explanation. Finally, an outlook will be given on how questions arisen as a result of this work may be resolved and on how Cu(In,Ga)Se_2 solar cells with an evaporated In_2S_3 may be further improved in the future.

7.1 Confirmed Cell Results

The utilisation of single phase, crystalline source material in combination with the developed buffer processing outlined in Section 5.1 led to new record efficiencies for Cu(In,Ga)Se_2 solar cells with an evaporated In_2S_3 buffer layer. To the authors knowledge, no higher efficiencies for chalcopyrite solar cells with other evaporated buffer layers have been reported so far, including reported efficiencies for evaporated CdS buffer layers (14.5 %, Rusu et al. [121]). The cell performance of a device with an evaporated In_2S_3 buffer showing high cell efficiencies has been independently confirmed. The device had a 50 nm thermally evaporated In_2S_3 buffer layer, deposited from powder PWD B on a standard absorber from the HZB absorber deposition process and was completed with the standard window and front contacts. After an annealing in air for 45 min. at a temperature of 200 °C, the short circuit current density was only 28.1 mA/cm^2 and MgF thin film (110 nm) was deposited on top of the device with the aim to decrease the reflection. The anti-reflection coating only slightly increased the short-circuit current density to 29.6 mA/cm^2 after the coating. The device showed an extremely high fill factor (76.0 %) and open circuit voltage (678 mV) and an efficiency of (15.3±0.2) % was measured at the HZB. The best cell of the corresponding CdS reference achieved an efficiency of (16.3±0.2) % (FF= 76.4, j_{SC} = 32.8 mA/cm^2, V_{OC}= 651 mV). The record efficiency of this In_2S_3 device has been independently confirmed at the Photovoltaic Calibration Laboratory at Fraunhofer Institut für Solare Energiesysteme

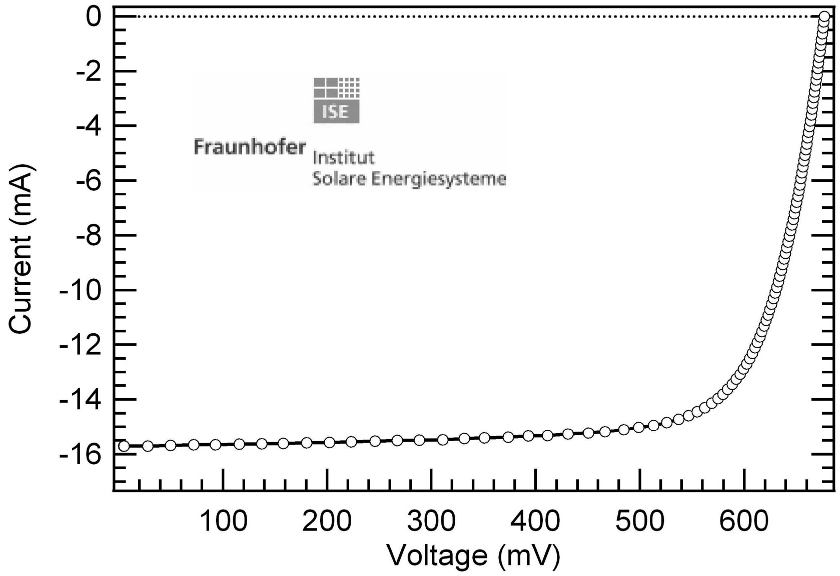

Figure 7.1: *IV*-curve under AM1.5 illumination of the record Cu(In,Ga)Se_2 device with an thermally evaporated (PVD) In_2S_3 buffer layer that was independently confirmed at the Fraunhofer ISE. The cell parameters are displayed in Table 7.1

Table 7.1: Record efficiency and cell parameters independently confirmed at the Fraunhofer ISE for a Cu(In,Ga)Se_2 device with thermally evaporated (PVD) In_2S_3 buffer corresponding to the *IV*-curve in Fig. 7.1. Cell area: 0.528 cm^2.

Absorber	Buffer	η (%)	FF (%)	j_{SC} (mA/cm^2)	V_{OC} (mV)
HZB	PVD In_2S_3	15.2	75.6	29.8	677

(Fraunhofer ISE), Freiburg, Germany. In Fig. 7.1 the IV-curve under illumination and the corresponding cell parameters are presented. Fig. 7.2 shows the corresponding quantum efficiency. A cell efficiency of 15.2±0.1 % has been established for this device by the Fraunhofer ISE (total area efficiency, area 0.528 cm^2), with the cell parameters tabulated in Table 7.1.

7.2 Transfer to Other Absorbers

7.2.1 Different Absorber Types

During the course of this work solar cells with evaporated In_2S_3 buffer layers have been prepared on Cu(In,Ga)Se_2 absorbers prepared at the Helmholtz-Zentrum Berlin (HZB). Here, the absorbers are deposited by a three stage process which is briefly introduced in Section 5.1 and in detail described by Kaufmann et al. in Ref.[12]. In order to demonstrate the suitability of the process also for other, similar absorber types, buffer layers have been applied additionally to Cu(In,Ga)Se_2 absorbers from an industrial pilot absorber

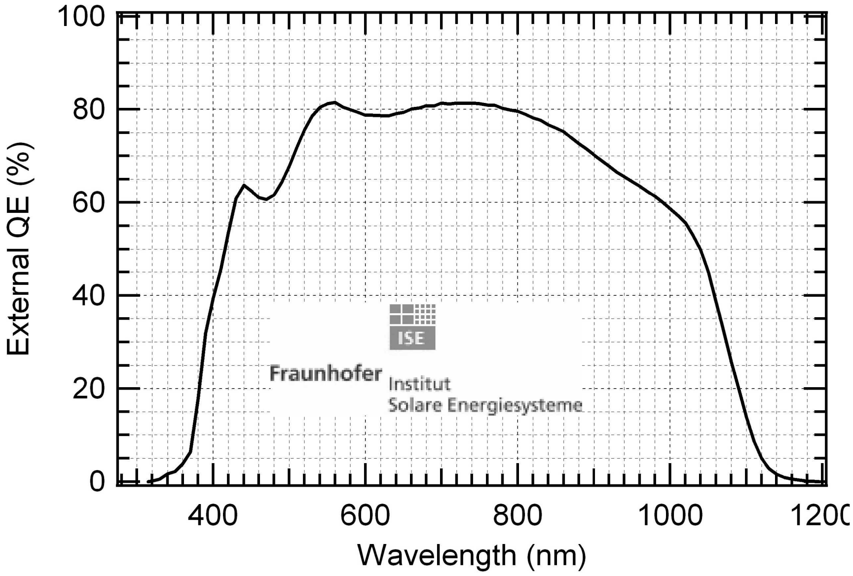

Figure 7.2: External quantum efficiency as measured at the Fraunhofer ISE for the record device with thermally evaporated In_2S_3 buffer displayed in Fig. 7.1.

line (Würth Solar GmbH & and Co KG, Schwäbisch Hall, Germany (Würth) [122],[89] and from the research laboratory at the Zentrum für Sonnenenergie- und Wasserstoff-Forschung, Stuttgart, Germany (ZSW) [123].

The best cell results, all achieved with source material PWD B, are presented together with their corresponding CdS references in Fig. 7.2 and Table 7.2. All three results have been obtained with devices annealed at 200 °C for 35-45 min. The efficiencies and short circuit current densities are presented with the total area of the device, as in the rest of this dissertation. Devices with In_2S_3 buffer layers obtained results comparable to the CdS references for all three absorber types, with an efficiency gap between In_2S_3 and CdS buffered devices in the range of 1-2 %. This is an indication for the quite universal feasibility of the buffer layer, e.g. it works for several similar absorber types and is not too sensitive to different absorber deposition methods and the corresponding variation of absorber surface conditions.

7.3 Discussion and Outlook

It is the intention of this section to review and combine the results obtained in the last chapters and give an outlook on how research can be stimulated by the results of this work.

The crystal structure of In_2S_3 was reviewed in detail at the beginning in Chapter 4. By measuring the X-ray diffraction of suitable reference samples the controversial literature data could be clarified. The details of the crystal structure of In_2S_3 were needed to identify suitable In_2S_3 source materials for the evaporation process as well as for the interpretation of the Cu diffusion in In_2S_3.

Solar cells have been found to significantly improve upon annealing at 200 °C, especially

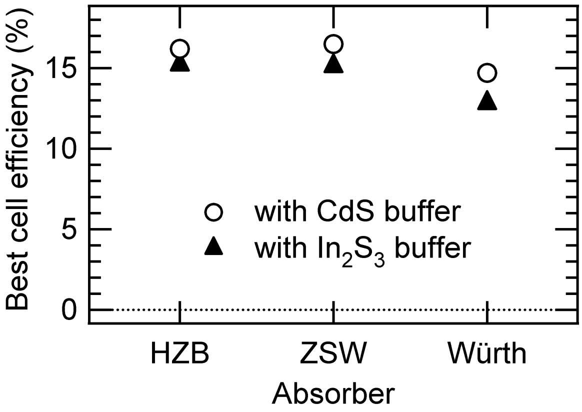

Figure 7.3: Best cell efficiencies obtained during the course of this work for annealed $Cu(In,Ga)Se_2$ devices with In_2S_3 buffer layers (triangles) and their corresponding CdS references (circles) for $Cu(In,Ga)Se_2$ absorbers from different laboratories. Würth: Würth Solar, ZSW: Zentrum für Solarenergie und Wasserstoff-Forschung, HZB: Helmholtz-Zentrum Berlin.

Table 7.2: Total area efficiencies and cell parameters for the best $Cu(In,Ga)Se_2$ solar cells (no anti-reflective coating) with evaporated (PVD) In_2S_3 buffer layers prepared during the course of this work with $Cu(In,Ga)Se_2$ absorbers provided by different laboratories (see also Fig. 7.3). The best reference cells from the same batches with CdS buffer layers are listed for comparison.

Absorber	Buffer	η (%) ±0.2 %	FF (%) ±0.2 %	j_{SC} (mA/cm^2) ±0.5 (mA/cm^2)	V_{OC} (mV) ±2mV
Würth	PVD In_2S_3	12.8	66.3	29.2	663
	CBD CdS	14.7	72.0	31.5	646
ZSW	PVD In_2S_3	15.1	68.5	33.2	664
	CBD CdS	16.5	71.2	34.7	663
HZB	PVD In_2S_3	15.4	72.7	33.7	628
	CBD CdS	16.2	74.4	34.0	639

in terms of their open circuit voltage and fill factor. The detailed analysis revealed a change in the recombination behaviour; From a mechanism with strong tunneling contribution associated with the buffer/absorber interface it changed to a recombination dominated by a mainly thermally activated recombination located in the space charge region. The latter dominant recombination mechanism is usual in highly efficient Cu(In,Ga)Se_2 devices with CdS buffer [94]. The short circuit current density decreased and as the quantum efficiency demonstrated these losses were mainly found in the longer wavelength part.

This can be understood, if a bandgap widening at the interface near region of the absorber is assumed. For an unchanged position of the Fermi level with respect to the conduction band (e.g. as a result of a pinning of the Fermi level through interface states, as postulated for highly efficient Cu(In,Ga)Se_2 devices with CdS buffer [13]), a wider bandgap increases the distance between valence band edge and Fermi level therefore decreases the hole concentration at the interface. This effectively decreases the recombination at the absorber/buffer interface, because for a recombination of the photo-generated electrons, holes are needed as recombination partners [13]. In order to effectively reduce the tunneling contribution of the interface recombination, the region with wider bandgap does not need to extend wide into the absorber, as the tunneling probability decreases rapidly for an increasing tunneling distance. The model of a widened bandgap is not contrasting to the observed changes in the quantum efficiency neither, as an increased bandgap $E_{g'}$ would in principle shift the absorption of photons with energy $E < E_{g'}$ deeper into the absorber and would reduce the spectral response at the corresponding wavelengths.

The assumption of a wider bandgap is supported by the diffusion experiments presented in Chapter 6, because the absorber bandgap depends on the Cu concentration. The bandgap of Cu(In,Ga)Se_2 indeed increases for decreasing Cu contents. Evidence for a wider bandgap in Cu-poor Cu(In,Ga)Se_2 has been given for example by Schmid et al. [15] in the case of $CuInSe_2$, where he showed that the bandgap energy of Cu depleted $CuIn_3Se_5$ is approximately 0.3 eV higher than for $CuInSe_2$.

No Cu depletion at the absorber side of the In_2S_3/ Cu(In,Ga)Se_2 interface was explicitly found, but the Cu diffusion out of the absorber and into the In_2S_3 implies a reduction of Cu in the absorber. If the Cu is assumed to diffuse into the 50 nm thick In_2S_3 layer during the annealing up to a concentration of 7 at.%, and if the interface near region of the absorber is assumed to transform completely into a Cu-depleted phase with composition Cu(In,Ga)$_3$$Se_5$, the width of the depleted region can be estimated to be ≈20 nm. In Fig. 7.4, a qualitative sketch of the outlined model is given for the device before and after annealing.

The results of this work therefore suggest the pronounced diffusion of Cu into the In_2S_3 during the annealing to be the key issue for the junction formation in high efficiency Cu(In,Ga)Se_2 solar cells with an In_2S_3- buffer.

If a Cu depletion in the interface near region is in fact the reason for the low recombination and high efficiency of these devices, varying Cu concentrations at the absorber surface are likely to influence the device performance of In_2S_3-buffered Cu(In,Ga)Se_2 solar cells significantly, and would be an indication for the validity of the assumptions.

Up to now the whole solar cell structure is optimised for the utilisation of CdS buffer layers. For the future improvement of In_2S_3-buffered devices a variation of the absorber

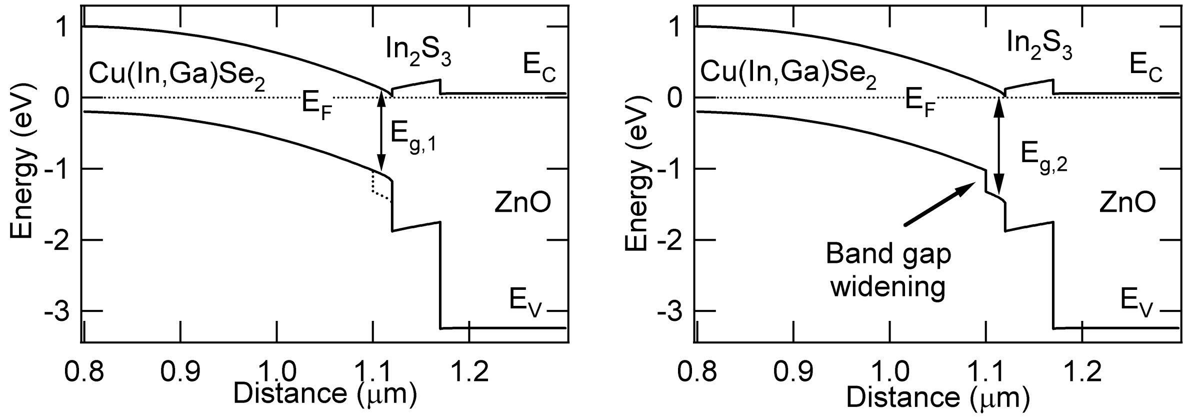

Figure 7.4: Qualitative sketch of the model proposed in the text, describing the expected changes in the band diagram of the In_2S_3-buffered solar cell upon annealing. Left: State before annealing. The changed valence band after the annealing is indicated by the dotted line. Right: After the annealing. The bandgap of the interface near region of the absorber is widened and the interface recombination decreases as a result of the Cu depletion.

preparation and surface composition as well as the ZnO might therefore lead to further improvement of the devices.

For example, based on the results of this work a systematic study of the influence of Cu-poor and Cu-rich prepared absorber layers would be interesting and could add additional details to the knowledge on the In_2S_3/Cu(In,Ga)Se_2-junction. A thickness variation of the ZnO front contact might be a way to further improve device performance, if the observed reflections (Fig. 5.10) for In_2S_3-buffered devices can be oppressed. A reduction of the In_2S_3 buffer layer thickness may be another way to increase the short circuit current density, under the condition that there is still complete coverage of the absorber. This could be achieved in a different experimental setup with rotating sample holders, for example. Finally, an in-situ deposition of the buffer layer would be desirable. For the experiments conducted during the course of this work, buffer layers had to be deposited in a separate vacuum chamber and samples had to be air-exposed during the transfer. Surface oxides as a result of the air-exposure are removed in the chemical bath for the reference samples with CdS buffer, but not for the thermally evaporated buffer layers. An in-situ buffer layer deposition would avoid the air-exposure, and could therefore further improve the quality of the buffer/ absorber junction.

The process of thermal evaporation is very promising from an industrial point of view, as it is in-line compatible and up-scaling is relatively easy. However, demands for an industrial implementation include several other aspects that have not been achieved so far, for example highest efficiencies and fast cycle times. The efficiency gap of 1-2 % to the CdS references has to be closed for the In_2S_3-buffered devices to really be competetive in practice. Some suggestions on how to further improve the device performance have been indicated above. The annealing treatment necessary for an optimal device performance is problematic in view of fast cycle times. Here, further investigation are necessary in order to reduce or omit the annealing treatment, e.g. through increased annealing temperatures/

changes in the substrate temperature during the In_2S_3 buffer layer deposition.

Chapter 8

Summary

In this work, thermally evaporated In_2S_3 thin films have been used as buffer layers in $Cu(In,Ga)Se_2$ solar cells. The aim was to prepare and systematically characterise highly efficient solar cell devices without cadmium, determine the factors limiting their performance and suggest ways for future improvements.

The state of the art $Cu(In,Ga)Se_2$ solar cell with CdS buffer layer was the starting point for this work and the role of the buffer layer as well as alternative buffer layer concepts were introduced in the beginning, together with some theoretical considerations needed for the physical interpretation of solar cell parameters.

High quality, crystalline $In_{2+x}S_3$ was successfully synthesised and used as a reference material for the structural characterisation of In_2S_3. Three modifications with tetragonal, cubic and trigonal symmetry were identified and characterised with X-ray diffraction (XRD) measurements in the temperature range from 31 °C to 1040 °C. A refinement by the Rietveld method was performed, extending the existing literature data on the structure of In_2S_3. In order to establish selection criteria for In_2S_3 source materials in´thin film deposition by thermal evaporation, three commercially available In_2S_3 powders were used as source materials and the structure and elemental composition of the powders as well as the corresponding thin films were analysed. The application of a crystalline, single phase source material was identified to be a key factor for controlled evaporation and thin film deposition.

Single phase In_2S_3 source material was found to be stable during the deposition process and could be used during multiple deposition runs. Resulting In_2S_3 thin films were stoichiometric and homogeneous with an indirect optical bandgap of (1.99 ± 0.5) eV.

The utilisation of crystalline, single phase source material and the development of appropriate buffer processing led to high efficiency solar cells. A key process for optimal device performance was post deposition annealing of the completed solar cells for 35 min. to 55 min. at a temperature of 200 °C. Annealing was found to improve mainly the fill factor and open circuit voltage of devices with an In_2S_3 buffer, independent of the atmosphere in which the annealing was carried out (e.g. in air or inert gas). The controlled and reproducible enhancement of the device performance during annealing allowed coherent analysis of the changes in the photo-generated charge carrier collection and the dominant recombination mechanism of the solar cell devices. Losses in the spectral response upon annealing observed at long wavelengths (700-1200 nm) were attributed to a reduction of the space charge region width at the In_2S_3/Cu(In,Ga)Se_2 junction.

The recombination of charge carriers could be reduced by annealing and the dominant recombination mechanism gradually changed. Prior to annealing, it was shown to have a high tunneling contribution (diode quality factors of up to 6) and was associated with a mechanism located at the In_2S_3/ Cu(In,Ga)Se_2 interface. In annealed devices, it was attributed to a thermally activated recombination in the space charge region. As a result of the reduced recombination the open circuit voltage of the ZnO/ In_2S_3/ Cu(In,Ga)Se_2/Mo devices could be reproducibly increased by 100 mV-150 mV upon annealing and devices were fabricated with open circuit voltages beyond those of the established CdS/ Cu(In,Ga)Se_2 reference cells. Thus, the potential of In_2S_3 to form high quality junctions with Cu(In,Ga)Se_2 could be demonstrated.

By a combination of bulk and surface sensitive analysis methods, a pronounced Cu diffusion from the Cu(In,Ga)Se_2 absorber into the In_2S_3 layer could be shown as a result of the annealing. In_2S_3/ Cu(In,Ga)Se_2-bilayer structures were analysed by: (1) high kinetic energy X-ray photoelectron spectroscopy (HIKE) probing the integral Cu signal of Cu in the In_2S_3 layer, (2) standard X-ray photoelectron spectroscopy detecting the increasing Cu content at the In_2S_3 surface and (3) energy-dispersive X-ray spectroscopy (EDX) measuring the Cu distribution in the In_2S_3 layer. All methods gave a clear proof that Cu diffuses into the In_2S_3 and indicated a solubility limit of 4-9 at.% for Cu in In_2S_3.

Based on the buffer processing developed and the observed Cu diffusion, new record efficiencies for Cu(In,Ga)Se_2 solar cells with an evaporated buffer layer could be obtained. The calibration laboratory of the Fraunhofer Institut für Solare Energiesysteme, Freiburg, has confirmed record cell efficiencies of (15.2 ±0.1) % (FF =75.6 %, j_{SC}= 29.8 mA/cm^2, V_{OC}=677 mV).

This work finishes with a summary and suggests ways how to further improve thin film Cu(In,Ga)Se_2 solar cells with In_2S_3 buffer layers in the future.

Appendix A

Material Analysis Techniques

A.1 Structural Analysis

A.1.1 X-ray diffraction (XRD)

X-ray diffraction (XRD) occurs when X-rays with a sufficiently small wavelength interact with atoms in a crystal. The reason is the periodic arrangement of the atoms in the crystal structure and sufficiently small means here wavelengths comparable to or smaller than the lattice parameters concerned. XRD is a standard technique for the determination of the crystal structure(s) of a given sample and is extensively described in any textbook on crystallography or solid state physics, see for example [32], [124]. The condition for a constructive interference from two lattice planes was formulated by Bragg in 1912 as (Bragg condition, see Fig. A.1) [125]:

$$\Delta x = 2d\sin(\Theta) = n\lambda \tag{A.1}$$

Here, Δx is the path difference between two X-ray beams reflected at subsequent lattice planes, Θ is the angle between incoming (outgoing) X-ray beam and lattice plane, d is the

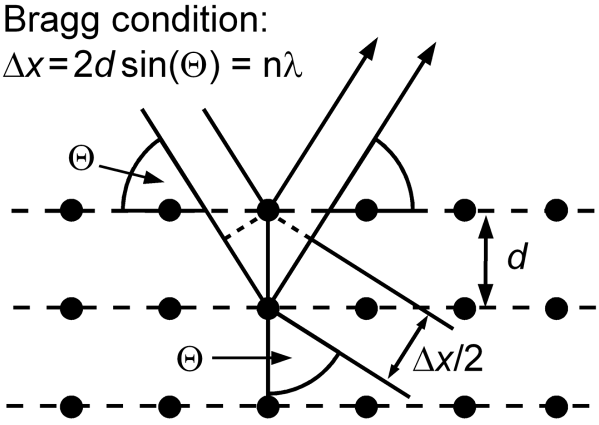

Figure A.1: Schematic representation of the geometry considered for the derivation of the Bragg condition.

spacing between the lattice planes, n the order of diffraction (a positive integral) and λ is the X-ray wavelength. The Bragg condition determines at which angle Θ_{hkl} reflection peaks will be found in a measured XRD pattern for a crystal plane with spacing d_{hkl}. The intensity I_{hkl} of the reflection of plane (hkl) (with hkl being the Miller indices of the plane) depends on the structure factor $F(hkl)$:

$$I_{hkl} \propto \|F(hkl)\|^2 . \tag{A.2}$$

$$F(hkl) = \sum_{i}^{N} f_i \exp(2\pi i h x_i + 2\pi i k y_i + 2\pi i l z_i). \tag{A.3}$$

Here the sum is carried out over all atoms i in the unit cell, f_i is the atomic form factor, a measure for the scattering power of the ith atom which depends on the atom type and the Bragg angle Θ, hkl the Miller indices of the scattering crystal plane and x_i, y_i, z_i are the coordinates of the ith atom in the unit cell.

This means, that with the use of Formula A.2 and A.3 the relative XRD intensities can be calculated for a known crystal structure. Unfortunately, it is not possible to calculate in turn the crystal structure directly from the measured intensities. This is due to the fact that when measuring the intensity only the amplitude of the structure factor is recorded and the phase information is lost.

However, it is normally possible to determine the crystal structure parameters indirectly. For this, the space group has to be determined through an analysis of the Bragg positions in a first step (or through comparison with similar crystals). Secondly, approximate lattice parameters and atomic positions have to be guessed. The XRD intensities corresponding to this guess can then be calculated and compared to the measured diffractogram. Finally, the structure parameters of the guess are refined until achieving best agreement between calculated and measured XRD intensities. This is the principle of XRD structure refinement methods such as the Rietveld refinement [126]. The Rietveld method was first developed for the refinement of neutron diffraction data but since then has been extended and extensively used for X-ray diffraction as well [127].

In this thesis, the program FULPROF has been used for the Rietveld refinement of XRD data [62][128][63]. As stated before, the Rietveld method is not able to calculate the crystal structure but rather refines the structure parameters defined by the user by minimising the weighted squared difference χ^2 between calculated and measured intensities. The fitted parameters include structural parameters of the sample (such as the lattice parameters, atomic positions, occupational levels, temperature factors, etc.) and global parameters (such as a zero point correction, profile shape parameters correlated to the experimental setup, background etc.). The background has been approximated by linear interpolation of manually set background points whose intensity was included in the refinement.

For a meaningful refinement of a set of structure parameters, the ratio of relevant reflections to refined intensity parameters should be at least 3, preferably 5 [129].

The two most important measures to qualify a refinement are always the graphical comparison of calculated and observed patterns including the residuum and the final evaluation if the used refined model is reasonable, i.e. considering the position and distance of adjacent atoms, etc. There exist several parameters that further describe the quality of a refinement, such as the different R-values (also called residual indices). These parameters and their definition as implemented in the FULLPROF program are summarised in Table A.1. The commonly stated and most important of these is the weighted profile R-value R_{wp} and the R-Bragg value R_{Bragg}. In general, for acceptable refinements on X-ray data this value decreases to below 10 % [129]. R-values stated here refer to background-subtracted ("peak-only") conventional R-values, not total R-values. The reduced χ^2_ν value should approximate 1 in the ideal case.

Table A.1: Definition of the quality factors used by the Rietveld refinement program FULLPROF [62]

$$\chi^2 = \sum_{i=1}^{n} w_i \left|y_i - y_{c,i}\right|^2$$

$$R_B = 100 \left[\frac{\sum\limits_h \left|I_{obs,h} - I_{calc,h}\right|}{\sum\limits_h I_{obs,h}}\right] \qquad \text{R-Bragg}$$

$$R_{wp} = 100 \left[\frac{\sum\limits_{i=1}^{n} w_i \left|y_i - y_{c,i}\right|^2}{\sum\limits_{i=1}^{n} w_i y_i^2}\right]^{0.5} \qquad \text{Weighted profile factor}$$

$$R_{exp} = 100 \left[\frac{(n-p)}{\sum\limits_{i=1}^{n} w_i y_i^2}\right]^{0.5} \qquad \text{Expected weighted profile factor}$$

$$\chi^2_\nu = (R_{wp}/R_{exp})^2 = \frac{\chi^2}{(n-p)} \qquad \text{Reduced } \chi^2$$

i :	index for datapoints	w_i:	weight factor ($w_i = 1/\sigma_i^2$)
n :	number of datapoints	σ_i^2:	variance
p :	number of ref. parameters	h:	index for Bragg positions
$(n-p)$:	degree of freedom	$I_{obs,h}$:	integrated observed intensity
y_i:	observed intensity	$I_{calc,h}$:	integrated calculated intensity
$y_{c,i}$:	calculated intensity		

Finally, a refined set of parameters is completed with its corresponding estimated standard deviations. These standard deviations state the precision of the fitted parameters, not their accuracy, i.e. this estimated deviation is a statistical error accounting for only the counting statistics, systematic errors can not be estimated by the the program. The estimated standard deviation (e.s.d) is in this sense not the experimental probable error, it is the minimum possible error arising from random errors alone [126].

If not stated otherwise, XRD patterns presented in this thesis have been recorded with a Brukner Axis D8 Advance diffractometer and Cu Kα irradiation. Powder samples have been analysed in Bragg-Brentano geometry (Θ - 2Θ mode), while thin film samples have been recorded in grazing incidence mode with a fixed angle of incidence in the range of 0.5-2.0°. In both cases the sample was mounted on a rotating sample holder.

A.1.2 Transmission Electron Microscopy (TEM)

Tranmision electron microscopy can offer high-resolution images (down to the sub-nanometer range) of thin samples. The transmission electron microscope used in this thesis is a Zeiss LIBRA FE 200 with an incorporated EDX spectrometer. Sample preparation for the TEM micrographs is described in Section 6.3. In a transmission electron microscope electrons are accelerated to typically 80-300 keV, focussed and directed onto the specimen. The electrons traverse and interact with the sample and are finally collected by an detecting unit after passing through the sample. Several different operation modes are possible depending on the incident electron beam (broad beam/ TEM or focussed beam mode/ scanning TEM mode (STEM)) and detecting geometry (detection of the electron-diffraction pattern or Bright-Field (BF)/ Dark-Field (DF) imaging). The TEM micrographs presented in this thesis have been obtained in BF TEM mode, while the EDX line scans have been recorded in the STEM mode of the microscope.

A.2 Chemical Analysis

A.2.1 Energy Dispersive X-ray Spectroscopy (EDX)

The interactions of electrons with matter when traversing the sample give rise to a variety of signals such as back-scattered and secondary electrons, Auger electrons, X-ray photons, etc. The Energy Dispersive X-ray spectrometer (EDX) attached to many electron microscopes analyses the energy of the emitted X-rays. These X-ray photons correspond to photons emitted in the XRF process as described before, with the only difference being the excitation source: X-rays in the case of XRF (photon-in photon-out process) and electrons with high kinetic energy (typically 5-30 keV for SEMs and 100-300 keV for TEMs) in the case of EDX.

In any case the energy of the emitted X-ray photons depends on the energy difference between the excited energy level and the relaxed energy level of the emitting atom and not on the excitation energy (given that the excitation energy is large enough to produce the emission). The positions of the emission lines in a EDX spectrum are therefore characteristic for the involved elements. The concentration of a given element is reflected in the intensity of the emission line.

The quantitative evaluation is however not straight-forward as the emission intensity of a specific line depends critically on many material and energy specific factors (the involved ionisation and scattering cross sections, absorption coefficients, fluorescence yields, etc.), which makes an extensive calibration with accurate reference samples necessary for an accurate quantitative analysis. However, for a qualitative comparison of different line scans, as is the aim of this thesis (Section 6.3), an examination of the net counts of the different elements can easily be accomplished. For the case of the In_2S_3/Cu(In,Ga)Se_2

samples, the ratio of the Cu / In concentration, which is approximately known for the Cu(In,Ga)Se_2 side, can then be approximated for the In_2S_3 side by the relation:

$$\frac{c_{Cu}}{c_{In}} \approx k \frac{I_{Cu}}{I_{In}} \tag{A.4}$$

Here, c_A is the concentration of element A, I_A is the EDX intensity and k is the k-factor.

In this approximation bulk effects (e.g. X-ray and electron absorption) and secondary fluorescence effects are neglected, which can be justified with regard to the the small sample thickness (50-100 nm).

A.2.2 X-ray Photoelecton Spectroscopy (XPS)

The principle of X-ray Photoelectron Spectroscopy (XPS) consists of the excitation of a sample with a monochromatic X-ray beam and the energetic analysis of the emitted photoelectrons. XPS is a standard technique for the surface analysis of chemical states and elemental compositions and its applications is covered by a variety of textbooks. For a more detailed description, the interested reader is referred to references [130],[131] or [132], for example. XPS is based on the external photo-electric effect [133] whose principle is depicted in Fig. A.2. An atom inside the sample is excited by the absorption of an incident X-ray photon. If the X-ray photon energy exceeds the energy necessary to expel an electron from the atom, an emitted photoelectron leaves the atom with a kinetic energy E_{kin} corresponding to:

$$E_{kin} = h\nu - E_{bin} - \phi. \tag{A.5}$$

Here, $h\nu$ is the photon energy, E_{bin} the binding energy of the electron and ϕ the work function of the sample, defined as the difference between the Fermi energy E_F and the vacuum energy level E_{vac} ($\phi = E_{vac} - E_F$). The atom is left behind ionised with a hole in the core level corresponding to the emitted photoelectron. This hole can be filled by an electron from the outer shells, the energy difference being released by an X-ray photon (radiative emission) or by the emission of another electron (Auger emission). Both phenomena give rise to other spectroscopic methods: X-ray fluorescence analysis (XRF) and Auger electron spectroscopy (AES), respectively.

The binding energy is characteristic for the element and the relevant energy level. By an energy-selective detection of the photoelectrons it is therefore possible to determine the elements present in a sample, given that the energy of the monochromatic X-ray beam is known. The XPS peaks of a given element are furthermore sensitive to small shifts in the corresponding energetic levels which are induced by the chemical state of the element.

Due to the strong interaction of electrons in the energy range 10-1000 eV with the surrounding atoms, the distance that an photoelectron may travel on average without an inelastic collision is only in the order of a few monolayers. This distance is known as the inelastic mean free path (IMFP). Calculations of the inelastic mean free path in the energy range 50-2000 eV have been carried out by Tanuma et al. using the Bethe equation for energy loss of charged particles in matter and some empirical material specific constants

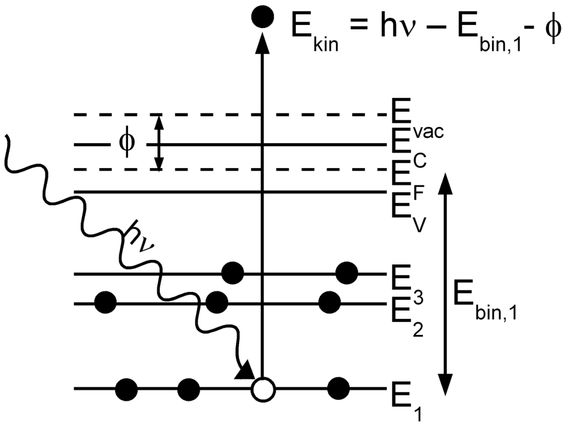

Figure A.2: Schematic representation of the energy levels involved in the photoelectron emission process.

[134], [135]. These calculations are the basis for the program QUASES-IMFP-TPP2M which is used if IMFPs are needed in this thesis [104].

The general absolute accuracy of this algorithm is unknown but estimated to be approximately 20%, while the relative accuracy, i.e. the ratio of two IMFPs calculated for the same material, is likely to be much better than 10% [105]. In the common energy range 10-1500 eV a typical IMFP is in the order of a 0.1-10 nanometers (as compared to up to 100 nm for the corresponding photons) which is the reason for the surface sensitivity of XPS.

Another approach to estimate the probing depth in XPS measurements is based on the attenuation length, which is defined as the characteristic length for the exponential decay of the intensity of emitted photoelectrons when passing through matter. The attenuation length also includes elastic scattering and is therefore generally smaller than the IMFP and easier to measure, but more difficult to predict.

Fig. A.3 shows the best fit to experimentally determined attenuation lengths which is known as the “universal curve” (Seah and Dench, 1979 [99]). It shows the approximated dependence of the attenuation length on the kinetic energies of the photoelectrons. The attenuation length was to a first approximation found to be independent of the material when it is expressed in monolayers. The curve shows a minimum at approximately 30 eV. It follows from this curve, that the depth, from which photoelectrons may be detected, increases for photoelectrons with much higher or lower kinetic energies. This is the basis for High KInetic Energy XPS (HIKE), a variation of XPS where the excitation energy is varied between 2-10 keV giving rise to different sampling depths.

The position of an XPS line provides the information necessary to identify the corresponding element and its chemical state. The line intensity, i.e. peak area, reflects the amount of the given element present in the surface near region of the sample. More precisely, the intensity I_A for a given photoelectron peak from element A at kinetic energy E_A of a homogenous sample is described by (following [130], [131]):

$$I_A = \sigma(h\nu)\; J\; L_A(\gamma)\; T(E_A)\; c_A\; \lambda_A(E_A)\; \cos(\Theta). \tag{A.6}$$

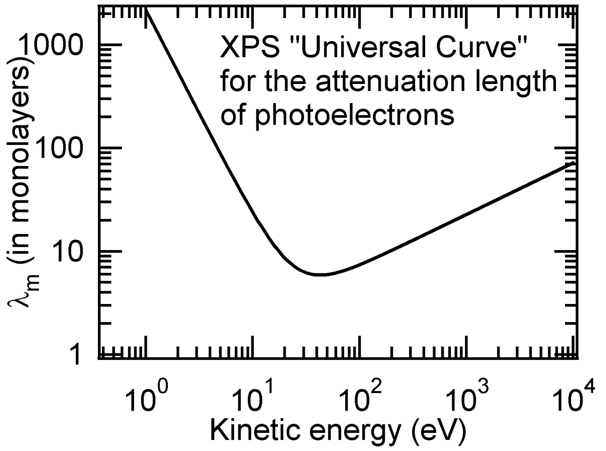

Figure A.3: "Universal curve" of Seah and Dench [99], showing the dependence of the attenuation length λ_m (in monolayers) on the kinetic energy E_{kin} (in eV) of the photoelectrons. The curve is based on a best fit to experimental data for a variety of materials. Displayed is the relation for inorganic compounds which is stated as $\lambda_m = 2170(E_{kin}/eV)^2 + 0.72(aE_{kin}/(eV\,nm)^{0.5}$, with the monolayer thickness a=1 nm.

Here $\sigma(h\nu)$ is the photoionisation cross section for the emission line of interest (from element A at the photon energy $h\nu$), J is the X-ray photon flux at the sample surface, $L_A(\gamma)$ is the angular asymmetry parameter of the photoelectron line concerned, γ is the angle between incident X-ray photons and outgoing photoelectrons, $T(E_A)$ is the spectrometer transmission function, c_A is the number density of atoms in the sample, $\lambda_A(E_A)$ is the inelastic mean free path of the photoelectrons of kinetic energy E_A in the sample and Θ is the angle between emission of photoelectrons and the sample normal.

The sensitivity factor S_A is introduced as:

$$S_A = \sigma(h\nu)\; J\; L_A(\gamma)\; T(E_A)\; \lambda_A(E_A)\; \cos(\Theta)\;, \Rightarrow S_A = I_A/c_A. \tag{A.7}$$

Hence by comparing the emission intensity of the emission lines from two elements with known sensitivity factors (which may be provided by reference measurements or comparison with tabulated literature data) it is easy to determine the elemental ratio:

$$\frac{c_A}{c_B} = \frac{I_A/S_A}{I_B/S_B}. \tag{A.8}$$

During the course of this thesis XPS has been performed in the CISSY-UHV-chamber ([108]), which is equipped with CLAM4 (Thermo VG Scientific) concentric semi-hemispherical analyser (CHA) and a Al Kα /Mg Kα X-ray tube. The transmission function of this electron analyser in the applied range of 120 eV-1200 eV is approximately proportional to $E_{kin}^0.5$ at a pass energy of 20 eV [136]. Evaluation of the spectra is carried out after a linear background subtraction and energy calibration to known reference XPS lines (typically Au 4f: 84.0 eV [137]). X-ray tube axis and spectrometer axis are arranged under approximately 55°. Under this so called magic angle of XPS [130] the angular asymmetry parameter L_γ is a constant and can be omitted in the quantification of XPS data.

A.2.3 X-ray Fluorescence Analysis (XRF)

Compositional analysis of thin films and powder tablets has been performed with an XRF Philips MagiX Pro PW2440 X-ray fluorescence analyser. X-ray fluorescence has been mentioned earlier: it occurs when the excess energy of an ionised, excited atom after a photo-ionisation process is released by the emission of an X-ray photon. The position of the X-ray fluorescence line is element specific and depends on the difference between the two electron levels involved. The calibration for the In_2S_3 thin film analysis in this thesis has been carried out with the use of an ILGAR ([91]) In_2S_3 reference sample whose composition had been determined with elastic recoil detection analysis (ERDA). The error in composition of this reference sample had been stated with 1 at.%. The absolute error of the XRF thin film analysis is limited by the accuracy of the composition of the reference sample. However, the relative error (i.e. when comparing different measurements using the same calibration) is considerably smaller and depends on the scattering of the XRF measurements. The standard deviation of the XRF data can be approximated with 0.3 at.% [138].

A.3 Optical Characterisation

Optical properties of thin films have been analysed by reflection/transmission measurements with an optical spectrometer (Cary 500 Scan UV-Vis-NR Spectrophotometer). The data evaluation has been carried out following Pankove [139]. If only simple reflections are considered, the relation between reflection R, transmission T and the absorption coefficient α for a thin film with thickness x can be stated as:

$$T = I_{transmitted}/I_{incident}. \tag{A.9}$$

$$T \approx (1 - R)\exp(-\alpha x). \tag{A.10}$$

Therefore the absorption coefficient follows from:

$$\alpha \approx -\frac{1}{x}\ln\left[\frac{T}{(1-R)}\right]. \tag{A.11}$$

The bandgap is related to the absorption coefficient [139]:

$$\alpha(h\nu) = A\frac{(E_g - h\nu)^m}{h\nu} \tag{A.12}$$

with $h\nu$ photon energy, A a constant and m a coefficient that depends on the nature of the transition (being 1/2 for an allowed direct transition and 2 for an allowed indirect transition.)

Appendix B

Results of the Rietveld Refinement

Rietveld refinements have been carried out for the three In_2S_3 modifications found during the temperature-dependent synchrotron-based XRD measurements of the $In_{2+x}S_3$ powder PP-SYN-113 (x=-0.13) (presented in section 4.1.3). In the applied temperature range of 31 °C-1049 °C, three phases were found:

(a) tetragonal β-In_2S_3 (below 441 °C)

(b) cubic α-In_2S_3 (446 °C- 776 °C)

(c) trigonal γ-In_2S_3 (above 811 °C)

The measured and calculated intensities, as well as the positions of the Bragg-reflexes and the residuals, have been presented in Fig. 4.3. In the following, a summary of parameters extracted from the Rietveld refinement for each phase will be presented. In the next section, the results will be discussed.

Table B.1: Results of the Rietveld refinement of PP-SYN-113 measured at 36 °C (tetragonal β-In_2S_3).

β-In_2S_3 (36 °C)

General

Crystal system	tetragonal	
Space group	$I4_1/amd$	
Origin choice	-1 at origin	
Lattice parameters	$a_0 = b_0 =$	(7.6231±0.0004)Å
	$c_0 =$	(32.358±0.004)Å
	$\alpha = \beta = \gamma =$	90 °

Atomic sites

atom	Wyckoff	x	y	z	Occ.*M	Biso
In1	8e	0	1/4	0.2046(2)	7.3	0.8
In2	8c	0	0	0	7.3	1.2
In3	16h	0	-0.0195(3)	0.3328(2)	14.6	0.9
S1	16h	0	-0.0044(21)	0.2515(7)	14.7	0.7
S2	16h	0	0.0080(23)	0.0774(7)	15.4	1.6
S3	16h	0	0.2006(20)	0.4134(7)	15.0	1.1

Refinement

R_B	1.34 %
R_{wp}	3.12 %
χ^2_ν	10.4
$\text{Ratio}_{h/p}$ (Effective number of Reflections)/ (Number of intensity parameters)	5.1

Table B.2: Results of the Rietveld refinement of PP-SYN-113 measured at 476 °C (cubic α-In_2S_3).

α-In_2S_3 (476 °C)

General

Crystal system	cubic	
Space group	$Fd\bar{3}m$	
Origin choice	-1 at origin	
Lattice parameters	$a_0 = b_0 = c_0 =$	(10.8315±0.0003)Å
	$\alpha = \beta = \gamma =$	90 °

Atomic sites

atom	Wyckoff	x	y	z	Occ.*M	Biso
In1	8a	1/8	1/8	1/8	5.1	2.4
In2	16d	1/2	1/2	1/2	15.6	3.5
S1	32e	0.2564(2)	0.2564(2)	0.2564(2)	32.0	2.7

Refinement

R_B	1.64 %
R_{wp}	2.77 %
χ^2_ν	7.9
Ratio$_{h/p}$ (Effective number of Reflections)/ (Number of intensity parameters)	6.3

Table B.3: Results of the Rietveld refinement of PP-SYN-113 measured at 826 °C (trigonal γ-In_2S_3).

γ-In_2S_3 (826 °C)

General

Crystal system	trigonal	
Space group	$P\bar{3}m1$	
Origin choice	-1 at origin	
Lattice parameters	$a_0 = b_0 =$	(3.8656±0.0002)Å
	$c_0 =$	(9.1569±0.0005)Å
	$\alpha = \beta =$	90 °
	$\gamma =$	120 °

Atomic sites

atom	Wyckoff	x	y	z	Occ. *M	Biso
In1	2d	1/3	2/3	0.8079(4)	0.9	3.9
In2	2d	1/3	2/3	0.6485(15)	0.2	6.2
S1	2d	1/3	2/3	0.3358(8)	1.1	4.3
S2	1a	0	0	0	0.6	8.9

Refinement

R_B	2.84 %
R_{wp}	2.96 %
χ^2_ν	11.4
$\mathrm{Ratio}_{h/p}$ (Effective number of Reflections)/ (Number of intensity parameters)	3.1

First, the crystal structure of the cubic α-In_2S_3 (space group $Fd\overline{3}m$, No.227) and not the tetragonal β-In_2S_3 found at room temperature will be presented. The space group $I4_1/amd$ (No.141) of the β-modification is a subgroup of the space group $Fd\overline{3}m$ and therefore the structure of the β-modification may easily be derived from the structure of the α-modification. Finally the crystal structure of the trigonal (high-temperature) γ-In_2S_3 will be presented.

Cubic α-In$_2$S$_3$

The unit cell of the α-In_2S_3 is sketched in Fig. B.1. It resembles the structure of a regular spinel, with In on both, octahedral and tetrahedral, cation sites. It should be remembered that the tetrahedral sites are not completely filled, approximately one third remains unoccupied (see Table B.2). The lattice parameters of the Rietveld refinement are close to, but slightly higher than data found in literature (e.g. Py et al. [115]: c_0=(10.774±0.002)Å). Fig. B.2 shows another representation of the structure of α-In_2S_3. In this case, the representation limits and viewing angle are chosen corresponding to the unit cell of the space group $I4_1/amd$, which is the space group of following phase: β-In_2S_3.

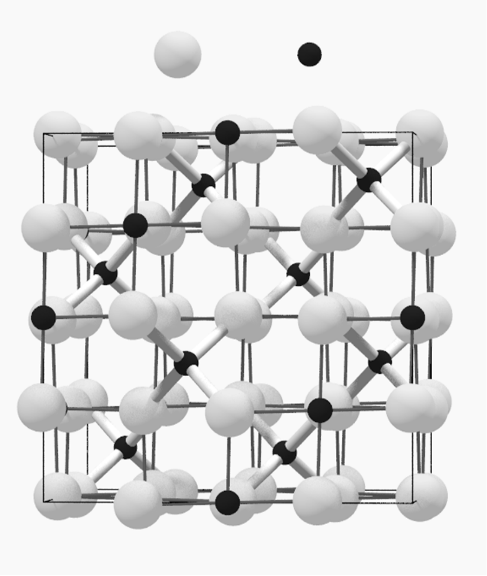

Figure B.1: Structural model of the unit cell of the α-modification of In_2S_3. The structure is spinel-type with S on the anion sites and In on the tetrahedral and octahedral cation sites. One third of the tetrahedral sites remains unoccupied. However, this is not reflected in this presentation, as vacancies are distributed statistically over all tetrahedral sites.

Tetragonal β-In$_2$S$_3$

The structure of the β-phase is very similar to the α-phase, except that the In-vacancies are ordered along a 4_1 screw axis parallel to the c-direction. Comparing Fig. B.2 and Fig. B.3 it is easy to find the unoccupied In sites. The ordering causes a small distortion of the lattice and consequently the corresponding structure is tetragonal. The lattice parameters and atom sites, found by Rietveld refinement, are in good agreement with references [140], [56]. The structural parameters published by Aldon et. al. [140] are presented in Table B.4 for comparison.

Table B.4: Structural parameters for β-In_2S_3 published by Aldon et al. [140].

Lattice parameters	$a_0 = b_0$	7.6143(3)Å
	$c_0 =$	32.3078(13)Å

atom	Wyckoff	x	y	z
In1	8e	0	1/4	0.2042(2)
In2	8c	0	0	0
In3	16h	0	0.0247(8)	0.3329(2)
S1	16h	0	0.0020(28)	0.2514(4)
S2	16h	0	0.0042(31)	0.0806(4)
S3	16h	0	0.0018(28)	0.4162(5)

Trigonal γ-In_2S_3

The γ-modification of In_2S_3 is trigonal. It is best described by layered structure of subsequent S-In-S-In-S slabs. The In atoms are now distributed over the octahedral sites in the still nearly cubic closed-packed S sublattice. This high-temperature phase cannot be quenched to room temperature, but Diehl et al. found that its crystal structure may be stabilized at room temperature by the substitution of about 5 % In by Sb or As [141]. The same authors presented crystallographic data for γ-In_2S_3(As) and γ-In_2S_3(Sb) [53]. They found a trigonal symmetry with space group $P\overline{3}m1$ (No. 164) and lattice parameters (I) In_2S_3(As): a_0 =(3.806±0.001) Å, c_0 =(9.044±0.003) Å and (II) (In_2S_3(Sb): a_0 =(3.831±0.001) Å, c_0 =(9.049±0.006) Å. The atomic sites for the case of In_2S_3(As) are displayed in Table B.5. Diehl et al. claimed two atomic sites for S (2d and 1a) and one for In (2d). A fourth atomic position (also at 2d) is occupied by the As atom, with an occupancy of 0.13. Fig. B.4 shows the arrangement of the In and S atoms following this structure, omitting the additional As site. Here the layer structure of the crystal can clearly be seen. To the authors knowledge, no further structural data on the high-temperature phase of pure γ-In_2S_3 has been reported so far. The Rietveld refinement showed that the introduction of a second In atom at position 2d is necessary for a good agreement between measurement and refinement. This position corresponds to the position occupied by the group V element in γ-In_2S_3(As), γ-In_2S_3(Sb). The parameters and atomic sites for the pure γ-In_2S_3 can be found in Table B.3. For pure γ-In_2S_3, no published data could be found. A structural model of the corresponding structure is presented in Fig. B.5.

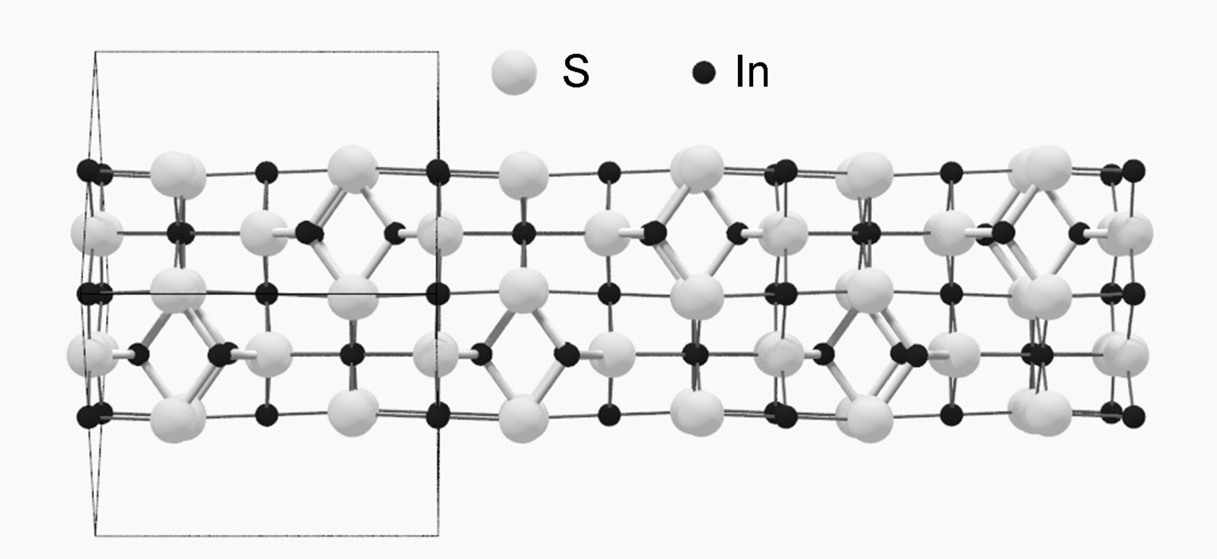

Figure B.2: Structural model of the α-modification of In_2S_3. The borders of the unit cell are marked with a thin line. In order to facilitate comparison, in this presentation the excerpt and viewing angle ([-120]-direction) of the crystal structure are chosen corresponding to the unit cell of the β-modification (Fig. B.3).

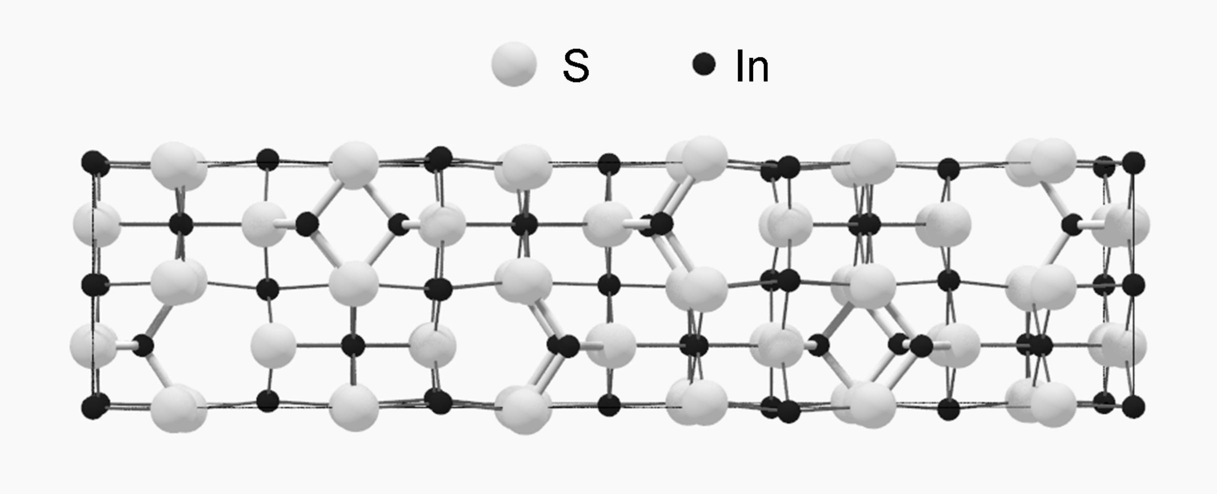

Figure B.3: Structural model of the unit cell of the β-modification of In_2S_3. The In atoms occupy the (octahedral and tetrahedral) cation sites and of the defect-spinel type structure. The bonds of the tetrahedral sites are drawn thicker for a better identification. The vacancies are ordered on tetrahedral sites along a 4_1 screw axis. The position of the vacancies are not marked in this presentation, but may be easily identified by comparing Fig. B.3 with the presentation of the cubic α-modification (Fig. B.2).

Table B.5: Structural parameters for γ-In_2S_3(As) published by Diehl et al. [53].

atom	Wyckoff	x	y	z	Occ.* M
S1	1a	0	0	0	1
S2	2d	1/3	2/3	0.3316(4)	2
In1	2d	1/3	2/3	0.8097(1)	1.72(4)
As1	2d	1/3	2/3	0.6117(8)	0.26(2)

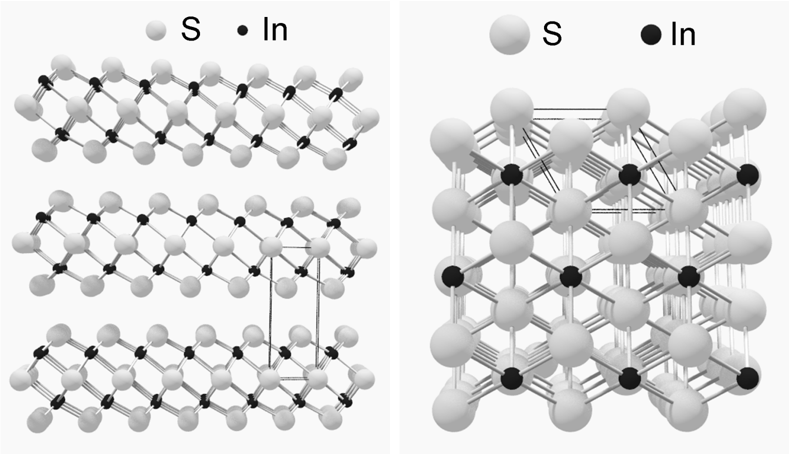

Figure B.4: Structural model of the γ-modification of In_2S_3 following Diehl et al. [53]. Left: View in [-120]-direction, for a good visualisation of the individual S-In-S-In-S slabs. Right: View in [001]-direction, the sulphur atoms form a cubic closed-packed sublattice with the In atoms occupying the octahedral interstices.

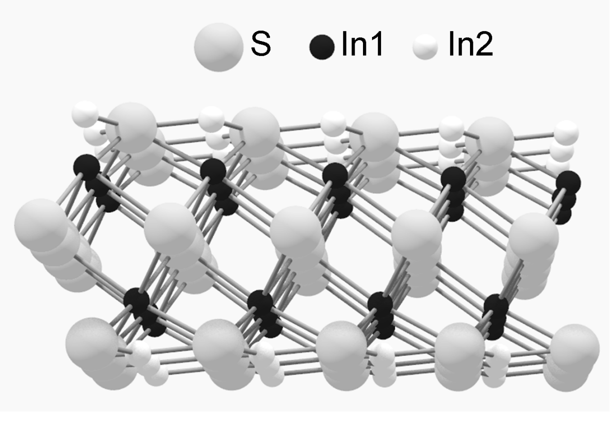

Figure B.5: Structural model of the γ-modification of In_2S_3 (following the Rietveld refinement carried out in this work). The sulphur atoms form a cubic closed-packed sublattice with the In1 (black) atoms in the octahedral interstices. The In2 (white) atoms are found between the slabs. However, the occupational level of the In2 sites (white) is very low (<0.2).

Appendix C

Chemical Analysis of Commercial In_2S_3 Powders

Pure In_2S_3 powder from four different suppliers had been previously analysed by a variety of methods and had been tested for its suitability as source material in a thermal evaporation or physical vapour deposition (PVD) process. In order to further investigate variations found in commercially available In_2S_3 powders, samples were sent to the Microanalytical Laboratory Pascher [77]. The aim was an exact chemical analysis with respect to the In/S ratio and O, Cl contaminations.

The tested powders correspond to the powders A (ordered from Testbourne), B (Alfa Aesar) and C (Strem Chemicals) introduced in Chapter 4.2.1. A Cl contamination in fresh powder A (ordered from Testbourne) and C (ordered from Strem) had already been identified by XPS and XRF as shown in Chapter 4.2.1. Powder B was the only powder that showed sharp XRD patterns in the as received state . Best cells could be prepared reproducibly with powder B which also showed no alteration/degradation in device performance for a complete evaporation series from fresh powder (1396.1 mg initial weight) up to nearly complete evaporation (residue of 57.9 mg) (total evaporation time nearly 1000 h).

Sample Index

Samples were analysed from fresh (as received) powder A, B and C. Additionally, two powder samples of a complete evaporation series of powder B (after being used for 670 min. and 970 min., in the thermal evaporation process) have been analysed in order to detect degradation/ alteration effects in the source material. Table C.1 shows the sample index for the samples of this section.

The evaporation series was started with (1396.1±0.1) mg. Multiple depositions runs were performed and powder was extracted from the crucible after 330 min. and 670 min. deposition time (a sample of (103.9±0.1)) mg that was not analysed and sample B02: (157.8±0.1) mg, respectively). After 970 min., no deposition could be detected any more and a white powder residue was left over (sample B03, 57.9 mg). Solar cells with buffer layers produced during the course of this series up to an accumulated deposition time of 670 min. showed no degradation as was demonstrated in Chapter 5.

Table C.1: Sample index of the samples analysed for composition at Microanalytical Laboratory Pascher.

	A01	B01	B02	B03	C01
supplier	Testbourne (pwd A)	Alfa Aesar (pwd B)	Alfa Aesar (pwd B)	Alfa Aesar (pwd B)	Strem (pwd C)
weight (g) (±0.0001)g	6.2945	1.2331	0.1578	0.0579	3.4551
comment	as received	as received	used for 670 min.	used for 970 min.	as received

Analysis Methods and Results

The applied analysis methods include inductively coupled plasma analysis by atomic absorption spectroscopy (ICP-AAS) for sulphur and indium, ion-exchange chromatography (IC) for chlorine after dissolving the sample in H_2O_2 (formation of HCl), vacuum-heat extraction (VH) for oxygen (this method consists of heating the sample to 2700 °C and subsequent quantitative analysis of the gas with a mass spectrometer) and CH-analysis (CH) for carbon and hydrogen (here the samples are weighed and then completely oxidised in a pure oxygen atmosphere, the resulting H_2O is then analysed by IR-spectroscopy and the CO_2 by conductometry.). A summary of the applied analysis methods with their corresponding abbreviations and the errors stated by the Microanalytical Laboratory Pascher can be found in Table C.2. The results of the analysis are presented in Fig. C.1.

Table C.2: Analysis methods applied for the compositional analysis of the commercial In_2S_3 powders at Microanalytical Laboratory Pascher.

	Abbrev.	Analysed elements	Sample mass (mg)	Error (%)
Inductively coupled plasma analysis by atomic absorption spectroscopy	ICP-AAS	In, S	5-6	0.5
Ion-exchange chromatography	IC	Cl	5-10	0.3
Vacuum-heat extraction	VH	O	10	0.5
CH-analysis	CH	C,H	15	0.05

In order to check the reproducibility, two samples have been processed for each powder (in Table C.1 these are named (I) and (II)). The difference of up to 2 at.% is an indication for the inhomogeneity of the powders, which is more pronounced for powder A and C, although the sample number is of course too low for a proper statistical analysis. As concerning the fresh (as received) powders the results show that

- Powder A and C have a lower In content than powder B (27-29 at.% compared to 40 at.%).

Element	**Method**		**Strem (fresh)**		**Testbourne (fr.)**		**Alfa (fresh)**		**Alfa (670min.)**		**Alfa (970min.)**	
			C01 (I)	C01 (II)	A01 (I)	A01 (II)	B01 (I)	B01 (II)	B02 (I)	B02 (II)	B03 (I)	B03(II)
In (114.82u)	ICP	weight %	66.900	66.500	67.100	66.900	71.100	70.900	72.600	72.900	77.200	78.900
		Mol / 100g	0.583	0.579	0.584	0.583	0.619	0.617	0.632	0.635	0.672	0.687
		atomic %	29.21	27.74	27.16	27.71	39.96	39.52	39.60	39.77	38.30	38.67
S (32.08u)	ICP	weight %	23.100	24.000	23.100	23.200	25.700	26.000	22.900	22.800	10.600	11.100
		Mol / 100g	0.720	0.748	0.720	0.723	0.801	0.810	0.714	0.711	0.330	0.346
		atomic %	36.103	35.839	33.461	34.396	51.693	51.869	44.702	44.521	18.824	19.472
O (15.9994u)	VHE	weight %	5.750	6.020	7.800	7.000	1.700	2.100	3.800	3.800	12.000	11.900
		Mol / 100g	0.359	0.376	0.488	0.438	0.106	0.131	0.238	0.238	0.750	0.744
		atomic %	18.02	18.02	22.65	20.81	6.86	8.40	14.87	14.88	42.73	41.86
Cl (35.453u)	IC	weight %	0.700	0.680	0.390	0.390	0.000	0.000	0.000	0.000	0.000	0.000
		Mol / 100g	0.020	0.019	0.011	0.011	0.000	0.000	0.000	0.000	0.000	0.000
		atomic %	0.99	0.92	0.51	0.52	0.00	0.00	0.00	0.00	0.00	0.00
H (1.0079u)	CH	weight %	0.300	0.350	0.340	0.340	0.020	0.000	0.010	0.010	0.000	0.000
		Mol / 100g	0.298	0.347	0.337	0.337	0.020	0.000	0.010	0.010	0.000	0.000
		atomic %	14.92	16.64	15.68	16.04	1.28	0.00	0.62	0.62	0.00	0.00
C (12.0112u)	CH	weight %	0.180	0.210	0.140	0.130	0.040	0.040	0.040	0.040	0.030	
		Mol / 100g	0.015	0.017	0.012	0.011	0.003	0.003	0.003	0.003	0.002	0.000
		atomic %	0.75	0.84	0.54	0.51	0.21	0.21	0.21	0.21	0.14	0.00
Summe		weight %	96.930	97.760	98.870	97.960	98.560	99.040	99.350	99.550	99.830	101.900
		Mol / 100g	1.994	2.087	2.152	2.103	1.550	1.563	1.597	1.596	1.755	1.777
		atomic %	100.00	100.00	100.00	100.00	100.00	100.00	100.00	100.00	100.00	100.00
In / S	atomic ratio	as is	0.809	0.774	0.812	0.806	0.773	0.762	0.886	0.893	2.035	1.986
		~In203	0.476	0.439	0.360	0.402	0.685	0.654	0.664	0.671	0.521	0.553
		~In203, H20	0.614	0.594	0.516	0.558	0.693	0.654	0.669	0.675	0.521	0.553
		~In2O3, OH	0.752	0.748	0.673	0.713	0.701	0.654	0.673	0.680	0.521	0.553

Figure C.1: Summary of the results of the compositional analysis. Explanation and discussion can be found in the text.

- Powder A and C have a lower S content than powder B (33-36 at.% compared to 52 at.%).
- This is due to a higher content of foreign atoms, e.g. O (A: 18 at.%; C: 22 at.%; B: 8 at.%), but also Cl, C and H.
- Powder A and C show a clear Cl contamination (0.5 at.% and 1.0 at.%, respectively). No Cl (<0.1 weight %) was found for sample B.
- The oxygen in the samples can be present in the form of H_2O, (OH), CO_2 or In_2O_3. The analysis shows that there is much more hydrogen present in sample A and C than in powder B (16 at.% compared to 1 at.%) which indicates the presence of H_2O or (OH).
- The In / S ratio is calculated in the last row of the table in four ways:
  (1) Calculating the ratio of at.% (In) / at.% (S) directly from the chemical analysis.
  (2) Assuming that all O is bound in In_2O_3 and subtracting the corresponding amount of at.% (In) from the total at.% (In) before calculating the ratio.
  (3) Supposing that all H is present in the form H_2O, subtracting the corresponding amount of O from the at.% (O) before calculating the In / S ratio as in (2).
  (4) The same as in (3) but supposing that all H is present in the form (OH). The best approximation for an In / S ratio corresponding to 0.667 as in In_2S_3 is found for sample A with (3)/(4), sample C (3), sample B (2). In sample B no significant amount of H_2O or OH is present and correcting for the small amount of In_2O_3 present in the sample the sample is stoichiometric In_2S_3 (In / S = 0.69-0.65).
- The amount of C was lowest for powder B, but comparable for all samples (0.2-0.8 at.%)

These findings strengthen the hypothesis that powder A and C have been synthesised throughs wet-chemical synthesis routes which include Cl precursors, probably as $InCl_3$ which have not been fully sulphurised.

The degradation/ alteration analysis of the complete evaporation series shows that following (2) even after 670 min. of deposition time (B02) the In / S ratio stays constant at 0.66-0.67. The oxygen content has slightly increased. The residue after 970 min. deposition time consists mainly of In_2O_3. The vapour pressure of In_2O_3 is much lower than the one of In_2S_3 at 720°C and therefore the small amount of In_2O_3 present at the beginning of the evaporation series just remains in the crucible, while the In_2S_3 evaporates.

The compositional analysis revealed several differences for the three as received powders. Powder A and C show a much higher contamination with O, Cl and H than powder B. This is probably due to a wet-chemical synthesis route including Cl containing precursors. Powder B did not show any Cl contamination and lower amounts of O (as received: below 10 at.%). The amount of In_2O_3 present in the beginning of the powder before the evaporation started was shown to remain inside the crucible as an residue. The In / S ratio stayed constant at approximately 0.67 even after 670 min. evaporation if the amount of In bound in In_2O_3 was substracted from the total In amount.

References

[1] A. Jäger-Waldau, *PV Status Report 2008*. ISBN: 978-92-79-10122-9: Joint Research Centre - Institute for Energy, Ispra, Italy, September 2008.

[2] M. Fawer and B. Magyar, *Solarenergie 2008- Stürmische Zeiten vor dem nächsten Hoch*. Bank Sarasin, 2008.

[3] E. Martinot and M. e. a. El-Ashrey, *Renewables 2007 - Global Status Report*. Renewable Energy Policy Network for the 21st Century (www.ren21.net), 2007.

[4] A. Strohm, L. Eisenmann, R. Gebhardt, A. Harding, T. Schlötzer, D. Abou-Ras, and H. Schock, "ZnO/In_2S_3/Cu(In,Ga)Se_2 solar cells fabricated by coherent heterojunction formation," *Thin Solid Films*, vol. 480-481, pp. 162–167, 2005.

[5] R. Miles, K. Hynes, and I. Forbes, "Photovoltaic solar cells: An overview," *Progress in Crystal Growth and Characterisation of Materials Research Bulletin*, vol. 51, no. 1-3, pp. 1–42, 2005.

[6] A. Jäger-Waldau, "Status of thin film solar cells in research, production and the market," *Solar Energy*, vol. 77, pp. 667–678, December 2004 2004.

[7] M. Green, K. Emery, Y. Hishikawa, and W. Warta, "Solar Cell Efficiency Tables (Version 33)," *Progress in Photovoltaics: Research and Application*, vol. 17, pp. 85–94, January 2009.

[8] N. Dhere, "Present status and future prospects of CIGSS thin film solar cells," *Solar Energy Materials and Solar Cells*, vol. 90, pp. 2181–2190, 2006.

[9] U. Rau and H.-W. Schock, *Solar Cells – Materials, Manufacture and Operation*, ch. Cu(In,Ga)Se_2 thin-film solar cells – (IIc-4), pp. 303–349. Elsevier, 2004.

[10] H.-W. Schock and R. Noufi, "CIGS-based solar cells for the next millenium," *Progress in Photovoltaics: Research and Applications*, vol. 8, pp. 151–160, 2000.

[11] I. Repin, M. Contreras, B. Egaas, C. DeHart, J. Scharf, C. Perkins, B. To, and R. Noufi, "19.9%-efficient ZnO/CdS/$CuInGaSe_2$ solar cell with 81.2% fill factor," *Progress in Photovoltaics: Research and Applications*, vol. 16, pp. 235–239, 2008.

[12] C. Kaufmann, A. Neisser, R. Klenk, and R. Scheer, "Transfer of Cu(In,Ga)Se_2 thin film solar cells to flexible substrates using an in situ process control," *Thin Solid Films*, vol. 480, pp. 515–519, June 2005.

[13] R. Klenk, “Characterisation and modelling of chalcopyrite solar cells,” *Thin Solid Films*, vol. 387, no. 1-2, pp. 135–140, 2001.

[14] A. Niemegeers, M. Burgelman, and A. De Vos, “On the CdS/CuInSe$_2$ conduction band discontinuity,” *Applied physics letters*, vol. 67, p. 843, 1995.

[15] D. Schmid, M. Ruckh, and H.-W. Schock, “A comprehensive characterization of the interfaces in Mo/CIS/CdS/ZnO solar cell structure,” *Solar Energy Materials and Solar Cells*, vol. 41-42, pp. 281–294, June 1996.

[16] S. Siebentritt, “Alternative buffer layers for chalcopyrite solar cells,” *Solar Energy*, vol. 77, pp. 767–775, December 2004.

[17] D. Hariskos, R. Menner, E. Lotter, S. Spiering, and M. Powalla, “Magnetron sputtering of indium sulphide as the buffer layer in Cu(In,Ga)Se$_2$-based solar cells,” in *20th European Photovoltaic Solar Energy Conference*, (Barcelona, Spain), pp. 1713–1716, 2005.

[18] N. Naghavi, D. Lincot, C. Björkman, T. Torndahl, C.-H. Fischer, N. Allsop, D. Hariskos, S. Spiering, R. Klenk, S. Buecheler, A. Tiwari, A. Ennaoui, T. Nakada, K. Kushiya, C. Guillen, J. Herrero, D. Abou-Ras, N. Barreau, and R. Menner, “Buffer layers and transparent conducting oxides for chalcopyrite-type thin film photovoltaic: Present status and current developments,” *Progress in Photovoltaics*, vol. -, pp. –, submitted.

[19] M. Contreras, T. Nakada, M. Hongo, A. Pudov, and J. Sites, “ZnO/ZnS(O,OH)/Cu(In,Ga)Se$_2$/Mo solar cell with 18.6% efficiency,” in *Proceedings of the World Conference on Photovoltaic Energy Conversion, Osaka, Japan*, vol. 3, pp. 570–573, 2003.

[20] A. Ennaoui, S. Siebentritt, M. Lux-Steiner, F. Karg, and W. Riedle, “High efficiency Cd-free CIGSSe thin film solar cells with solution grown zinc compound buffer layers,” *Solar Energy Materials and Solar Cells*, vol. 67, p. 31, March 2001.

[21] C. Platzer-Björkman, J. Kessler, and L. Stolt, “Atomic layer deposition of Zn(O,S) buffer layers for high efficiency Cu(In,Ga)Se$_2$ solar cells,” in *Proceedings of the 3rd World Conference on Photovoltaic Energy Conversion, Osaka, Japan*, pp. 461–464, 2003.

[22] T. Negami, T. Aoyagi, T. Satoh, S. Shimakawa, S. Hayashi, and Y. Hashimoto, “Cd free CIGS solar cells fabricated by dry processes,” in *Proceedings of the 29th IEEE Photovoltaic Specialist Conference, New Orleans, USA*, pp. 656–659, 2002.

[23] H. Muffler, M. Bär, C.-H. Fischer, R. Gay, F. Karg, and M. Lux-Steiner, “Sulfidic Buffer Layers for Cu(InGa)(S,Se)$_2$ Solar Cells Prepared by Ion Layer Gas Reaction (ILGAR),” in *Proceedings of the 28th IEEE Photovoltaic Specialist Conference, Anchorage, Alaska, USA*, pp. 610–613, 2000.

[24] Y. Ohtake, S. Chaisitsak, A. Yamada, and M. Konagai, “Characterization of $ZnIn_xSe_y$ Thin Films as a Buffer Layer for High Efficiency $Cu(InGa)Se_2$ Thin-Film Solar Cells,” *Japanese Journal of Applied Physics*, vol. 37, pp. 3220–3225, 1998.

[25] S. Chaisitsak, Y. Tokita, H. Miyazaki, R. Mikami, A. Yamada, and M. Konagai, “Control of preferred orientation for $Cu(In,Ga)Se_2$ thin films and its effect on solar cell performance,” in *Proceedings of the 17th European Solar Energy Conference, Munich, Germany*, pp. 1011–1014, 22-26 October 2001.

[26] N. Naghavi, S. Spiering, M. Powalla, B. Cavanna, and D. Lincot, “High-Efficiency Copper Indium Gallium Diselenide (CIGS) Solar Cells with Indium Sulphide Buffer Layers Deposited by Atomic Layer Chemical Vapor Deposition (ALCVD),” *Progress in Photovoltaics: Research and Applications*, vol. 11, no. 7, pp. 437–443, 2003.

[27] N. Allsop, A. Schönmann, H.-J. Muffler, M. Bär, M. Lux-Steiner, and C.-H. Fischer, “Spray-ILGAR indium sulfide buffers for $Cu(In,Ga)(S,Se)_2$ solar cells,” *Progress in Photovoltaics: Research and Applications*, vol. 13, pp. 607–616, 2005.

[28] D. Hariskos, M. Ruckh, U. Rühle, T. Walter, H. Schock, J. Hedström, and L. Stolt, “A novel cadmium free buffer layer for $Cu(In,Ga)Se_2$ based solar cells,” *Solar Energy Materials and Solar Cells*, vol. 41/42, pp. 345–353, 1996.

[29] S. Spiering, L. Bürkert, D. Hariskos, M. Powalla, B. Dimmler, C. Giesen, and M. Heuken, “MOCVD indium sulphide for application as a buffer layer in CIGS solar cells,” *Thin Solid Films*, vol. 517, pp. 2328–2331, February 2009.

[30] N. Barreau, “Indium sulfide and relatives in the world of photovoltaics,” *Solar Energy*, vol. in press, pp. 1–9, 2008.

[31] P. Pistor, R. Caballero, D. Hariskos, V. Izquierdo-Roca, R. Wächter, S. Schorr, and R. Klenk, “Quality and stability of compound indium sulphide as source material for buffer layers in $Cu(In,Ga)Se_2$ solar cells,” *Solar Energy Materials and Solar Cells*, vol. 93, pp. 148–152, January 2009.

[32] C. Kittel, *Introduction to Solid State Physics.* John Wiley and Sons, Inc, New York, Chichester, Brisbane, Toronto, Singapore, 6th ed., 1986.

[33] R. Fahrenbruch, A.L. Bube, *Fundamentals of Solar Cells - Photovoltaic Solar Energy Conversion*, vol. 1. 111 fifth Avenue, New York, New York 10003: Academic Press, 1983.

[34] P. Würfel, *Physik der Solarzellen.* Spektrum Akademischer Verlag, Heidelberg Berlin, 2000.

[35] H. Lewerenz, H.J. Jungblut, *Photovoltaik- Grundlagen und Anwendungen*, vol. 1. Springer Verlag, 1995.

[36] W. Schottky, “Vereinfachte und erweiterte Theorie der Randschichtgleichrichter,” *Zeitschrift für Physik*, vol. 118, pp. 539–542, Februar 1942.

[37] W. Gärtner, "Depletion-Layer Photoeffects in Semiconductors," *Physical Review of Scientific Instruments*, vol. 116, pp. 84–87, October 1959.

[38] R. Klenk and H.-W. Schock, "Photocurrent collection in thin film solar cells - calculation and characterization for $CuGaSe_2$/(Zn,Cd)S," in *Proceedings of the 12th European Photovoltaic Solar Energy Conference*, (Amsterdam, Netherlands), p. 1588, 11th-15th April 1994.

[39] W. Schockley and W. Read, "Statistics of the Recombination of Electrons and Holes," *Physical review*, vol. 87, no. 5, pp. 835–842, 1952.

[40] I. Hengel, *Ladungsträgertransport und Rekombinationsmechanismen in Chalkopyrit-Dünnschichtsolarzellen.* Phd thesis, Freie Universität Berlin, Fachbereich Physik, 2000.

[41] T. Walter, R. Herberholz, and H. Schock, "Distribution of Defects in Polycrystalline Chalcopyrite Thin Films," *Solid State Phenomena*, vol. 51-52, pp. 309–316, 1996.

[42] U. Rau, "Tunneling-enhanced recombination in Cu(In,Ga)Se_2 heterojunction solar cells," *Applied Physics Letters*, vol. 74, pp. 111–113, 1999.

[43] M. Turcu and U. Rau, "Fermi level pinning at CdS/Cu(In,Ga)$(S,Se)_2$ interfaces: effect of chalcopyrite alloy composition," *Journal of Physics and Chemistry of Solids*, vol. 64, no. 9-10, pp. 1591–1595, 2003.

[44] V. Nadenau, U. Rau, A. Jasenek, and H. Schock, "Electronic properties of $CuGaSe_2$-based heterojunction solar cells. Part I. Transport analysis," *Journal of Applied Physics*, vol. 87, no. 1, pp. 584–593, 2000.

[45] F. Padovani and R. Stratton, "Field and thermionic field emission in Schottky barriers," *Solid-State Electronics*, vol. 9, pp. 695–707, July 1966.

[46] S. Hegedus and W. Shafarman, "Thin Film Solar Cells: Device Measurements and Analysis," *Progress in Photovoltaics*, vol. 12, no. 2-3, pp. 155–176, 2004.

[47] H. Ansell and R. Boorman, "Phase relationships in the In-S system," *Journal of the Electrochemical Society*, vol. 118, no. 1, pp. 133–136, 1971.

[48] A. Zavrazhnow, A. Naumov, P. Anorov, E. Goncharov, V. Sidei, and V. Pervov, "T-x Phase Diagram of the In-S System," *Inorganic Materials*, vol. 42, no. 12, pp. 1294–1298, 2006.

[49] A. Likforman, M. Guittard, A. Tomas, and J. Flahaut, "Mise en évidence d'une solution solide de type spinelle dans le diagramme de phase du systeme In—S," *Journal of Solid State Chemistry*, vol. 34, pp. 353–359, October 1980.

[50] A. Miller and A. Searcy, "Thermodynamic Stabilities as a Function of Composition for Indium Sulphide Phases from Mass Spectroscopy Intensity vs. Time Data," *The Journal of Physical Chemistry*, vol. 69, no. 11, pp. 3826–3832, 1965.

[51] W. Duffin and J. Hogg, “Crystalline phases in the system In-In_2S_3,” *Acta Crystallografica*, vol. 20, pp. 566–569, 1966.

[52] T. Gödecke and K. Schubert, “On the Phase Diagram InS_M,” *Zeitschrift für Metallkunde*, vol. 76, pp. 358–364, May 1985.

[53] R. Diehl, C. Carpentier, and R. Nitsche, “The crystal structure of γ-In_2S_3 stabilized by As or Sb,” *Acta Crystallografica B*, vol. 32, pp. 1257–1260, 1976.

[54] G. King, “The space group of beta-In_2S_3,” *Acta Crystallographica*, vol. 15, p. 512, May 1962.

[55] J. Goodyear and G. Steigmann, “Twinning in a Cation-deficient Spinel Structure,” *Proceedings of the Physical Society*, vol. 78, pp. 491–495, October 1961.

[56] G. Steigmann, H. Sutherland, and J. Goodyear, “The crystal structure of beta-In_2S_3,” *Acta Crystallographica*, vol. 19, pp. 967–971, December 1965.

[57] J. V. Landuyt, H. Hatwell, and S. Amelinckx, “The domain structure of beta-In_2S_3 ”single crystals” due to the ordering of indium vacancies,” *Materials Research Bulletin*, vol. 3, no. 6, pp. 519–528, 1968.

[58] H. Hahn and W. Klingler, “Ueber die Kristallstruktur des In_2S_3 und In_2Te_3,” *Zeitschrift fuer anorganische Chemie*, vol. 260, no. 1-3, pp. 97–109, 1949.

[59] J. Binsma, L. Gilling, and J. Bloem, “Phase relations in the system Cu_2S-In_2S_3,” *Journal of Crystal Growth*, vol. 50, no. 2, pp. 429–436, 1980.

[60] D. Bartzokas, C. Manolikas, and J. Spyridelis, “Electron Microscopic Study of the Destabilization of Stabilized γ-Phase of Indium Sesquisulphide,” *Physica Status Solidi (a)*, vol. 47, pp. 459–476, 1978.

[61] S. Schorr and G. Geandier, “In-situ investigation of the temperature dependent structural phase transition in $CuInSe_2$ by synchrotron radiation,” *Crystal Research and Technology*, vol. 41, no. 5, pp. 450–457, 2006.

[62] J. Rodriguez-Carvajal, “Fullprof suite: Crystallographic tools for rietveld, profile matching & integrated intensity refinements of x-ray and/or neutron data.” http://www.ill.eu/sites/fullprof/index.html.

[63] J. Rodriguez-Carvajal, “Recent Developments of the Program FULLPROF,” *Commission on Powder Diffraction (IUCr)-Newsletter*, vol. 26, pp. 12–19, 2001.

[64] B. Asenjo, A. Chaparro, M. Gutiérrez, J. Herrero, and C. Maffiote, “Study of the electrodeposition of In_2S_3 thin films,” *Thin Solid Films*, vol. 480-481, pp. 151–156, June 2005.

[65] T. Asikainen, M. Ritala, and M. Leskelä, “Growth of In_2S_3 thin films by atomic layer epitaxy,” *Applied Surface Science*, vol. 82/83, pp. 122–125, December 1994.

[66] R. Nomura, K. Konishi, and H. Matsuda, "Single-source organometallic chemical vapour deposition process for sulphide thin films: Introduction of a new organometallic precursor Bu(n)In(SPr)j2 and preparation of In2S3 thin films," *Thin Solid Films*, vol. 198, no. 1-2, pp. 339–345, 1991.

[67] R. Yoosuf and M. Jayaraj, "Optical and photoelectrical properties of beta-In_2S_3 thin films prepared by two-stage process," *Solar Energy Materials and Solar Cells*, vol. 89, pp. 85–94, October 2005.

[68] N. Barreau, S. Marsillac, J. Bernède, T. Nasrallah, and S. Belgacem, "Optical Properties of Wide Band Gap Indium Suphide Thin Films obtained by Physical Vapour Deposition," *Physica Status Solidi (a)*, vol. 184, pp. 179–186, March 2001.

[69] S. Narushima, M. Hiroki, K. Ueda, K.-I. Shimizu, T. Kamiya, M. Hirano, and H. Hosono, "Electrical properties and local structure of n-type conducting amorphous indium sulphide," *Philosophical Magazine Letters*, vol. 84, no. 10, pp. 665–671, 2004.

[70] S. Spiering, S. Chowdhury, A. Dresel, D. Hariskos, A. Eicke, and M. Powalla, "Evaporated indium sulphide as buffer layer in Cu(In,Ga)Se_2-based solar cells," in *21st European Photovoltaic Solar Energy Conference 2006* (J. Poortmans, H. Ossenbrink, E. Dunlop, and P. Helm, eds.), (Dresden), pp. 1847–1852, WIP- Renewable Energies, 2006.

[71] A. Timoumi, H. Bouzouita, M. Kanzari, and B. Rezig, "Fabrication and characterization of In_2S_3 thin films deposited by thermal evaporation technique," *Thin Solid Films*, vol. 480-481, pp. 124–128, 2005.

[72] P. Kumar, T. John, K. C.S., K. Vijayakumar, T. Abe, and Y. Kashiwaba, "Effects of thickness and post deposition annealing on the properties of evaporated In_2S_3 thin films," *Journal of Material Science*, vol. 41, no. 17, pp. 5519–5525, 2006.

[73] F. Jacob, N. Barreau, S. Gall, and J. Kessler, "Performance of $CuIn_{(1-x)}Ga_xSe_2$/(PVD)In_2S_3 solar cells versus gallium content," *Thin solid Films*, vol. 515, pp. 6028–6031, 2007.

[74] Testbourne LTD, UK. http://www.testbourne.com/.

[75] Alfa Aesar, GmbH & Co KG., Germany. http://www.alfa-chemcat.com/.

[76] Strem Chemicals, Inc., Germany. http://www.strem.com/.

[77] E. Pascher, Labor für Mikroanalyse. http://www.mikrolabor.info/, An der Pulvermühle 1, 53424 Remagen, Germany, 2008.

[78] A. Miller and A. Searcy, "Sublimation of Indium Sesquisulfide," *Journal of Physical Chemistry*, vol. 67, no. 11, pp. 2400–2404, 1963.

[79] K. Kambas, A. Anagnostopoulos, S. Ves, B. Ploss, and J. Spyredelis, "Optical Absorption Edge Investigation of $CdInS_4$ and beta-In_2S_3 Compounds," *Physica Status Solidi (b)*, vol. 127, no. 1, pp. 201–208, 1985.

[80] R. Bube and W. McCarroll, "Photoconductivity in indium sulphide powders and crystals," *Journal of Physics and Chemistry of Solids*, vol. 10, pp. 333–335, August 1959.

[81] H. Nakanishi, S. Endo, and T. Irie, "Fundamental Optical Absorption in Crystals of the $CdIn_2S_4$-In_2S_3 System," *Japanese Journal of Applied Physics*, vol. 19-Supplement 3, no. Supplement 3 (Proceedings of the 4th International Conference on Ternary and Multinary Compounds, Tokyo, 1980), pp. 261–266, 1980.

[82] S. Radautsan, N. Syrbu, V. Tezlevan, K. Sherban, and E. Strumban, "Optical and Photoelectrical Properties and Band Structure of Single Crystals of Solid Solutions of the System $(CdS)_{3x}$-$(In_2S_3)_{1-x}$," *Physica Status Solidi (a)*, vol. 15, no. 1, pp. 295–302, 1973.

[83] S.-H. Choe, T.-H. Bang, N.-O. Kim, H.-G. Kim, C.-I. Lee, M.-S. Jin, S.-K. Oh, and W.-T. Kim, "Optical properties of β-In_2S_3 and β-In_2S_3:Co^{2+} single crystals," *Semiconductor Science and Technology*, vol. 16, pp. 89–102, February 2001.

[84] N. Barreau, "Bandgap properties of indium sulfide thin-films grown by co-evaporation," *Thin Solid Films*, vol. 517, pp. 2316–2319, February 2009.

[85] N. Barreau, J. Bernède, and S. Marsillac, "Study of the new b-In_2S_3 containing Na thin films. Part II: Optical and electrical characterization of thin films," *Journal of Crystal Growth*, vol. 241, no. 1-2, pp. 51–56, 2002.

[86] N. Barreau, J. Bernède, and J. Kessler, "Influence of oxygen, sodium and copper on the properties of PVD-grown indium sulfide," in *Proceeding of the 19th European Solar Energy Conference*, (Paris, France), pp. 223–226, 7-11 June 2004.

[87] T. Nakada, M. Mizutami, Y. Hagiwara, and A. Kunioka, "High-efficiency Cu(In,Ga)Se_2 thin-film solar cells with a CBD-ZnS buffer layer," *Solar Energy Materials and Solar Cells*, vol. 67, no. 1-4, pp. 255–260, 2001.

[88] M. Igalson and C. Platzer-Björkman, "The influence of buffer layer on the transient behavior of thin film chalcopyrite devices," *Solar Energy Materials and Solar Cells*, vol. 84, pp. 93–103, 2004.

[89] M. Powalla and B. Dimmler, "Scaling up issues of CIGS solar cells," *Thin Solid Flms*, vol. 361-362, pp. 540–546, 2000.

[90] Hariskos, D., Zentrum für Sonnenenergie- und Wasserstoff-Forschung, Stuttgart, Germany. personal communication.

[91] N. Allsop, A. Schönmann, A. Belaidi, H.-J. Muffler, B. Mertesacker, W. Bohne, E. Strub, J. Röhrich, M. Lux-Steiner, and C.-H. Fischer, "Indium sulfide thin films deposited by the spray ion layer gas reaction technique," *Thin Solid Films*, vol. 513, pp. 52–56, August 2006.

[92] U. Rau, D. Braunger, R. Herberholz, and H.-W. Schock, “Oxygenation and air-annealing effects on the properties of Cu(In,Ga)Se_2 films and devices,” *Journal of Applied Physics*, vol. 86, no. 1, pp. 497–505, 1999.

[93] M. Igalson, P. Zabierowski, D. Przado, A. Urbaniak, M. Edoff, and W. Shafarman, “Understanding defect-related issues limiting efficiencies of CIGS solar cells,” *Solar Energy Materials and Solar Cells*, vol. -, pp. – Corrected Proof, Article in Press, 2009.

[94] M. Turcu and U. Rau, “Compositional trends of defect energies, band alignments, and recombination mechanism in the Cu(In,Ga)(Se,S)$_2$ alloy system,” *Thin Solid Films*, vol. 431-432, pp. 158–62, 2003.

[95] M. Bär, N. Allsop, I. Lauermann, and C.-H. Fischer, “Deposition of In_2S_3 on Cu(In,Ga)(S,Se)$_2$ thin film solar cell absorbers by spray ion layer gas reaction: Evidence of strong interfacial diffusion,” *Applied Physics Letters*, vol. 90, no. 13, pp. 132118–1–3, 2007.

[96] D. Abou-Ras, “Interfacial layer formations between Cu(In,Ga)Se_2 and In_xS_y layers,” *Journal of Applied Physics*, vol. 98, pp. 123512 (1–7), 2005.

[97] D. Abou-Ras, D. Rudman, G. Kostorz, S. Spiering, M. Powalla, and A. Tiwari, “Microstructural and chemical studies of interfaces between Cu(In,Ga)Se_2 and In_2S_3 layers,” *Journal of Applied Physics*, vol. 97, p. 084908, 2005.

[98] N. Barreau, S. Gall, S. Marsillac, J. Kessler, and A. Rockett, “The influence of copper and sodium diffusion across the Cu(In,Ga)Se_2/In_2S_3 interface on solar cell properties,” in *20th European Photovoltaic Solar Energy Conference*, (Barcelona, Spain), pp. 1717–1720, 2005.

[99] M. Seah and W. Dench, “Quantitative electron spectroscopy of surfaces: A standard data base for electron inelastic mean free paths in solids,” *Surface and Interface Analysis*, vol. 1, no. 1, pp. 2–11, 1979.

[100] S. Spiering, A. Eicke, D. Hariskos, M. Powalla, N. Naghavi, and D. Lincot, “Large-area Cd-free CIGS solar modules with In_2S_3 buffer layer deposited by ALCVD,” *Thin Solid Films*, vol. 451-452, pp. 562–566, 2004.

[101] F. Schaefers, M. Mertin, and M. Gorgoi, “KMC-1: A high resolution and high flux soft x-ray beamline at BESSY,” *Review of Scientific Instruments*, vol. 78, pp. 123102 (1–14), December 2007.

[102] M. Gorgoi, S. Svensson, F. Schäfers, G. Öhrwall, M. Mertin, P. Bressler, O. Karis, H. Siegbahn, A. Sandell, H. Rensmo, W. Doherty, C. Jung, W. Braun, and W. Eberhardt, “High Kinetic Energy Photoelectron Spectroscopy Facility at BESSY: Progress and First Results,” *Nucl. Instr. Meth.*, vol. (accepted), pp. 1–12, 2008.

[103] “http://www.bessy.de/upload/bitpdfs/hike.pdf.”

[104] S. Tanuma, C. Powell, and D. Penn, “Calculations of electron inelastic mean free paths. V. Data for 14 organic compounds over the 50-2000 eV range,” *Surface and Interface Analysis*, vol. 21, pp. 165–176, 1993.

[105] S. Tougaard, “QUASES IMFP TPP2M: IMFP calculation by the TPP2M formula.” http://www.quases.com/.

[106] N. Barreau, J. Bernède, C. Deudon, L. Brohan, and S. Marsillac, “Study of the new b-In_2S_3 containing Na thin films Part I: Synthesis and structural characterization of the material,” *Journal of Crystal Growth*, vol. 241, no. 1-2, pp. 4–14, 2002.

[107] L. Kazmerski, O. Jamjoum, P. Ireland, S. Deb, R. Mickelsen, and W. Chen, “NIST XPS Database Entry,” *Journal of Vacuum Science and Technology*, vol. 19, pp. 467–471, September 1981.

[108] J. Reichardt, “X-ray-emission- and photoelecton-spectroscopy of chalcopyrite thin-film solar cells,” Master’s thesis, Humboldt Universität Berlin, Germany, 2003.

[109] D. Schmid, M. Ruckh, and H.-W. Schock, “Photoemission studies on Cu(In,Ga)Se_2 thin films and related binary selenides,” *Applied Surface Science*, vol. 103, pp. 409–429, December 1996.

[110] D. Liao and A. Rockett, “Cu depletion at the CuInSe2 surface,” *Applied Physics Letters*, vol. 82, p. 2829, April 2003.

[111] C. Battistoni, L. Gastaldi, A. Lapiccirella, G. Mattogno, and C. Viticoli, “(NIST XPS database entry),” *Journal of Physics and Chemistry of Solids*, vol. 47, p. 899, 1985.

[112] J. Yeh and I. Lindau, “Atomic subshell photoionization cross sections and asymmetry parameters: $1< Z <103$,” *Atomic Data and Nuclear Data Tables*, vol. 32, pp. 1–155, January 1985.

[113] VG Scientifics, “Specifications of the VG CLAM IV electron energy analyser.”

[114] W. Jost, *Diffusion in Solids, Liquids, Gases*. Academic Press Inc., Publishers, New York, 1952.

[115] F. Py, M. Womes, J. Durand, J. Olivier-Fourcade, J. Jumas, J. Esteva, and R. Karnatak, “Copper in In_2S_3: a study by X-ray diffraction, diffuse reflectance and X-ray absorption,” *Journal of Alloys and Compounds*, vol. 178, no. 1-2, pp. 297–304, 1992.

[116] L. Gastaldi and L. Scaramuzza, “Single-crystal structure analysis of the spinel copper pentaindium octasulphide,” *Acta Crystallografica B*, vol. 36, pp. 2751–2753, 1980.

[117] A. Lafond, C. Guillot-Deudon, S. Harel, A. Mokrani, N. Barreau, S. Gall, and J. Kessler, “Structural study and electronic band structure investigations of the solid solution $Na_xCu_{(1-x)}In_5S_8$ and its impact on the Cu(In,Ga)Se_2/In_2S_3 interface of solar cells,” *Thin Solid Films*, vol. 515, no. 15, pp. 6020–6023, 2007.

[118] J. Crank, *The Mathematics of Diffusion.* Oxford Science Publications, 2nd edition ed., 1975.

[119] H. Carslaw and J. Jaeger, *Conduction of Heat in Solids.* Oxford at the Claredon Press, 2nd edition ed., 1959.

[120] D. Abou-Ras, *Structural and chemical analyses of buffer layers in Cu(In,Ga)Se$_2$ thin-film solar cells.* PhD thesis, Swiss Federal Institute of Technology, 2005.

[121] M. Rusu, T. Glatzel, A. Neisser, C. Kaufmann, S. Sadewasser, and M. Lux-Steiner, "Formation of the physical vapor deposited CdS/Cu(In,Ga)Se$_2$ interface in highly efficient thin film solar cells," *Applied Physics Letters*, vol. 88, pp. 143510 / 1–3, 2006.

[122] Würth Solar GmbH & Co.KG. www.wuerth-solar.de, 30.04.2009.

[123] G. Voorwinden, R. Kniese, and M. Powalla, "In-line Cu(In,Ga)Se$_2$ co-evaporation processes with graded band gaps on large substrates," *Thin Solid Films*, vol. 431-432, pp. 538–542, May 2003.

[124] D. Sands, *Introduction to crystallography.* Physical Chemistry Monograph Series, W.A. Benjamin, New York, Amsterdam, 1969.

[125] W. Bragg, "The diffraction of short electromagnetic waves by a crystal," *Proceedings of the Cambridge Philosophical Society*, vol. 17, pp. 43–57, 1913.

[126] R. Young, H. Rietveld, E. Prince, T. Sabine, R. Hill, J. Richardson, and R. e. a. Snyder, *The Rietveld Method.* No. 5 in IUCr Monographs on Crystallography 5, Internation Union of Crystallography, Oxford Science Press, 1993.

[127] H. Rietveld, "A Profile Refinement Method for Nuclear and Magnetic Structures," *Journal of Applied Crystallography*, vol. 2, p. 65, June 1969.

[128] J. Rodriguez-Carvajal, "FULLPROF: A Program for Rietveld Refinement and Pattern Matching Analysis," in *Abstracts of the Satellite Meeting on Powder Diffraction of the XV Congress of the IUCR*, (Toulouse, France), p. 127, 1990.

[129] L. Cusker, R. Von Dreele, D. Cox, D. Louer, and P. Scardi, "Rietveld refinement guidelines," *Journal of Applied Crystallography*, vol. 32, pp. 36–50, 1999.

[130] G. Smith, *Surface Analysis by Electron Spectroscopy - Measurement and Application.* Updates in Applied Physics and Electrical Technology, Plenum Press, New York and London, 1994.

[131] J. Moulder, W. Stickle, P. Sobol, and K. Bomben, *Handbook of X-ray Photoelectron Spectroscopy.* Perkin-Elmer Corporation, Physical Electronics Division, Minnesota, USA, 1992.

[132] M. Seah, D. Briggs, J. Rivière, S. Hofmann, and R. Olson, *Practical Surface Analysis - by Auger and X-ray Photoelectron Spectroscopy.* John Wiley and Sons, Chichester, New York, Brisbane, Toronto, Singapore, 1983.

[133] H. Hertz, "Ueber einen Einfluss des ultravioletten Lichtes auf die electrische Entladung," *Annalen der Physik und Chemie*, vol. 267, no. 8, pp. 983–1000, 1887.

[134] S. Tanuma, C. Powell, and D. Penn, "Calculation of Electron Inelastic Mean Free Paths for 31 Materials," *Surface and Interface Analysis*, vol. 11, pp. 577–589, November 1988.

[135] S. Tanuma, C. Powell, and D. Penn, "Calculations of electron inelastic mean free paths. II. Data for 27 elements over the 50-2000 eV range," *Surface and Interface Analysis*, vol. 17, pp. 911–926, 1991.

[136] L. Weinhardt, *Elektronische und chemische Eigenschaften von Grenzflächen und Oberflächen in optimierten Cu(In,Ga)(S,Se)2 Dünnschichtsolarzellen.* PhD thesis, Bayrische Julius-Maximilians-Universität Würzburg, 2005.

[137] M. Seah, G. Smith, and M. Anthony, "(NIST XPS database entry)," *Journal of Surface and Interface Analysis*, vol. 15, p. 293, 1990.

[138] N. Rega, *Photolumineszenz von epitaktischen Cu(In,Ga)Se_2-Schichten.* PhD thesis, Freie Universität Berlin, Germany, 2004.

[139] J. L. Pankove, *Optical processes in semiconductors*, vol. 1. Dover Publications, Inc New York, USA, 1975.

[140] L. Aldon, M. Uhrmacher, C. Branci, L. Ziegler, J. Roth, P. Schaaf, H. Metzner, J. Olivier-Fourcade, and J. Jumas, "Pertubed angular correlation study of the thiospinel beta-In_2S_2 ," *Physical Review B*, vol. 58, no. 17, pp. 11303–11312, 1998.

[141] R. Diehl and R. Nitsche, "Vapour Growth of three In_2S_3 Modifications by Iodine Transport," *Journal of Crystal Growth*, vol. 28, pp. 306–309, 1975.

Statement

I hereby declare that this submission is my own work and that, to the best of my knowledge and belief, it contains no material previously published or written by another person, except where due acknowledgement is made in the text. I also declare that the intellectual content of this thesis is the product of my own work, even though I may have received assistance from others on style, presentation and language expression.

Erklärung

Hiermit versichere ich, dass ich diese Arbeit selbständig verfasst und keine anderen als die angegebenen Hilfsmittel verwendet habe. Die Arbeit enthält, nach meinem besten Wissen und Gewissen, weder bereits von anderen Personen veröffentlichte Materialien noch wurden jegliche Teile dieser Arbeit bereits einer anderen Universität oder ähnlichen Bildungsstätte zur Erlangung eines Abschlusses oder Titels vorgelegt, außer entsprechendes Material ist als solches gekennzeichnet.

Berlin, 29.05.2009

Paul Pistor - List of Publications - May 2009

- **P. Pistor**, N. Allsop, W. Braun, R. Caballero, C. Camus, C. Fischer, M. Gorgoi, A. Grimm, B. Johnson, T. Kropp, S. Lehmann, H. Mönig, S. Schorr, A. Weber, R. Klenk, *"Cu in In_2S_3: interdiffusion phenomena analysed by high kinetic energy X-ray photoelectron spectroscopy"*. Physica Status Solidi (a) (2008), vol. 206, pp. 1059 -1062

- H, Mönig, I. Lauermann, A. Grimm, C. Camus, C. Kaufmann, **P. Pistor**, C. Jung, T. Kropp, M. Lux-Steiner, C. Fischer, *"Controlled variation of the information depth by angle dependent soft x-ray emission spectroscopy: A study on polycrystalline Cu(In,Ga)Se_2"*. Applied Surface Science (2008), vol. 255, pp. 2474-2477

- **P. Pistor**, R. Caballero, D. Hariskos, V. Izquierdo-Roca, R. Wächter, R. Klenk: *"Physical vapour deposition of compound In_2S_3 as buffer layer in Cu(In,Ga)Se_2 solar cells: material characterisation and device performance"*. Solar Energy Materials and Solar Cells (2008), vol. 93, pp. 148-152

- **P. Pistor**, R. Klenk: *"On the advantage of a buried pn-junction in chalcopyrite solar cells: An urban legend?"*. Oral presentation and published in: Proceedings of NUMOS (International Workshop on Numerical Modelling of Thin Film Solar Cells), Gent, 28-30 March 2007. , 2007, pp. 179-182, Workshop Proceedings

- M. Pfänder; E. Lückert, **P. Pistor**: *"Infrared temperature measurements on solar trough absorber tubes"*. Solar Energy (2007), vol.81, no.5, pp. 629-635

- **P. Pistor**, V. Chu, D. Prazeres, J. Conde, *"pH sensitive photoconductor based on poly(para-phenylene-vinylene)"*. Sensors and Actuators B (Chemical) (2007), vol.123, no.1, pp. 153-157

- I. Kötschau, A. Weber, **P. Pistor**, I. Lauermann, C. Fischer, H. Schock, *"Advanced X-ray methods for chalcogenide thin film analysis"*. Thin Solid Films, 515 (2007), pp. 5992-5996

- M. Bär, S. Lehmann, M. Rusu, A. Grimm, I. Kötschau, I. Lauermann, **P. Pistor**, S. Sokoll, T. Schedel-Niedrig, M. Lux-Steiner, C. Fischer, L. Weinhardt, C. Heske, C. Jung: *"Cd^{2+}/NH_3 treatment-induced formation of a CdSe surface layer on $CuGaSe_2$ thin-film solar cell absorbers"*. Applied Physics Letters 86 (2005), pp. 222107/1-3

- S. Lehmann, M. Bär, D. Fuertes-Marron, **P. Pistor**, S. Wiesner, M. Rusu, I. Kötschau, I. Lauermann, A. Grimm, S. Sokoll, C. Fischer, T. Schedel-Niedrig, M. Lux-Steiner, C. Jung: *"$CuGaSe_2$-$CuGa_3Se_5$ phase transition in CCSVT-grown thin films"*. Thin Solid Films 511-512 (2006), pp. 623-627

- M. Powalla, F. Kessler, D. Hariskos, G. Voorwinden, A. Tiwari, D. Bremaud, M. Edoff, S. Schleussner, L. Stolt, R. Dimmler, R. Wächter, R. Klenk, **P. Pistor**, D. Abou-Ras, H. Schock, O. Kerrec, P. Grand, D. Lincot, N. Naghavi, A. Perez-Rodriguez, S. Auvray: *"Highly productive manufacturing of CIS-based large-area*

modules.”. In: 22nd European Photovoltaic Solar Energy Conference, 3 - 7 September 2007, Milan, Italy, 2007, pp. 1930-1934, Conference Proceedings

Curriculum Vitae

For reasons of dataprotection, the curriculum vitae is not included in the online version.

Acknowledgements

This is the time and place to thank the many helping hands that supported me on my way through this work. First of all, I would like to thank Prof. Lux-Steiner for accepting me as a PhD student at her department at the Helmholtz-Zentrum Berlin, for her guidance through this work and the many hours she spent discussing with me. I am also very thankful to Prof. Brewer to volunteer to act as co-examiner for this work.

My tutor Reiner Klenk for excellent tutoring, with your knowledge and experience, good questions and discussions, lots of patience and a very good sense of criticism you were very helpful during this journey.

I am gratefull to all the current and former members of our group for the discussions, help in the day to day work and the very nice working atmosphere.

I would like to thank all people that assisted me in the preparation of solar cells, namely Raquel Caballero, Thorsten Rissom, Christian Kaufmann from the SE3 department providing me with Cu(In,Ga)Se_2 absorbers, Dimitri Hariskos, Georg Voorwinden and Rolf Wächter for Cu(In,Ga)Se_2 absorbers from the Zentrum für Sonnenenergie- und Wasserstoff-Forschung / Würth Solar, and Michael Kirsch, Carola Kelch and Katleen Kraft for providing CdS, ZnO, metal grids and technical assistance.

Partial financial support for this work by the European Commission under contract number FP-6-019757 (LARCIS) is gratefully acknowledged.

Many thanks go to:

- Sebastian Lehmann and Susan Schorr for helping me with the synchrotron-based XRD measurements at ESRF and to master the complicated first steps with the FULLPROF program on Rietveld refinements. Sebastian, thanks for your patience to discuss crystallographic stuff with me.

-Roland Mainz for sharing his IGOR applets with me and the rest of the department and many fruitful discussion on solar cell physics.

-Daniel Abou-Ras and Sebastian Schmidt for help on the TEM preparation and the EDX measurements. I hope we can do some more and of course thanks a lot for getting me in the woods and the many discussions on In_2S_3.

-Everybody from the CISSY-group for letting me use the CISSY and enabling me the participation at the BESSY beamtimes and many discussions concerning XPS and XES. Mihaela Gorgoi for technical assistance at the HIKE beamline at BESSY.

-Although finally the interesting results concerning the surface photovoltage have not found there way into this work I would like to thank Thomas Dittrich for help and discussions.

-The soccer team of the HZB for many bruises and lots of fun.

-All the people around me that showed comprehension and patience especially during the end of this time.

Special thanks go to my parents for the continuous and unlimited support at all time.

Finally and most of all I thank you, enana, for being there when I need you, giving me strength in the hard times and enjoying with me the happy times. And of course Leo (and Otto) for having lots of patience with the me these days.

Zusammenfassung

In dieser Arbeit wurden thermisch verdampfte In_2S_3-Schichten als Pufferschicht in Dünnschicht-Solarzellen auf der Basis von Cu(In,Ga)Se_2 verwendet. Ziel der Arbeit war es, hocheffiziente Solarzellen zu präparieren, sie systematisch zu untersuchen und so die Faktoren zu identifizieren, die die Wirkungsgrade dieser Solarzellen limitieren.

Ausgangspunkt für die Untersuchungen waren hocheffiziente Cu(In,Ga)Se_2-Solarzellen mit konventioneller CdS-Pufferschicht aus einer chemischen Badabscheidung. Auf die Rolle des Puffers bei der Ausbildung eines effizienten pn-Übergangs und auf alternative Pufferkonzepte wurde am Anfang der Arbeit eingegangen. Die allgemeinen theoretischen Zusammenhänge, die die Grundlage für die physikalische Interpretation von Dünnschicht-Solarzellen bilden, wurden eingangs in einem eigenen Kapitel behandelt.

Hochwertige, kristalline $In_{2+x}S_3$-Referenzproben wurden erfolgreich aus den Elementen synthetisiert und als Referenzen für eine Bestimmung der Kristallstruktur verwendet. Unter Bezug auf Literaturdaten konnten die tetragonale, kubische und trigonale Struktur von drei Modifikationen im Temperaturbereich von 31 °C bis 1040 °C mit Hilfe von Röntgenbeugung identifiziert und die Strukturdaten nach der Rietveld-Methode verfeinert werden. Im Anschluss wurde die Verwendbarkeit von drei kommerziell erhältlichen In_2S_3-Pulvern für eine Dünnschicht-Präparation untersucht. Hierfür wurden ihre Struktur und Zusammensetzung sowie die strukturellen, chemischen und optischen Eigenschaften der aus ihnen resultierenden Dünnschichten analysiert. Es wurde gezeigt, dass der Einsatz von kristallinem, einphasigem In_2S_3-Ausgangsmaterial die Voraussetzung für eine kontrollierte Verdampfung ist. Mit kristallinem, einphasigem In_2S_3-Pulver konnten stöchiometrische, homogene In_2S_3-Dünnschichten mit einer indirekten Bandlücke von $(1.99 \pm 0.05\,\mathrm{eV})$ abgeschieden werden.

Durch Verwendung von einphasigem, kristallinem Ausgangsmaterial und der Entwicklung einer geeigneten Pufferprozessierung konnten hocheffiziente Cu(In,Ga)Se_2-Solarzellen mit In_2S_3-Pufferschichten präpariert werden. Eine Schlüsselrolle bei der Pufferprozessierung spielte dabei das Tempern der fertigen Solarzellen für 35 min.- 55 min. bei einer Temperatur von 200 °C. Der Temperprozess verbesserte in erster Linie den Füllfaktor und die Leerlaufspannung der Solarzellen, unabhängig davon ob an Luft oder in einer Inertgas-Atmosphäre getempert wurde. Die kontrollierte und reproduzierbare Verbesserung der Solarzellparameter ermöglichte eine systematische Analyse der durch Tempern herbeigeführten Veränderungen in Bezug auf die Ladungsträgersammlung und die dominanten Rekombinationsmechanismen. Dazu wurden Strom-Spannungs-Kennlinien in Abhängigkeit von Beleuchtung und Temperatur sowie die Quantenausbeute ausgewertet. Eine abnehmende Rotempfindlichkeit der Quantenausbeute (im Wellenlängenbereich von ungefähr

700 nm bis 1200 nm) nach dem Tempern deutete auf eine Verringerung der Raumladungszonenweite hin.

Die Ladungsträger-Rekombination konnte durch Tempern stark reduziert werden und es wurde eine Veränderung des dominierenden Rekombinationsmechanismus beobachtet. Bei ungetemperten Proben konnte er einer stark tunnel-unterstützte Grenzflächenrekombination zugeordnet werden (mit Dioden-Faktoren von bis zu 6). Nach dem Tempern war die Rekombination vergleichber mit CdS-gepufferten Referenzzellen und wurde mit einer thermisch aktivierten Rekombination in der Raumladungszone assoziiert. Durch die verringerte Rekombination nach dem Tempern konnte die Leerlaufspannung von ZnO/ In_2S_3/ Cu(In,Ga)Se_2/ Mo -Solarzellen reproduzierbar um 100 mV-150 mV erhöht werden.

Um eine Erklärung für die Verringerung der Rekombination in getemperten Proben zu finden, wurde die chemische Zusammensetzung von In_2S_3/Cu(In,Ga)Se_2-Schichtstapeln mit einer Kombination aus oberflächen- und volumensensitiven Methoden vor und nach dem Tempern untersucht. Hier konnte eine ausgeprägte Diffusion von Kupfer aus der Cu(In,Ga)Se_2-Schicht in die In_2S_3-Schicht nachgewiesen werden. Im Einzelnen wurden dazu untersucht: (1) das integrale Kupfer-Signal von Kupfer in der In_2S_3-Schicht mit Hilfe von Hochenergie-Photoelektronen-Spektroskopie (HIKE), (2) die ansteigende Kupfer-Konzentration an der In_2S_3-Oberfläche mit konventioneller Photoelektronen-Spektroskopie (XPS) und (3) die Kupfer- Verteilung in der In_2S_3-Schicht mit energiedispersiver Röntgenspektroskopie (EDX). Mit allen drei Methoden wurde eine klare Kupfer-Diffusion in das In_2S_3 und eine Löslichkeitsgrenze von 4 % bis 9 % für Kupfer in In_2S_3 gezeigt.

Auf Grund der entwickelten Pufferprozessierung und der nachgewiesenen Kupfer-Diffusion konnten neue Rekordwirkungsgrade für Solarzellen mit Cu(In,Ga)Se_2-Absorbern und verdampften Pufferschichten erzielt werden. Eine unabhängige Messung am Photovoltaik-Kalibrierlabor des Fraunhofer Institutes für Solare Energiesysteme, Freiburg, ergab einen Zellwirkungsgrad von 15.2±0.1 % (FF=75.6, j_{SC}= 29.8 mA/cm^2, V_{OC}=677 mV).

Am Ende dieser Arbeit wurden die Ergebnisse zusammengefasst und Wege vorgeschlagen, wie die Wirkungsgrade von Cu(In,Ga)Se_2-Solarzellen mit In_2S_3-Puffer in Zukunft weiter verbessert werden könnten.